SCALAR FIELDS IN COSMOLOGY AND THEIR APPLICATIONS BEYOND THE STANDARD COSMOLOGICAL MODEL

A DISSERTATION SUBMITTED TO THE GRADUATE DIVISION OF THE UNIVERSITY OF HAWAIʻI AT MĀNOA IN PARTIAL FULFILLMENT OF THE REQUIREMENTS FOR THE DEGREE OF

DOCTOR OF PHILOSOPHY

IN

PHYSICS

MAY 2025

By

Omar Fawzy Muhammed Ramadan

Dissertation Committee:

Jeremy Sakstein, Chairperson
David Rubin
Istvan Szapudi
Jason Kumar
Malik Younsi

Keywords: Cosmology, Scalar Field, Hubble Tension, Dark Energy, CP-violating ALPs

Abstract

This dissertation investigates key challenges in cosmology and astrophysics through the development and analysis of models for early dark energy, dynamical dark energy, and CP-violating axion-like particles (ALPs). First, we introduce a novel early dark energy (EDE) model, @EDE, aimed at resolving the Hubble tension by injecting energy before recombination to reduce the sound horizon size and increase the inferred value of H_0, thereby addressing the tension between early- and late-time cosmological measurements. We analyze the model's impact on the Universe's expansion history and test its viability against cosmological data. Next, we examine two dynamical dark energy models—the single-exponential quintessence model and the pixelated dark energy model—in light of recent DESI BAO observations, which show a growing preference for time-varying dark energy over a cosmological constant. While the w_0–w_a parameterization provides a better fit to the DESI data than ΛCDM, the quintessence model fails to replicate the rapid low-redshift transition in the equation-of-state implied by the data. In contrast, the pixelated model, in its simplest form with a constant pixel growth rate, is marginally preferred over ΛCDM. However, extending it to allow for time-dependent growth significantly enhances its ability to match the observed equation-of-state behavior. Lastly, we explore the cosmological and astrophysical effects of CP-violating axion-like particles, deriving constraints on their properties and evaluating their influence on neutron star structure and the mass-radius relationship. This work provides fresh theoretical perspectives and practical tools to address unresolved questions in modern cosmology and astrophysics.

"*My hair is Nu; my face is Ra; my eyes are Hathor; my ears are Wepwawet; my nose is She who presides over her lotus leaf; my lips are Anubis; my molars are Selkis; my incisors are Isis the goddess; my arms are the Ram, the Lord of mendes; my breast is Neith, Lady of Sais; my back is Seth; my phallus is Osiris; my muscles are the Lords of Kheraha; my chest is he who is greatly majestic; my belly and my spine are Sekhmet; my buttocks are the Eye of Horus; my thighs and my calves are Nut; my feet are Ptah; my toes are living falcons; there is no member of mine devoid of a god, and Thoth is the protection of all my flesh*"

–The Egyptian Book of the Dead, Spell 42

Acknowledgments

This work would not have been possible without the constant support and guidance of my dear father, Fawzy Ramadan. He is the role model I strive to emulate, even if only in the smallest fraction. His hard work, sacrifices, and the values he instilled in me have been the foundation upon which everything I have achieved is built. Words cannot fully express his profound influence on my life, but I am forever grateful for his wisdom, strength, and unyielding belief in me. None of this would have been possible without him.

I am also grateful to my loving wife. Her constant encouragement, patience, and love have been a source of strength throughout this journey. Her support in both the good times and the challenging moments has meant everything.

Lastly, I am deeply thankful to my family and friends for their unwavering support and belief in me. Your encouragement has been a constant source of motivation throughout this journey.

Preface

This dissertation is based on research carried out throughout my Ph.D., culminating in the following four publications:

1. O. F. Ramadan, T. Karwal, and J. Sakstein, "Attractive proposal for resolving the Hubble tension: Dynamical attractors that unify early and late dark energy," *Phys. Rev. D* **109**, 063525 (2024) [arXiv:2309.08082].

2. O. F. Ramadan, J. Sakstein, and D. Rubin, "DESI constraints on exponential quintessence," *Phys. Rev. D* **110**, L041303 (2024) [arXiv:2405.18747].

3. J. J. Heckman, O. F. Ramadan, and J. Sakstein, "First constraints on a pixelated universe in light of DESI observations," *Phys. Rev. D* **111**, 023510 (2025) [arXiv:2406.04408].

4. O. F. Ramadan, J. Sakstein, and D. Croon, "Cosmology and Astrophysics of CP-Violating Axions," [arXiv:2408.02294].

The specific contributions I made to each publication are outlined below:

- **Article 1:** Original research is presented in Chapter 4. Building on the initial idea proposed by the advisor to apply the dynamical systems framework to early dark energy models to address the Hubble tension, I surveyed the literature for scalar field potentials satisfying the attractor conditions, derived the dynamical system and performed the linear stability analysis, and identified potentials capable of unifying both early- and late-time dark energy behavior within a single scalar field framework. I implemented the dynamical attractor model with a double-exponential scalar potential into the CLASS Boltzmann solver [1, 2], performed the full numerical analysis including likelihood code setup, conducted cosmological parameter inference using both MCMC and nested sampling methods on the UH HPC cluster, generated all figures and performed all calculations, and contributed substantially to the interpretation of results and manuscript preparation.

- **Article 2:** Original research is presented in Chapter 5.1. Implemented the single-exponential quintessence model into the CLASS Boltzmann solver [1, 2], performed the full numerical analysis including likelihood code setup, conducted cosmological parameter inference using MCMC methods on the UH HPC cluster, generated all figures and tables, wrote the results section, and carried out the statistical interpretation of findings.

- **Article 3:** Original research is presented in Section 5.2. Implemented the predictions for the dark energy equation of state given by Eqn. (5.9) into the CLASS Boltzmann solver [1, 2], performed the full numerical analysis including likelihood code setup, conducted cosmological parameter inference using MCMC methods on the UH HPC cluster, generated all figures and tables, and wrote the results section including the statistical interpretation of findings.

- **Article 4:** Original research is presented in Chapters 7, 8, and 9. On the theoretical side, derived the minima of the CP-violating ALP potential (Eqn. (7.10)), the critical density ρ_c above which the minima disappear, and the effective mass m_{eff} (Eqn. (7.11)). In the cosmological context in Chapter 8, I derived the critical redshift at which minima form (Eqn. (8.2)), solved the cosmological Klein-Gordon equation both numerically (Eqn. (8.1)) and analytically (Eqn. (8.6), later confirmed by the advisor), and derived the timescale t_{break} (Eqn. (8.5)) marking the onset of sinusoidal oscillations in the early Universe. Carried out calculations related to nucleon mass variation and derived all relevant cosmological bounds. Independently reproduced the cosmological scenarios presented in Subsection 8.2, although they were initially identified and derived by my advisor. Generated all cosmological figures; D. Croon later modified figure color schemes for visual clarity. Modified publicly available code from Ref. [3] to incorporate model-specific constraints in the cosmological bounds plot (Fig. 8.1) and astrophysical bounds plot (Fig. 9.2), with subsequent color adjustments made by D. Croon.

  On the astrophysical side in Chapter 9, solely derived the modified Tolman-Oppenheimer-Volkoff (TOV) equations (Section 9.2) appropriate for the CP-violating ALP model, developed a custom numerical solver for the

modified TOV system (Section 9.3), parallelized the code using Python's `ProcessPoolExecutor`, and conducted the full numerical analysis on the UH HPC cluster. Calculated constraints on neutron star mass-radius relationships, and interpreted the results. The translation of Post-Newtonian (PPN) parameters γ and β into the language of CP-violating ALPs (Section 9.6) was carried out by the advisor, while the subsequent calculation of bounds was performed by the student. Contributed substantially to the writing of the results sections and the interpretation of findings. Wrote the appendix section detailing the numerical algorithm and contributed to the writing of figure captions, but did not contribute substantially to the main text of the manuscript.

In all cases, I was the primary contributor to the analytical derivations, numerical implementations, data analysis, and production of results, under the supervision and guidance of Dr. Jeremy Sakstein.

Contents

List of Figures

List of Tables

Part I

Overview of Standard Cosmology

1 State of Modern Cosmology

> *"So, we need not dwell upon the feature of illusion. Rather let us, recognizing the real nature of the Universe, seek to understand its mental laws, and endeavor to use them to the best effect in our upward progress through life, as we travel from plane to plane of being"*
>
> – Three Initiates, The Kybalion 1908

In 1915, Albert Einstein revolutionized our understanding of gravity with the publication of his General Theory of Relativity (GR) [4]. In contrast to Newtonian gravity—which describes gravity as a force acting instantaneously at a distance between masses—GR offers a geometric interpretation: gravity arises from the curvature of spacetime caused by energy and momentum. In this framework, the motion of matter and radiation is governed by the geometry of spacetime, with particles and light following geodesics shaped by that curvature.

This curvature is governed by the Einstein field equations, which relate the geometry of spacetime—encoded in the symmetric rank-2 metric tensor $g_{\mu\nu}$—to the energy and momentum content described by the stress-energy tensor $T_{\mu\nu}$. As a result, all forms of energy and momentum act as sources of gravity, determining how matter and light move through spacetime.

The first major test of GR came on May 29, 1919, during a total solar eclipse. Sir. Arthur Eddington led expeditions to Sobral, Brazil, and Príncipe, an island off the west coast of Africa, to observe starlight bending around the Sun's gravitational field, a prediction of GR. The successful observation of light bending as it passed near the Sun validated Einstein's theory, providing compelling evidence that spacetime curvature influenced the paths taken by light rays [5], in agreement with GR's predictions.

This pivotal experiment not only confirmed the theory but also marked the birth of modern cosmology. It opened the door to a new understanding of cosmic phenomena, from black holes to the expanding Universe itself. The Friedmann-Lemaître-Robertson-Walker (FLRW) metric [6, 7], a family of isotropic and homogeneous solutions to the Einstein field equations, further extended the applications of GR to the cosmos by providing a cosmological model that describes a homogeneous and isotropic Universe, laying the foundation for modern cosmological models. Among these, the ΛCDM model is known as the standard cosmological model. ΛCDM is the widely accepted framework that best fits a wide array of cosmological data, including the large scale structure (LSS) of the Universe [8], the cosmic microwave background (CMB), and the expansion of the Universe [9, 10]. This model builds on the FLRW metric by incorporating two key components: a cosmological constant, Λ, and cold dark matter (CDM).

The cosmological constant, Λ, is often associated with the vacuum energy of spacetime and represents a form of dark energy—an energy component, responsible for the accelerated expansion of the Universe. It is characterized by a constant energy density and a constant equation of state (EoS) of $w = -1$, none of which change over time. Observations of distant supernovae [11, 12], the CMB [10], and baryon acoustic oscillations (BAO) [13, 14] all provide strong evidence that the Universe is not only expanding but doing so at an accelerated rate. In addition, weak gravitational lensing surveys, such as the Kilo-Degree Survey (KiDS) [8], further support this by mapping the distribution of dark matter and measuring the growth of structure, offering independent confirmation of the role of dark energy in driving the expansion. The addition of Λ allows the ΛCDM model to account for this accelerating expansion and provides a good fit to the observed data.

On the other hand, CDM represents a form of invisible matter that interacts gravitationally but not electromagnetically, meaning it does not emit, absorb, or reflect light. Observational evidence for dark matter comes from several key sources. For example, rotation curves of spiral galaxies show that stars orbit at nearly constant speeds even far from the galactic center, where visible matter alone cannot explain the gravitational pull [15]. Gravitational lensing, particularly in systems like the Bullet Cluster, reveals mass distributions that

cannot be accounted for by baryons alone [16]. The "cold" aspect of CDM refers to the suggestion that dark matter particles are slow-moving, non-relativistic, which plays a crucial role in the formation of LSS [17, 18]. The cold nature allows dark matter to clump and collapse into regions of overdensities in the early Universe which leaves behind regions of underdensities. These small fluctuations in density serve as the seeds for structure formation. If dark matter were "hot" and relativistic, its particles would smooth out these fluctuations by streaming out of the overdense regions, suppressing the formation of galaxies and clusters [9, 19, 20]. However, because CDM lacks the thermal energy needed to escape gravitational wells, it remains bound within these overdensities, allowing them to grow over time. This process leads to the hierarchical formation of structure, where small structures such as galaxies form first, later merging to form larger structures like galaxy clusters [21]. CMB measurements [9, 10] provide further evidence for CDM by revealing patterns of temperature anisotropies that trace fluctuations in the early Universe. Without CDM, the early density fluctuations would have not grown enough to form the distribution of galaxies and galaxy clusters we currently observe [9, 19]. The success of the ΛCDM model in explaining the observed large-scale cosmic web is largely due to this cold nature of dark matter [22].

In summary, the ΛCDM model incorporates Λ to explain the accelerating expansion of the Universe and CDM to explain the formation of structure. Together, these components make ΛCDM the most successful cosmological model to date, as it provides a comprehensive explanation for the evolution of the Universe from the early stages to the present-day.

For the aforementioned reasons, ΛCDM is known as the concordance model in cosmology. However, despite the success of ΛCDM, it comes with its own theoretical limitations. Firstly, the microphysics of both dark matter and energy are not fully understood within the model [23–25]. Secondly, advancements in technology over recent decades have unveiled new observational challenges to the validity of ΛCDM, as the model no longer accommodates all recent cosmological datasets, leading to the emergence of cosmological tensions.

A "cosmological tension" refers to a discrepancy between measurements of the same cosmological parameter obtained from different observational datasets or methods. In essence, when two different approaches to measuring a quantity

yield results that are statistically inconsistent, this discrepancy is referred to as a *tension*. Tensions can be strong, statistically significant, or weak, statistically insignificant. The literature adopts the standard threshold for statistical significance of $\sim 1.96\sigma$ which corresponds to a p-value of 0.05 (e.g., $p \leq 0.05$) in hypothesis testing. Among these tensions, the *Hubble tension* is the most statistically significant tension in modern cosmology to date. This tension arises from the conflicting values of the Hubble constant—the rate at which the Universe is expanding today, H_0. The values of H_0 inferred from early-Univsere measurements, such as those from the CMB [9, 10] and BAO [13, 26–28], are systematically lower, while late-Universe, direct measurements, such as those from distance ladder calibrations [29, 30] and gravitationally lensed quasars [31], yield higher values. The strongest tension in data, now reaching $\sim 5\sigma$, exists between the ΛCDM model's fit to CMB data, which gives $H_0 = (67.4 \pm 0.5)$ km/s/Mpc [10], and measurements from the SH0ES collaboration, which determined $H_0 = (73.04 \pm 1.04)$ km/s/Mpc [30] using a Cepheid and type-Ia supernova distance ladder.

Another tension in cosmology is the S_8 tension, sometimes referred to as the σ_8 tension, albeit weaker than the Hubble tension, it arises from discrepancies in the measurement of the clustering amplitude of matter in the Universe. S_8 is a parameter that describes the clustering strength on scales of $8h^{-1}$ Mpc, where h is the Hubble constant in units of 100 km/s/Mpc. Physically, S_8 quantifies how matter is distributed and the extent to which it clumps under gravity. A higher value of S_8 corresponds to more pronounced structure formation, meaning a greater amplitude of matter fluctuations, while a lower S_8 implies less clustering. The tension manifests as a mismatch between S_8 values inferred from early-Universe observations, such as those from the CMB [10], which predict more structure, and the late-Universe data from LSS surveys, such as weak gravitational lensing, cosmic shear, and galaxy clustering [8, 32], which predicts less structure. Recent analyses find that CMB-based measurements give $S_8 = 0.827 \pm 0.016$, whereas late-Universe data from surveys like KiDS-1000 [8] and DES Year 3 [32] suggest a lower value of $S_8 = 0.776 \pm 0.017$. This S_8 tension, currently around $2 - 3\sigma$, raises questions about the consistency of the ΛCDM model across different epochs.

Lastly, recent datasets such as Union3 [33] and the 5-year results of the Dark Energy Survey supernova program (DESY5) [34] have shown mild preferences for dynamical dark energy over a cosmological constant Λ, generally at the 1–2σ level. In contrast, the Dark Energy Spectroscopic Instrument (DESI) [35] has reported a stronger preference, reaching up to 3.9σ, primarily driven by BAO measurements. For instance, the Union3 dataset, which combined over 2,000 supernovae, suggests slight deviations from a constant Λ. DESY5 provides high-precision measurements of the expansion history from supernovae alone, while DESI contributes constraints from BAO and galaxy clustering, with its findings showing a more statistically significant tension with the ΛCDM baseline at the 3.9σ level. These datasets hint at possible deviations in the dark energy equation of state, $w(z)$, suggesting that a dynamical dark energy model may provide a better fit. While these tensions are not yet definitive, they motivate further investigation into alternatives to the cosmological constant. In this dissertation, I explore such alternatives within the framework of GR, focusing on scalar field extensions that address open problems including the Hubble tension, the nature of dark energy, and dark matter.

Scalar fields play a crucial role in various areas of cosmology, offering flexible theoretical frameworks for understanding both the early and late stages of the Universe. They are already fundamental to particle physics, quantum field theory, and arise naturally in string theory from the compactification of higher dimension theories to a four-dimensional spacetime. In cosmology, scalar fields are often real, single-component fields that take a value at every point in space and time with no direction. While real scalar fields are commonly employed, more general cases may involve complex scalar fields, which could include a phase. In cosmological contexts, they are fundamental in models of quintessential dark energy [36–40], which propose that the dynamic nature of scalar fields could drive the observed acceleration of the Universe's expansion. They are often used in such models because they are the simplest framework that can model a dynamical dark energy. Additionally, scalar fields have also been employed to develop models of dark matter such as fuzzy dark matter [41, 42] and axion-like particles (ALPs) [43, 44]. In such models, ultra-light scalar fields, typically with masses 10^{-24} eV $< m < 10^{-22}$ eV, could account for dark matter in the Universe and are proposed as alternative models to the well-motivated

Weakly Interacting Massive Particles (WIMPs) [45]. Moreover, scalar-tensor theories, which couple scalar-fields to GR, offer potential modifications to GR; these theories imply that scalar fields can alter the gravitational interaction at cosmological scales aiming to explain the bizarre phenomena that we associate with dark energy and dark matter. For dark matter, the scalar field mass needs to be sufficiently light to affect megaparsec scales, while for dark energy, it must operate on gigaparsec or horizon scales H_0^{-1} [24, 46–49].

The structure of this dissertation is organized as follows. It comprises five main parts. The current part serves as a general introduction to cosmology and the applications of scalar fields within this domain, while Parts II-IV explore specific research topics that are connected to the main theme of this dissertation: scalar fields in cosmology and their implications beyond the standard cosmological model. Each part includes a domain-specific literature review, detailed research findings, and a concluding summary. Finally, Part V offers a summary of the key findings and outlines future research directions.

In Part II, I present my research on scalar field resolutions that attempt to address the Hubble tension. Specifically, I utilize a scalar field model within a dynamical systems framework. This work has been published in Physical Review D [50].

In Part III, I derive the Bayesian posteriors for two distinct dynamical dark energy models in light of the recent dataset published by the DESI collaboration, one of which is a scalar field model and the other is motivated by string theory. I also compare my findings with DESI's and provide hints for future studies. The work for this part is divided into two sections, one for each model. Both the scalar field model and the string-theory-inspired model have been published in Physical Review D [51, 52].

Lastly, Part IV explores the cosmological and astrophysical implications of CP-violating ALPs with Yukawa couplings to baryonic matter. Cosmologically, the model offers a unique dynamical dark energy framework, distinct from standard axion quintessence [53], driven by the CP-violating coupling. This framework provides a potential unification of dark energy and dark matter through a single scalar field. Astrophysically, the coupling introduces a phenomenology that could influence the structure of compact objects, particularly their mass-radius relationships. Additionally, novel constraints on the ALP parameter space were

derived, offering valuable guidance for future experimental efforts. This work is currently under peer review with the Journal of Cosmology and Astroparticle Physics (JCAP) and is accessible on arXiv [54].

With this roadmap in place, we now begin by reviewing the principles and theoretical basis of the standard model of cosmology, ΛCDM.

1.1 Modern Cosmology

Following the foundational principles laid out by GR, cosmologists have endeavored to formulate a comprehensive theory that describes the Universe on the largest scales. Central to this pursuit is the *cosmological principle* which states that the Universe is isotropic (the same in all directions) and homogeneous (the same at every point); this principle has proven to be remarkably successful in explaining observed cosmological phenomena such as the CMB, BAO, and the LSS of the Universe [9, 10, 14, 26–28, 55]. The FLRW metric embodies the cosmological principle, providing the most general metric compatible with the assumptions of homogeneity and isotropy. It describes a spacetime with maximally symmetric spatial slices—meaning that, at each moment in time, the spatial geometry has the highest number of symmetries possible for a space with constant curvature. This metric forms the foundation of the ΛCDM model and is given by

$$ds^2 = -dt^2 + a(t)^2\left(\frac{dr^2}{1-kr^2} + r^2 d\Omega^2\right), \tag{1.1}$$

Here, $a(t)$ is the scale factor that describes how distances in the Universe expand or contract over time, r is the comoving radial coordinate, and $d\Omega$ represents the surface area element on a unit 2-sphere. The parameter k denotes the spatial curvature, with $k = 0$ for a flat Universe, $k = +1$ for a closed Universe corresponding to a 3-sphere, and $k = -1$ for an open Universe corresponding to a 3-hyperboloid. The cosmological principle reduces the ten independent components of the metric to a single dynamical degree of freedom, $a(t)$, due to the imposed symmetries. The metric also has a rescaling symmetry upon the transformation

$$a \to \lambda a, \quad r \to r/\lambda, \quad k \to \lambda^2 k, \tag{1.2}$$

which means that the geometry of the spacetime is invariant under the simultaneous transformations of a, r, and k. This allows us to fix $a(t_0) \equiv 1$ where t_0 is the current age of the Universe. This renders $a(t)$ dimensionless and the dimensions are then absorbed into r and k. Before diving into the equations, it is worth defining some useful quantities that are often used in cosmology. The Hubble parameter

$$H(t) = \frac{\dot{a}}{a}, \tag{1.3}$$

where a dot denotes a derivative with respect to time, is the rate at which the Universe is expanding (or contracting). This is a physical observable that is constrained through observations. The value of the Hubble parameter today is known as the *Hubble constant*, H_0, which I briefly mentioned above. The constant was introduced by Edwin Hubble and suggested an expanding Universe through the relation

$$v = H_0 D, \tag{1.4}$$

where v is the recessional velocity of a distant object, H_0 is the Hubble constant, and D is the proper distance to the object. This relationship implies that objects farther away recede faster, suggesting an expanding Universe.

1.1.1 Distances

For a precise definition of physical distances and velocities, we must distinguish between the *physical distance* x, and the *comoving distance* r, which appears in the FLRW metric. Comoving distance, r, measures the distance between objects moving with the cosmic expansion which remains fixed as the Universe expands. In contrast, physical distance, x, includes the effect of cosmic expansion, and it related to comoving distance via the scale factor

$$x = a(t)r\,. \tag{1.5}$$

To find the physical velocity, we difference x with respect to time

$$v_{phys} = \frac{dx}{dt} = a(t)\frac{dr}{dt} + r\frac{da}{dt} = v_{peculiar} + Hx\,, \tag{1.6}$$

where $v_{peculiar}$ is the *peculiar velocity* of the object—the velocity measured by an observer moving with the *Hubble flow*—and Hx is the Hubble flow, the component of velocity due to the cosmic expansion.
Another common quantity often used is the *redshift*. One can use the FLRW metric (1.1) to show that the wavelength of a photon is proportional to the scale factor such that $\lambda \propto a(t)$. This allows the introduction of a new physical quantity

$$z \equiv \frac{\lambda_{obs} - \lambda_{emitted}}{\lambda_{emitted}}\,, \tag{1.7}$$

where λ_{obs} is the observed wavelength of a photon today, and $\lambda_{emitted}$ is the wavelength of the photon when it was emitted from its source. The redshift quantifies the fractional difference between the observed and emitted wavelengths. Using $\lambda \propto a(t)$, where $a(t_0) = 1$, we can relate the redshift to the scale factor through

$$1 + z = \frac{1}{a(t)}\,. \tag{1.8}$$

This allows us to use z as our dynamical parameter, which is often more convenient than the scale factor in cosmological calculations. At the present time, corresponding to $a(t_0) = 1$, the redshift is $z = 0$, and it increases as we observe events further back in time.

Aside from the distances mentioned above, there are other types of distances useful in cosmology, such as the *luminosity distance* and the *angular diameter distance*. The former is used when relating the observed brightness of an object to its absolute luminosity. It is defined such that the observed flux F of an object at a distance r with absolute luminosity L is given by

$$F = \frac{L}{4\pi r^2}\,. \tag{1.9}$$

This equation is valid only for a static Minkowski Universe. To generalize the concept of luminosity distance to an expanding Universe, several factors modify the relationship between observed flux and intrinsic luminosity in an FLRW spacetime. First, when light from a distant source, such as a supernova, reaches an observer today (at t_0), the proper area of a sphere centered on the source is $4\pi r^2$, where r is the comoving distance. As a result, the observed flux F is reduced by a factor of $1/4\pi r^2$ due to geometric spreading of light.

Additionally, the rate of photon arrival at the observer is diminished by a factor of $1/(1+z)$. This reduction arises because the expansion of the Universe stretches the time intervals between successive wave fronts of light, effectively reducing the observed frequency of photon arrivals. Furthermore, the energy of each photon received by the observer is also diminished. Specifically, the energy E_{obs} of the observed photons today is less than the energy E_{emitted} at the time they were emitted by the source, reduced by another factor of $1/(1+z)$. This is a direct consequence of redshifting. Taking these effects together, the observed flux F relates to the intrinsic luminosity L of the source through a modified equation for an expanding Universe

$$F = \frac{L}{4\pi D_L^2} \tag{1.10}$$

where $D_L = (1+z)r$ is the luminosity distance.

The *angular diameter distance* D_A, on the other hand, relates the physical size of an object to its observed angular size θ through

$$D_A = \frac{L}{\theta}\,, \tag{1.11}$$

where L is the physical size of the object. In a flat FLRW Universe, the angular diameter distance is related to the comoving distance r by

$$D_A = \frac{r}{1+z}\,, \tag{1.12}$$

which corresponds to the distance between the observer and the object at the time the light was emitted. Furthermore, the luminosity distance and angular diameter distance are connected by the relationship

$$D_A = \frac{D_L}{(1+z)^2}\,. \tag{1.13}$$

With these foundational concepts established, we now turn to the Friedmann Universe, which describes the dynamics of an expanding cosmos governed by the FLRW metric.

1.1.2 Friedmann Universe

To find the evolution equations, one needs to treat both sides of the Einstein field equations. The equations are given by

$$G_{\mu\nu} \equiv R_{\mu\nu} - \frac{1}{2} R g_{\mu\nu} = \frac{8\pi G}{c^4} T_{\mu\nu}, \tag{1.14}$$

where $G_{\mu\nu}$ is the definition of the Einstein tensor, $R_{\mu\nu}$ is the Ricci tensor, R is the Ricci scalar, $g_{\mu\nu}$ is the metric tensor, $T_{\mu\nu}$ is the energy-momentum tensor, c is the speed of light, and G is the gravitational constant. From now on, we will work in natural units where $\hbar = c = 1$. We also use a metric with a mostly positive signature $(-,+,+,+)$, which is the standard convention in cosmology.

The FLRW metric in Eqn. (1.1) is used to find the left-hand side of the Eqn. 1.14. Then, we need to specify the energy-momentum (EM) tensor. It is standard in GR and cosmology to model the Universe's components as non-interacting fluids represented by a perfect fluid's EEM tensor. This assumption stems from the cosmological principle, which imposes homogeneity and isotropy on large scales. A perfect fluid is the most general description consistent with these symmetries, characterized by uniform pressure and energy density. It is given by

$$T_{\mu\nu} = (\rho + P) U_\mu U_\nu + P g_{\mu\nu} = \mathrm{diag}(\rho, P, P, P)\,, \tag{1.15}$$

where ρ, P, and U^μ are the energy density, pressure, and the four-velocity vector of the fluid relative to an observer, respectively. The four-velocity is normalized and time-like

$$U^\mu U_\mu = g^{\mu\nu} U_\mu U_\nu = -1 \tag{1.16}$$

where $U^\mu = (1, 0, 0, 0)$ for a comoving observer. The pressure, P, of a perfect fluid is related to the energy density, ρ, through the EoS, $P = P(\rho)$. In cosmology, we often use a simple EoS of a *barotropic* fluid, which takes the form

$$P = w\rho\,, \tag{1.17}$$

where $w = P/\rho$ is the EoS parameter. We will often refer to w simply as the EoS. Since the standard cosmology model includes a cosmological constant,

Λ, we will find the evolution equations with a cosmological constant included. The Einstein field equations with a cosmological constant are given by

$$G_{\mu\nu} + \Lambda g_{\mu\nu} = 8\pi G T_{\mu\nu}\,, \tag{1.18}$$

Using the FLRW metric in Eqn. (1.1), EM tensor in Eqn. (1.15),in Eqn. (1.18), we find

$$H^2 \equiv \left(\frac{\dot{a}}{a}\right)^2 = \frac{8\pi G}{3}\rho + \frac{\Lambda}{3} - \frac{k}{a^2}\,, \tag{1.19}$$

$$\frac{\ddot{a}}{a} = -\frac{4\pi G}{3}(\rho + 3P) + \frac{\Lambda}{3}\,, \tag{1.20}$$

From now on, we will drop the curvature terms as the Universe is spatially flat according to the most up-to-date experiments [9]. It is worth noting that ρ and P above are the sum of all contributions from the different species. Since they are not interacting, the EM tensor is covariantly conserved, independently, such that $\nabla_\mu T_i^{\mu\nu} = 0$ is true for any cosmological species i. This leads to a continuity equation for each species

$$\dot{\rho}_i + 3H(\rho_i + P_i) = 0. \tag{1.21}$$

Eqns. (1.17), (1.19), (1.20), and (1.21) close the system of equations and can be used to evolve a Universe, provided knowledge of the cosmological species, their EoS, and initial conditions for their densities. The standard cosmological model contains three components: non-relativistic matter (baryonic and dark), radiation, and a cosmological constant. The EoS for each component is

$$w = \begin{cases} 0 & \text{non-relativstic matter,} \\ \frac{1}{3} & \text{radiation,} \\ -1 & \text{vacuum.} \end{cases} \tag{1.22}$$

For the EoS above, or any arbitrary constant EoS, we can solve Eqn. (1.21) to find

$$\rho = \rho_0 a^{-3(1+w)} = \begin{cases} \rho_0 a^{-3} & \text{non-relativstic matter,} \\ \rho_0 a^{-4} & \text{radiation,} \\ \rho_0 & \text{vacuum.} \end{cases} \tag{1.23}$$

An illuminating way to rewrite the first Friedmann equation is by combining Eqns. (1.19), (1.21), and (1.22) to find

$$H(a)^2 = H_0^2 \left[\frac{\Omega_{\gamma,0}}{a^4} + \frac{\Omega_{b,0} + \Omega_{c,0}}{a^3} + \Omega_{\Lambda,0} \right] \tag{1.24}$$

where H_0 is the Hubble constant, γ refers to radiation, b to baryons, and c to cold dark matter. $\Omega_{X,0} \equiv \rho_{X,0}/\rho_{crit}$ is the density parameter today of species X, $\rho_{crit} = 3H_0^2 M_{\rm Pl}^2$ is the *critical density*, $M_{\rm Pl} = 1/\sqrt{8\pi G}$ is the reduced Planck mass, and Λ is determined such that the Universe is closed today through the Friedmann constraint

$$1 = \Omega_m + \Omega_r + \Omega_\Lambda. \tag{1.25}$$

Going forward, we will drop the 0 subscript from the density parameters, $\Omega_{X,0}$, and we will use Ω_X to specify the density parameter of species X today for convenience. Note that the above constraint is only true for a spatially flat Universe. The total density, ρ, adds up to the critical density ρ_{crit} only for a flat Universe. By substituting Eqns. (1.23) into the first Friedmann equation (1.19), we find analytical solutions for $a(t)$ for single-component Universes

$$a(t) \propto t^{\frac{2}{3(1+w)}} = \begin{cases} t^{\frac{2}{3}} & \text{non-relativstic matter,} \\ t^{\frac{1}{2}} & \text{radiation,} \\ e^{Ht} & \text{vacuum,} \end{cases} \tag{1.26}$$

where, for the case of vacuum, the Hubble parameter H is a constant and given by $H = \sqrt{\frac{\Lambda}{3}}$. This is known as the de Sitter (dS) solution (or space), where the scale factor increases exponentially with time, and the Universe is always expanding ($\ddot{a} > 0$).

Having established the Friedmann equations and the energy-momentum contributions from different species, we now turn to the standard ΛCDM

cosmological model, which offers a precise description of the Universe's evolution based on observational constraints.

1.2 Standard ΛCDM Cosmology

The ΛCDM model, as mentioned previously, often referred to as the concordance model in cosmology, is the standard framework for understanding the evolution and LSS of the Universe. The model is built upon the Friedmann Universe discussed in the previous section. It contains two key components: dark energy, represented by a cosmological constant, Λ, and CDM. Together with ordinary matter and radiation, these components account for the observed expansion history and structure formation in the Universe. The best-fitting values for the density parameters in the ΛCDM model are provided by the Planck collaboration [9, 10] and are listed in Table 1.1. The evolution of the

Parameter	**Value**
Ω_c	0.261
Ω_b	0.049
Ω_γ	$\sim 10^{-5}$
Ω_Λ	0.6889

Table 1.1: The density parameters for cosmological species and their respective values according to the best-fitting model to the Planck collaboration 2018 [9].

density parameters in Table 1.1 is shown in Fig. 1.1. From this, we observe that the Universe began in a radiation-dominated era, transitioned through matter-radiation equality, and entered a matter-dominated phase. This was followed by matter-vacuum equality, ultimately leading to dark energy dominating the cosmic energy budget and driving the Universe toward an exact de Sitter (dS) state. This sequence aligns with the dilution rates found analytically in Eqns. (1.23): radiation dilutes as a^{-4}, matter as a^{-3}, and dark energy remains constant, as a^0. Consequently, radiation decays fastest, followed by matter, leaving dark energy to dominate.

At first glance, the Universe appears to be composed primarily of baryonic matter, radiation, and other standard model particles, yet these collectively

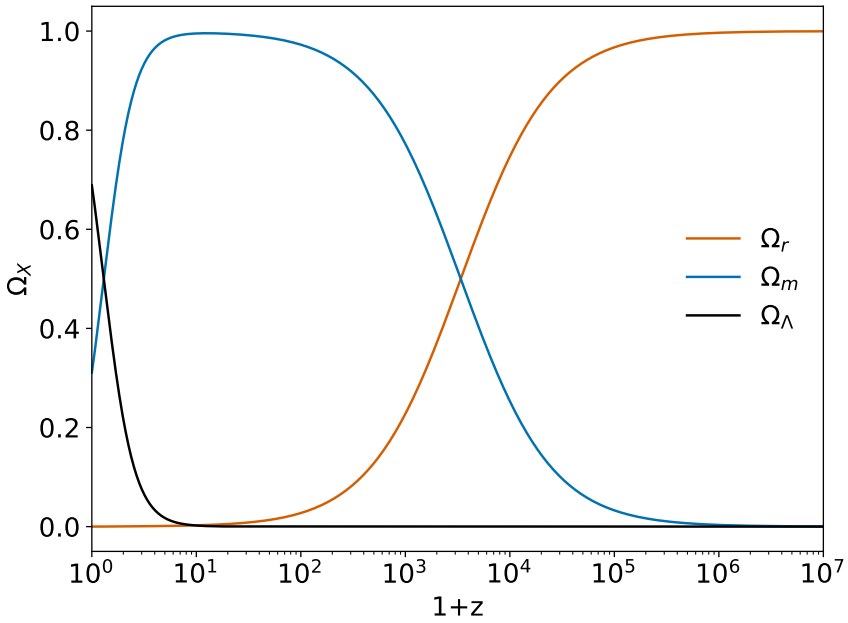

Figure 1.1: The evolution of the density parameters for the best-fitting standard ΛCDM model according to Planck 2018 [9].

represent only about 5% of the total energy density [10]. Dark matter comprises approximately 25%, providing the gravitational framework for structure formation, while dark energy constitutes around 69%, driving the observed accelerated expansion. In the following subsections, I briefly review the existing literature on dark matter and dark energy.

1.2.1 Dark Matter

In 1933, Fritz Zwicky observed that the Coma cluster was rotating at a velocity too high to be gravitationally bound by the visible mass alone [56, 57]. He hypothesized the existence of "dunkle Materie" (German for dark matter) to account for the missing mass required to explain the gravitational binding of the cluster. This marked the first inference of dark matter, suggesting that there was far more to the Universe than meets the eye. The dark matter hypothesis gained traction as more sophisticated observational techniques emerged in the 1980s. Notably, Vera Rubin and collaborators provided compelling evidence through their detailed studies of galaxy rotation curves [15, 58]. They showed

that the rotational speeds of stars in galaxies remained constant at radii where they should have decreased if only visible matter existed. This discrepancy indicated that a significant portion of the mass in galaxies was invisible and not accounted for by baryons. Currently, various cosmological surveys, particularly the CMB measurements by the Planck satellite [9, 10], BAO observations [13, 14, 26–28], and type Ia supernovae [59], have provided further evidence for the existence of dark matter. These surveys conclude that dark matter constitutes approximately 25% of the Universe's total energy budget today within the ΛCDM framework.

Despite its strong observational support, the nature of dark matter remains elusive. It is still uncertain whether dark matter is an undetected form of matter—such as a new particle species—or instead reflects a breakdown of our understanding of gravity on cosmological scales. Over the past few decades, numerous theoretical candidates for dark matter have been proposed.

One of the leading candidates is Weakly Interacting Massive Particles (WIMPs), which are hypothetical particles that interact gravitationally and through weak-scale interactions, although not necessarily mediated by the Standard Model's $W^{\pm}$ and Z^0 bosons. WIMPs naturally arise in various extensions of the Standard Model, including supersymmetry (SUSY) [45]. Large-scale direct detection experiments, such as XENON1T [60] and LUX-ZEPLIN (LZ) [61], aim to detect WIMP interactions with ordinary matter but have so far yielded null results, placing increasingly stringent limits on their properties.

Another well-explored candidate is the axion, a pseudoscalar particle originally proposed to resolve the strong CP problem in quantum chromodynamics (QCD) [62, 63]. Axions could also serve as dark matter if they were produced abundantly in the early Universe. Experimental efforts, such as the Axion Dark Matter Experiment (ADMX) [64] and the CERN Axion Solar Telescope (CAST) [65], are actively searching for axions through their predicted coupling to photons.

Other proposed candidates include sterile neutrinos, which are heavier cousins of the known neutrinos and could account for dark matter if they interact only via gravity [66]. Additionally, models like fuzzy dark matter propose ultra-light bosons with masses on the order of $m \sim 10^{-22}\,\mathrm{eV}$. At this low mass scale, the particle's de Broglie wavelength, $\lambda = 1/m$, becomes comparable to galactic

scales ($\sim$ kpc), giving it wave-like properties that suppress structure formation at small scales. This may resolve certain small-scale issues within ΛCDM, such as the overprediction of small dark matter halos, by smoothing out density fluctuations below a scale comparable to the Jeans scale [41, 42].

While particle extensions to ΛCDM remain the leading approach to explain dark matter, another common strategy is to modify gravity itself. One such framework is Modified Newtonian Dynamics (MOND), proposed by Milgrom in 1983 [67]. MOND modifies Newton's law of gravity at extremely low accelerations, suggesting that phenomena attributed to dark matter, such as galaxy rotation curves, might instead arise from a breakdown of gravity, as we know it, on galactic scales. Although MOND explains certain galactic dynamics without invoking dark matter, it struggles to account for observational constraints such as those inferred from the CMB anisotropies and large-scale structure formation [68, 69].

A related theory, Tensor-Vector-Scalar gravity (TeVeS), developed by Bekenstein [70], extends MOND by introducing additional fields to address cosmological observations, including lensing and structure growth, that MOND alone cannot handle. Despite these advancements, modified gravity theories remain under investigation and face challenges in fitting all observations as successfully as the ΛCDM model.

In summary, while particle dark matter models such as WIMPs, axions, and sterile neutrinos are actively being explored in both theoretical and experimental contexts, modified gravity theories like MOND and TeVeS offer alternative explanations for the phenomena attributed to dark matter. The true nature of dark matter—or whether it reflects the need to revise our understanding of gravity—remains one of the profound mysteries of modern cosmology.

1.2.2 Dark Energy

In the late 1990s, two independent teams revolutionized cosmology by providing concrete evidence that the Universe's expansion is accelerating [11, 12]. Using Type Ia supernovae as standard candles, they demonstrated that a Universe with $\Lambda = 0$ is inconsistent with observations, leading to the coining of the term "dark energy." In the standard ΛCDM model, dark energy is modeled

as a cosmological constant that maintains a fixed energy density even as the Universe expands, as previously discussed. However, the cosmological constant faces several theoretical challenges.

One major issue is the cosmological constant problem, which reflects a deep fine-tuning challenge. Quantum field theory (QFT) predicts a vacuum energy density around 120 orders of magnitude larger than the observed value of Λ [71–73]. Without a symmetry to suppress or forbid contributions to Λ, there is no reason for the vacuum energy to be as small as observed—already requiring extreme fine-tuning. But even if Λ is manually set to a small value, loop corrections from quantum fields continue to push it back up toward the cutoff scale. This radiative instability means that Λ must be re-tuned order by order. Both the large initial mismatch and the instability under quantum corrections stem from the same underlying issue: the lack of a symmetry protecting the smallness of Λ.

Another challenge is the coincidence problem: why is the energy density of Λ of the same order of magnitude as the present-day matter energy density, given their vastly different evolutionary histories? This apparent alignment suggests either extraordinary fine-tuning or the need for a deeper mechanism to explain it [74–76].

To address these theoretical challenges, along with recent observational hints favoring dynamical dark energy discussed in the introduction, various alternative models propose dynamic components or modifications to ΛCDM physics. These approaches aim to mitigate fine-tuning and provide mechanisms for the apparent alignment of energy densities, potentially offering insights beyond a static Λ.

A natural extension beyond the cosmological constant is to introduce scalar fields that evolve with cosmic time, resulting in dynamical dark energy. Quintessence models, for instance, describe dark energy as a slowly rolling scalar field whose potential energy drives the Universe's accelerated expansion [37]. This framework allows the energy density to evolve, potentially resolving the coincidence problem by enabling the dark energy density to track matter density over cosmic history. However, quintessence does not fully resolve fine-tuning concerns, as the field's initial conditions must still align with the observed expansion history.

Building on this, k-essence models modify the kinetic term of the scalar field's Lagrangian, allowing the field's dynamics to respond more directly to the Universe's expansion [77, 78]. In these models, the dark energy density can dynamically track the matter density during radiation and matter domination, and later deviate to drive accelerated expansion. This behavior alleviates the coincidence problem by making the dark energy density comparable to the matter density only at late times without requiring finely tuned initial conditions [79]. Additionally, because the dynamics are governed by the kinetic function rather than a finely tuned potential, some k-essence models avoid introducing an explicit cosmological constant. However, this omission does not in itself resolve the cosmological constant problem, as the vacuum energy remains UV-sensitive and radiatively unstable unless protected by a symmetry. Instead, k-essence shifts the mechanism for late-time acceleration to the scalar field's kinetic sector, thereby reducing the model's sensitivity to initial conditions while leaving the UV-sensitivity of vacuum energy unaddressed [77–79].

Other scalar field models, such as chameleon dark energy, introduce additional complexity by allowing the field's effective mass to depend on the local matter density [80, 81]. This density dependence enables the field to have a short range in high-density regions, such as within galaxies, avoiding conflicts with solar system constraints. In low-density environments, the field's influence extends over large scales, contributing to cosmic acceleration. The coupling between the scalar field and matter provides a mechanism for the field's energy density to evolve alongside matter density, directly addressing the coincidence problem.

Interacting dark energy models extend this coupling further by allowing energy exchange between dark energy and dark matter [82]. This interaction dynamically adjusts the relative energy densities of the two components, maintaining a comparable scale over cosmic history and offering a novel approach to resolving the coincidence problem [83].

Beyond scalar fields, modified gravity models provide an entirely different perspective by altering the gravitational framework itself. In $f(R)$ gravity, the Einstein-Hilbert action is generalized to include a functional dependence on the Ricci scalar, $f(R)$, which can mimic the effects of dark energy without introducing additional fields [47]. Similarly, the Dvali-Gabadadze-Porrati (DGP)

model embeds our 4D Universe in a 5D spacetime, modifying gravity at large scales to explain cosmic acceleration geometrically [84].

Lastly, holographic dark energy models, rooted in the holographic principle, propose that the dark energy density is tied to the Universe's horizon size [85]. By linking the energy density to the Hubble parameter, $\rho_\Lambda \propto H^2$, these models provide a dynamic mechanism that addresses both the fine-tuning and coincidence problems.

Despite the diversity of these approaches, none have yet surpassed ΛCDM in comprehensively fitting cosmological data. However, the fine-tuning and coincidence problems, along with emerging observational tensions, underscore the need to explore these alternatives. Before delving into the main body of this dissertation, a foundational understanding of scalar fields and their cosmological applications is necessary.

1.3 Scalar Field Cosmology

Scalar fields play a vital role in modern theoretical physics for several reasons. They are the simplest type of field in terms of mathematical structure, having a single value at every point in space and time, denoted as $\phi(\mathbf{x}, t)$. This simplicity makes scalar fields much easier to work with compared to vector or tensor fields, which introduce additional degrees of freedom and more complex interactions. In their simplest form, scalar fields require only a potential $V(\phi)$ and an equation of motion to describe their dynamics. Furthermore, they can model various phenomena without necessitating new interactions or modifications to existing ones. For these reasons, scalar fields provide a flexible framework for describing a wide range of physical phenomena across various subfields of physics. In cosmology, they appear in proposed models of inflation [86, 87], dark matter [41–43], dynamical dark energy [36–40, 72], and scalar-tensor theories of gravity [48, 88–90].

The simplest action for a cosmological scalar field, which interacts only through gravity and is therefore minimally coupled to gravity, is given by

$$S = \int d^4x\sqrt{-g}\left[\frac{M_{\rm Pl}^2 R}{2} - \frac{1}{2}\nabla_\mu\phi\nabla^\mu\phi - V(\phi)\right] + S_{\rm SM} + S_{\rm DM}\,, \tag{1.27}$$

where the action includes the Hilbert-Einstein action, the kinetic term, the potential term, and the decoupled Standard Model (SM) and dark matter (DM) sectors, described by $S_{\rm SM}$ and $S_{\rm DM}$. Given the cosmological principle, the scalar field depends only on time. Substituting the flat FLRW metric, Eqn. (1.1) with $k = 0$, into the action and minimizing it, we find the Klein-Gordon (KG) equation

$$\ddot{\phi} + 3H\dot{\phi} + \frac{dV(\phi)}{d\phi} = 0\,, \tag{1.28}$$

which governs the dynamics of the scalar field. This equation resembles a harmonic oscillator with a damping term known as *Hubble friction*. In an FLRW background, the scalar field behaves like a perfect fluid as a consequence of the symmetries of the FLRW metric, with an energy-momentum tensor given by

$$T_{\mu\nu} = \partial_\mu\phi\partial_\nu\phi - g_{\mu\nu}\left[\frac{1}{2}\partial^\mu\phi\partial_\nu\phi - V(\phi)\right]. \tag{1.29}$$

The corresponding energy density, pressure, and EoS are given by

$$\rho_\phi = \frac{1}{2}\dot{\phi} + V(\phi), \quad p_\phi = \frac{1}{2}\dot{\phi} - V(\phi), \tag{1.30}$$

$$w_\phi = \frac{p_\phi}{\rho_\phi} = \frac{\frac{1}{2}\dot{\phi} - V(\phi)}{\frac{1}{2}\dot{\phi} + V(\phi)}. \tag{1.31}$$

To understand the field's dynamics, note that the effective mass of the field around a local minimum is given by

$$m_{eff}(\phi) = \sqrt{\frac{d^2V(\phi)}{d\phi^2}}\,, \tag{1.32}$$

which sets the energy scale that separates the overdamped regime, where Hubble friction dominates and the field remains frozen, from the underdamped regime, where the field can evolve or oscillate around the minimum. In Fig. 1.2, I illustrate the evolution of a toy model for a cosmological scalar field with a simple quadratic potential, $V(\phi) = \frac{1}{2}m_\phi^2\phi^2$.

The figure is obtained by solving the KG equation, Eqn. (1.28), during radiation domination, with $H(t) = 1/2t$. In the early Universe, when $H(t) \gg$

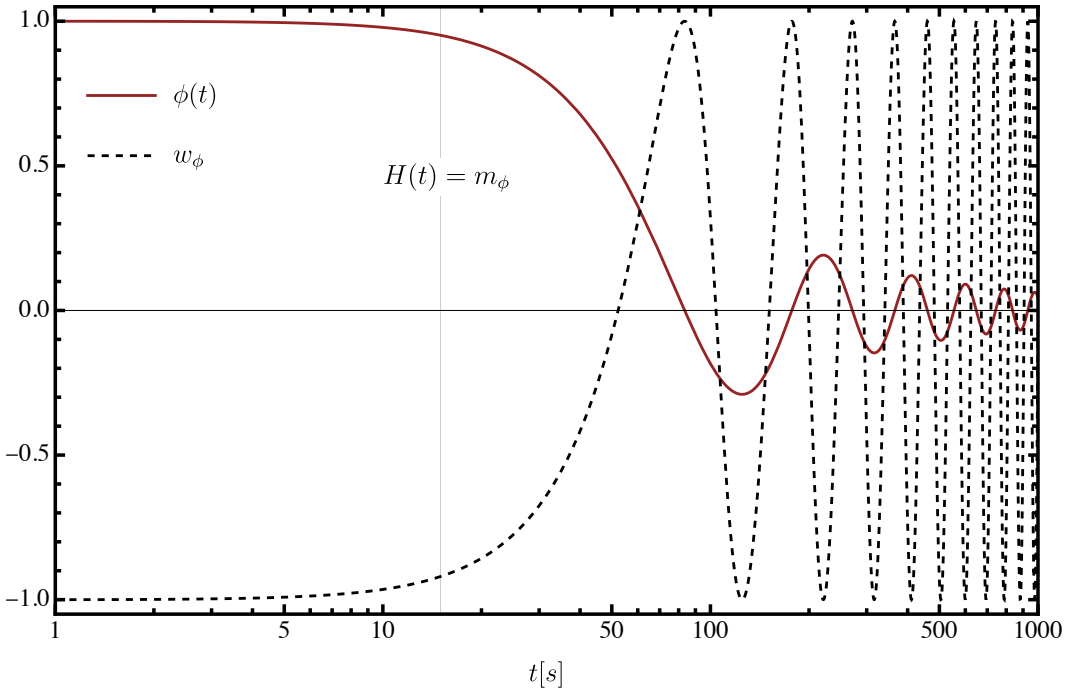

Figure 1.2: The evolution of a toy model for a cosmological scalar field with a simple quadratic potential, $V(\phi) = \frac{1}{2}m_\phi^2\phi^2$ in a radiation-dominated Universe.

$m_{\text{eff}}(\phi)$, the field is overdamped by Hubble friction, causing it to remain *frozen* with an EoS of $w_\phi \approx -1$. As the Hubble parameter decreases and approaches the field's effective mass, $H(t) \gtrsim m_{\text{eff}}(\phi)$, the field begins to *thaw*. Finally, when $H(t) \approx m_{\text{eff}}(\phi)$, the system transitions to an underdamped state, allowing the field to oscillate around its local minimum.

This demonstrates the versatility of scalar fields in cosmology. Thawing scalar fields are ideal candidates for dynamical dark energy, as their EoS can deviate from that of a cosmological constant, allowing for models where dark energy has $w_\phi > -1$. Conversely, oscillating scalar fields are excellent candidates for dark matter, as their coherent oscillations around the minimum of a quadratic (or nearly quadratic) potential yield an average equation of state $w_\phi \approx 0$, mimicking pressureless CDM [41, 91, 92]. This behavior arises when the field enters the underdamped regime, i.e., when $H(t) \lesssim m_{\text{eff}}(\phi)$. To behave as viable dark matter, the field must be sufficiently abundant and have suppressed pressure support to allow clustering on cosmological scales. See Subsection 1.2.1 for a broader review of particle and scalar field dark matter candidates.

The distinction between scalar field models in cosmology primarily refers to their cosmological dynamics, which depend on the choice of potential—governing how the field evolves—and the mass of the field, which determines the epoch at which it starts to thaw. For instance, modeling dark energy requires a field that has remained frozen since the early Universe and has only recently started thawing. This necessitates a scalar field with a mass on the order of the Hubble constant today, $m_\phi \sim H_0 \approx 10^{-33}\,\mathrm{eV}$. With the building blocks of cosmology now established, we are prepared to delve into the main body of this dissertation.

Part II

Attractive proposal for resolving the Hubble tension: Dynamical attractors that unify early and late dark energy

2 The Hubble Tension

"As above, so below; as below, so above."

– Three Initiates, The Kybalion 1908

In the previous chapter, I discussed the limitations of the concordance model, ΛCDM. In this chapter, I turn the focus to the Hubble tension, introduced in Chapter 1, as it becomes central to the discussion here. To remind the reader, the most significant tension lies between the value of the Hubble constant inferred from ΛCDM's fit to CMB data and the direct measurements by the SH0ES collaboration, currently at the 5σ level [93, 94] between the CMB data from the Planck mission and SH0ES collaboration [30] based on the Cepheid-calibrated distance ladder and type-Ia supernovae. This persistent discrepancy between early- and late-Universe measurements of H_0 highlights a potential shortcoming of the ΛCDM model and raises whether new physics may be required to reconcile these measurements. The current state of the Hubble tension is visually summarized in Fig. 2.1, adapted from Di Valentino et al. [94].

Despite extensive investigations to uncover a systematic error that might explain the Hubble tension [30, 99–104], the discrepancy has not only persisted but intensified. It seems implausible that a single systematic error could impact the diverse methods used to calibrate the cosmic distance ladder, given that different physics governs each type of celestial object involved. Alternatively, it would require an unlikely coincidence of multiple uncorrelated systematic errors to uniformly bias H_0 measurements upward across various methods.

One notable exception is the possibility that systematic effects impact the calibration and cosmological samples of Type Ia supernovae differently. In such a case, a single systematic—such as environmental dependencies related to host galaxy properties—could potentially reconcile the observed Hubble

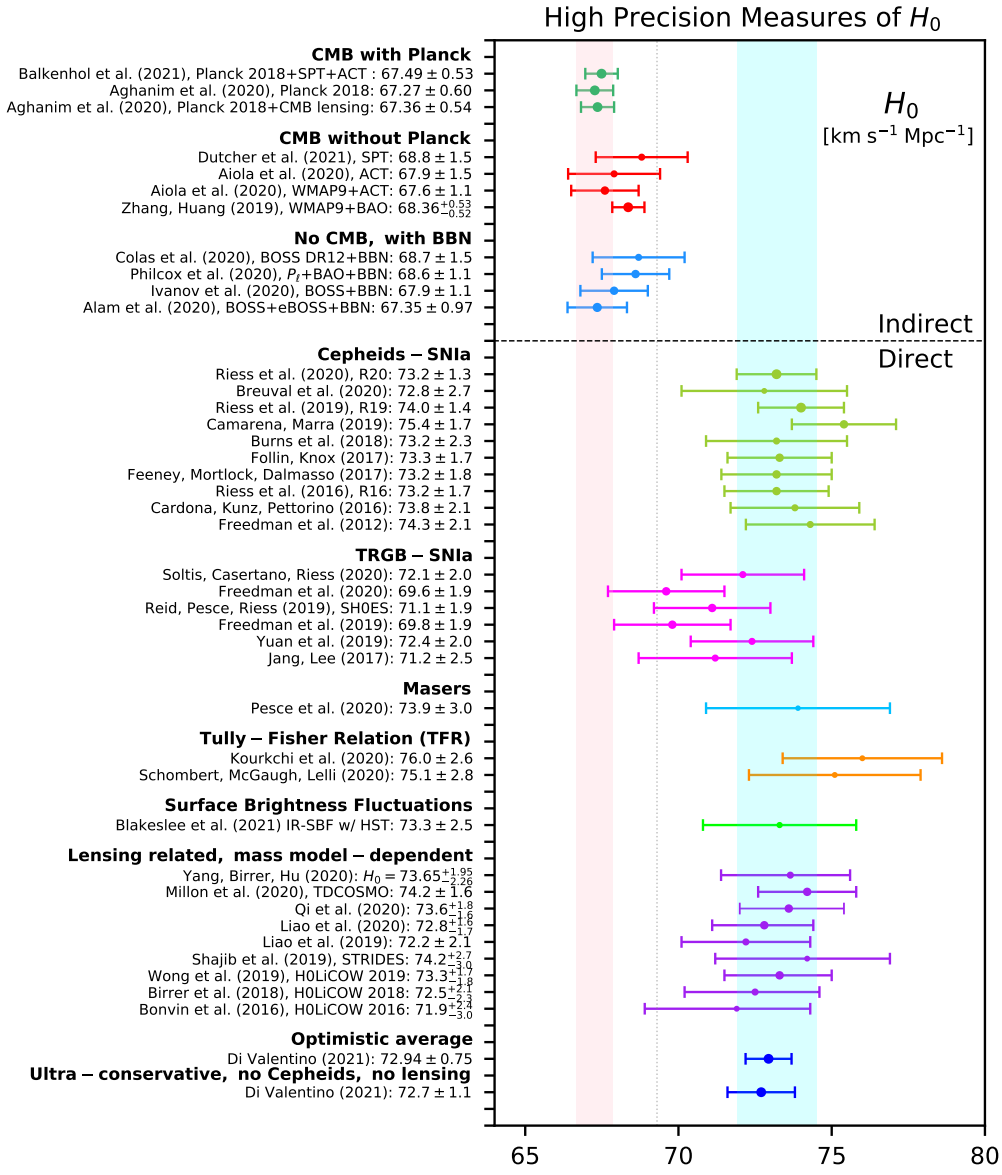

Figure 2.1: Whisker plot displaying the constraints on the Hubble constant, H_0, at the 68% confidence level, derived from various direct and indirect measurements conducted over the years. In this context, *direct* measurements refer to late-Universe determinations, while *indirect* measurements are early-Universe inferences obtained through model-dependent fits to CMB, BBN, or other early-Universe data. The cyan band indicates the $H_0 = 73.2 \pm 1.3$ km/s/Mpc measurement from the SH0ES 2020 measurement [29], while the light pink band represents the $H_0 = 67.4 \pm 0.5$ km/s/Mpc inferred value by Planck 2018 [10]. Copyright notice: Di Valentino et al [94].

tension without invoking new physics. For instance, Rigault et al. [105, 106] demonstrated that supernovae in locally star-forming regions, typical of Cepheid-host galaxies, are intrinsically fainter after standardization than those in passive environments. Accounting for this bias lowers the inferred value of H_0 and can resolve the tension. Similarly, Wojtak and Hjorth [107] showed that adopting a more appropriate extinction law for dusty Cepheid-host galaxies reduces H_0 by several km/s/Mpc, significantly alleviating the discrepancy with Planck. These results suggest that a single well-motivated systematic—either in local environment or extinction modeling—can substantially reduce, or even resolve, the Hubble tension.

Therefore, the growing disparity between early- and late-Universe H_0 measurements has increasingly led researchers to consider the possibility that this tension may stem from novel physics beyond the current standard model of cosmology [94, 108]. There are numerous approaches to addressing the Hubble tension, usually divided into two categories: early-Universe and late-Universe solutions. The former suggest theoretical modifications to the physics prior to recombination, $z > 1100$, whereas the latter modified the physics after recombination, $z < 1100$, or reassess local systematics.

Pre-recombination solutions are motivated by the idea of modifying the early expansion rate, specifically by changing the *sound horizon* at recombination without affecting late-Universe observables. The sound horizon, r_s, represents the maximum distance that acoustic waves in the primordial photon-baryon plasma could travel before recombination, effectively setting a characteristic scale for the CMB's acoustic peaks. By reducing the sound horizon, the inferred value of H_0 increases, potentially bridging the gap between early- and late-Universe measurements. Importantly, this must be done carefully to avoid disrupting the well-established physics of the CMB, such as the angular scale of the acoustic peaks or the relative heights of the peaks [108]. Additionally, any viable solution must preserve consistency with late-time probes such as BAO and LSS measurements; for a detailed discussion of the sound horizon and its connection to the Hubble tension, see Section 2.1.

One notable pre-recombination mechanism employs an axion-like scalar field, first proposed by Karwal & Kamionkowski [109], who showed that such a component could not exceed $\sim 2\%$ of the total energy density at recombination

without spoiling the CMB fit. Subsequent analyses by Poulin et al. [110] demonstrated that a $\sim 5\%$ injection at $z \approx 3000$ can alleviate the Hubble tension while diluting away rapidly afterward. However, this scenario mildly degrades the high-ℓ CMB power-spectrum fit and increases the clustering amplitude S_8 by 1–2 σ relative to weak-lensing data [111, 112]. We specifically mention this axion-based mechanism because it was the first concrete realization of the class of *Early Dark Energy* (EDE) models—which we review in detail in Section 2.1.1—and because EDE models more broadly have received the most extensive theoretical [108] and observational scrutiny [113, 114]. The other proposals, while conceptually interesting, remain less quantitatively developed and a few examples are summarized below.

- **Rock 'n' Roll.** Rapid scalar-field oscillations produce a transient dark-energy-like injection before recombination but must avoid altering the CMB damping tail [115].
- **Extra light relics ($\Delta N_{\rm eff} > 0$).** Additional relativistic species speed up the early expansion, shrinking the sound horizon, yet Big Bang nucleosynthesis and LSS constraints limit $\Delta N_{\rm eff} \lesssim 0.4$ [116, 117].
- **Interacting neutrinos.** New neutrino self-interactions suppress free-streaming and shift the acoustic phase, but CMB power-spectrum fits and oscillation experiments impose strong upper bounds [118, 119].
- **Non-minimal dark sectors.** Early dark radiation or dark matter–radiation conversion can mimic EDE's effect, though residual energy at $z < 1100$ tends to worsen agreement with CMB and BAO data [120].
- **Decaying dark matter.** Allowing a small fraction of dark matter to decay into radiation before recombination reduces the sound horizon but conflicts with CMB lensing and relic-abundance constraints [121].

A broad spectrum of post-recombination proposals has also been explored; key examples are summarized below.

- **Phantom dark energy ($w < -1$).** Super-accelerating dark energy raises H_0 but violates the null energy condition and can lead to ghost instabilities or a "big rip" [122].

- **Modified gravity.** $f(R)$ or scalar-tensor theories can enhance late-time expansion, yet most variants are excluded by Solar-System tests and the GW170817 constraint on the speed of gravitational waves [25, 90].

- **Interacting or emergent dark energy.** Energy exchange within the dark sector or time-dependent dark energy densities can lift H_0, but typically introduce fine-tuning and degrade fits to large-scale structure [123, 124].

Despite the breadth of alternatives, EDE remains the only mechanism shown to raise the CMB-inferred H_0 to $\sim 70\,\mathrm{km/s/Mpc}$ while preserving BAO distances to better than 0.1% and reducing the tension to below 2σ in combined Planck+BAO+SH0ES fits [110, 111].

2.1 Early Dark Energy

Broadly speaking EDE denotes any exotic fluid—typically a scalar field—that behaves like dark energy at early times with an EoS of $w \approx -1$, remaining frozen by Hubble friction until its effective mass becomes comparable to $m \sim H$ near recombination. At that moment—usually around matter–radiation equality ($z_c \sim 3400$)—it contributes approximately 10% of the total energy density of the Universe before rapidly diluting away [125, 126]. This transient energy injection reduces the sound horizon r_s, thereby raising the inferred Hubble constant H_0 while leaving other cosmological observables, such as the CMB power spectrum and LSS, largely unaffected [110–112]. The axion-like realization discussed above [109, 110] provides the canonical example of this class of models.

2.1.1 Phenomenology of Early Dark Energy

To see quantitatively how the transient EDE injection raises the inferred value of H_0, we examine its effect on the key distance scales. The injection of EDE temporarily increases the expansion rate, which is given by[1]

$$H(z) = H_0\sqrt{\Omega_m(1+z)^3 + \Omega_r(1+z)^4 + \Omega_{EDE}(z)}\,. \tag{2.1}$$

[1] $H(z')$ also includes contributions from vaccum energy, but we ignore them since they are negligible at the relevant epochs.

The sound horizon at recombination, $r_s(z_*)$, where $z_* \sim 1100$, is sensitive to changes in the expansion rate prior to recombination and is given by

$$r_s(z_*) = \int_{z_*}^{\infty} \frac{c_s(z')dz'}{H(z')}\,, \tag{2.2}$$

where $c_s(z')$ is the sound speed in the photon-baryon plasma. Any change in the sound horizon affects the angular size of the first CMB acoustic peak

$$\theta_* = r_s(z_*)/D_A(z_*)\,, \tag{2.3}$$

which is tightly constrained by *Planck* observations [127] to 0.03% precision, based on the TT,TE,EE+lowE+lensing+BAO data combination [128]. Here, $D_A(z_*)$ is the angular diameter distance to recombination and is given by

$$D_A(z_*) = \int_0^{z_*} \frac{dz'}{H(z')}\,. \tag{2.4}$$

To maintain the observed angular size θ_*, a reduction in $r_s(z_*)$ due to EDE must be accompanied by a corresponding reduction in the angular diameter distance. Since $D_A(z_*)$, however, depends on $H(z)$, and therefore H_0, this balancing act naturally results in a higher inferred value of H_0. From Eqns. (2.4)-(2.1), we obtain

$$H_0 = \frac{1}{D_A(z_*)} \int_0^{z_*} \frac{dz'}{\sqrt{\Omega_m(1+z')^3 + \Omega_r(1+z')^4 + \Omega_{EDE}(z')}} \tag{2.5}$$

Thus, EDE increases the inferred value of H_0 as a direct consequence of reducing the sound horizon $r_s(z_*)$, while still allowing consistency with other cosmological observables, such as the CMB power spectrum and LSS.

2.1.2 Theoretical and Observational Challenges

Despite its appeal, EDE models face several challenges. A prominent issue is the *coincidence problem*: the energy density of EDE must peak precisely at the right epoch, shortly before recombination, around matter-radiation equality ($z \approx 3400$), with a fractional density of $\Omega_{\rm EDE} \approx 0.1$ to effectively increase the

inferred H_0 [125, 129–132]. Unlike the coincidence problem associated with late-time dark energy (LDE), this issue is unique to EDE and arises from the fine-tuning required for the timing and amplitude of EDE's early contribution. Several proposals attempt to address this by introducing mechanisms that naturally trigger the EDE phase. For instance, models coupling the EDE scalar field to neutrinos suggest that as neutrinos transition from relativistic to non-relativistic—a process coinciding with matter-radiation equality—they inject energy into the EDE field, activating it at the appropriate epoch [129, 133, 134]. Other approaches explore connections between EDE and the dark sector, such as couplings to dark matter, which could provide a unified explanation [130, 135]. Another concern is the $\sim 3\sigma$ tension in S_8, the amplitude of matter fluctuations on $8\,h^{-1}\,\mathrm{Mpc}$ scales, introduced in Chapter 1. EDE models often exacerbate this discrepancy [111, 136] by predicting a higher dark matter energy density than ΛCDM.

While embedding EDE within UV-complete theories remains challenging, recent work has clarified both the theoretical constraints and the model-building options. Rudelius [137] showed—using the axion Weak Gravity Conjecture (WGC) [138, 139]—that the decay constants favored by EDE lie near, or even beyond, quantum-gravity bounds, indicating an intrinsic need for tuning. McDonough and Scalisi [140] nevertheless demonstrated that a canonical periodic EDE potential can be realized in a string framework once the requisite non-perturbative effects are arranged with care. Cicoli et al. [141] then extended this approach to fully stabilized models that reproduce the desired early energy injection and timing, but again only with delicately chosen microscopic parameters. Collectively, these studies show that UV-completing EDE is possible in principle, yet typically comes at the price of significant fine-tuning and model-building complexity.

EDE has been criticized for its ad hoc nature, appearing isolated from other dark sector components such as late-time dark energy and dark matter and for adding new parameters that introduce degeneracies and complicate parameter estimation. Several works have explored this criticism, noting the lack of a compelling theoretical framework that unifies EDE with other dark sector phenomena [111, 112, 136, 142, 143]. Taken together, these issues mean that any viable EDE scenario must be formulated so that—over its entire allowed

parameter range—its predicted CMB, BAO, and LSS signatures stay within current observational limits while the extra energy density fades promptly after recombination.

Motivated by these challenges, I propose a new approach to resolving the Hubble tension: *Attractive Early Dark Energy* (@EDE). This model employs a single quintessence scalar field, ϕ, governed by a nonlinear potential that unifies both EDE and LDE within a cohesive framework. By recasting the cosmological evolution equations into an autonomous system of differential equations and analyzing them using a dynamical systems framework, @EDE eliminates the need for fine-tuning. The evolution of the Universe is determined by the structure of the dynamical system's phase space, such that the onset and decay of EDE arise dynamically from the field evolution, without the need for externally imposed transitions near the desired epoch. Additionally, @EDE offers a theoretically compelling solution by merging EDE and LDE, reducing the degrees of freedom typically required to address the Hubble tension and the properties of LDE. This consolidation minimizes reliance on *ad hoc* ingredients.

While my collaborators and I were in the process of publishing our work, two independent groups proposed similar unification schemes for LDE and EDE [144, 145]. Although their approaches differ from ours, their emergence highlights the growing interest in unified dark energy frameworks.

Having motivated the need for a model whose early-time behavior emerges dynamically, we now turn in Chapter 3 to the key concepts and techniques of dynamical systems theory, which will provide the toolkit for constructing and analyzing @EDE in detail.

3 Dynamical Systems in Cosmology

"Nothing rests; everything moves; everything vibrates."

– Three Initiates, The Kybalion 1908

This chapter builds on the motivation outlined at the end of the previous chapter, where the use of dynamical systems was introduced as a natural framework to address the fine-tuning problems in EDE models. While the theory itself is extensive, this discussion will not encompass the entire theoretical framework. Instead, I introduce only the fundamental elements of dynamical systems theory relevant to this dissertation. For a more comprehensive treatment, I recommend referring to the textbook by Stephen Wiggins (1990) [146], which offers a comprehensive exploration of the topic. Those looking for an application of these principles specific to cosmology should refer to the work by Copeland et al.(2006) [37] and the more recent work by Bahamonde et al.(2018) [147], which thoroughly outlines their use in cosmological contexts. This chapter will cover the basics of dynamical systems, linear stability theory, and provide examples of how these concepts are applied within the cosmological framework.

3.1 What is a dynamical system?

Dynamical systems provide a powerful framework for analyzing the time evolution of systems, whether they are as simple as a swinging pendulum or as complex as the large-scale structure of the Universe. But what exactly consti-

tutes a dynamical system? At its core, a dynamical system is characterized by the following:

1. **State parameters:** Variables that describe the state of the system at a given moment in time.

2. **Phase space:** A parameter space that encompasses all possible states of the system, providing a complete description of its dynamics.

3. **Governing equations:** Differential equations that dictate how the state parameters evolve and interact over time.

Theoretically, any system that evolves over time can be modeled as a dynamical system. The challenge lies in formulating a closed set of differential equations that fully capture the system's evolution, especially in cases involving unknown physics or complex interactions. In cosmology, the ΛCDM model can be cast as a dynamical system by rewriting the Friedmann equations in the form of an *autonomous system*—a system of differential equations where the independent variable does not appear explicitly. This recasting allows one to study the system's qualitative behavior using its state variables alone. While this approach is powerful, applying it to more elaborate cosmological models can be non-trivial. However, applying this framework to more elaborate cosmological models can be non-trivial. Constructing an autonomous system requires identifying appropriate state variables and rewriting the governing equations in terms of them. A phase space is compact when each state variable is confined to a closed and bounded set, so trajectories cannot escape to infinity and all asymptotic behavior remains within the phase-space region. While it is often advantageous to work within a compact phase space to ensure that all asymptotic behaviors are captured, this is not strictly necessary—non-compact phase spaces can also yield meaningful dynamical analysis. The main difficulty lies in obtaining a closed, self-consistent set of autonomous equations when the underlying physics is complex or involves new fields, interactions, or couplings [147]. In such cases, analyzing the system's long-term behavior or steady-state configurations becomes more challenging.

Mathematically, an autonomous dynamical system is typically expressed as follows [146]

$$\dot{\mathbf{x}} = \mathbf{f}(\mathbf{x}), \tag{3.1}$$

where $\mathbf{x} = (x_1, x_2, x_3, ..., x_n) \in X$ represents a state in the phase space $X \subseteq \mathbb{R}^n$, and f is a function $f : X \longrightarrow X$. The derivative is with respect to some time parameter, $t \in \mathbb{R}$, that is not required to be the physical time. Essentially, $f(\mathbf{x})$ is a vector field on $\mathbb{R}^n$

$$f(\mathbf{x}) = (f_1(\mathbf{x}), f_2(\mathbf{x}), ..., f_n(\mathbf{x})). \tag{3.2}$$

This formulation represents a dynamical system with n coupled differential equations that describe the evolution of n variables over time. A solution to Eqn. (3.1) is called a *trajectory*, which traces the path of the system through phase space as it evolves.

Dynamical systems can be formulated to accommodate any number of dimensions, including infinite, and may be discrete or continuous. However, since cosmological dynamical systems are typically finite-dimensional and continuous, this discussion will focus exclusively on those cases.

Definition (*Fixed point or critical point*). The autonomous system (3) is said to have a fixed point if there exists $\mathbf{x} = \mathbf{x_0}$ if and only if $f(\mathbf{x_0}) = 0$.

A fixed point represents a state where the system is at "rest." However, the mere existence of such a point does not ensure that it will be reached or that the system will remain at this point indefinitely. This brings us to the concept of the stability of fixed points. A fixed point, $\mathbf{x}_0$, is considered stable if all trajectories, $\mathbf{x}(t)$, originating near it remain close to it over time, and it is deemed asymptotically stable if it is stable and all nearby solutions converge to the fixed point as $t \to \infty$. Such points are often categorized as *attractors*. Conversely, unstable points, which drive solutions away from them, are referred to as *repellers*. To understand their nature, one can linearize the system around the fixed points in question, allowing for further analysis of stability and behavior near these critical points.

3.2 Linear Stability Theory

Linear stability theory provides a method to analyze the stability of fixed points in a dynamical system. Considering the system described by Eqn. (3.1), where the right-hand side is a vector field as defined in Eqn. (3.2), and assuming that f is differentiable over X, we can expand each component of the field around the fixed point, $\mathbf{x_0}$ as

$$f_i(\mathbf{x}) = f_i(\mathbf{x_0}) + \sum_{j=1}^{n} \frac{\partial f_i}{\partial x_j}(\mathbf{x_0}) y_j + \frac{1}{2!} \sum_{j,k=1}^{n} \frac{\partial^2 f_i}{\partial x_j x_k}(\mathbf{x_0}) y_j y_k + ..., \tag{3.3}$$

where $y_i = x_i - x_0$. Linear stability theory focuses only on the first-order terms of this expansion. The object of interest here is $\partial f_i / \partial x_j$, which forms the stability matrix, also known as the Jacobian matrix in vector calculus

$$J = \frac{\partial f_i}{\partial x_j} = \begin{bmatrix} \frac{\partial f_1}{\partial x_1} & \cdots & \frac{\partial f_1}{\partial x_n} \\ \vdots & \ddots & \vdots \\ \frac{\partial f_n}{\partial x_1} & \cdots & \frac{\partial f_n}{\partial x_n} \end{bmatrix}. \tag{3.4}$$

The eigenvalues of the matrix determine the stability of the fixed point x_0. However, linear stability theory sometimes does not fully capture the stability characteristics of a fixed point.

Definition (*Hyperbolic Point*): A fixed point $\mathbf{x} = \mathbf{x_0} \in X \subset \mathbb{R}^n$ within the system $\dot{\mathbf{x}} = \mathbf{f}(\mathbf{x})$ is called *hyperbolic* if all eigenvalues of its Jacobian matrix $J(\mathbf{x_0})$ have non-zero real parts. Conversely, if any eigenvalue has a zero real part, the point is classified as *non-hyperbolic*.

Linear stability theory is valid only for hyperbolic points, where the Jacobian matrix's eigenvalues have no zero real parts. For non-hyperbolic points, where at least one eigenvalue has a zero real part, the behavior of the system near the fixed point cannot be fully described by linear stability theory. In such cases, more advanced techniques, such as Lyapunov's method or the center manifold theorem, are required. While these methods provide powerful tools for analyzing stability in more complex systems, they fall outside the scope of this work and will not be discussed here. For further details, interested readers are referred to external resources [146, 147].

3.2.1 Example: 2D Dynamical System

A straightforward example of a dynamical system is a 2D autonomous system

$$\dot{x} = f(x, y), \quad \dot{y} = g(x, y). \tag{3.5}$$

let us assume the system has a fixed point (x_0, y_0) such that $f(x_0, y_0) = 0$ and $g(x_0, y_0) = 0$. If f and g are smooth functions, the Jacobian matrix is given by

$$J = \begin{bmatrix} f_{,x} & f_{,y} \\ g_{,x} & g_{,y} \end{bmatrix}, \tag{3.6}$$

where $f_{,x} \equiv \frac{\partial f}{\partial x}$, and similar notation applies for the other derivatives. To assess the stability of the fixed point, we linearize the system near (x_0, y_0) and study the evolution of small perturbations,

$$\boldsymbol{\delta}(t) = \begin{bmatrix} x(t) - x_0 \\ y(t) - y_0 \end{bmatrix}. \tag{3.7}$$

The linearized system takes the form

$$\dot{\boldsymbol{\delta}}(t) = J(x_0, y_0)\, \boldsymbol{\delta}(t), \tag{3.8}$$

where $J(x_0, y_0)$ is the Jacobian matrix evaluated at the fixed point. The general solution is a linear combination of modes, $\boldsymbol{\delta}(t) \sim \mathbf{v}\, e^{\lambda t}$, where λ and $\mathbf{v}$ are the eigenvalues and eigenvectors of J, respectively. The eigenvalues for this 2D system are given by

$$\lambda_{1,2} = \frac{1}{2}(f_{,x} + g_{,y}) \pm \frac{1}{2}\sqrt{(f_{,x} - g_{,y})^2 + 4 f_{,y} g_{,x}}, \tag{3.9}$$

The signs of the real parts of $\lambda_{1,2}$ determine the stability: if both eigenvalues have negative real parts, perturbations decay and the fixed point is stable; if any eigenvalue has a positive real part, perturbations grow and the fixed point is unstable. Complex eigenvalues with non-zero real parts lead to oscillatory spirals, while purely imaginary eigenvalues correspond to centers with closed orbits. If one or more eigenvalues have zero real parts, the fixed point is

classified as non-hyperbolic, and linear stability theory alone cannot determine its behavior. The stability of the fixed point is summarized in Table 3.1.

Eigenvalues (λ_1, λ_2)	**Description of Equilibrium Point**
$\lambda_1 > 0, \lambda_2 > 0$	Unstable node (*repeller*): All trajectories are repelled from the point.
$\lambda_1 < 0, \lambda_2 < 0$	Stable node (*attractor*): All trajectories converge to the point as $\lim_{t\to\infty} \mathbf{x}(t) = \mathbf{x_0}$.
$\lambda_1 > 0, \lambda_2 < 0$	Saddle point: Trajectories are attracted in one direction and repelled in another.
$\lambda_1 = \alpha + i\beta, \lambda_2 = \alpha - i\beta$	If $\alpha < 0$, *stable spiral*: Trajectories spiral toward the point while oscillating.
$\lambda_1 = \alpha + i\beta, \lambda_2 = \alpha - i\beta$	If $\alpha > 0$, *unstable spiral*: Trajectories spiral away from the point while oscillating.
$\lambda_1 = i\beta, \lambda_2 = -i\beta$	Centre point: Trajectories oscillate around the point in closed orbits without converging or diverging.
$\lambda_1 = 0, \lambda_2 > 0$	Non-hyperbolic: Generally unstable due to $\lambda_2 > 0$ repelling trajectories in one direction. More analysis needed as linear stability theory is sufficient.
$\lambda_1 = 0, \lambda_2 < 0$	Non-hyperbolic: Behavior is undetermined by linear stability theory.
$\lambda_1 = 0, \lambda_2 = 0$	Non-hyperbolic: Behavior is undetermined by linear stability theory.

Table 3.1: Classification of fixed points based on the eigenvalues, λ_1 and λ_2, of the stability matrix for a 2D system.

The table outlines the stability characteristics of fixed points based on eigenvalue configurations. Below, we elaborate on the key types of equilibrium points:

1. **Stable and unstable nodes:** Fixed points where all eigenvalues have the same sign. Negative eigenvalues correspond to *attractors*, drawing nearby trajectories toward equilibrium. Positive eigenvalues result in *repellers*, driving trajectories away.

2. **Saddle points:** Fixed points with eigenvalues of mixed signs. These points attract trajectories along one direction and repel them along another.

3. **Spiral points:** Complex eigenvalues with non-zero real parts lead to spiraling behavior. If the real part is negative, trajectories spiral inward (*stable spiral*); if positive, they spiral outward (*unstable spiral*).

4. **Centre points:** Points with purely imaginary eigenvalues are called *neutrally stable*, meaning that small perturbations neither grow nor decay over time. Trajectories form closed orbits around the point.

5. **Non-hyperbolic points:** Fixed points with one or more zero eigenvalues. Linear stability theory cannot determine the behavior at such points. Advanced techniques are needed to analyze their dynamics.

This detailed understanding is essential for predicting the evolution of the system, assessing long-term behaviors, and exploring the impact of varying the initial conditions. In cases where the system possesses a single stable node, it will invariably converge to this point regardless of the initial conditions.

Although the current example is limited to two dimensions, the procedure described here generalizes directly to higher-dimensional systems. In such cases, the Jacobian matrix is constructed in the same manner, and the stability of fixed points is determined by the signs of the real parts of its eigenvalues. For a complete derivation in n-dimensions (including zero-eigenvalue cases), see Strogatz [148] or Guckenheimer & Holmes [149]. This framework is applied in the following sections to analyze cosmological dynamical systems. The ΛCDM model serves as a realistic 2D example in Section 3.3, while scalar field models in Section 3.4 introduce higher-dimensional phase spaces that require the same stability analysis tools.

3.3 Dynamical ΛCDM

Having established the foundational concepts of dynamical systems, we now turn our attention to their applications in cosmology. In this section, we explore how the concordance ΛCDM model can be reformulated within the dynamical systems framework. By rewriting the governing equations of ΛCDM,

specifically Eqns. (1.19)-(1.22), the model simplifies to a system involving only two parameters, (Ω_m, Ω_r) and is written as

$$\Omega_m' = \Omega_m(3\Omega_m + 4\Omega_r - 3)\,, \tag{3.10}$$

$$\Omega_r' = \Omega_r(3\Omega_m + 4\Omega_r - 4)\,, \tag{3.11}$$

where the prime denotes d/dN, and $N = \log(a)$. The parameter Ω_Λ is determined from the Friendmann constraint in Eqn. (1.25). This reformulation not only reduces the complexity of the system but also provides valuable insights into the evolution of the Universe without the need to solve it numerically. The system admits three fixed points, each corresponding to a distinct cosmological epoch:

1. $C = (0, 0)$: Represents the dark energy-dominated epoch.
2. $M = (1, 0)$: Represents the matter-dominated epoch.
3. $R = (0, 1)$: Represents the radiation-dominated epoch.

The Jacobian matrices evaluated at these fixed points are

$$J(C) = \begin{bmatrix} -3 & 0 \\ 0 & -4 \end{bmatrix}, \quad J(M) = \begin{bmatrix} 3 & 4 \\ 0 & -1 \end{bmatrix}, \quad J(R) = \begin{bmatrix} 1 & 0 \\ 3 & 4 \end{bmatrix}, \tag{3.12}$$

and their corresponding eigenvalues and stability classifications are listed in Table 3.2.

Fixed point	**Eigenvalues** (λ_1, λ_2)	**Stability**
C	$(-3, -4)$	Stable node
M	$(-1, 3)$	Saddle point
R	$(1, 4)$	Unstable node

Table 3.2: The fixed points of dynamical ΛCDM with their corresponding eigenvalues and stability.

As summarized in Table 3.2, the dynamical ΛCDM system is characterized by one unstable node, one saddle point, and one stable attractor. The attractor C guarantees that, irrespective of the initial conditions, the Universe ultimately

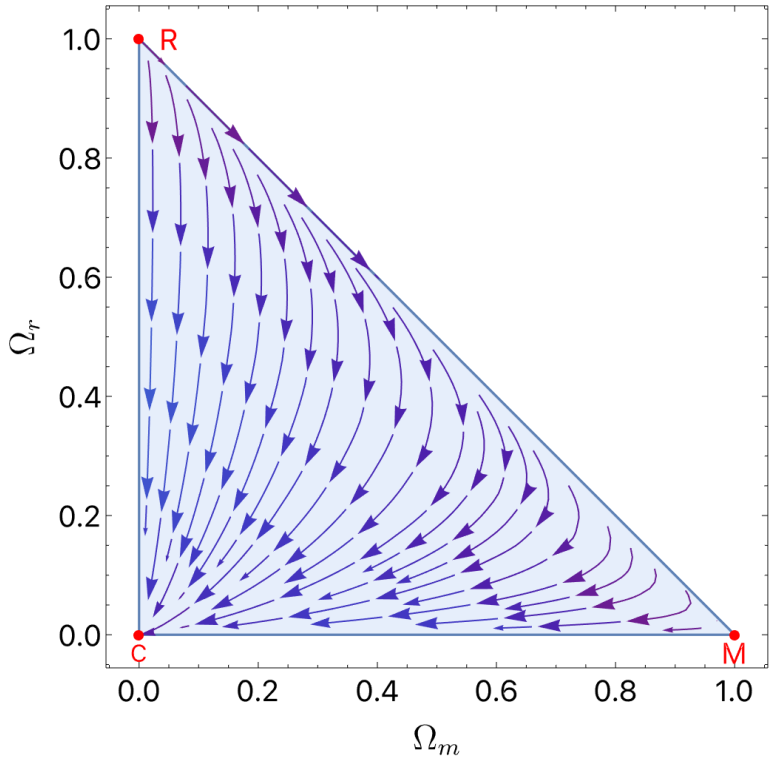

Figure 3.1: Stream plot of the phase space of the ΛCDM dynamical system. Regardless of initial conditions, the Universe ends up in dark energy domination at point C, where $\Omega_\Lambda = 1$. The evolution of the system follows the expected trajectory from ΛCDM. Initially starting from the unstable node representing radiation domination, the system moves towards the saddle point of matter domination, eventually concluding at the attractor, indicating dark energy domination.

reaches a state dominated by dark energy. This behavior aligns perfectly with the ΛCDM predictions discussed earlier in Section 1.2.

The phase-space trajectory in Fig. 3.1 reinforces the robustness of the dynamical systems approach. The graph is generated by plotting a stream plot of the vector fields in Eqns. 3.10 and 3.11 without explicitly solving the equations. The stream plot captures the flow of the system through phase space, illustrating how the Universe evolves naturally from radiation domination, through matter domination, and ultimately to dark energy domination. This behavior emerges directly from the structure of the dynamical system.

3.4 Dynamical Quintessence

Having demonstrated the utility of dynamical systems in capturing the evolution of the ΛCDM model, we now turn our attention to a broader class of models that incorporate scalar fields.

In the simplest case, where the scalar field interacts only through gravity and remains decoupled from other species, its dynamics can be described by the action in Eqn. (1.27). The scalar field's density and pressure are introduced into the Friedmann equations as additional terms, such that $\rho = \sum_i^N \rho_i = \rho_m + \rho_r + \rho_\phi$, with a similar expression for the pressure. The evolution of the scalar field is governed by the KG equation, Eqn. (1.28), which describes its dynamics under the influence of its potential, $V(\phi)$. In the context of dynamical systems, the scalar field's total density parameter, Ω_ϕ, is conventionally split into two contributions: one from the field's potential energy and the other from its kinetic energy. These are given by

$$\Omega_k = \frac{\dot{\phi}^2}{6M_{\rm Pl}^2 H^2}, \qquad \Omega_v = \frac{V(\phi)}{3M_{\rm Pl}^2 H^2}, \tag{3.13}$$

such that $\Omega_\phi = \Omega_k + \Omega_v$, where Ω_k and Ω_v represent the density contributions from the scalar field's kinetic and potential energies, respectively. Notably, in this project, any mention of Ω_k refers to the kinetic term of the scalar field and is unrelated to the curvature of the Universe. The inclusion of these densities modifies the Friedmann constraint from Eqn. (1.25) to

$$\Omega_m + \Omega_r + \Omega_k + \Omega_v = 1 \tag{3.14}$$

To systematically analyze these components within the dynamical systems framework, we introduce two key parameters, λ and Γ, that facilitate the description of the scalar field's dynamics [37]

$$\lambda \equiv -M_{\rm Pl}\frac{V_{,\phi}}{V(\phi)}, \tag{3.15}$$

$$\Gamma \equiv \frac{V(\phi)V_{,\phi\phi}}{V_{,\phi}^2}. \tag{3.16}$$

where $V_{,\phi} \equiv \mathrm{d}V/\mathrm{d}\phi$ and $V_{,\phi\phi} \equiv \mathrm{d}^2V/\mathrm{d}\phi^2$. These parameters, known as the *roll* and *tracker* parameters [37], respectively, enable the reformulation of the KG equation and the Friedmann equations into an autonomous system of differential equations

$$\Omega_m' = \Omega_m(3\Omega_m + 4\Omega_r + 6\Omega_k - 3) \tag{3.17}$$

$$\Omega_r' = \Omega_r(3\Omega_m + 4\Omega_r + 6\Omega_k - 4), \tag{3.18}$$

$$\Omega_k' = \Omega_k(3\Omega_m + 4\Omega_r + 6\Omega_k - 6) + \lambda\Omega_v\sqrt{6\Omega_k}, \tag{3.19}$$

$$\begin{aligned}\Omega_v' = {} & \Omega_v(3\Omega_m + 4\Omega_r + 6\Omega_k - \lambda\sqrt{6\Omega_k}) \\ & + \lambda\Omega_v\sqrt{6\Omega_k},\end{aligned} \tag{3.20}$$

$$\lambda' = -\lambda^2(\Gamma(\phi) - 1)\sqrt{6\Omega_k}, \tag{3.21}$$

As a consistency check, setting $\Omega_k, \Omega_v, \lambda$, and Γ to zero and using the appropriate constraint in Eqn. (1.25) recovers the ΛCDM system given by Eqns. (3.10) and (3.11). The equation for λ', Eqn. (3.21) essentially mirrors the KG equation in an alternative form. Addiotionally, the Friedmann constraint, allows us to eliminate one of the Ω's in terms of the others, reducing the dimensions of the system by one. I choose to eliminate Ω_m as it plays less of a crucial role in our work. From here on, we will eliminate Eqn. (3.17) by setting $\Omega_m = 1 - \Omega_r - \Omega_k - \Omega_v$.

The inclusion of the scalar field introduces additional complexity, as the system is no longer inherently autonomous. This is because the parameters λ and Γ—which characterize the scalar field potential—typically depend on the field ϕ, which evolves with time. This introduces explicit time dependence into the system through $\lambda(\phi(t))$ and $\Gamma(\phi(t))$, breaking the autonomy. To restore autonomy, one of the following conditions must be met:

1. $\lambda' = 0$, implying λ is constant. This corresponds to an exponential potential, $V(\phi) = V_0 \exp(-\lambda\phi/M_{\mathrm{Pl}})$, and eliminates the explicit time dependence.
2. $\lambda(\phi)$ is invertible, allowing $\phi(\lambda)$ to be expressed explicitly and $\Gamma(\phi)$ to be rewritten as $\Gamma(\lambda)$, thereby removing $\phi(t)$ from the equations.
3. Additional differential equations governing the evolution of Γ must be introduced to dynamically close the system.

The first case results in a three-dimensional phase space, $\{\Omega_r, \Omega_k, \Omega_v\}$, which has been comprehensively examined in the literature [36, 37]. I will briefly discuss its relevance in the next subsection. In the scenario where $\lambda(\phi)$ is invertible, leading to $\Gamma \equiv \Gamma(\lambda)$, the dynamics of the system are captured within four-dimensional phase space $\{\Omega_r, \Omega_k, \Omega_v, \lambda\}$. The fixed points of the dynamical system corresponds to points where Eqns. (3.17)-(3.21) are simultaneously equal to zero. To find the general fixed points independently of the choice of potetial, we can find the roots of (3.21) λ_* such that

$$\lambda_*^2(\Gamma(\lambda_*) - 1) = 0, \tag{3.22}$$

and substituting the roots $\lambda = \lambda_*$ into Eqns. (3.17)-(3.20) to obtain the fixed points. The potential-independent fixed points are listed in Table 3.3 with their stability and existence conditions. It is worth noting that the points O_λ and D exist at all times where they represent the non-physical null solution and cosmological constant (potential energy-dominated) respectively.

Point A* represenets a kinetic-energy dominated Universe and it is either unstable or saddle point, which is not a physical scenario for LDE. Point B* is a scaling solution where the field is subdominant and its density depends on the background EoS, w, for the dominant species; it can be either stable or saddle point and it is not valid for LDE either. However, it is a valid point to represent either the radiation or matter era with EoS of 1/3 or 0 respectively. Lastly, point C* is a scalar dominated solution where the field has both potential and kinetic energy contributions and is the only valid fixed point for a dynamical dark energy.

For a comprehensive analysis of the general fixed points and their behaviors, we refer readers to [37, 147]. Bahamonde et al. (2018) [147] also provide a detailed list of commonly used potentials in the literature where $\Gamma = \Gamma(\lambda)$.

3.4.1 Example: Single Exponential

Equipped with the tools of dynamical systems, we now analyze the evolution of a Universe with a single exponential quintessence potential. The potential is given by

$$V(\phi) = V_0 e^{-\beta \frac{\phi}{M_{\rm Pl}}}. \tag{3.23}$$

Using Eqn. (3.15), we find that $\lambda(\phi) = \alpha$ (where β is constant) and $\Gamma(\phi)-1 = 0$, which implies $\lambda' = 0$. Consequently, the dynamical system reduces to

$$\Omega_r' = \Omega_r(3\Omega_m + 4\Omega_r + 6\Omega_k - 4), \tag{3.24}$$

$$\Omega_k' = \Omega_k(3\Omega_m + 4\Omega_r + 6\Omega_k - 6) - \alpha\Omega_v\sqrt{6\Omega_k}, \tag{3.25}$$

$$\Omega_v' = \Omega_v(3\Omega_m + 4\Omega_r + 6\Omega_k + \alpha\sqrt{6\Omega_k}) - \alpha\Omega_v\sqrt{6\Omega_k} \tag{3.26}$$

However, the system exhibits a symmetry under the combined transformation $\lambda \to -\lambda$ and $\phi \to -\phi$, which leaves the dynamics invariant. This allows us to set $\beta > 0$ without loss of generality, thereby simplifying the analysis of the fixed points. The system admits seven fixed points, listed with their stability behavior in Table 3.4. Understanding the dynamics and evolution of the Universe in this model depends critically on the value of α, as it determines the existence and stability of the fixed points. The fixed points identified in this system are

1. **Point A**:A quintessence-potential-dominated Universe with $w_\phi = -1$. This solution exists for all α but is a saddle point, making it unsuitable for describing LDE.

2. **Point B**: A quintessence-kinetic-dominated Universe with $w_\phi = 1$. This represents a stiff-fluid solution, which can be either unstable or a saddle point and is incompatible with the observational constraint of LDE.

3. **Point C**: A radiation-dominated solution, characterized by $\Omega_r = 1$. This is always a saddle point and represents the early radiation-dominated phase of the Universe.

4. **Point D**: A matter-dominated solution, with $\Omega_m = 1$. Like Point C, it is a saddle point and corresponds to the intermediate matter-dominated phase.

5. **Point E**: A scalar field-dominated solution that exists for $\alpha < \sqrt{6}$. It is stable and suitable for LDE if $\alpha < \sqrt{3}$. The EoS is $w_\phi = -1 + \alpha^2/3$, which allows for a smooth transition to dark energy domination.

6. **Point F**: A matter-scaling solution, stable if $\sqrt{3} < \alpha < \sqrt{24/7}$. For $\alpha > \sqrt{24/7}$, it becomes a stable spiral, leaving Point E as the global attractor.

7. **Point G**: A radiation-scaling solution, which is always a saddle point. It corresponds to the early Universe when radiation dominated the energy density.

To match observations of an accelerating expansion dominated by dark energy at late times, setting $\alpha < \sqrt{3}$ ensures that Point E is the global attractor. Under this condition, only Points A, B, C, D, and E exist in the phase space. The cosmological evolution begins in radiation domination, represented by $\Omega_r = 1$ at Point C. The Universe then evolves towards matter domination at Point D and eventually transitions to the stable global attractor at Point E, which corresponds to dark energy domination with $\Omega_\phi = 1$.

This comprehensive exploration of dynamical systems, spanning from the ΛCDM framework to scalar field cosmology and the single-exponential potential, lays the groundwork for studying @EDE. By delving into the stability and phase-space dynamics of these models, we have established a robust foundation for understanding how scalar fields can drive the Universe's evolution from a dynamical system perspective. With this introduction complete, we now turn our attention to @EDE.

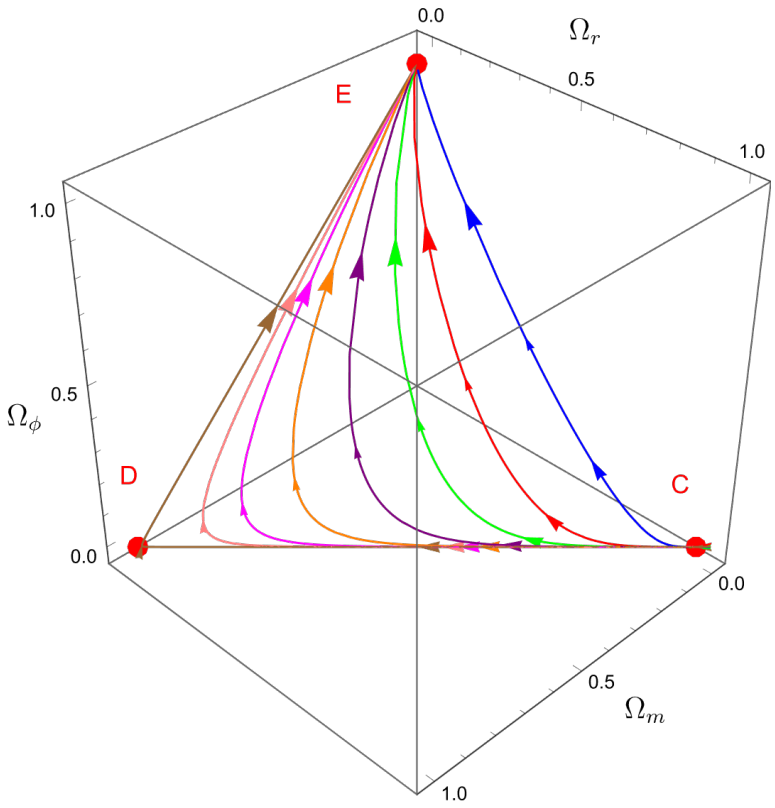

Figure 3.2: Phase space projectiles of a single exponential quintessence potential. Each trajectory differs in initial conditions of Ω_m, Ω_r, and Ω_ϕ. Regardless of the initial conditions, the Universe always ends up in dark energy dominance at point E, where $\Omega_\phi = 1$.

#	$\boldsymbol{\Omega_\phi}$	$\boldsymbol{\Omega_X}$	**Existence**	**Condition**	**Stability**	$\boldsymbol{w_\phi}$
O_λ	0	0	Always	None	Saddle	0
A^*	1	0	$\forall\lambda_*$	$\lambda_* > -\sqrt{6}$ and $\Gamma'_* > 0$ $\lambda_* < -\sqrt{6}$ $\Gamma'_* < 0$	Unstable node Saddle Saddle	1
B^*	$\frac{3(1+w)}{\lambda_*^2}$	$1 - \frac{3(1+w)}{\lambda_*^2}$	$\lambda_* \geq \sqrt{3(1+w)}$	$\lambda_*\Gamma'_* > 0$ $\lambda_*\Gamma'_* < 0$	Stable node Saddle	w
C^*	1	0	1	0 and $\lambda_*\Gamma'_* > 0$ $\sqrt{3(1+w)} \leq \lambda_* < \sqrt{6}$ $\lambda_*\Gamma_* < 0$	Stable node Saddle Saddle	$-1 + \frac{\lambda_*^2}{3}$
D	1	0	Always	$\lambda^2[\Gamma(\lambda) - 1]\|_{\lambda=0} > 0$ $\lambda^2[\Gamma(\lambda) - 1]\|_{\lambda=0} < 0$	Stable node Saddle	-1

Table 3.3: Fixed points of the potential-independent dynamical system when $\lambda(\phi)$ is invertible. Ω_X represents the density parameter of the dominant species — either matter or radiation — i.e., $X = m, r$. Each distinct value of λ_* that solves Eqn. (3.22) gives rise to a set of fixed points A*, B*, and C*. $\Gamma'_* = \Gamma'(\lambda_*)$. Note that point O_λ exists independently of the potential, and point D has $\lambda = 0$ that corresponds to a pure cosmological constant. Point D always exists provided $\lambda = 0$ is accessible in the phase space.

#	Ω_m	Ω_r	Ω_ϕ	Existence	Condition	Stability	w_ϕ
A	0	0	1	$\forall\, \lambda_*$	-	Saddle	-1
B	0	0	1	$\forall\, \lambda_*$	$\lambda_* < \sqrt{6}$ $\lambda_* > \sqrt{6}$	Unstable node Saddle	1
C	0	1	0	$\forall\, \lambda_*$	-	Saddle	0
D	1	0	0	$\forall\, \lambda_*$	-	Saddle	0
E	0	0	1	$\lambda_* < \sqrt{6}$	$0 < \lambda_* < \sqrt{3}$ $\sqrt{3} < \lambda_* < 2$ $2 < \lambda_* < \sqrt{6}$	Stable node Saddle Saddle	$-1 + \frac{\lambda_*^2}{3}$
F	$1 - \frac{3}{\lambda_*^2}$	0	$\frac{3}{\lambda_*^2}$	$\lambda_* > \sqrt{3}$	$\sqrt{3} < \lambda_* < \sqrt{24/7}$ $\lambda_* > \sqrt{24/7}$	Stable node Stable spiral	0
G	0	$1 - \frac{4}{\lambda_*^2}$	$\frac{4}{\lambda_*^2}$	$\lambda_* > 2$	$2 < \lambda_* < \sqrt{64/15}$ $\lambda_* > \sqrt{64/15}$	Saddle Saddle spiral	1/3

Table 3.4: Fixed points and the stability of the phase space of a single exponential quintessence potential. Note that points F and G correspond to point B* in Table 3.3 with w fixed to the dominant species with point G corresponding to radiation domination and point F corresponding to matter dominance. For the single exponential in Eqn. (3.23), $\lambda_* = \alpha$

4 Attractive Early Dark Energy

> *"Everything is Dual; everything has poles; everything has its pair of opposites; like and unlike are the same; opposites are identical in nature, but different in degree; extremes meet; all truths are but half-truths; all paradoxes may be reconciled."*
>
> – Three Initiates, The Kybalion 1908

With the foundational principles of cosmology, dynamical systems, and scalar field cosmologies established, we are now prepared to introduce our model: *Attractive Early Dark Energy*. This framework is designed to unify EDE and LDE, aiming to address the Hubble tension while minimizing additional degrees of freedom. A key motivation behind this model is to eliminate the coincidence problem associated with conventional EDE, in which the timing and amplitude of the energy injection must be finely tuned to impact the sound horizon at recombination. Our approach seeks to generate this behavior dynamically, without fine-tuning.

4.1 Model and Framework

The action of the theory is identical the one layed out in Eqn. (1.27). To effectively model both EDE and LDE, the potential we select must meet specific criteria to function as EDE in the early Universe and subsequently as LDE in the later Universe. We gain insights on the characteristics of the potential by examining Table 3.3, we find that the potential needed to construct @EDE models must meet the following criteria:

1. The existence of fixed point B* as an EDE saddle point, where λ_* is chosen to ensure that the field has $\Omega_\phi \sim 10\%$, becoming sub-dominant around matter-radiation equality $z \sim 3400$.

2. The presence of fixed point C* as a stable, late-time global attractor suitable for LDE, necessitating that λ_* leads to an EoS $w_\phi \sim -1$. This implies that the scalar field acts as a source of dynamical dark energy, providing a stable dark energy component at late times.[1]

Given the requirements that a saddle B* point nessitates $\lambda_*\Gamma'_* < 0$ and a stable C* point demands $\lambda_*\Gamma'_* > 0$, our model requires the potential to exhibit two distinct roots, λ_*, satisfying Eqn. (3.22). Upon reviewing well-known potentials in the literature, I identified two potentials that fulfill the criteria above

$$V(\phi) = V_\alpha e^{-\alpha\frac{\phi}{M_{\rm Pl}}} + V_\beta e^{-\beta\frac{\phi}{M_{\rm Pl}}}, \tag{4.1}$$

$$V(\phi) = V_0\left(\eta + e^{-\alpha\frac{\phi}{M_{\rm Pl}}}\right)^{-\beta}. \tag{4.2}$$

The first is the double exponential potential (4.1) that has been extensively analyzed within the context of quintessence LDE and is naturally derived from string theory frameworks [150]. The second potential (4.2) is engineered to behave as a a non-dynamical cosmological constant in the late-Universe [151, 152]. Since the second potential asymptotes to a non-dynamical cosmological constant at late times, it does not align with our objective of exploring fully dynamical dark energy models. In contrast, the double exponential potential satisfies the required dynamical criteria while remaining theoretically motivated. For these reasons, we focus our analysis on the double exponential potential.

Preferring to explore naturally arising and theoretically motivated models and purely dynamical models, our investigation will concentrate on the double exponential potential.

[1] While fixed point D represents a viable late-time DE solution, it corresponds to a purely cosmological constant scenario that is non-dynamical and thus less appealing for our objectives that favor dynamical explanations.

4.2 Background Dynamics

The double exponential potential introduces a rich dynamical structure due to having two independent exponential terms. The potential's roll parameter is foung to be

$$\lambda(\phi) = \frac{\alpha V_\alpha e^{-\frac{\alpha\phi}{M_{\rm Pl}}} + \beta V_\beta e^{-\frac{\beta\phi}{M_{\rm Pl}}}}{V_\alpha e^{-\frac{\alpha\phi}{M_{\rm Pl}}} + V_\beta e^{-\frac{\beta\phi}{M_{\rm Pl}}}}. \tag{4.3}$$

As $\phi \to \pm\infty$, λ is confined within the interval $\beta \leq \lambda \leq \alpha$. By taking derivatives of the potential in Eqn. (4.1), and using the definitions of λ and Γ from Eqns. (3.15) and (3.16), we find

$$\Gamma(\lambda) = 1 - \frac{(\alpha - \lambda)(\beta - \lambda)}{\lambda^2}, \tag{4.4}$$

revealing that Eqn. (3.22) has two distinct roots: $\lambda_* = \alpha$ and $\lambda_* = \beta$.

To study the dynamics of the double exponential potential, we begin by imposing the condition $\alpha > \beta$. This choice ensures that as the scalar field evolves toward larger values of ϕ, the roll parameter $\lambda(\phi)$ decreases from α to β. Since a large λ corresponds to a steep potential and fast-rolling (kinetic-energy–dominated) behavior, and a small λ corresponds to a flatter potential and slow-rolling (potential-energy–dominated) behavior, this setup naturally supports a transition from early-time acceleration (EDE-like behavior) to a late-time dark energy phase with $w_\phi \sim -1$.

Once we further impose $\alpha > 2$ and $\beta < \sqrt{3}$, the roles of these roots in cosmology become clear. The condition $\alpha > 2$ ensures that $\lambda_* = \alpha$ corresponds to a saddle point that dominates in the early-Universe, which we designate as the *EDE saddle*. Meanwhile, $\beta < \sqrt{3}$ guarantees that $\lambda_* = \beta$ acts as a stable attractor governing the late-Universe, referred to as the *LDE attractor*. This hierarchy establishes a natural separation between early- and late-time dynamics, with the two exponential terms in the potential playing distinct roles in shaping the field's behavior. Assuming an energy scale hierarchy such that

$V_\alpha \gg V_\beta$, reflecting the dominance of the α-term during the early Universe and the β-term during the late Universe, the potential simplifies to

$$V(\phi) \approx \begin{cases} V_\alpha e^{-\alpha \frac{\phi}{M_{\rm Pl}}}, & \text{at early times,} \\ V_\beta e^{-\beta \frac{\phi}{M_{\rm Pl}}}, & \text{at late times,} \end{cases} \tag{4.5}$$

assuming initial conditions align appropriately, meaning that the field is initially frozen due to Hubble friction in the early Universe, i.e., $\dot{\phi}_i \approx 0$. This is consistent with attractor-like behavior under the slow-roll approximation $\ddot{\phi} \approx 0$. Moreover, the shift symmetry of the potential implies that the choice of ϕ_i is arbitrary, and the dynamics are governed primarily by $\dot{\phi}_i$. This setup ensures that the α-term dominates initially, leading to an early-time behavior characterized by $\lambda_* \approx \alpha$. Consequently, justifying the following approximation

$$\lambda_* \approx \begin{cases} \alpha, & \text{at early times,} \\ \beta, & \text{at late times.} \end{cases} \tag{4.6}$$

Thus, the early-Universe is predominantly influenced by the α-exponential term, while the late-Universe is governed by the β-exponential term. This separation allows for an independent examination of the phase space dynamics associated with each exponential, facilitating a clear analysis of their respective roles in cosmology. The fixed points for a single exponential, which serve as a reference for each phase, are detailed in Table 3.4.

Focusing initially on the early times when $\lambda_* = \alpha$, during the radiation-dominated epoch, we associate point G in Table 3.4 with EDE contributing a fractional energy density[2]

$$\Omega_\phi = \frac{3(1+w)}{\alpha^2} \approx f_{\rm ede}. \tag{4.7}$$

Note that the relation in Eqn. (4.7) is approximate because it holds strictly only at the fixed point during the radiation-dominated epoch, where $w = 1/3$ and $\lambda = \alpha$ is constant. In realistic cosmological scenarios, λ evolves dynamically and

[2]Technically, the expression in Eqn. (4.7) aligns with point B* in Table 3.3. Point G in Table 3.4 is derived by substituting $w = 1/3$, indicative of the radiation era. We maintain the generality of Eqn. (4.7) for subsequent discussions.

the field may not be exactly at the fixed point, especially during the transition phases. Therefore, Ω_ϕ approaches but does not exactly equal the fixed-point value, justifying the use of the approximation symbol.

Previous analyses on EDE models suggest that resolving the H_0 tension requires $f_{\rm ede} \sim 0.1$ [108], which implies $\alpha \approx \sqrt{40}$. This value ensures that point G, corresponding to the early Universe, acts as a saddle point in the dynamical system. At late times, as $\lambda_* = \beta$, the system's evolution is directed towards either point E or F, based on the value of β. For $\beta < \sqrt{3}$, the system tends towards point E, the global attractor, describing a scalar-dominated Universe with the EoS

$$w_\phi = -1 + \frac{\beta^2}{3}. \tag{4.8}$$

Given the most recent observations available at the time of this publication, the preferred dark energy EoS was $w \approx -1$ with high precision [32]. This observation leads us to predict that $\beta \ll 1$. Our choice of parameters also dictate that point F acts as a saddle during the matter-dominated epoch, with the scalar field contributing a fraction of the matter density. We refer to this fixed point as the *dark matter saddle*, highlighting its role in the field's intermediate evolution during matter domination.

Theoretical predictions can be further explored through a qualitative analysis of the parameter space, which also aids our subsequent data analysis. Figs. 4.1, 4.2, and 4.3 illustrate how variations in α, β, and V_α influence the system, focusing particularly on the most affected quantities: α and V_α primarily affect Ω_ϕ, whereas β defines the EoS for LDE as seen in Eqn. (4.8). I created all the graphs for this work using the Cosmic Linear Anisotropy Solving System (`CLASS`) code [1, 2] to compute the cosmological quantities of interest and generated the plots with Python's `matplotlib` package.

Beginning with Fig. 4.1, it is observed that larger values of α diminish the amplitude of the EDE injection, aligning with the predictions from Eqn. (4.7). As for the injection redshift z_c, variations in α influence the effective mass m of the field

$$m(\phi) = \alpha \frac{\sqrt{V_\alpha}}{M_{\rm Pl}} e^{-\frac{\alpha\phi}{2M_{\rm Pl}}}, \tag{4.9}$$

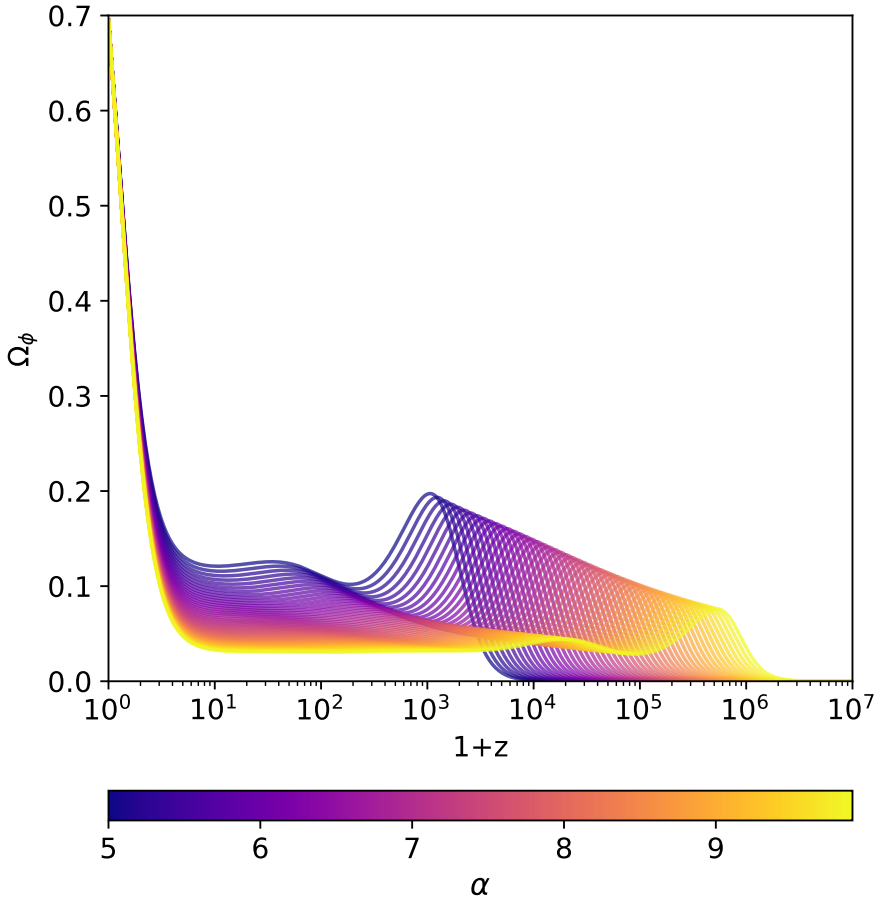

Figure 4.1: Evolution of Ω_ϕ as a function of redshift when α is varied. The parameters $\beta = 0.01$, $\log_{10} V_\alpha = -7.8$ were fixed, and ΛCDM parameters were set according to the ΛCDM best-fit values given in Table 4.2. Increasing α not only reduces the fractional EDE injection but also shifts this injection to earlier epochs.

with the injection occurring when $m(\phi(z)) = H(z)$. During the radiation-dominated era, assuming a radiation-dominated Universe, the redshift of injection z_c can be approximated by

$$z_c \sim \left(\frac{V_\alpha \alpha^2 e^{-\alpha \frac{\phi}{M_{\mathrm{Pl}}}}}{\Omega_r H_0^2 M_{\mathrm{Pl}}^2} \right)^{1/4} - 1, \tag{4.10}$$

indicating that as α increases, the injection is pushed to earlier times, as seen in Fig. 4.1.

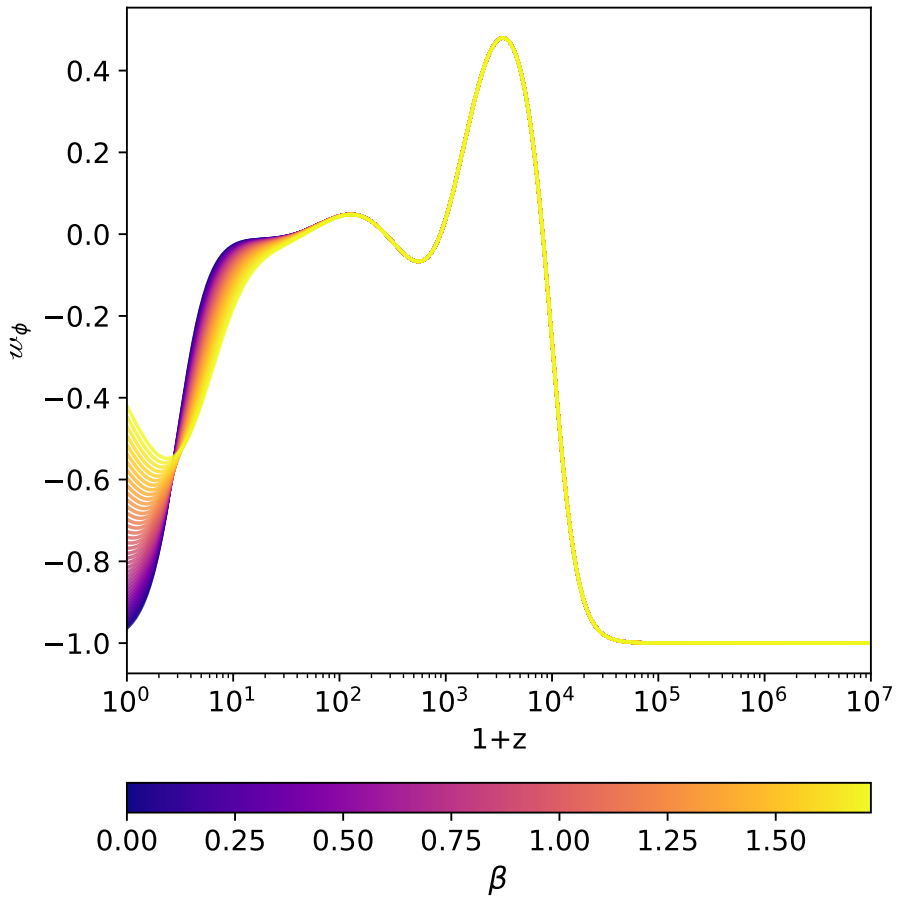

Figure 4.2: Evolution of the EoS w_ϕ for the scalar field ϕ as a function of redshift, varying β. Like in Fig. 4.1, we fixed $\alpha = \sqrt{40}$ and $\log_{10} V_\alpha = -7.8$. The case where $\beta = 0$ is equivalent to a cosmological constant scenario for late dark energy (LDE). Note that β impacts the dynamics primarily in the LDE era around $z \sim O(10)$, altering the dark energy's behavior towards its observed value.

Turning to Fig. 4.2, which demonstrates the effects of varying β, we observe that, in line with our earlier predictions, changes in β do not affect the high redshift dynamics but significantly influence the EoS of dark energy at lower redshifts, consistent with Eqn. (4.8).

Lastly, Fig. 4.3 demonstrates that V_α exhibits significant degeneracy with α. An increase in V_α boosts the field's mass as dictated by Eqn. (4.9), which in turn pushes the energy injection to occur at higher redshifts. Additionally, this change influences the amplitude of energy injection, which indirectly depends on the background EoS $w(z)$, as shown in Eqn. (4.7). Since $w(z)$ generally increases with redshift, an increased V_α incereases f_{ede}.

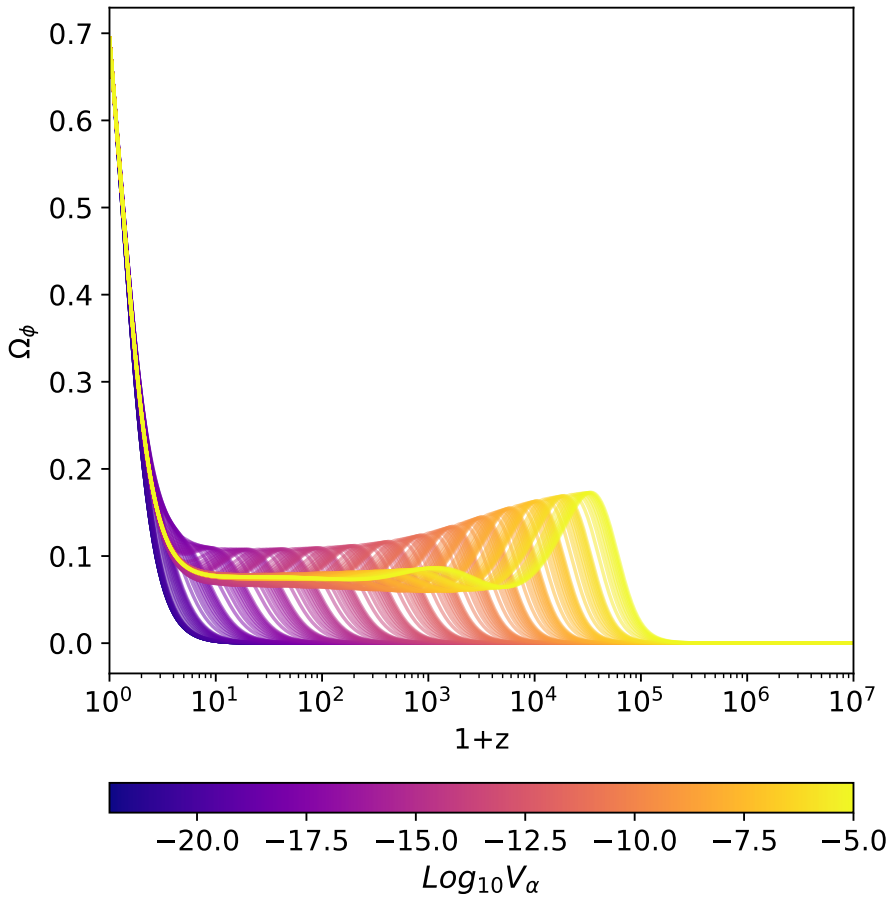

Figure 4.3: Evolution of Ω_ϕ as a function of redshift, varying V_α. Parameters $\alpha = \sqrt{40}$ and $\beta = 0.01$ were fixed, with the ΛCDM parameters consistent with those in Fig. 4.1. Increasing V_α leads to both a larger and earlier energy injection. Unlike increases in α, which also shift the injection to higher redshifts, increasing V_α enhances the amplitude of the injection.

Given our predictions, some degree of parameter tuning or careful selection of initial conditions might be necessary to mitigate the H_0 tension, though

potentially less extensively than required by traditional EDE models.[3] The extent to which this constitutes "fine-tuning" largely depends on the potential's nature and whether the parameter values remain stable under radiative corrections.

In our fiducial model, the double exponential potential emerges from string theory [150], suggesting that the model's parameters could be inherently determined by the underlying physics. Thus, the challenge becomes identifying specific string theory realizations where these parameters naturally align to both address the H_0 tension and provide a plausible explanation for LDE.

To summarize, the Universe in our scenario is expected to first approach the EDE saddle point during the radiation epoch, characterized by a transient but subdominant contribution from the scalar field. It then transitions to the dark matter saddle, where a fraction of the dark matter is composed of the non-clustering scalar field. Finally, the system settles into the *LDE attractor*, representing the late-time dominance of dark energy with $w_\phi \sim -1$. This progression is illustrated in Figs. 4.4-4.6, where we plot the evolution of the fractional energy densities in ΛCDM and @EDE, the EoS w_ϕ of @EDE, and the fractional difference of the Hubble expansion rate $\Delta H/H$ compared to the standard ΛCDM evolution, respectively. The introduction of @EDE induces a notable localized increase in $H(z)$ during the early Universe, driven by the transient scalar contribution. This is followed by a period of constant fractional enhancement to $H(z)$ and, at late times, a decrease in $H(z)$ relative to ΛCDM due to the scalar field's equation of state deviating from $w_\phi = -1$.

We now proceed to evaluate our fiducial @EDE model against observational data.

[3]The adjustment in β reflects standard fine-tuning practices associated with quintessence models, and is not a unique feature of the @EDE framework.

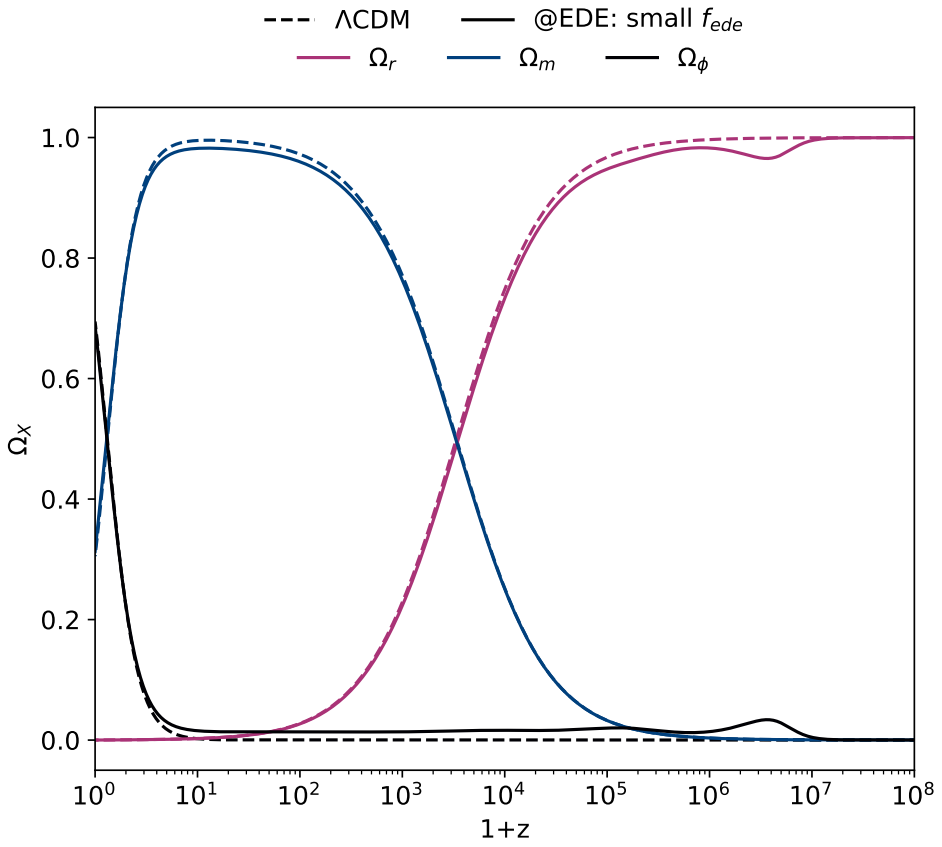

Figure 4.4: Comparative evolution of fractional energy densities Ω_X in matter, radiation, and the @EDE scalar between the best-fit @EDE model (solid curves) and the ΛCDM baseline (dashed curves). The best-fit parameters for @EDE, detailed in Table 4.2, arise from the model explorations that excludes ΛCDM from the prior detailed in Section 4.4. Notably, when ΛCDM parameters are permitted within the @EDE prior, the resulting fit is indistinguishable from ΛCDM.

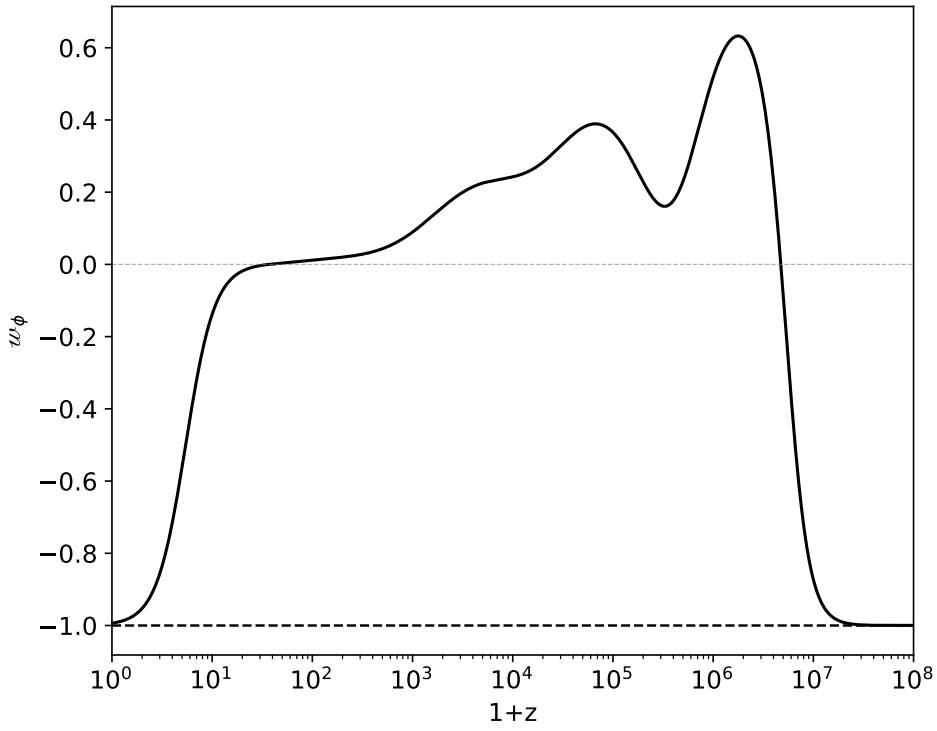

Figure 4.5: Evolution of the EoS w_ϕ for the @EDE scalar field, which begins from an initial frozen state with $w_\phi = -1$ to a dynamic phase, acting as EDE around $z \sim 10^5$, mimicking matter ($w_\phi \approx 0$) during the matter-dominated era, and finally stabilizing close to $w_\phi = -1$ as it dominates the late-time Universe. This illustration uses the best-fit @EDE parameters from Fig. 4.4.

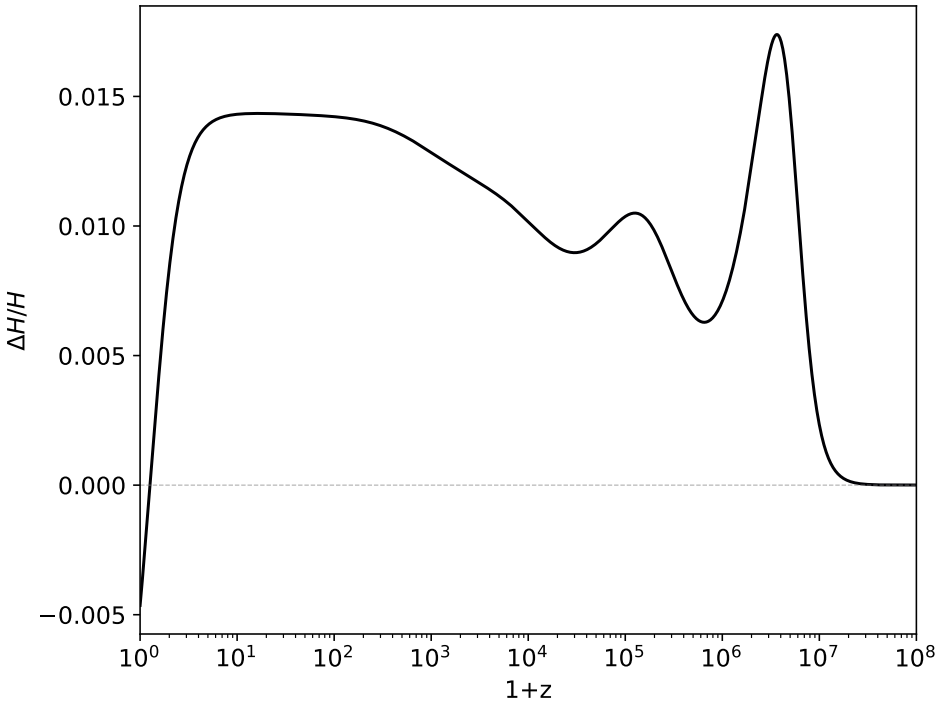

Figure 4.6: The fractional change in the Hubble parameter $H(z)$, induced by the @EDE model relative to the baseline ΛCDM model. We use the same model parameters as in Fig. 4.4-4.5, illustrating the impact of @EDE adjustments on the expansion rate across different epochs.

4.3 Methodology and Data

I modified the `CLASS` [1, 2] code to numerically solve the coupled Friedmann-Klein-Gordon equations for the double-exponential potential and to evolve its perturbations. `CLASS` already has a base EDE model implemented, but I had to extend the default model by including the double-exponential potential defined in Eqn. (4.1). Initially, I employed the Markov Chain Monte Carlo (MCMC) method [153, 154] using the Metropolis–Hastings algorithm, which is already implemented in the `Cobaya` cosmological sampler framework [155].

MCMC methods are designed to efficiently explore multi-dimensional parameter spaces by constructing chains of samples with the goal of deriving the posterior distribution, giving a prior and a likelihood function. However, due to significant degeneracies between the model parameters α and V_α, which describe the steepness and amplitude of the potential, respectively, the MCMC chains failed to converge. Degeneracies occur when the likelihood remains nearly constant for multiple combinations of parameter values, making it difficult for MCMC to discern the preferred region of the parameter space. This often results in slow convergence, poor sampling efficiency, and lack of converge in some scenarios. In our case, the chains failed to converge.

To address these issues, I transitioned to the `PolyChord` (`PC`) algorithm [156], a nested sampling method specifically designed for efficiently exploring high-dimensional and degenerate parameter spaces. In nested sampling algorithms, *live points* are a set of randomly initialized sample points in the parameter space. Each live point represents a possible state of the model's parameters with an associated likelihood value. The core idea of `PC` is to iteratively replace the live point with the lowest likelihood with a new sample drawn from a region of higher likelihood. This process progressively refines the exploration towards regions of the parameter space with higher posterior density.

The replacement of low-likelihood live points with higher-likelihood samples allows the algorithm to gradually focus on the regions of the parameter space that have the highest posterior density, without getting trapped in local maxima. This iterative updating continues until the remaining live points together contribute an insignificant fraction of the total posterior mass. In other words, the algorithm stops once the remaining live points no longer significantly affect

the final estimate of the posterior. One key advantage of `PC` over MCMC is that it also provides a direct estimate of the model's Bayesian evidence, $\mathcal{Z}$, which quantifies the relative likelihood of different models.

In this analysis, I configured `PC` with a number of live points set to $n_{\text{live}} = 35D$, where D is the dimensionality of the parameter space as suggested by [156]. This choice ensures a sufficient number of live points to effectively sample the complex and degenerate regions of the parameter space. The convergence criterion was determined by setting the posterior mass contained in the live points, $\mathcal{Z}_{\text{live}}$, to be within 1% of the total evidence $\mathcal{Z}$, i.e., $\mathcal{Z}_{\text{live}} = 10^{-2}\mathcal{Z}$. This criterion indicates that when the remaining unexplored portion of the posterior mass becomes negligible, the algorithm has adequately sampled the parameter space and can stop.

I have analyzed the results using `GetDist` [157], a Python package designed for exploring and visualizing Monte Carlo samples generated by cosmological samplers like MCMC or nested sampling algorithms. `GetDist` offers a variety of statistical tools for examining the posterior distributions of model parameters, including calculations of mean values, standard deviations, credible intervals, and marginalized distributions. To interpret the results visually, I generated 1D marginalized posterior distributions for individual parameters and 2D contour plots to illustrate parameter degeneracies and correlations (see Fig. 4.7). These 2D plots are particularly useful for identifying regions of high posterior density and understanding how different parameters interact or exhibit degeneracies. I also created a summary table listing the posterior mean values and 68% confidence intervals for all relevant cosmological parameters (see Table 4.2).

4.3.1 Datasets

We used the data combination that has become standard for EDE and Hubble tension investigations [108] in order to ensure a like-for-like comparison with previous works:

1. **Cosmic microwave background (CMB) data**: We used CMB data from Planck 2018 [10] comprising of the low-ℓ TT and EE data, along with the high-ℓ `plik-lite` likelihood and the gravitational lensing data [9]. We used `plik-lite` instead of the full `plik` likelihoods to reduce the

dimensionality of the parameter space, removing nuisance parameters that would significantly slow down `PC`. The datasets consist of $N_{CMB} = 2352$ data points.

2. **Baryon acoustic oscillations (BAO)**: We used BAO data that is consistent with the CMB including the 6dF galaxy survey (6dFGS) [26], SDSS DR7 [27] and, SDSS-III DR12 [28] which, combined, constrain the distance-redshift relation with $N_{BAO} = 5$ data point spanning $0.01 < z < 0.61$ using spectroscopic methods on galactic data.

3. **Supernovae (SNe)**: We used the Pantheon [59] data which surveyed the redshifts and magnitudes of 1048 Type Ia Supernovae ranging from $0.01 < z < 2.3$. An updated version, Pantheon+[55] was released while this manuscript was in preparation. We do not expect our results to change with updated data as the CMB strongly constrains and excludes the fiducial @EDE scenario explored here.

4. **Cepheid distance ladder** H_0: We use the SH0ES direct measurement of $H_0 = (74.03 \pm 1.42)$km/s/Mpc [158] as a best-case test scenario to check whether our scenario resolves the Hubble tension and to mitigate prior volume projection effects in EDE cosmologies [136, 159]. A new, more precise, measurement [160] of $H_0 = (73.29 \pm 0.90)$ km/s/Mpc was released when we were preparing this work for submission, but updating the H_0 likelihood we use would have a minimal impact on our results because CMB data dominate our constraints.

4.3.2 Parameter Space

To explore @EDE cosmology, I sampled over the ΛCDM parameters: the physical densities of baryons ω_b, and cold dark matter ω_c, the amplitude of the primordial power spectrum expressed as $\ln(10^{10}A_s)$ and its tilt n_s, the optical depth to reionization $\tau_{\rm reio}$, and the present-day expansion rate H_0. In addition to these, the @EDE-specific parameters such as α, β, and V_α, which govern the behavior of the @EDE scalar potential, were varied.

We fixed the initial condition ϕ_i by exploiting a symmetry of the potential where the action remains invariant under $\phi \to \phi + \phi_0$, and $V_k \to V_k e^{k\frac{\phi_0}{M_{\rm Pl}}}$

for $k = \alpha, \beta$, with ϕ_0 as a constant. This symmetry allowed us to set ϕ_i to an arbitrary value without loss of generality. We make the choice of setting $\phi_0 = -4.583 M_{\rm Pl}$.

For $\dot{\phi}_i$, I fixed it using attractor initial conditions. Given that the field is initially frozen, I determined $\dot{\phi}_i$ in `CLASS` by setting $\ddot{\phi} = 0$ in the KG equation in Eqn. (1.28), under the assumption of a slow-roll and approximating the potential as $V(\phi) \approx V_\alpha e^{-\alpha \frac{\phi}{M_{\rm Pl}}}$, considering that the β-exponential becomes significant only later. From this, the initial $\dot{\phi}_i$ condition was derived as $\dot{\phi}_i = \frac{\alpha V_\alpha}{3H_i} e^{-\alpha \frac{\phi_i}{M_{\rm Pl}}}$.

Finally, at late times, the dynamics are dominated by the β-exponential, converging to fixed point E, detailed in Table 3.4 with $\lambda_* = \beta$. The scalar acts as LDE with an EoS given by Eqn. (4.8). To ensure the Universe remains closed, I modified `CLASS` to solve for V_β such that $V(\phi) = V_\beta e^{-\beta \frac{\phi_0}{M_{\rm Pl}}} = 3H_0^2 M_{\rm Pl}^2 \Omega_\phi$ where ϕ_0 is the field value at the present-day, $z = 0$. Fixing ϕ_i, $\dot{\phi} i$, and V_β, effectively reduced the dimensionality of the @EDE model's parameter space from 12 to 9 dimensions—six ΛCDM parameters and three specific to @EDE: α, β, and V_α.

We have used uninformative priors for the ΛCDM parameters and set specific prior for the @EDE parameters to constrain $f_{\rm ede}$ to sub-dominant levels; the priors are given in Table 4.1. The *wide @EDE prior* explores a range allowing $0 \leq f_{\rm ede} \leq 0.268$ and $z_c \geq 1000$, parameterizing the maximal fractional energy density $f_{\rm ede}$ at the redshift z_c. Ultimately, we found that the best-fitting @EDE model is almost indistinguishable from ΛCDM, and that our expected scenario described in the Section 4.2 is disfavored with high statistical significance. To probe this further, we conducted additional and independent analysis with *narrow priors* centered on the theoretical values derived in Section 4.2. This restricted prior range targets $10^3 \leq z_c \leq 10^8$ and excludes ΛCDM by forcing an @EDE energy injection of $0.033 \leq f_{\rm ede} \leq 0.1$. These cosmologies, along with ΛCDM, are scrutinized in the forthcoming Section.

4.4 Results and Cosmological Constrains

Our analysis begins by considering an @EDE scenario that incorporates a wide range of priors, allowing for the inclusion of the ΛCDM limit by setting $\alpha = 0$

Parameter	**Wide Prior**	**Narrow Prior**
ΛCDM Parameters		
$\ln 10^{10} A_s$	$\mathcal{U}[1.61, 3.91]$	$\mathcal{U}[1.61, 3.91]$
n_s	$\mathcal{U}[0.8, 1.2]$	$\mathcal{U}[0.8, 1.2]$
ω_b	$\mathcal{U}[0.005, 0.1]$	$\mathcal{U}[0.005, 0.1]$
ω_c	$\mathcal{U}[0.08, 0.3]$	$\mathcal{U}[0.08, 0.3]$
$\tau_{\rm reio}$	$\mathcal{U}[0.01, 0.8]$	$\mathcal{U}[0.01, 0.8]$
H_0	$\mathcal{U}[50, 100]$	$\mathcal{U}[50, 100]$
Scalar Field Parameters		
α	$\mathcal{U}[0, 17]$	$\mathcal{U}[8.5, 15]$
$\log_{10} V_\alpha$	$\mathcal{U}[-50, -6]$	$\mathcal{U}[-15, -9]$
β	$\mathcal{U}\left[0, \sqrt{3}\right]$	$\mathcal{U}\left[0, \sqrt{3}\right]$
Derived Parameters		
f_{ede}	$[0, 0.268]$	$[0.033, 0.100]$
$\log_{10} z_c$	$[3, 9.82]$	$[3.13, 8.06]$

Table 4.1: Priors for @EDE parameters that include ΛCDM (wide priors) and exclude it (narrow priors). Both models and ΛCDM share the same prior for the ΛCDM parameters $\{\ln 10^{10} A_s, n_s, \omega_b, \omega_c, \tau_{\rm reio}, H_0\}$.

and $V_\alpha = 0$, eliminating any EDE phase, and $\beta = 0$ implies a cosmological constant-like LDE. This enables a direct evaluation of how well each model fits the data, provides constraints on H_0, and assesses any statistical preference for @EDE compared to ΛCDM. We refer to this model as *@EDE: wide priors* in the discussions that follow.

Contrary to our theoretical expectations, the @EDE model is not preferred over the standard ΛCDM model, indicating that @EDE does not resolve the Hubble tension. The data favors a scenario that closely mimics ΛCDM within 1σ, effectively excluding any early injection of energy density that may resemble EDE, as shown in Fig. 4.7. In practice, @EDE remains frozen throughout cosmic history, acting like a cosmological constant with $w_\phi = -1$ and with

the scalar potential dominated by $V_\beta e^{-\beta\frac{\phi}{M_{\rm Pl}}}$. This behavior makes the @EDE cosmology indistinguishable from ΛCDM in Figs. 4.4-4.6. The marginalized posteriors and the best-fitting parameters for this model are listed in Table 4.2. The strong preference for ΛCDM over @EDE is not due to prior volume effects within the model. It can be seen from Table 4.2 that the best-fit parameters are well within 1σ of the mean values, indicating that the likelihood peak aligns closely with the sample mean. The posteriors for @EDE align perfectly with those for ΛCDM, leading to the conclusion that our fiducial @EDE model fails to resolve the Hubble tension, with the best-fit increase in H_0 being a negligible $\Delta H_0 = 0.15$km/s/Mpc. Despite adding three additional parameters in @EDE, there is an insignificant improvement in the goodness-of-fit, with $\Delta\chi^2 = -0.28$. The statistical expectation, for three extra parameters, is that we expect a minimal improvement of $\Delta\chi^2 = -3$, which underscores the data's stronger preference for ΛCDM over @EDE.

To further investigate the limitations of our fiducial @EDE model and gain insights into developing a model that better aligns with the data, resolves the Hubble tension, and unifies early and late dark energy, we now examine an @EDE model with restricted priors that exclude ΛCDM. This approach, referred to as *@EDE: narrow priors* in the subsequent analysis, forces an @EDE injection to explore its effects more thoroughly.

4.4.1 Excluding ΛCDM from the prior

The narrow priors constrain $0.033 \leq f_{\rm ede} \leq 0.1$ and $10^3 < z_c \leq 10^8$, ensuring a minimum @EDE energy injection of 3.3%. It is important to note that these phenomenological parameters, α and V_α, are sampled from uniform (flat) priors, resulting in the smallest injection at $z_c \simeq 3.6 \times 10^6$ and the largest $f_{\rm ede}$ at $z_c \simeq 5 \times 10^4$. The full priors can be found in Table 4.1.

In this restricted scenario, the data favor $\alpha = 15$ and $\log_{10} V_\alpha = -15$, both at the boundaries of their respective narrow-prior ranges, as shown in Table 4.1. This results in $z_c \simeq 3.7 \times 10^6$ and $f_{\rm ede} \simeq 3.4\%$. This optimal fit diminishes the influence of @EDE on observables by minimizing the energy injection, thus pushing @EDE dynamics into a redshift range where data sensitivity is lower. The Planck CMB is sensitive to new physics injections up to a maximum redshift

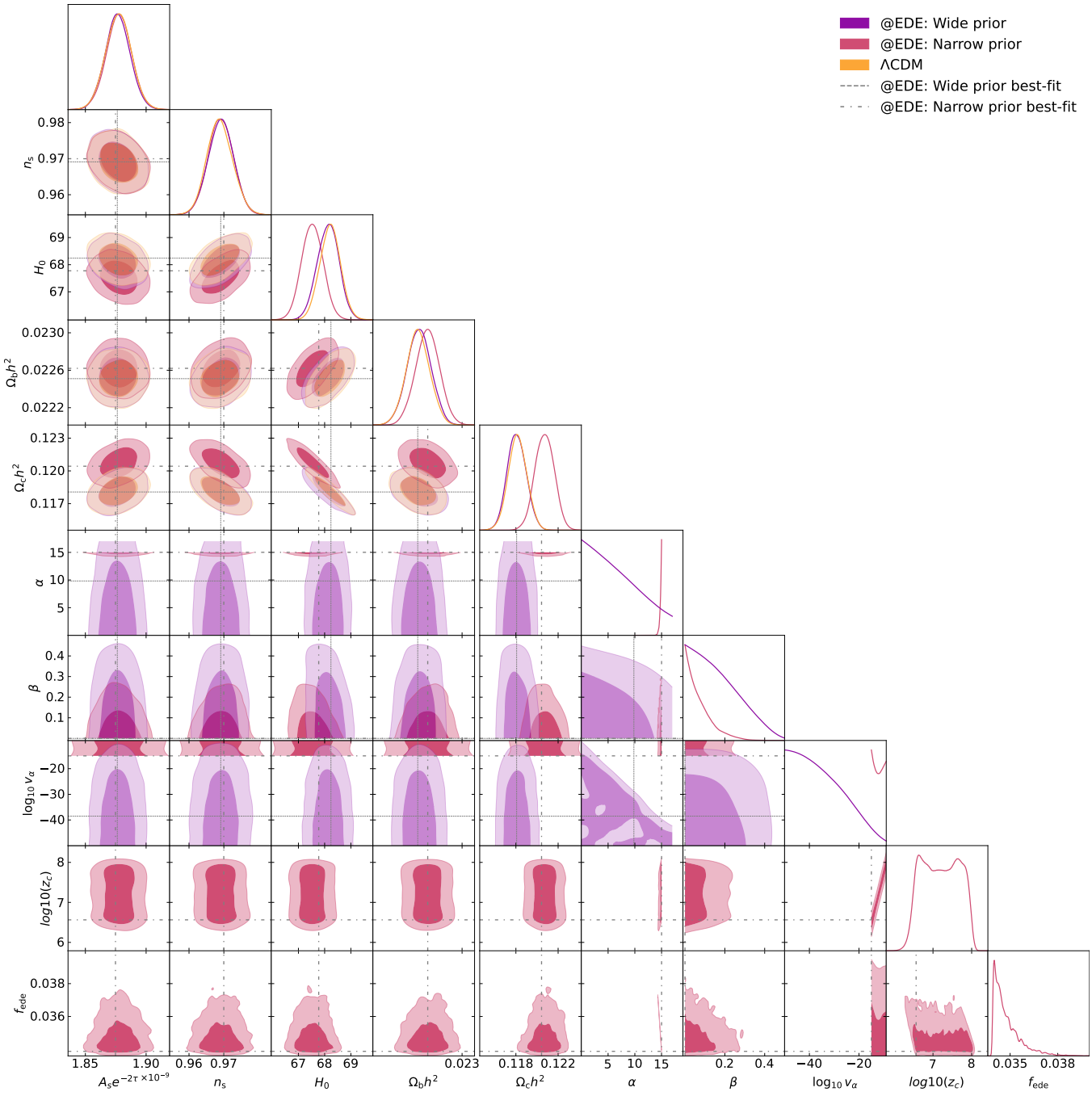

Figure 4.7: Marginalized posteriors for various cosmologies fit to Planck2018 + BAO + SNe + SH0ES data. We examine @EDE with wide priors that encompass ΛCDM (purple), @EDE with narrow priors that exclude ΛCDM (pink), and ΛCDM itself (orange). The horizontal and vertical lines indicate the best-fit points for @EDE under wide (densely dashed) and narrow (dash-dotted) priors.

Parameter	ΛCDM	**@EDE: wide priors**	**@EDE: narrow priors**
$\log(10^{10}A_s)$	$3.052(3.045) \pm 0.015$	$3.051(3.052)^{+0.013}_{-0.016}$	$3.083(3.085) \pm 0.017$
n_s	$0.9689(0.9687)^{+0.0034}_{-0.0039}$	$0.9691(0.9691) \pm 0.0036$	$0.9691(0.9700) \pm 0.0036$
ω_b	$0.02251(0.02249) \pm 0.00013$	$0.02253(0.02251) \pm 0.00013$	$0.02262(0.02262) \pm 0.00013$
ω_c	$0.11816(0.11840) \pm 0.00088$	$0.11808(0.11807) \pm 0.00089$	$0.12072(0.12043) \pm 0.00091$
τ_{reio}	$0.0599(0.0593) \pm 0.0076$	$0.0597(0.0599)^{+0.0066}_{-0.0080}$	$0.0751(0.0769) \pm 0.0088$
D_A	(12.76)	(12.76)	(12.62)
r_{s*}	(144.85)	(144.92)	(143.12)
$100\theta_*$	(1.042009)	(1.042049)	(1.040470)
H_0	$68.21(68.09) \pm 0.39$	$68.13(68.24) \pm 0.41$	$67.53(67.77) \pm 0.41$
σ_8	$0.8084(0.8084) \pm 0.0061$	$0.8069(0.8080)^{+0.0058}_{-0.0066}$	$0.7729(0.7758) \pm 0.0069$
S_8	$0.813(0.815) \pm 0.010$	$0.813(0.812) \pm 0.010$	$793(0.792) \pm 0.010$
α	-	$< 8.53(9.82)$	$> 14.8(15)$
β	-	$< 0.213(0)$	$< 0.0883(1.69 \times 10^{-6})$
$\log_{10} V_\alpha$	-	$< -30.9(-38.5)$	(-15)
f_{ede}	-	-	$0.03480(0.03388)^{+0.00017}_{-0.00092}$
$\log_{10} z_c$	-	-	$7.20(6.56) \pm 0.46$
$\chi^2_{CMB}(\Delta)$	1013.99	1014.64(+0.65)	1052.70(+38.71)
$\chi^2_{BAO}(\Delta)$	5.23	5.24(+0.01)	7.98(+2.75)
$\chi^2_{H_0}(\Delta)$	15.45	14.56(−0.89)	17.45(+2.00)
$\chi^2_{Pantheon}(\Delta)$	1034.82	1034.77(−0.05)	1035.41(+0.59)
$\chi^2(\Delta)$	2069.49	2069.21(−0.28)	2113.54(+44.05)
$\chi^2_{red}(\Delta)$	0.6089	0.6093(+0.0004)	0.6224(+0.0135)

Table 4.2: Marginalized posteriors for ΛCDM and two @EDE cosmologies with different priors, showing mean (best-fit) $\pm 1\sigma$. The @EDE scenario with wide priors includes ΛCDM as a nested model, while the narrow priors exclude ΛCDM. The wide-priors model does not list f_{ede} and z_c as there is no EDE phase in that scenario, just LDE. We also show the various χ^2 ($\Delta\chi^2$) broken down by data set and their differences relative to ΛCDM.

of $z \lesssim 10^6$ [109, 161, 162]. For injections occurring at earlier times, @EDE effectively behaves like an additional matter-tracking component, similar to tracking early dark energies [163–165], and will align with the same upper-limit constraints as tracker early dark energies.

As we enforce a non-zero @EDE energy injection, ΛCDM parameters are forced to adjust in compensation, leading to the parameter shifts illustrated

in Fig. 4.7 and Table 4.2. These shifts can be understood within the CMB framework as follows. Initially, at $z \sim 10^7$, the scalar field starts to roll and enters an EDE phase, contributing approximately $f_{\rm ede} \simeq 3.39\%$ to the Universe's energy budget. Typically, after this early-Universe peak in Ω_ϕ, EDEs dilute away and no longer impact cosmology. However, @EDE loses about half of its fractional energy density, then settles into the matter domination epoch—corresponding to point F, the dark matter saddle—where it dilutes like matter and contributes between 1.33% and 1.37% to the Universe's energy budget. This contribution persists until the dark energy attractor takes over, leading @EDE to contribute the LDE that dominates the Universe today.

To understand how @EDE neccisitates the ΛCDM parameters to change, to accomodate the CMB data, we need to understand how @EDE affects the background dynamics and the perturbations. If the ΛCDM parameters are fixed, the inclusion of @EDE decreases the sound horizon size r_s. The presence of this additional component in the early Universe, which does not cluster like matter, causes the gravitational potentials $\Phi + \Psi$ in the Newtonian gauge [166] to decay relative to a ΛCDM Universe, enhancing the early integrated Sachs-Wolfe (ISW) effect. It also increases $H(z)$ at early times, causing modes to enter the horizon sooner and shifting the oscillations in the Sachs-Wolfe (SW) effect at recombination. The changes in the gravitational potentials $\Phi + \Psi$ are visualized in Fig. 4.9.

Additionally, the persistent component of @EDE in the late Universe contributes to the late ISW effect and reduces the angular diameter distance D_A to the CMB. The reduction in D_A cannot fully offset the decrease in r_s, leading to a decrease in the precisely measured angular size θ_* of the sound horizon. Overall, @EDE increases the power in the first CMB peak and lower multipoles, as well as shifts the CMB peaks.

When the ΛCDM parameters are allowed to vary in the presence of @EDE, they compensate for its effects through changes in H_0, ω_b, and ω_c. A significant increase in ω_c and a slight increase in ω_b suppresses the TT power spectrum and counteract the enhanced early and late ISW effects, as well as the shifts in the SW effect at recombination. With higher densities for both matter species, matter-radiation equality occurs earlier and at a higher redshift, z_{eq}, counteracting the decay in the gravitational potentials $\Phi + \Psi$. The increase in

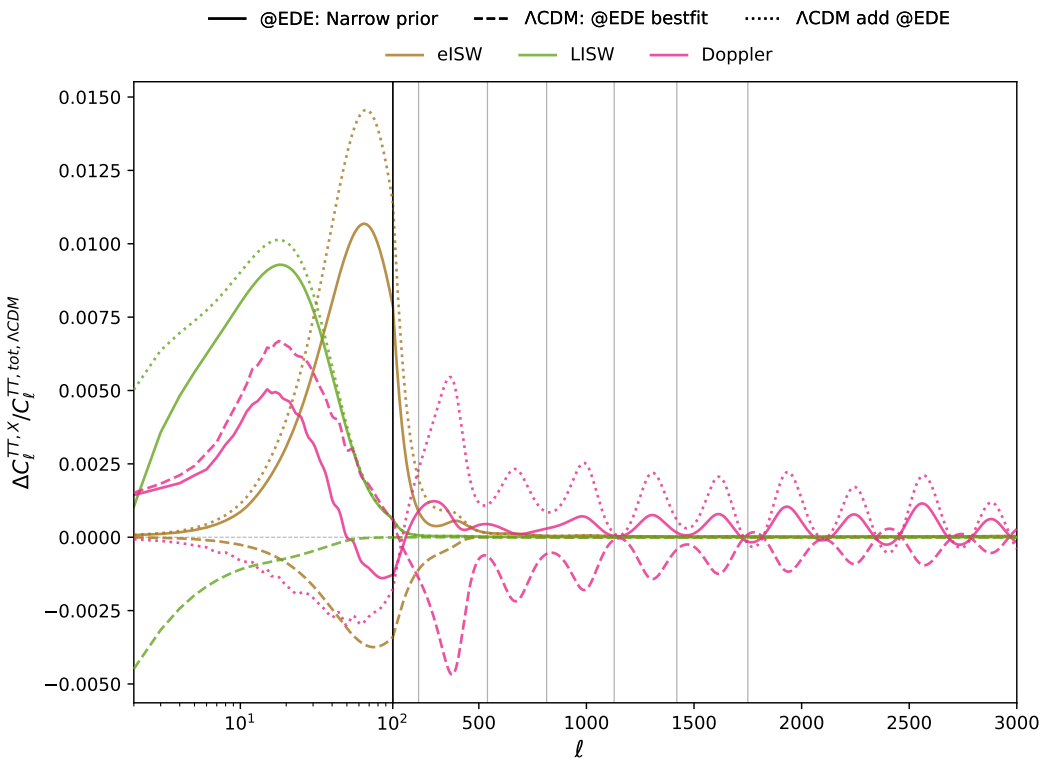

Figure 4.8: Breakdown of the CMB temperature spectrum C_ℓ^{TT} components for the narrow priors model. The early integrated Sachs-Wolfe (eISW) effect is shown in beige, the late integrated Sachs-Wolfe (LISW) effect in green, and the Doppler effect in pink. Solid lines represent the best-fitting *@EDE: Narrow prior* model, dashed lines represent the best-fitting ΛCDM parameters of *@EDE: Narrow prior* (excluding @EDE injection), and dotted lines represent the best-fitting ΛCDM model with the best-fitting @EDE injection, illustrating the separate impacts of shifting ΛCDM parameters and the @EDE injection.

ω_c impacts both the sound horizon r_s and the angular diameter distance D_A, leading to an increase in θ_* beyond the observed value. The subsequent increase in ω_b and slight decrease in H_0 attempt to correct this shift in θ_* and the positions of the CMB peaks. The effects of the *@EDE: Narrow Priors* model on the components of the CMB temperature spectrum C_ℓ^{TT} are illustrated in Fig. 4.8.

Fig. 4.11 illustrates the competing effects as the ΛCDM parameters adjust to compensate for the influence of @EDE. Despite these adjustments, the

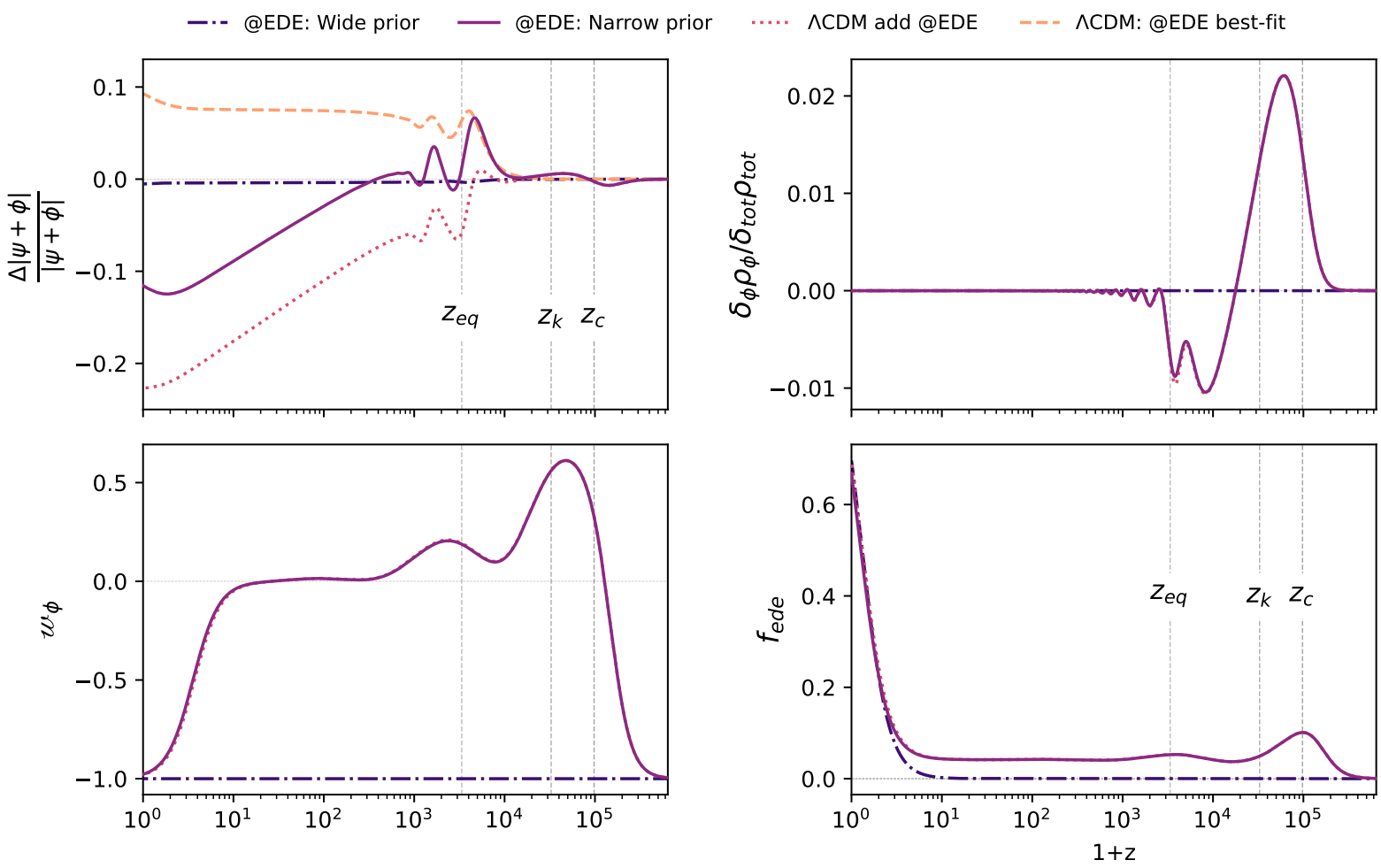

Figure 4.9: Evolution of cosmological perturbations for different cosmologies for the mode $k = 0.1$ Mpc. The dashed vertical lines mark key redshifts: z_{eq} (matter-radiation equality), z_c (peak of EDE injection), and z_k (horizon entry of mode $k = 0.1$ Mpc). The dash-dotted blue curve shows the @EDE best-fit for wide priors including ΛCDM, while the solid purple curve excludes ΛCDM with narrow priors. The dashed orange curve represents ΛCDM parameters adjusted to the best-fit from the @EDE narrow prior scenario. The dotted pink curve shows @EDE parameters at the narrow-prior best fit, with ΛCDM parameters set to the ΛCDM best-fit. These curves illustrate how ΛCDM and @EDE parameters interact and compensate to fit the data. Effectively, the dashed orange and dotted pink curves combine to form the solid purple curve. *Top-left*: Fractional Weyl gravitational potential relative to ΛCDM. *Top-right*: Density perturbation density of the scalar field relative to the total perturbation density. *Bottom-left*: Equation of state (EoS) for @EDE. *Bottom-right*: Fractional @EDE energy density injection.

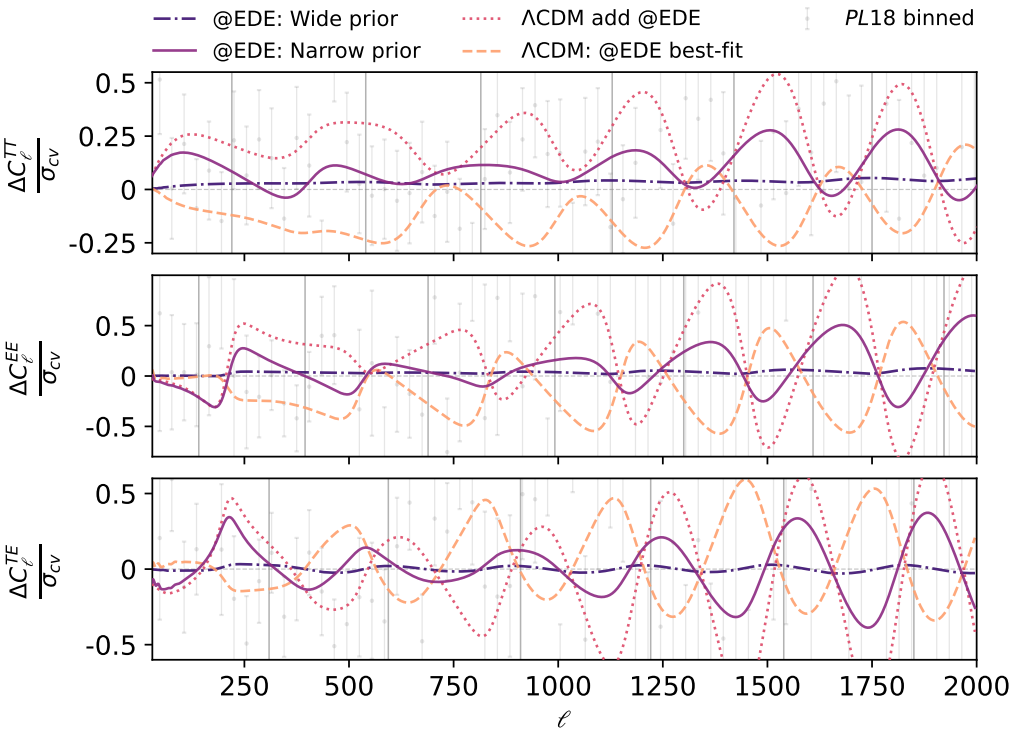

Figure 4.10: CMB residuals for various cosmologies relative to the ΛCDM best-fit, expressed as a fraction of cosmic variance. Light gray data points represent binned measurements from Planck 2018. Solid dark gray vertical lines indicate peak locations in all spectra. *Left:* The dash-dotted blue curve shows the @EDE best-fit for wide priors that include ΛCDM, while the solid purple curve represents @EDE with narrow priors excluding ΛCDM. The dashed orange curve is a ΛCDM cosmology with parameters set to the best fit from the @EDE narrow prior scenario. The dotted red curve represents an @EDE cosmology with ΛCDM parameters set to the ΛCDM best fit and @EDE parameters at the narrow-prior best fit. These curves illustrate the trade-offs and compensations between ΛCDM and @EDE parameters in fitting the data. The dashed orange and dotted red residual curves collectively approximate the solid purple.

parameter shifts ultimately fail to provide a satisfactory fit, resulting in a significantly worsened fit to the CMB data with a relative $\Delta\chi^2 = +44.05$ compared to ΛCDM. The fit to BAO data also deteriorates, with a $\Delta\chi^2 = +2.75$. BAO observations are in strong agreement with CMB data within the ΛCDM framework, showing consistency between r_s, D_A, and $H(z)$ at various redshifts

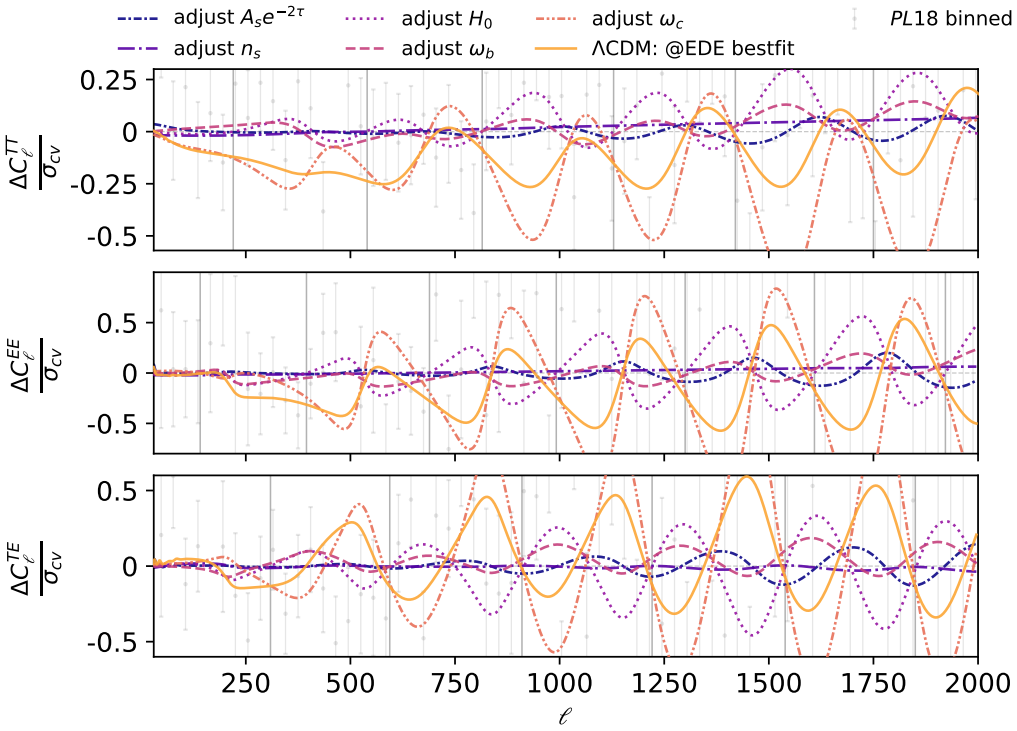

Figure 4.11: Breakdown of the dashed orange curve from Fig. 4.10 (shown here in solid orange) into its individual parameter shifts, highlighting the contributions of specific ΛCDM parameter adjustments. The most significant changes are due to ω_c, causing overall suppression of the power spectrum and shifting peaks to larger angular scales, and H_0,resulting in a compensating shift of peaks to smaller angular scales.

[28]. The introduction of @EDE disrupts this consistency, leading to an increased χ^2 for the BAO data.

Ultimately, two opposing effects prevent @EDE from being a viable solution to the Hubble tension. To match the height of the first CMB peak, ω_c must be increased to counteract the additional early ISW effect from @EDE's early-Universe injection [108, 167, 168]. Conversely, to maintain the peak's position, ω_c must be decreased to ensure a good fit to θ_* through shifts in D_A. Since both conditions cannot be met simultaneously, @EDE is not favored by the data, and the posteriors align more closely with a ΛCDM-like Universe.

4.5 Summary

In this project, I proposed a unified framework for explaining both early and late dark energy using a single scalar field — @EDE. This approach has the potential to simultaneously address the Hubble tension and drive the late-time acceleration of the Universe's expansion, without the necessity for fine-tuning the model parameters. The coincidence between the onset of EDE and matter-radiation equality is naturally explained by a saddle point in the dynamical system during the radiation epoch, which attracts solutions regardless of their initial conditions. Similarly, late dark energy emerges as a global attractor of the system at late times.

We investigated a fiducial @EDE model based on a double exponential potential, which finds its origins in string theory. Regrettably, this particular model did not receive support from the data. The reason lies in the dynamical system also exhibiting a saddle point during the matter-dominated era, where the scalar field contributes a fraction of non-clustering dark matter to the Universe's energy budget. This contribution decreases the angular diameter distance D_A to the CMB. Moreover, similar to other EDE models, the early ISW effect is amplified. To offset this amplification, an increase in ω_c is required, but the decrease in D_A demands a reduction in ω_c. Since it is impossible to find a single value of ω_c that simultaneously compensates both effects, the model fails to provide a satisfactory fit to the data.

Part III

The Implications of DESI BAO Y1 On the phenomonology of Dark Energy

5 DESI 2024 Y1 Release: Dynamical Dark energy?

> *"Everything flows, out and in; everything has its tides; all things rise and fall; the pendulum-swing manifests in everything; the measure of the swing to the right is the measure of the swing to the left; rhythm compensates."*
>
> – Three Initiates, The Kybalion 1908

As discussed in Chapter 1, ΛCDM faces theoretical limitations and growing observational tensions. While various alternative models have been proposed, none have yet matched ΛCDM's consistency with existing data. Recent analyses indicate mild preferences for dynamical dark energy, warranting further investigation. In this chapter, I examine two dynamical dark energy models in light of the growing evidence from the Union3 [33], DESY5 [34], and DESI [35] datasets, which suggest a preference for such models.

Among these datasets, DESI provides the first strong evidence favoring dynamical dark energy. In its first-year results released in April 2024, the collaboration reported a preference for a dynamical dark energy model over ΛCDM [35], with the strongest tension reaching $\sim 3.9\sigma$. DESI's project design, which examines BAO's imprint in large-scale structure and redshift-space distortions (RSD) across a broad redshift range, is aimed at probing dark energy's role in cosmic expansion by collecting spectra from millions of galaxies and quasars.

When analyzed in combination with Planck and Atacama Cosmology Telescope (ACT) CMB measurements, and Type Ia supernovae data from Pantheon+ [55], Union3 [33], and DESY5 [34], DESI's findings exhibit statistically significant preference for thawing dark energy at the levels of 2.5σ, 3.5σ, and

3.9σ respectively. In these scenarios, the EoS of dark energy, $w(z)$, evolves over time, contrasting with the ΛCDM model where $w(z) = -1$ remains constant. This preference for thawing dark energy is highlighted when the data is analyzed using the phenomenological Chevallier-Polarski-Linder (CPL) parameterization [169, 170], expressed as

$$w(z) = w_0 + w_a(1 - a), \tag{5.1}$$

where w_0 and w_a are free parameters fitted to observational data. The DESI analysis reports the strongest tension at $w_0 = -0.727 \pm 0.067$ and $w_a = -1.05^{+0.31}_{-0.27}$ based on a combined analysis of CMB, DESI, and DESY5 datasets. While parameterizations such as Eqn. (5.1) are useful for hypothesis testing and data characterization, they do not inherently provide a complete physical framework, as they are not derived from first principles and may fail to capture the dynamics of dark energy at high redshifts [170–174].

Notably, since the release of DESI data, extensive studies have examined its compatibility with ΛCDM and implications for dynamical dark energy models [174–181]. Some studies focus on fitting established models including interacting and quintessential dark energy against DESI findings [182–185]. However, DESI's preference for dynamical dark energy has sparked discussions over potential systematic effects. For instance, studies have explored how assumptions in Halo Occupation Distribution (HOD) models might bias BAO measurements [186]. Moreover, redshift inaccuracies in Lyman-α forest correlations have been investigated, indicating potential biases in quasar redshift estimations [187]. These findings emphasize the importance of rigorously addressing systematic uncertainties to accurately interpret DESI's data within the framework of dark energy models. As of now, it remains unclear whether the observed tension is genuine or a result of systematic biases, underscoring the need for further data and analysis to reach a definitive conclusion.

In the following sections, we examine the implications of fitting two theoretically motivated dark energy models from the literature to the observational results.

5.1 DESI Constraints on Exponential Quintessence

The first model I analyze is the single-exponential quintessence model [36], a cornerstone of dark energy research due to its natural emergence in theories beyond the Standard Model, such as string theory and supergravity [150, 188, 189]. While the phenomenology of cosmological scalar fields, quintessential dark energy, and the single-exponential quintessence model has already been discussed in Section 1.3, Section 3.4, and Subsection 3.4.1 respectively, a brief review is included here for completeness.

Quintessential dark energy models [36, 37, 147, 190, 191] attribute dark energy to a scalar field ϕ with mass m_ϕ. Initially, the field is frozen at its initial value due to Hubble friction, resulting in an EoS of $w = -1$. As the Hubble parameter $H(z)$ decreases and becomes comparable to m_ϕ, the field begins to thaw, leading to deviations in the EoS, such that $w \gtrsim -1$, as shown in Fig. 1.2. The phenomenology of quintessence dark energy strongly depends on the choice of the potential. The single-exponential potential [36] is given by

$$V(\phi) = V_0 e^{-\lambda \frac{\phi}{M_{\rm Pl}}} , \tag{5.2}$$

where V_0 and λ are model parameters. The action describing the theory involves a minimally coupled scalar field interacting with gravity, as given by Eqn. (1.27). From this action, the equation of motion for the scalar field is given by Eqn. (1.28), while the field's density, pressure, and EoS are defined in Eqns. (1.30) and (1.31), respectively. In the context of a FLRW universe, the scalar field is treated as a perfect fluid, with its density parameter specified by Eqn. (3.13).

Despite the complexity introduced by the non-linearity of the Klein-Gordon equation of motion in Eqn. (1.28) and the Friedmann equations, the phase space of exponential quintessence is well understood. This clarity arises because these equations can be transformed into an autonomous form, enabling the application of the dynamical systems methods detailed in Chapter 3 to identify steady-state solutions [36, 37, 50, 147], as found in Subsection 3.4.1. The

resulting system of equations includes a dark energy-dominated global attractor with $\Omega_\phi = 1$ and EoS

$$w_\phi = -1 + \frac{\lambda^2}{3}, \tag{5.3}$$

provided that $\lambda < \sqrt{3}$, which is point E in Table 3.4. This potential can realize a thawing DE scenario where, at early times, the field remains frozen with $w_\phi \approx -1$. As it thaws and begins to roll, it approaches an attractor near $z \sim 1$, which coincides with the present phase in the cosmological timeline. However, the attractor is not yet reached, as doing so would imply a DE-dominated universe, inconsistent with current observations, where w would remain constant. This results in mild sensitivity to the initial conditions.

5.1.1 Methodology

I now evaluate this scenario using the DESI data by fitting it to the combined datasets of CMB+DESI+Union3. The CMB datasets include Planck 2018 CMB spectra [10], CMB gravitational lensing data from a combination of Planck 2020 lensing [127, 192] and ACT DR6 [193, 194]; this is consistent with the data combination utilized by DESI in that we use the same Planck and ACT likelihoods employed in the DESI analysis. I incorporated the exponential potential into `CLASS` [1, 2] to model the cosmological evolution and used the `Cobaya` [155] framework for sampling via the MCMC [153, 154] algorithm. Convergence was deemed when the Gelman-Rubin criterion $R - 1 < 0.01$ [195] was satisfied. I utilized `GetDist` [157] for chain analysis and plotting.

The initial conditions were set based on the following assumptions. For the initial field value ϕ_i, I leveraged a model symmetry: $\phi \to \phi + \phi_0$, $V_0 \to V_0 \exp(\lambda\phi_0/M_{\rm Pl})$ where ϕ_0 is a constant, which permits fixing ϕ_i without loss of generality. Hence, I arbitrarily set $\phi_i = -4.583 M_{\rm Pl}$.

For the initial field velocity $\dot{\phi}_i$, I used attractor initial conditions. At early times, the field is nearly frozen, justifying the slow-roll approximation, meaning $\ddot{\phi} = 0$ in Eqn. (1.28), yielding $\dot{\phi}_i = \frac{\lambda V_0}{3H_i} \exp(-\lambda\phi_i/M_{\rm Pl})$. Lastly, I modified `CLASS` to dynamically determine V_0 such that $V_0 = 3H_0^2 M_{\rm Pl}^2 \Omega_\phi$ to close the universe. I also fitted the w_0–w_a parameterization to the same dataset combination for a fair comparison. Although DESI already performed this fit, I reproduced

Parameter & Model	**F**lat **ΛC**DM	$\boldsymbol{w_a w_a}$**C**DM	$\boldsymbol{w_\phi}$**C**DM
Sampled Parameters			
$\log(10^{10}A_{\rm s})$	$3.053(3.059)^{+0.013}_{-0.014}$	$3.040(3.040)\pm0.013$	$3.056(3.051)\pm0.013$
$n_{\rm s}$	$0.9681(0.9688)\pm0.0036$	$0.9657(0.9668)\pm0.0038$	$0.9691(0.9692)\pm0.0037$
$\Omega_b h^2$	$0.02245(0.02247)\pm0.00013$	$0.02238(0.02242)\pm0.00014$	$0.02248(0.02249)\pm0.00014$
$\Omega_c h^2$	$0.11876(0.11856)\pm0.00084$	$0.11968(0.11982)\pm0.00097$	$0.11840(0.11839)\pm0.00089$
$100\theta_*$	$1.04199(1.04193)\pm0.00028$	$1.04187(1.04185)\pm0.00029$	$1.04202(1.04199)\pm0.00029$
$\tau_{\rm reio}$	$0.0590(0.0614)\pm0.0071$	$0.0526(0.0529)\pm0.0072$	$0.0608(0.0588)^{+0.0070}_{-0.0084}$
w_0	$\cdots$	$-0.656(-0.679)\pm0.099$	$\cdots$
w_a	$\cdots$	$-1.22(-1.14)^{+0.42}_{-0.34}$	$\cdots$
λ	$\cdots$	$\cdots$	$0.60(0.74)^{+0.38}_{-0.27}$
Derived Parameters			
H_0[km/s/Mpc]	$67.92(67.98)\pm0.39$	$66.52(66.61)\pm0.94$	$66.92(66.613)^{+0.99}_{-0.77}$
Ω_m	$0.3075(0.3065)\pm0.0051$	$0.3227(0.3221)\pm0.0095$	$0.3162(0.3189)^{+0.0070}_{-0.010}$
w_ϕ	$\cdots$	$\cdots$	$-0.936(-0.919)^{+0.038}_{-0.064}$
$\boldsymbol{\chi^2}$ **statistics**			
$\chi^2_{bf}(\Delta)$	2835.45	2822.10(−13.5)	2832.87(−2.58)
χ^2_{bf}/DoF	1.21	1.21	1.21
Tension Level	$\cdots$	3.02σ	1.24σ(n.s.)

Table 5.1: Marginalized posteriors for flat ΛCDM, w_0w_aCDM, and quintessence models using CMB+DESI+Union3 datasets, showing the mean (best-fit) and the 68% confidence interval where the ΛCDM parameters share the same prior across models. We also show the best-fitting $\chi^2_{bf}(\Delta)$, where $\Delta = \chi^2_{{\rm b}f,model} - \chi^2_{{\rm b}f,\Lambda{\rm CDM}}$ represents the difference between the best-fitting χ^2 values with respect to ΛCDM. The level of tension with ΛCDM are reported in the final row with "n.s." indicating an insignificant tension.

it within my own pipeline using the same likelihoods, priors, and nuisance parameters (where available). This is important because MCMC sampling is inherently stochastic: chains are initialized randomly, and convergence behavior can vary slightly even with the same settings. Re-running the w_0–w_a model

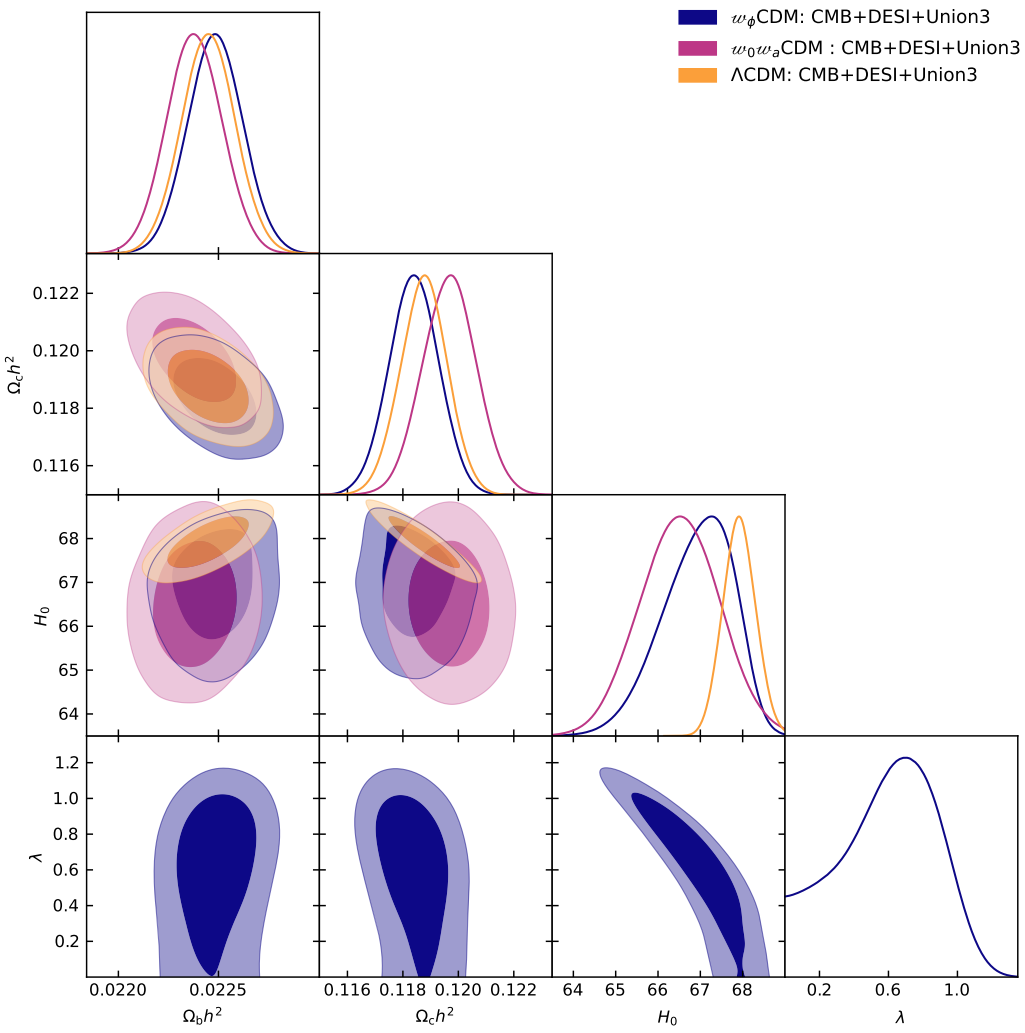

Figure 5.1: Marginalized posteriors for the cosmological models studied in this work using CMB + DESI + Union3 data. The inner contours denote the 68% confidence level, while the outer contours denote the 95% CL. Both w_0w_aCDM and quintessence models encompass the ΛCDM limit.

ensures that any differences observed arise purely from the physics of the models and not from differences in implementation or sampling noise.

5.1.2 Results and Conclusions

Our findings are detailed in Table 5.1, with 2D contours and marginalized posteriors illustrated in Fig. 5.1. We confirm the DESI result that the w_0–w_a

parameterization is preferred over ΛCDM at the level of $\sim 3\sigma$, but find no statistically significant preference for the exponential quintessence model. Consequently, we conclude that both ΛCDM and exponential quintessence are less favored compared to the w_0–w_a model.

The reason for the shortcomings of the quintessential model can be seen in Fig. 5.2, where we plot $w(z)$ for the best-fitting w_0–w_a and exponential quintessence models. Both models exhibit $w(z) > -1$ at the present time, trending towards more negative values in the past. However, the w_0–w_a model reaches $w = -1$ more rapidly. As noted by DESI [35] and further examined by [175], the DESI preference for thawing dark energy is driven by low-redshift anomalies in the supernovae and DESI BAO data as the higher redshift DESI points align with ΛCDM.

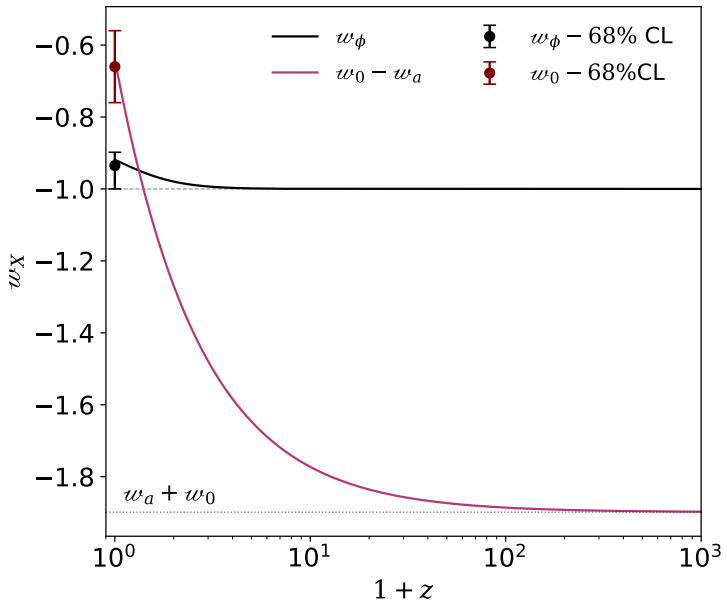

Figure 5.2: The equation of state for the best-fitting exponential quintessence model (w_ϕ, black) and the CLP parameterization (red). The dashed line corresponds to the ΛCDM model with $w_\Lambda = -1$, and the dotted line represents $w_0 + w_a$, which is the asymptotic EoS for the CLP parameterization for $z \gg 0$. We also show the marginalized posteriors for the EoS today for both models with the combination of CMB+DESI+Union3 datasets at the 68% level.

The w_0–w_a parameterization accommodates the low redshift points by having $w_0 > -1$ and a large negative w_a value, ensuring a quick return to $w \approx -1$. The increasing negative w values at higher redshifts are not problematic because DE is subdominant during this epoch, and the model behaves similarly to ΛCDM. In addition, the CPL parameterization is only valid for $z \sim \mathcal{O}(1)$. In contrast, the EoS for the exponential model varies less dramatically due to the slow-rolling field. The EoS approaches $w = -1$ at higher redshifts when DE is subdominant, preventing the model from fitting each data point as effectively.

This suggests that quintessence potentials with sharper features, such as hill-top or plateau models, may better fit the data due to their ability to allow for more rapid variations in $w(z)$ around the onset of DE. Indeed, [174] reached a similar conclusion using a different approach, where they derived an equivalent w_0–w_a parameterization for three classes of quintessence models, finding that while exponential models fall outside the DESI 1σ contours, hill-top and plateau models are consistent with the data.

5.2 First Constraints on a Pixelated Universe in Light of DESI

Now, we turn to the second model I analyzed. In this section, I examine the *pixelated dark energy* (pixelated DE) model [196, 197], a UV-complete framework for dark energy motivated by F-theory. Compactification of extra dimensions within this framework results in a four-dimensional spacetime with a time-dependent cosmological constant. In this setup, dark energy is conceptualized as discrete units, or "pixels," whose number, $N(t)$, evolves over time. This evolution drives a dynamic cosmological constant

$$\Lambda(t) = \frac{8\pi^2}{\ell_s^2} \frac{1}{N(t)}\,, \tag{5.4}$$

where ℓ_s is the string length. The time dependence of $\Lambda(t)$ leads to an effective EoS for dark energy

$$w(t) = -1 + \frac{\Gamma(t)}{3H(t)}\,, \tag{5.5}$$

where $H(t)$ is the Hubble parameter, and $\Gamma(t) \equiv \dot{N}(t)/N(t)$ describes the growth or decay rate of the pixels.

The evolution of this model depends on the time dependence of $N(t)$, which requires a specific string theory framework to derive. As this remains an open problem, it lies beyond the scope of this dissertation. In this project, my contribution was specific to fitting the predictions of the pixelated DE model to DESI data and derive its posteriors. So, I will only focus on testing the model's observational predictions using cosmological data. For a comprehensive introduction to the pixelated dark energy model, I encourage the readers to refer to [196, 197].

5.2.1 The Pixelated Dark Energy Model

The simplest and best-motivated model of pixelated DE assumes a constant growth rate, Γ [196, 197]. This model can be written on the form of the CPL parameterization which streamlines comparisons to the findings of DESI. The EoS in Eqn. (5.5) can be shown to be

$$w_0 = -1 + \frac{\Gamma}{3H_0}, \tag{5.6}$$

$$w_a = -\frac{1}{2}\Omega_m \frac{\Gamma}{H_0}, \tag{5.7}$$

$$w(a) = w_0 + w_a(1-a), \tag{5.8}$$

where H_0 is the present-day Hubble parameter, Ω_m is the matter density parameter, and a is the scale factor. A detailed derivation of these expressions is provided in Appendix A.

In the regime of interest, near present-day values, achieving $w_0 > -1$ and $w_a < 0$, which align with the predictions of DESI, implies that $\dot{N} > 0$. The derivation in Appendix A assumes that Γ is approximately constant, meaning $\dot{\Gamma}/\Gamma \ll H_0$ and that $\Gamma/H_0 \ll 1$, so that higher-order terms may be neglected [197]. Although assuming a constant Γ simplifies the analysis, it is generically expected that Γ varies over time. We will explore the implications of a time-dependent Γ later on, in Subsection 5.2.3.

While pixelated DE fits within the broader CPL parameterization, it is more constrained. In the CPL latter, w_0 and w_a are independent parameters, whereas the former, with constant Γ, is a one-parameter extension of ΛCDM. This is because w_a can be expressed as

$$w_a = -\frac{3}{2}\Omega_m(1+w_0)\,, \tag{5.9}$$

rendering w_a a derived parameter, dependent on w_0 and Ω_m. The dependence on Ω_m distinguishes pixelated DE from CPL, where w_0 and w_a are generally independent of Ω_m.

Since Ω_m is jointly constrained in cosmological data analyzes, the DESI bounds reported in [35] cannot be directly applied to the pixelated DE model because these analyses do not account for the covariances induced by the relation in Eqn. (5.9). Indeed, [175] noted that the DESI covariances of Ω_m with other cosmological parameters are significant. Therefore, it is essential that the relation in Eqn. (5.9) is explicitly fit to DESI data, or more generally, to the full set of cosmological data, through an independent analysis. With this motivation in mind, we now test the pixelated DE model against cosmological observations for the first time.

5.2.2 Methodology

I modified the cosmological solver `CLASS` [1, 2] to evolve the cosmology of pixelated DE according to Eqn. (5.8), using the relation in Eqn. (5.9) to compute w_a. For the standard w_0–w_a parameterization, I sampled over the six ΛCDM parameters $\{A_s, n_s, 100\theta_*, \Omega_b h^2, \Omega_c h^2, \tau_{reio}\}$, plus $\{w_0, w_a\}$. In contrast, for pixelated DE, Eqn. (5.9) defines w_a as a derived parameter. Thus, I only sampled over $\{A_s, n_s, 100\theta_*, \Omega_b h^2, \Omega_c h^2, \tau_{reio}, w_0\}$ and modified `CLASS` to compute w_a from the sampled w_0 and Ω_m.

I fitted both models to the same datasets used in Subsection 5.1.1, replacing the supernova dataset Union3 [33] with DESY5 [34], as the latter is newer and provides tighter constraints on the dark energy EoS. This change in dataset is specific to the pixelated DE analysis; the DESY5 likelihood was not publicly available at the time the first model in Section 5.1 was studied. As in

Parameter & Model	**Flat ΛCDM**	$w_a w_a$**CDM**	**Pixelated Dark Energy**
Sampled Parameters			
$\log(10^{10}A_s)$	$3.051(3.048) \pm 0.013$	$3.041(3.041) \pm 0.013$	$3.058(3.058) \pm 0.014$
n_s	$0.9674(0.9664) \pm 0.0035$	$0.9658(0.9676) \pm 0.0038$	$0.9694(0.9697) \pm 0.0038$
$\Omega_b h^2$	$0.02243(0.02243) \pm 0.00013$	$0.02238(0.02237) \pm 0.00014$	$0.02249(0.02251) \pm 0.00013$
$\Omega_c h^2$	$0.11907(0.11931) \pm 0.00083$	$0.11963(0.11948) \pm 0.00097$	$0.11835(0.11858) \pm 0.00091$
$100\theta_*$	$1.04195(1.04207) \pm 0.00028$	$1.04189(1.04184) \pm 0.00029$	$1.04203(1.04198) \pm 0.00028$
$\tau_{\rm reio}$	$0.0579(0.0569) \pm 0.0069$	$0.0530(0.05337) \pm 0.0073$	$0.0615(0.0613)^{+0.0068}_{-0.0088}$
w_0	...	$-0.733(-0.705) \pm 0.068$	$-0.949(-0.955) \pm 0.025$
w_a	...	$-1.01(-1.01)^{+0.34}_{-0.28}$	$-0.025(-0.021)^{+0.015}_{-0.013}$
Derived Parameters			
H_0[km/s/Mpc]	$67.78(67.73) \pm 0.37$	$67.21(67.13) \pm 0.65$	$66.76(66.85)^{+0.66}_{-0.59}$
Ω_m	$0.3095(0.3104) \pm 0.0049$	$0.3159(0.3163) \pm 0.0065$	$0.3175(0.3172) \pm 0.0064$
$\boldsymbol{\chi^2}$ **Statistics**			
$\chi^2_{bf}(\Delta)$	4450.75	4434.11(−16.64)	4446.99(−3.76)
$\chi^2_{bf,CMB}(\Delta)$	2771.89	2770.62(−1.27)	2773.56(+1.67)
$\chi^2_{bf,BAO}(\Delta)$	17.82	11.93(−5.89)	18.50(+0.68)
$\chi^2_{bf,SNe}(\Delta)$	1646.51	1637.82(−8.69)	1640.80(−5.71)
χ^2_{bf}/DoF	1.072	1.068	1.071
Tension Level	···	3.49σ	1.62σ

Table 5.2: Marginalized posteriors for flat ΛCDM, $w_0 w_a$CDM, and pixelated DE models using CMB + DESI + DESY5 likelihoods, showing the mean(best fit) and the 68% confidence interval. The ΛCDM parameters share the same prior across models, and only the priors of $\{w_0, w_a\}$ parameters differ in $w_0 w_a$CDM and pixelated DE. We also show the best fitting $\chi^2_{bf}(\Delta)$, where $\Delta = \chi^2_{\rm bf,model} - \chi^2_{\rm bf,\Lambda CDM}$ is the difference between the best fitting χ^2 values, subtracted from that of ΛCDM. The statistically significant tension levels with ΛCDM are reported as well.

Section 5.1, the MCMC sampling was performed using the `Cobaya` code [155], with convergence determined by the Gelman-Rubin criterion, $R-1 < 0.01$ [195].

For pixelated DE, I imposed the priors $w_0 \sim \mathcal{U}[-1, 1]$, which reflect the requirement in Eqn. (5.7) that $w(a) \geq -1$ in pixelated DE, while for the w_0-w_a parameterization I imposed an uninformative wide prior with $w_0 \sim \mathcal{U}[-3, 1]$ and $w_a \sim \mathcal{U}[-3, 2]$. Lastly, I analyzed and plotted our chains using `GetDist` [157].

5.2.3 Results and Conclusions

Our results are summarized in Table 5.2, with 2D contour plots and 1D marginalized posteriors shown in Fig. 5.4. For the standard CPL parameterization, our findings are consistent with DESI [35], yielding $w_0 = -0.733 \pm 0.068$ and $w_a = -1.01^{+0.34}_{-0.28}$. We confirm DESI's conclusion that this model is favored over ΛCDM at approximately the 3.5σ level. In contrast, the pixelated DE model gave results of $w_0 = -0.949 \pm 0.025$ and $w_a = -0.024^{+0.015}_{-0.013}$. We also derived the posterior for the growth rate of pixels, obtaining a 68% confidence interval for Γ_0/H_0:

$$\frac{\Gamma_0}{H_0} = 0.145 \pm 0.075\,, \tag{5.10}$$

with a best-fit value of $(\Gamma/H_0)_{\text{best fit}} = 0.135$. This result suggests that the pixel number is increasing at a rate slower than the universe's expansion.

Our analysis indicates a mild preference for the pixelated DE model over ΛCDM, with a best-fit improvement of $\Delta\chi^2_{\text{bestfit}} = -3.76$, corresponding to a tension level of 1.62σ. Statistically, a comparable performance to ΛCDM requires $\Delta\chi^2_{\text{bestfit}} = -1$ per additional degree of freedom, and our result slightly exceeds this threshold. This implies that the model's added complexity allows it to better fit the data than ΛCDM, though not as significant as the CPL model, which achieves a best-fit improvement of $\Delta\chi^2_{\text{bestfit}} = -16.64$ for two additional degrees of freedom, corresponding to a tension of 3.49σ.

From Table 5.2, we see that the preference for pixelated DE over ΛCDM is primarily driven by the fit to the supernova dataset DESY5, which gives an improvement of $\Delta\chi^2_{\text{bestfit}} = -5.71$ compared to ΛCDM. However, the pixelated DE model underperforms relative to ΛCDM when considering the remaining datasets combined.

Despite its alignment with the CPL parameterization of dark energy and its mild improvement over ΛCDM, the pixelated DE model with a constant Γ fails to provide a fit on a similar statistical level as the CPL model. Theoretical limitations arise from the fixed relationship between w_0 and w_a, as described by Eqn. (5.9), which constrains the variability of $w(z)$ and prevents it from adequately matching data across different redshifts. Specifically, supernovae and DESI data at redshifts $z \lesssim 0.51$ exhibit deviations from ΛCDM predictions,

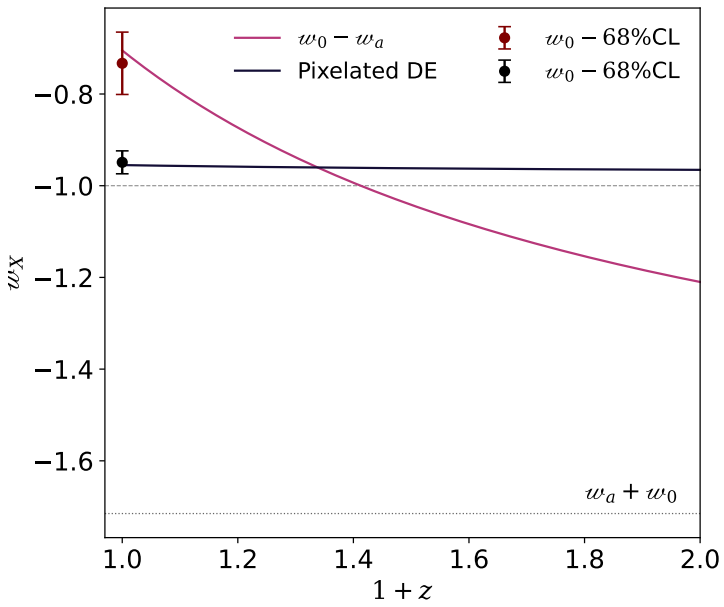

Figure 5.3: The best fitting EoS for the w_0–w_a model and pixelated DE. The CPL parameterization suggests that the dark energy fluid initially has an equation of state of $w_a + w_0 = -1.72$, represented by the dotted line, for $z \gtrsim 10^3$. The EoS evolves around redshift $z \approx 10^3$, crossing the phantom line $w = -1$ at $z \approx 0.4$, coinciding with the onset of dark energy domination. The black solid line is the EoS of pixels in which the field starts frozen at $w = -0.976$ and evolves to $w_0 = -0.955$ today. The dashed line represents the EoS for a cosmological constant, $w_\Lambda = -1$. We also show the 68% confidence level posteriors of w_0 for both $w_0 w_a$CDM and pixelated DE in red and black, respectively.

while DESI data at higher redshifts remain consistent. For further insights, see the discussions in [35, 51, 174, 175, 185].

The CPL model accommodates data across all redshifts by setting $w_0 > -1$ and a large, negative w_a, with $w_a \approx 2w_0$. This ensures that $w(z)$ rapidly approaches -1 for $z > 0.51$. In contrast, the w_0–w_a parameterization derived from pixelated DE lacks such flexibility. Eqns (5.6) and (5.7) indicate that w_0 deviates from -1 by an amount proportional to Γ/H_0. To fit low-redshift data, Γ/H_0 must be approximately $\mathcal{O}(10^{-1})$, which results in $w_a \sim \mathcal{O}(10^{-2})$ due to suppression by a factor of $\Omega_m \approx 0.3$. As a result, the EoS evolves very slowly

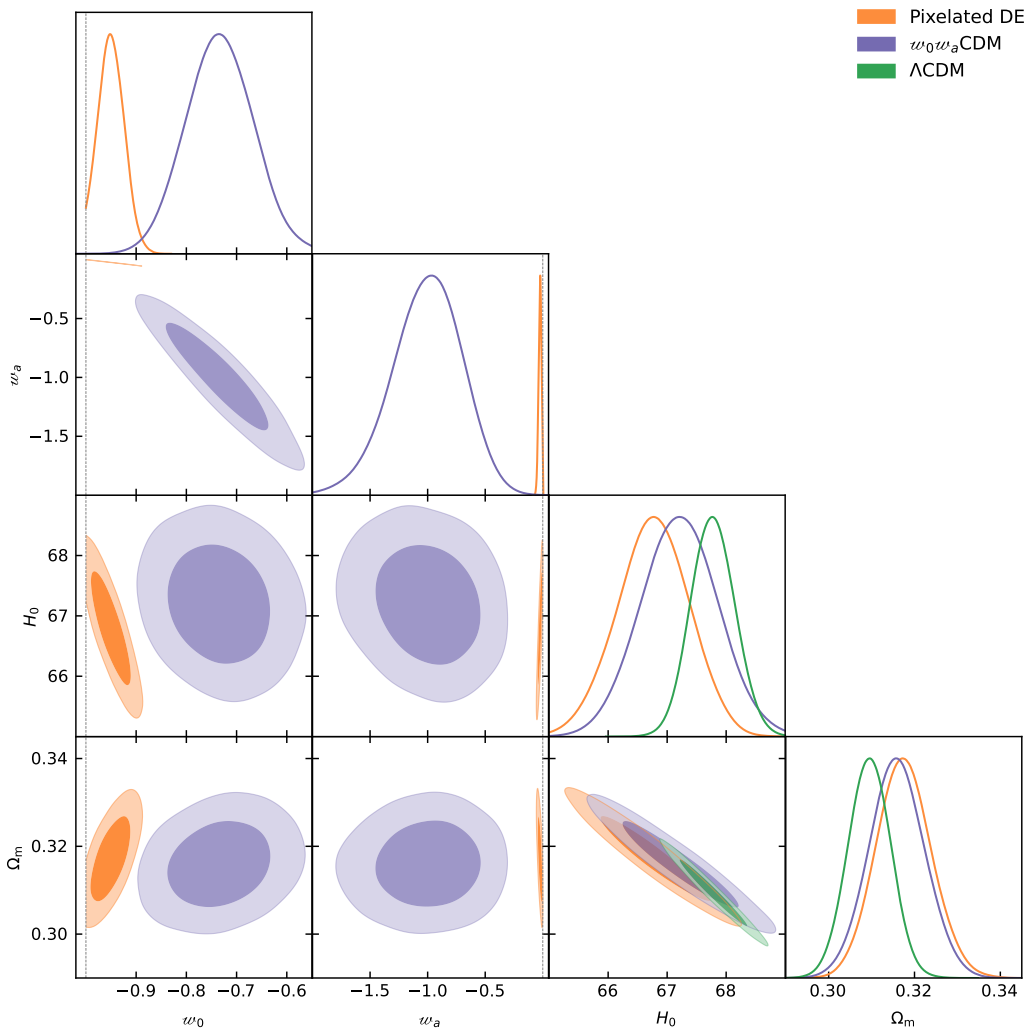

Figure 5.4: Marginalized posteriors for different cosmologies fitted to CMB + DESI + DESY5. The inner contours represent the 68% confidence level (CL) where the outer is 95% CL. The dashed lines indicate the ΛCDM limit with $w_0 = -1$ and $w_a = 0$. Both w_0w_aCDM and pixelated DE include the ΛCDM limit, with pixelated DE being marginally preferred over ΛCDM.

over the relevant redshift range, preventing the model from adequately fitting all data.

This behavior is illustrated in Fig. 5.3, which compares the best-fit EoS for the CPL and pixelated DE models as functions of redshift. For $z > 0$, the CPL

model's EoS transitions rapidly from $w > -1$ to $w = -1$, while the pixelated DE EoS remains nearly constant.

The insights gained from this study can guide the development of UV-complete models of dark energy that align with observational data. A key aspect is breaking the constraint between w_0 and w_a that limits $|w_a| < w_0$. The constraint relation can be relaxed by considering a time-dependent pixel growth rate Γ instead of assuming it to be constant. To derive the more general form of the pixelated DE EoS, we start with the Friedmann equation while substituting $\Lambda(t) = \Lambda_0/N(t)$ with $\Lambda_0 = 8\pi^2/l_s^2$ to find

$$H^2(t) = \frac{\Omega_m H_0^2}{a(t)^3} + \frac{H_0^2(1-\Omega_m)N_0}{N(t)}\,, \tag{5.11}$$

where $N_0 = N(t_0)$ is the number of pixels at the present time, and Λ_0 has been replaced by N_0 using $\Lambda_0 = 3H_0^2 N_0(1-\Omega_m)$. We then, Taylor expand the above equation around $a = 1$ and substitute it in Eqns. (5.5) to find

$$w_0 = -1 + \frac{\Gamma_0}{3H_0}\,, \tag{5.12}$$

$$w_a = -\frac{1}{2}\Omega_m \frac{\Gamma_0}{H_0} - \frac{\Gamma_1}{3H_0^2} - (1-\Omega_m)\frac{\Gamma_0^2}{6H_0^2}\,, \tag{5.13}$$

where

$$\Gamma_0 = \left.\frac{\dot{N}}{N}\right|_0 \quad \text{and} \quad \Gamma_1 = \left.\frac{\ddot{N}}{N^2}\right|_0 - \Gamma_0^2, \tag{5.14}$$

with subscript zeros indicating quantities evaluated at the present time t_0. This implies the EoS also depends on $\ddot{N}/N^2$. We can combine Eqns. (5.12) and (5.13) to obtain

$$w_a = -\frac{3}{2}[(1+w_0)(1+w_0-w_0\Omega_m)] - \frac{\Gamma_1}{3H_0^2} \tag{5.15}$$

This generalization extends the flexibility of the one-parameter model by allowing w_a to take more negative values than the constant Γ model, potentially improving the fit due to its additional degree of freedom. Unlike the constant Γ model, which is more rigid and requires $|w_a|$ to be on the order of $\mathcal{O}(1)$, this generalization enables a more nuanced adjustment of dark energy behavior closer

to the present day. Ideally, a full MCMC analysis would be required to obtain precise posterior constraints on the new parameters Γ_0 and Γ_1, incorporating correlations and variations across the full parameter space. However, conducting such an analysis was beyond the scope of my agreed contribution to this project. As a preliminary step, I instead use the posteriors of the w_0–w_a fit and map them into equivalent values of Γ_0 and Γ_1 via Eqns. (5.12) and (5.13). This allows us to estimate what values of these parameters would yield a comparable fit to the data, giving a rough sense of the parameter ranges consistent with observational constraints. I extract approximate means and 68% confidence intervals, finding

$$\frac{\Gamma_0}{H_0} = 0.80 \pm 0.20 \quad \text{and} \quad \frac{\Gamma_1}{H_0^2} = 2.41 \pm 0.72, \tag{5.16}$$

with the best fitting values $(\Gamma_0/H_0)_{\text{best fit}} = 0.88$ and $(\Gamma_1/H_0^2)_{\text{best fit}} = 2.61$. This corresponds to the 68% confidence level for the pixel number acceleration

$$\frac{\ddot{N}}{N^2 H_0^2} = 3.09^{+0.93}_{-1.20}, \tag{5.17}$$

with the best-fitting value $[\ddot{N}/(NH_0)^2]_{\text{best fit}} = 3.39$. These results suggest that the current pixel growth rate is comparable to the universe's expansion rate and is beginning to increase. Determining the full time-dependence of the pixel decay rate in the UV-construction and verifying if this scenario is viable remains crucial. As an example, [197] noted that larger jumps in pixel numbers from thermal and quantum events could accelerate pixel growth. Therefore, a detailed fit including the extra parameter Γ_1 would provide significant insights into the microphysical dynamics of pixels.

5.3 Insights from Dynamical Dark Energy Models

This chapter investigated the potential of two dark energy models—the single-exponential quintessence model and the pixelated dark energy model—to address tensions between ΛCDM and emerging evidence for thawing dark energy.

The single-exponential quintessence model, while theoretically appealing and motivated by its natural emergence in string theory, lacked the flexibility to account for the rapid variations in $w(z)$ required by observations, particularly at $z \sim 0.5$. The data suggests that scalar field models must incorporate steeper potentials, such as hill-top or plateau models, to allow for sharper transitions in $w(z)$ around the onset of dark energy domination. Without these features, the single-exponential model struggles to resolve the low-redshift anomalies highlighted by supernovae and BAO data.

In contrast, the pixelated dark energy model, rooted in a UV-complete framework, was marginally preferred over ΛCDM, with a best-fit improvement of $\Delta\chi^2_{\text{best fit}} = -3.76$. However, its fixed relationship between w_0 and w_a, governed by a constant pixel growth rate Γ, limited its adaptability to fit the observational data fully. Further analysis revealed that incorporating time-dependent dynamics into Γ allows the model to relax this fixed relationship, enabling greater variability in $w(z)$ and potentially achieving a fit comparable to the CPL parameterization.

Together, these results highlight the importance of dynamical flexibility in dark energy models, whether through evolving scalar potentials or time-dependent cosmological constant, to align theoretical predictions with the observational evidence for thawing dark energy.

Part IV

Cosmology and Astrophysics of CP-Violating Axions

6 Axions and ALPs

> *"... I regard consciousness as fundamental. I regard matter as derivative from consciousness. We cannot get behind consciousness. Everything that we talk about, everything that we regard as existing, postulates consciousness."*
>
> – Max Planck, The Observer 1931

In this chapter, I provide a literature review of axions and ALPs as they appear in high-energy physics and cosmology. Although the research focus of this part is exclusively on CP-violating ALPs, a broad overview of the field is necessary to properly contextualize their origin and phenomenology. I begin by briefly summarizing the development of axions as a solution to the strong CP problem in Section 6.1, followed by a discussion of ALPs arising from string theory compactifications and other beyond-the-Standard-Model frameworks (BSM) [43, 44, 198–200] in Section 6.2. These particles are of significant theoretical and experimental interest due to their potential to solve long-standing problems such as the strong CP problem [62, 63, 201, 202] and to serve as viable dark matter candidates [43, 44, 203].

Building on this foundation, I turn to the class of CP-violating ALPs, which arise naturally in UV theories with intrinsic CP violation and have been studied since the 1980s [3, 204–207]. Unlike the canonical QCD axion, these ALPs inherit scalar—specifically, Yukawa-like—couplings to nucleons that induce long-range fifth forces [204]. Despite their theoretical appeal, such couplings remain largely unexplored in cosmology and astrophysics. This work is motivated by their potential to uncover new phenomenology, novel constraints, and fresh directions for model-building. Section 6.3 presents a detailed review of the UV origin and motivation for these interactions, setting the stage for the theoretical

framework developed in Chapter 7 and the cosmological and astrophysical analyses in Chapters 8 and 9.

6.1 From Axions to ALPs

The study of ALPs traces back to the axion, a particle originally proposed to address the strong CP problem in Quantum Chromodynamics (QCD). The QCD Lagrangian includes a CP-violating term

$$\mathcal{L}_{\theta\text{QCD}} = \frac{\theta_{\text{QCD}}}{32\pi^2}\text{Tr}\Big(G_{\mu\nu}\tilde{G}^{\mu\nu}\Big), \tag{6.1}$$

where θ_{QCD} is a parameter that quantifies the extent of CP-violating interactions, $G_{\mu\nu}$ is the gluon field strength tensor, and $\tilde{G}^{\mu\nu} = \epsilon^{\mu\nu\alpha\beta}G_{\alpha\beta}/2$ is its dual tensor. This term arises due to the "θ-vacua" of QCD (for further details, see [210]). Furthermore, it predicts an electric dipole moment (EDM) for the neutron

$$d_n \approx 3.6 \times 10^{-16}\theta_{\text{QCD}}\, e\,\text{cm}, \tag{6.2}$$

where e is the elementary charge. Experimental measurements constrain the neutron EDM to $|d_n| < 2.9 \times 10^{-26}\, e\,\text{cm}$ at the 90% confidence level [211], implying that $\theta_{\text{QCD}} < 10^{-10}$. This suppression raises a fine-tuning problem, as no fundamental mechanism explains its small value. Additionally, θ_{QCD} could theoretically receive $\mathcal{O}(1)$ contributions from the observed CP-violation in the electroweak (EW) sector [212], further complicating the issue.

Roberto Peccei and Helen Quinn proposed a solution in 1977 by promoting θ_{QCD} to a dynamical field [62]. This introduced the Peccei-Quinn (PQ) symmetry, a global $U(1)$ symmetry that becomes spontaneously broken at a high energy scale. The spontaneous breaking of the PQ symmetry gives rise to a pseudo-Nambu-Goldstone boson, the axion [213, 214], with a continuous shift symmetry characterized by transformations of the form $a(\mathbf{x}) \to a(\mathbf{x}) + a_0$ where a is the axion field and a_0 is an arbitrary constant. This symmetry ensures that the axion dynamically adjusts to cancel the θ_{QCD} term, effectively driving it to zero and eliminating CP violation in the strong interactions.

The axion's dynamics are further shaped by non-perturbative QCD effects, particularly instantons, which mediate tunneling between distinct vacuum states of the QCD vacuum [210]. These vacua are separated by energy barriers, and transitions between them break the continuous shift symmetry, leaving behind a residual discrete symmetry

$$a(\mathbf{x}) \to a(\mathbf{x}) + 2\pi n f_a, \tag{6.3}$$

where n is an integer and f_a is the axion decay constant, the energy scale at which the PQ symmetry breaks. This symmetry breaking gives rise to a periodic potential for the axion

$$V(a) = \Lambda^4 \left[1 - \cos\left(\frac{a}{f_a}\right)\right], \tag{6.4}$$

where Λ is an energy scale and is determined by the QCD dynamics. Specifically, $\Lambda^4 = m_a^2 f_a^2$, where m_a is the mass of the axion.

This potential allows the axion to settle into one of its vacuum states, dynamically determining the value of θ_{QCD}. If the initial misalignment angle of the axion field, $\theta_i = a_i/f_a$, lies within the range $\theta_i \in [-\pi, \pi]$, the axion will naturally roll down the potential and settle into the minimum where $\theta = 0$, resolving the strong CP problem without fine-tuning. This process is aided by the friction caused by the expansion of the universe, known as Hubble friction, which overdamps the axion field when $H \gg m_a$ and delays its motion. Once $H \sim m_a$, the field begins coherent oscillations around the potential minimum, locking in its contribution to the energy density as cold dark matter (see Eqn. (1.28) and Fig. 1.2), and follows the usual cosmological timeline predicted by ΛCDM, including the QCD phase transition and the axion field's oscillations around the potential minimum [43].

This potential allows the axion to settle into one of its vacuum states, dynamically determining the value of θ_{QCD}. If the initial misalignment angle of the axion field, $\theta_i = a_i/f_a$, lies within the range $\theta_i \in [-\pi, \pi]$, the axion will roll down the potential and settle into the nearby minimum, $\theta = 0$. More generally, depending on the value of θ_i, the axion can settle into any of the degenerate minima at $\theta = 2\pi n$, where n is an integer. All such vacua are CP-conserving

because the θ_{QCD} parameter in the QCD Lagrangian is defined modulo 2π, and CP violation vanishes at $\theta = 0 \bmod 2\pi$. Therefore, all minima are physically equivalent and solve the strong CP problem. This process is aided by the friction caused by the expansion of the universe, known as Hubble friction, which overdamps the axion field when $H \gg m_a$ and delays its motion. Once $H \sim m_a$, the field begins coherent oscillations around the potential minimum, locking in its contribution to the energy density as cold dark matter (see Eqn. (1.28) and Fig. 1.2), and follows the usual cosmological timeline predicted by ΛCDM, including the QCD phase transition and the axion field's oscillations around the potential minimum [43].

The specific value of θ_i is determined by the initial conditions of the axion field in the early universe. In post-inflationary scenarios, the axion field is uncorrelated beyond the horizon scale and randomly samples all possible values in different Hubble patches. As a result, the axion can populate multiple minima, leading to the formation of topological defects like domain walls [215, 216]. In contrast, in pre-inflationary scenarios, the axion field is homogenized by inflation, and θ_i is set to a single value across the observable universe. In this case, θ_i is essentially a free parameter of the model and can lie anywhere in $[-\pi, \pi]$, including near $\theta = 0$. The $\theta = 0$ minimum is not preferred dynamically over the others—it is only selected if the initial misalignment happens to be near it. For more detailed discussions, see [43, 217].

Whether the axion field samples a single value or many depends on when the PQ symmetry breaks relative to inflation. In post-inflationary scenarios—where the PQ symmetry breaks after inflation—the axion field is uncorrelated beyond the horizon scale and randomly samples all possible values in different Hubble patches. As a result, the axion can populate multiple minima, leading to the formation of topological defects like domain walls [215, 216]. In contrast, in pre-inflationary scenarios—where the PQ symmetry breaks before or during inflation—the axion field is homogenized across the observable universe, and θ_i is set to a single value. In this case, θ_i is essentially a free parameter of the model and can lie anywhere in $[-\pi, \pi]$, including near $\theta = 0$. The $\theta = 0$ minimum is not preferred dynamically over the others—it is only selected if the initial misalignment happens to be near it. For more detailed discussions, see [43, 217].

However, if θ_i starts outside this range, such as $|\theta_i| > \pi$, the axion can end up in one of the other minima of the potential at $\theta = 2\pi n$, where n is an integer. These other minima are CP-conserving but do not correspond to $\theta_{\text{QCD}} = 0$, and therefore do not solve the strong CP problem. The value of θ_i is determined by the conditions of the early universe, such as those during or before inflation.

Although the original Peccei-Quinn-Weinberg-Wilczek axion model was ruled out, viable extensions such as the KSVZ [218, 219] and DFSZ [220, 221] models remain consistent with experimental constraints. Additionally, the axion framework inspired the study of ALPs, which generalize the axion concept to pseudo-scalars with diverse origins and couplings. ALPs are central to BSM physics, with implications for dark matter, dark energy, and early Universe cosmology [43, 198].

6.2 ALP in String Theory

In string theory, ALPs naturally arise as the manifestation of higher-dimensional fields reduced to four-dimensional effective fields after compactification. While the QCD axion was originally proposed to solve the strong CP problem, ALPs share many of its properties but are not necessarily tied to the QCD sector. Instead, they appear in a variety of string compactifications, leading to a diverse spectrum of light pseudoscalar particles with important phenomenological implications [198, 222].

ALPs in string theory commonly emerge from the compactification of higher-dimensional form fields such as the Kalb-Ramond two-form field, $B_{\mu\nu}$. When extra spatial dimensions are compactified, components of such fields behave as pseudoscalar fields in four dimensions. These fields typically inherit shift symmetries from the higher-dimensional gauge symmetries, making them behave like axions. The shift symmetry prevents large quantum corrections to their mass, making them light and stable [198].

Furthermore, ALPs can also arise from the moduli fields that describe the geometry of the compact dimensions in string theory. In this context, moduli are scalar fields that parameterize the size and shape of the extra dimensions. Kähler moduli refer to fields controlling the overall volumes of internal cycles, while complex structure moduli describe the shape, or complex geometry,

of the compact space. The imaginary parts of these moduli often exhibit shift symmetries, making them natural candidates for axion-like particles. The complexified Kähler moduli, in particular, lead to ALPs that can couple to gauge fields, enriching the phenomenological possibilities for these particles [223].

While QCD axions have been designed to address the strong CP problem, ALPs, on the other hand, are not limited to QCD-related phenomena and can couple to various sectors. For example, ALPs can couple to photons through interactions of the form

$$\mathcal{L}_{a\gamma\gamma} = g_{a\gamma\gamma} a F_{\mu\nu} \tilde{F}^{\mu\nu}, \tag{6.5}$$

where $g_{a\gamma\gamma}$ is the ALP-photon coupling constant, $F_{\mu\nu}$ is the electromagnetic field strength tensor, and $\tilde{F}^{\mu\nu}$ is its dual. Such couplings could lead to observable effects in astrophysical settings, such as the conversion of axions to photons in the presence of strong magnetic fields, potentially detectable by experiments like CAST, ADMX, or future axion haloscopes [224].

The concept of the "axiverse" refers to the broad range of ALPs predicted by string compactifications, with masses spanning from 10^{-22} eV, suitable for fuzzy dark matter, to $\sim 10^{-33}$ eV, relevant for dark energy and EDE [110, 222]. The properties of these particles depend on the specific details of string compactification, such as the geometry of the extra dimensions and the influence of non-perturbative effects [198]. While ALPs share the same potential form as the QCD axion, given in Eqn. (6.4), the energy scale Λ is determined by the compactification properties and associated dynamics.

In addition to offering a rich phenomenology, the axiverse concept provides a natural setting for the emergence of ultralight scalar fields, including ALPs. While many ALPs preserve CP symmetry, the possibility of intrinsically CP-violating ALPs opens up new directions for both theory and observation. We now turn to the UV origin and motivation for CP-violating ALPs, which are the primary focus of this work.

6.3 CP-Violating ALPs: UV Origin and Motivation

The previous sections explained how axions and ALPs arise from the PQ mechanism [62, 63, 213, 214] and from string-theoretic compactifications that generate large "axiverse" spectra [198, 222]. Most phenomenological studies assume that the resulting interactions conserve CP, yet in generic UV completions there is no symmetry that enforces such alignment [205, 209, 223]. Once irreducible phases are present—whether in heavy-fermion Yukawa matrices [205], complex moduli VEVs [223], or in the vacuum misalignment of multiple axions [209]—CP-odd scalar interactions that flip sign under CP emerge as naturally as their CP-even counterparts. Because new sources of CP violation are central to long-standing puzzles such as the baryogenesis problem [225], ALPs with intrinsic CP-violating couplings constitute a theoretically motivated and experimentally promising sector.

Such couplings enter through three broad UV mechanisms. First, complex phases in string compactifications propagate to the low-energy pseudoscalar sector whenever Kähler or complex-structure moduli acquire VEVs, generically inducing non-zero scalar Yukawa couplings [198, 222]. Second, in field-theoretic extensions of the PQ mechanism, misaligned vacuum directions among several axions leave the lightest eigenstate with both CP-even and CP-odd interactions [209]. Third, integrating out heavy electroweak-charged fermions with complex phases generates at one loop the operator $aF_{\mu\nu}F^{\mu\nu}$ alongside the familiar CP-even $aF_{\mu\nu}\tilde{F}^{\mu\nu}$ [205]. These examples make clear that CP violation is the default outcome unless an additional discrete symmetry is imposed.

Having established the UV origin of CP-odd interactions, it is useful to encapsulate their low-energy phenomenology in a model-independent effective Lagrangian. At energies below the symmetry-breaking scale—set by the axion decay constant f_a—these interactions manifest as couplings between the ALP and Standard Model fields, including fermions ψ and gauge bosons, via higher-dimensional operators. Representative terms capturing scalar and pseudoscalar couplings to fermions and gauge bosons include

$$\mathcal{L}_{\text{EFT}} = -a\,\bar{\psi}\big(g_s^{\psi} + ig_p^{\psi}\gamma_5\big)\psi + \frac{a}{M}\Big(c_F F_{\mu\nu}F^{\mu\nu} + c_{\tilde{F}} F_{\mu\nu}\tilde{F}^{\mu\nu}\Big) + \cdots\,, \tag{6.6}$$

where the mass m_a and decay constant f_a are treated as independent parameters [226], and M is an effective cutoff scale associated with higher-dimensional operators, unrelated to the confinement scale Λ appearing in the axion potential of Eqn. (6.4). Here, ψ denotes a generic Standard Model fermion, and the interaction $-a\bar{\psi}\psi$ corresponds to a Yukawa coupling. Because the ALP field a is CP-odd, terms like the Yukawa interaction and $aF_{\mu\nu}F^{\mu\nu}$ flip sign under a CP transformation and therefore signal explicit CP violation whenever g_s^ψ or c_F is nonzero. In contrast, the pseudoscalar structures proportional to g_p^ψ and $c_{\tilde{F}}$ are CP-even.

The scalar and pseudoscalar couplings g_s^ψ and g_p^ψ are, in general, species-dependent, with distinct values for electrons (g_s^e), up quarks (g_s^u), down quarks (g_s^d), nucleons (g_s^N), and so on, with analogous expressions for g_p. In conventional CP-conserving frameworks, ALP couplings to fermions arise from Higgs mixing or heavy fermion loops and are purely pseudoscalar [227, 228]. However, in UV completions with intrinsic CP violation, scalar couplings to fermions and gauge bosons arise generically [205, 209, 223], and their low-energy effects are encoded in operators such as $a\bar{e}e$, $a\bar{q}q$, and $a\bar{N}N$.

In this work, we focus specifically on the Yukawa coupling between the ALP and nucleons, parameterized by the scalar vertex g_s^N. This CP-violating interaction, though theoretically motivated, has received comparatively less attention than its CP-conserving counterparts. The remainder of this section reviews current laboratory and astrophysical constraints on the scalar interaction term $-a\, g_s^N \bar{N}N$, providing context for the parameter space explored in subsequent chapters.

6.3.1 Laboratory Tests and Astrophysical Constraints

Scalar couplings to nucleons, g_s^N, induce spin-independent monopole-monopole interactions that manifest as long-range fifth forces [204]. These macroscopic effects arise when two scalar vertices are present—e.g., between nucleons—leading to a Yukawa-type potential of the form

$$V(r) = -\frac{g_s^1 g_s^2}{4\pi r} e^{-m_a r}, \tag{6.7}$$

which modifies Newtonian gravity as

$$V(r) = -\frac{G_N m_1 m_2}{r}\left(1 + \alpha e^{-\lambda_C r}\right), \quad \text{with} \quad \alpha \equiv \frac{g_s^1 g_s^2}{4\pi G_N m_1 m_2}. \tag{6.8}$$

Here, $\lambda_C \equiv m_a^{-1}$ is the ALP Compton wavelength, which sets the range of the fifth force: lighter ALPs mediate longer-range interactions, while heavier ALPs yield shorter-range effects. The dimensionless coefficient α quantifies the strength of the ALP-mediated force relative to standard Newtonian gravity. Other combinations, such as scalar-pseudoscalar (monopole-dipole) or pseudoscalar-pseudoscalar (dipole-dipole), arise in spin-polarized systems [3] but lie beyond the scope of this work.

The most direct experimental probes of scalar-mediated fifth forces come from precision tests of the Weak Equivalence Principle (WEP), which provide sensitivity to long-range scalar interactions arising from CP-violating ALP couplings. The WEP states that all test bodies fall at the same rate in a gravitational field, regardless of their composition. However, if the ALP couples differently to distinct test masses, then the resulting Yukawa interaction modifies the Newtonian potential as shown in Eqn. (6.8). Because the dimensionless coefficient α depends on the coupling strengths g_s^1 and g_s^2 of the scalar to the test masses, objects with different compositions will experience slightly different accelerations in the presence of the same external source. This deviation constitutes a direct violation of the WEP and constraints the scalar-mediated fifth forces, typically in the $|\alpha| - \lambda$ parameter space[1].

The Eöt-Wash group conducted a sequence of increasingly precise laboratory tests of the WEP [229–231]. These experiments compared the accelerations of different material test masses—such as beryllium, copper, lead, aluminum, and titanium—suspended on torsion balances and measured their differential accelerations toward attractors spanning a wide range of length scales. The 1994 study [229] tested WEP violation toward the Earth, the Sun, and even the Galactic Center, aiming to probe whether the dark matter halo sourcing the Galaxy's gravitational field might induce composition-dependent accelerations.

[1] In this subsection, we use λ and λ_C interchangeably to denote the range of the scalar-mediated fifth force. This matches the convention used in fifth-force experiments, where the force range is typically denoted by λ.

While no significant violations were found for terrestrial or solar attractors, a mild $\sim 2.5\sigma$ signal was observed in the galactic case. At the time, this was interpreted as a potential hint of non-gravitational interactions between dark matter and ordinary matter, though later tests with improved sensitivity—most notably the 2007 follow-up [231]—ruled out such a signal, confirming null results over the full range. The 1999 uranium-attractor setup [230] extended the search down to $\lambda \sim 1$ cm, while also improving the 1994 constraints at intermediate ranges $\sim 10 - 1000$ km. The 2007 torsion pendulum test [231], using Be and Ti test masses and continuously rotating apparatus, achieved the most stringent constraints to date down to roughly a meter, $\lambda \gtrsim 1\,\mathrm{m}$.

A follow-up experiment was carried out by the MICROSCOPE satellite mission [232], which measured the differential acceleration between titanium and platinum test masses in orbit, building directly on the torsion-balance methodology pioneered by Eöt-Wash. The satellite's space-based environment provided exceptional thermal and vibrational stability, allowing for enhanced sensitivity to composition-dependent forces. A follow-up analysis of the full dataset [233] confirmed the null result with significantly reduced uncertainties. MICROSCOPE placed leading constraints on scalar fifth forces with ranges $\lambda \gtrsim 10^5$ m and improved upon Eöt-Wash bounds by an order of magnitude in this regime, although Eöt-Wash is still the leading bound for $1\,\mathrm{m} \lesssim \lambda \lesssim 10^5$ m.

In addition to WEP tests, fifth forces can also be constrained by laboratory measurements of Newton's inverse-square law (ISL). Unlike WEP experiments, which test composition dependence, ISL tests probe deviations in the overall strength or distance scaling of gravity, regardless of material. They are especially sensitive to short-range scalar interactions, making them a complementary probe to WEP-based bounds.

The most sensitive constraints in the micron regime come from microelectromechanical and cantilever-based force measurements. The IUPUI group performed a precision test of the ISL at length scales from 30 to 8000 nm using a torsional micro-oscillator [234]. By measuring the differential torque induced between a rotating attractor and a microfabricated test mass, they were able to constrain scalar forces with ranges down to the nanometer scale. This experiment improved upon their earlier 2007 limits [235] by more than an order of magnitude. Complementary constraints were obtained by the Stanford

group, which used cryogenic microcantilevers to probe forces between closely spaced gold-coated surfaces [236]. Their setup tested gravitational deviations at separations of 5–15, μm, yielding bounds on scalar forces in a regime just above that of the IUPUI experiment.

At relatively larger distances, the Eöt-Wash group tested the ISL at sub-millimeter scales by measuring the torque induced between test masses in the presence of a periodically varying source mass. Their 2007 experiment [237] probed gravitational interactions in the force range of 55 μm to 9.53 mm, placing leading constraints on deviations from Newtonian gravity across the probed range. A follow-up study in 2020 [238] employed improved noise suppression and refined data analysis, leading to even tighter limits on scalar-mediated forces across most of the same range. The 2020 bounds remain dominant, except for a narrow region near 0.5 mm where the earlier limits are marginally stronger.

Another collaboration, The HUST group, conducted a series of ISL tests between 2007 and 2020 using torsion pendula with advanced electrostatic shielding [239–242]. These experiments targeted gravitational interactions at relatively larger sub-millimeter distances, with sensitivity spanning approximately 40 μm to 2 mm. Their experimental design enabled precise measurements of the torque between closely spaced masses while minimizing vibrational and electromagnetic noise. The 2020 results [242] improved these bounds by refining environmental suppression techniques.

An earlier but still relevant ISL test was carried out at the University of California, Irvine [243]. Using a torsion balance with copper test masses and attractors, this experiment measured torques over separations ranging from 2 to 105 cm. Though superseded in precision at shorter ranges by the HUST experiment, the Irvine test remains valuable for constraining very light ALPs with $\lambda \gtrsim 1$ cm.

Taken together, WEP and ISL experiments span an impressive range of force lengths, covering scalar-mediated interactions from $\lambda \sim 30$ nm up to $\lambda \to \infty$. Microelectromechanical and cantilever-based ISL tests probe the shortest ranges, down to tens of nanometers [234, 236], while sub-millimeter torsion balance experiments by Eöt-Wash and HUST extend this reach to a few millimeters [237, 238, 242]. At longer distances, up to several meters and beyond, WEP tests

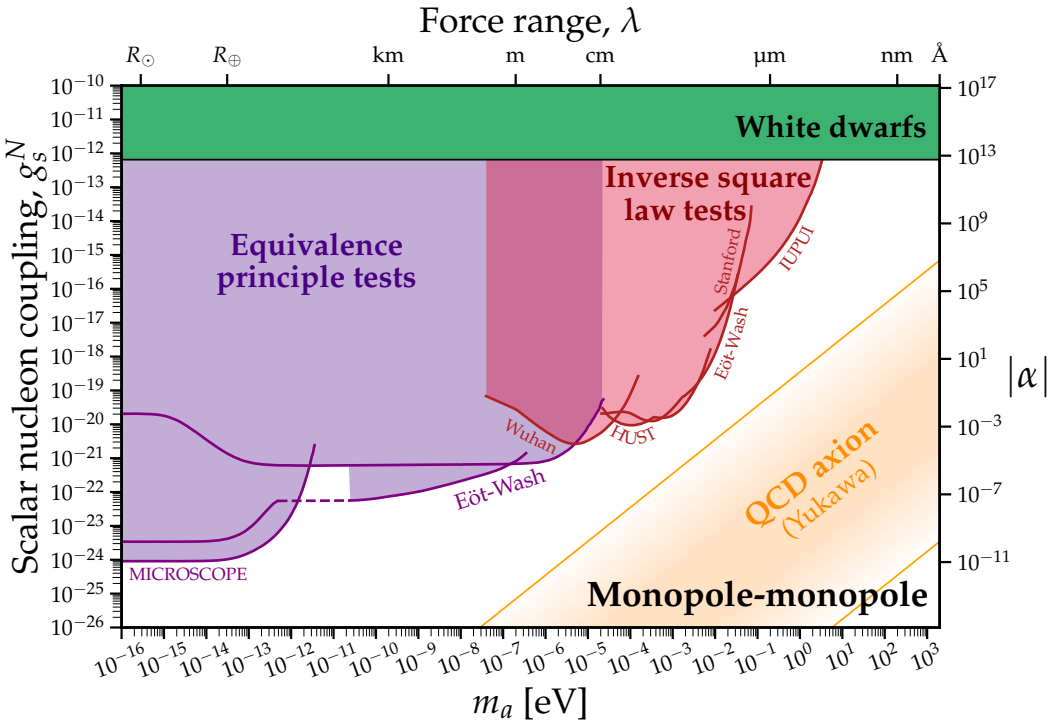

Figure 6.1: Constraints on the scalar ALP–nucleon Yukawa coupling g_s^N vs. m_a. The top axis shows the corresponding fifth-force range $\lambda = m_a^{-1}$, while the right axis shows the strength of the force relative to gravity, $|\alpha|$. Laboratory constraints are shown in red (inverse-square law tests) [234, 237, 238, 242, 243] and purple-blue (equivalence principle tests) [229–232]. The green region shows astrophysical limits from white dwarf cooling [260]. The QCD axion band indicates the parameter space of conventional axion models. This figure is based on and adapted from the open-source repository of Ref. [244].

using Earth-based [230, 231] and astronomical attractors [229], as well as the MICROSCOPE satellite mission [232, 233], provide robust constraints. Collectively, these experiments rule out composition-dependent fifth forces across over 10 orders of magnitude in range. As with the WEP experiments, ISL results are typically expressed as exclusion regions in the $|\alpha| - \lambda$ plane, which have been systematically mapped into the ALP coupling parameter space in the $g_s^N - m_a$ plane by O'Hare and Vitagliano [3, 244] under the assumption of universal baryon number coupling.

On the astrophysical side, energy-loss arguments from red giant stars place novel constraints on the parameter space. The dominant process is $\gamma + {}^4\mathrm{He} \to {}^4\mathrm{He} + a$, where in-medium effects allow plasmons to convert into ALPs in helium-burning stellar cores [245]. This channel is uniquely sensitive to CP-violating scalar couplings of the form $-a\, g_s^N \bar{\psi}\psi$, which modify energy transport in stars without relying on spin-dependent or pseudoscalar interactions. The most recent bound, $g_s^N \lesssim 1.1 \times 10^{-12}$, was derived by O'Hare [3] based on the calculations from Hardy and Lasenby [245], including resonant plasmon mixing and thermal corrections to the emission rate. This constraint builds upon earlier foundational studies [246–248] and is mass-independent for masses below $\sim 10\,\mathrm{keV}$. The bound extends to larger masses, $m_a \sim \mathrm{eV} - 10\,\mathrm{keV}$, compared to WEP and ISL tests, while simultaneously complementing them through partial overlap in the ranges probed.

A more recent and sensitive stellar constraint arises from energy-loss arguments in white dwarf stars, where anomalous cooling affects the observed luminosity function [260]. In these dense, degenerate stars, ALPs are predominantly produced via electron-nucleus bremsstrahlung, $e + {}^A Z \to e + {}^A Z + a$, in carbon/oxygen cores. The resulting energy loss alters the white dwarf luminosity function, allowing precise bounds on scalar ALP emission. The latest analysis [260] derives the constraint $g_s^N \lesssim 6.5 \times 10^{-13}$, covering the same mass range as earlier red giant cooling bounds [3, 245].

The resulting bounds are summarized in Fig. 6.1, which is similar to the original exclusion plot of Ref.[3], but replaces the red giant energy-loss constraint with the updated white dwarf luminosity function bound, reflecting the improved sensitivity to g_s^N. The plot was generated by adapting the open-source code from O'Hare et al. [3] and [244].

With the theoretical origin, UV motivation, and current laboratory and astrophysical bounds on the CP-violating scalar ALP–nucleon coupling established, we now turn to an exploration of the qualitative features of the model studied here. The next chapter investigates the phenomenology of the effective interaction $-a\, g_s^N \bar{N} N$, focusing on its coupling to baryonic matter and the resulting dynamics. This sets the stage for the cosmological and astrophysical analyses presented in the chapters that follow.

7 CP-Violating ALPs: Theoretical Framework

"The highest reach of injustice is to be deemed just when you are not."

– Plato

This chapter marks the beginning of the original contributions of this dissertation. I develop and analyze the scalar field dynamics of CP-violating ALPs in matter-rich environments, uncovering new phenomenological behavior that arises from their scalar Yukawa coupling to baryons.

I begin by formulating the EFT for ALP-nucleon coupling, which provides a minimal low-energy description of scalar interactions with baryonic matter. This framework also admits an interpretation as a conformal scalar-tensor theory, which we will establish in the course of the chapter. The results presented here form the theoretical foundation for the cosmological and astrophysical implications explored in the following chapters.

7.1 Effective Field Theory and Scalar Couplings

At energies below the MeV scale, where quarks are confined inside nucleons, the effective field theory describing ALP-matter interactions takes the form[1]

$$S_a = \int \mathrm{d}^4x\sqrt{-g}\left[-\frac{1}{2}\partial_\mu a\partial^\mu a - V(a) - \sum_{\psi=n,p} m_\psi\left(1+\frac{a}{\mu_\psi}\right)\bar{\psi}\psi + \cdots\right], \quad (7.1)$$

where the Yukawa interaction is summed over neutrons ($\psi = n$) and protons ($\psi = p$) and μ_ψ are mass scales governing the strength of Yukawa interactions between the ALP and nucleons. Here, μ_ψ serves as the cutoff scale for the EFT, beyond which the effective description is no longer valid. The ellipsis ($\cdots$) includes other ALP interactions and higher-order terms irrelevant to this analysis. This nucleon-level description bypasses the complexities of high-energy quark-gluon interactions while capturing the phenomenologically relevant physics. The bare ALP potential we use in this work is

$$V(a) = m_a^2 f_a^2\left[1 - \cos\frac{a}{f_a}\right]. \quad (7.2)$$

This potential mirrors the periodic form found in QCD axion models, where non-perturbative instanton effects generate a cosine potential with an amplitude Λ^4 that depends on QCD dynamics (see Eqn. (6.4)) [217]. For the QCD axion, the mass is determined once the PQ scale f_a is fixed, resulting in $m_a \propto 1/f_a$. In contrast, for general ALPs, we treat m_a and f_a as independent parameters and use this form as a phenomenologically motivated template that preserves the expected periodicity of axion-like fields [198, 222] as mentioned in Section 6.3.

To connect μ_ψ in the effective action above to the scalar coupling g_s^N, we adopt the definition $g_s^N \equiv m_\psi/\mu_\psi$ to enable direct comparison with the existing bounds [3]. Also, since the bounds of interest are coupled to the baryon number, we will set $g_s^n = g_s^p = g_s^N$, or equivalently $\mu_n = \mu_p = \mu$, making the bounds discussed in Subsection 6.3.1 directly apply to our model.

[1]The pseudoscalar CP-conserving interaction to nucleons in Eqn. (6.6) has been omitted since we focus exclusively on scalar interactions.

While the action in Eqn. (7.1) aligns with descriptions in particle physics literature [198, 222], in cosmological and astrophysical contexts this action is equivalent to a conformal scalar-tensor theory [252–254], corresponding to the Einstein frame action in Eqn. (C.4). For more about this framework, see Appendix C where the equivalence between both actions is explicitly shown in Section C.4 for $a/\mu \ll 1$, which is always valid in our case since μ marks the breakdown of the EFT. In scalar-tensor theories, the *Einstein frame metric* $g_{\mu\nu}$ satisfies Einstein's equations, while matter fields such as neutrons and protons follow geodesics determined by the *Jordan frame metric* $\tilde{g}_{\mu\nu} = A(a)^2 g_{\mu\nu}$, where $A(a)$ is the conformal coupling function[2] and is given by $A(a) = \exp(a/\mu) \approx 1 + a/\mu$ to leading order. We must then derive the equations of motion in this framework in order to study the model in the right context which is done in Section C.3 and yields

$$\Box a - \frac{\mathrm{d}V(a)}{\mathrm{d}a} + \sum_{i=n,p} T_i \frac{\mathrm{d}\ln A_i(a)}{\mathrm{d}a} = 0\,, \tag{7.3}$$

where $\Box$ is the d'Alembertian operator and the effective potential is identified to be

$$V_{\text{eff}}(a) = V(a) - \sum_{i=n,p} T_i \ln A_i(a)\,, \tag{7.4}$$

where T_i is the trace of the energy-momentum tensor for species i. Since we chose $\mu_n = \mu_p = \mu$, the conformal coupling functions for both species are identical, i.e., $A_n(a) = A_p(a) = A(a) = 1 + a/\mu$. This allows us to factor out the logarithmic derivative

$$\sum_{i=n,p} T_i \frac{\mathrm{d}\ln A_i(a)}{\mathrm{d}a} = \left(\frac{\mathrm{d}\ln A(a)}{\mathrm{d}a}\right) \sum_{i=n,p} T_i = \frac{T}{\mu}\,, \tag{7.5}$$

where $T = T_n + T_p$ is the total trace of the energy-momentum tensor. The equation of motion then becomes

$$\Box a - \frac{\mathrm{d}V_{\text{eff}}(a)}{\mathrm{d}a} = 0\,, \tag{7.6}$$

[2]Note that if $\mu_p \neq \mu_n$ then $A_p(a) \neq A_n(a)$ and similary for the Jordan metric $\tilde{g}^{(p)}_{\mu\nu} \neq \tilde{g}^{(n)}_{\mu\nu}$.

where the effective potential is identified to be

$$V_{\text{eff}}(a) = V(a) - \frac{T}{\mu}a\,. \tag{7.7}$$

These simplified expressions for the equation of motion and effective potential form the basis for analyzing how the ALP responds to different environments as we explore in the next section.

7.2 Field Dynamics and Critical Density

For non-relativistic sources and cosmological contexts, where pressure contributions are negligible, the trace of the energy-momentum tensor simplifies to $T_i \approx -\rho_i$. In this limit, the total trace becomes $T \approx -\rho$, and the effective potential simplifies to

$$V_{\text{eff}}(a) = m_a^2 f_a^2 \left[1 - \cos\left(\frac{a}{f_a}\right)\right] + \frac{\rho}{\mu}a\,, \tag{7.8}$$

and the the equation of motion in Eqn. (7.6) reduces to

$$\Box a - m_a^2 f_a \sin\left(\frac{a}{f_a}\right) - \frac{\rho}{\mu} = 0\,, \tag{7.9}$$

where $A'(a) = 1/\mu$ have been substituted. Although the fully relativistic form of the trace is $T = -\rho + 3P$, it is only relevant in extremely dense environments—such as near nuclear densities or in the cores of relativistic stars when $P \sim \rho$—both of which are described by realistic nuclear EoS. These EoSs are typically implemented numerically or fitted to complex analytic forms with over a dozen parameters [255, 257, 259], making $P(\rho)$ so intricate that T cannot be expressed in any transparent or readable form. As a result, qualitative insight into the scalar field dynamics is lost without fully numerical treatment. To retain analytic control and clarity, we adopt the approximation $T = -\rho$ throughout this section. The full relativistic expression will be reinstated when we turn to the astrophysical regime in a later chapter.

The CP-violating scalar coupling to nucleons introduces a matter-dependent linear term in the potential, causing it to tilt in proportion to the ambient density

ρ. As the density increases, the potential becomes increasingly asymmetric, and its minimum shifts accordingly. This tilting mechanism is the key qualitative feature of the model and gives rise to the novel scalar field phenomenology that follows. By minimizing the effective potential in Eqn. (7.8), we find that discrete vacua associated with the standard ALP potential persist as long as the density remains below a critical threshold, $\rho_c \equiv \mu f_a m_a^2$, which we refer to as the *critical density*. The corresponding minima are given by

$$a_{min} = -f_a \arcsin\left(\frac{\rho}{\rho_c}\right) + 2\pi n f_a \,, \tag{7.10}$$

where n represents an integer indexing the discrete vacua. The critical density ρ_c serves as a threshold: as ρ approaches or exceeds this value, the potential undergoes qualitative changes. Specifically, when $\rho > \rho_c$, the potential loses its discrete minima entirely, transitioning to an effectively linear profile dominated by the CP-violating interaction. We refer to this phenomenon, where the minima disappear, as the *destabilization* of the potential. This tilting phenomenon is

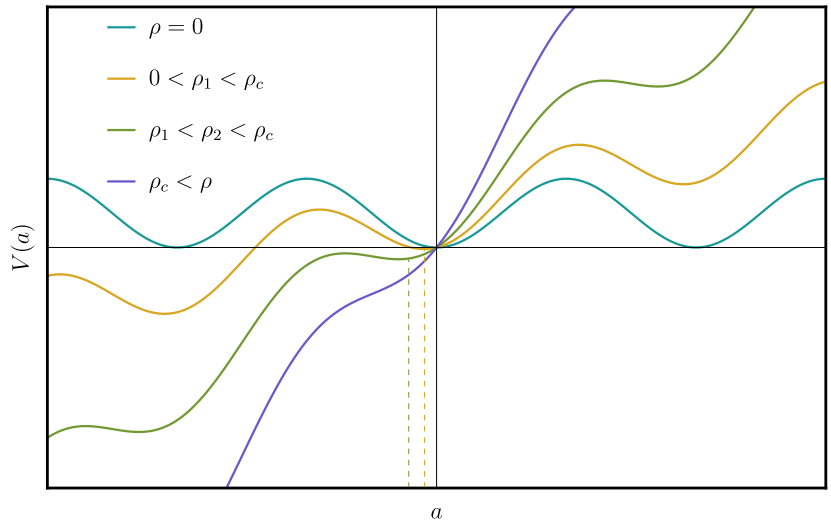

Figure 7.1: Effective potential for $\rho = 0$, $0 < \rho_1 < \rho_c$, $\rho_1 < \rho_2 < \rho_c$, and $\rho > \rho_c$, shown in teal, orange, green, and purple, respectively. The dashed lines in orange and green indicate the minima for ρ_1 and ρ_2, respectively, illustrating how tilting the potential shifts the VEV. For $\rho > \rho_c$, the potential loses its discrete minima and transitions to a linear profile dominated by the CP-violating interaction.

illustrated in Fig. 7.1. At $\rho = 0$, the potential exhibits symmetric minima. As ρ increases but remains below ρ_c, the potential tilts progressively, with the VEV shifting toward smaller values, as indicated by the dashed lines for ρ_1 and ρ_2. When $\rho > \rho_c$, the potential no longer has minima, instead transitioning into an effectively linear profile dominated by the CP-violating interaction. To further illustrate this behavior, Fig. 7.2 shows the effective potential at various densities, gradually increasing from $\rho \ll \rho_c$ to $\rho \gg \rho_c$. When $\rho \gg \rho_c$, the linear term dominates, rendering the potential effectively linear and destabilizing the ALP field.

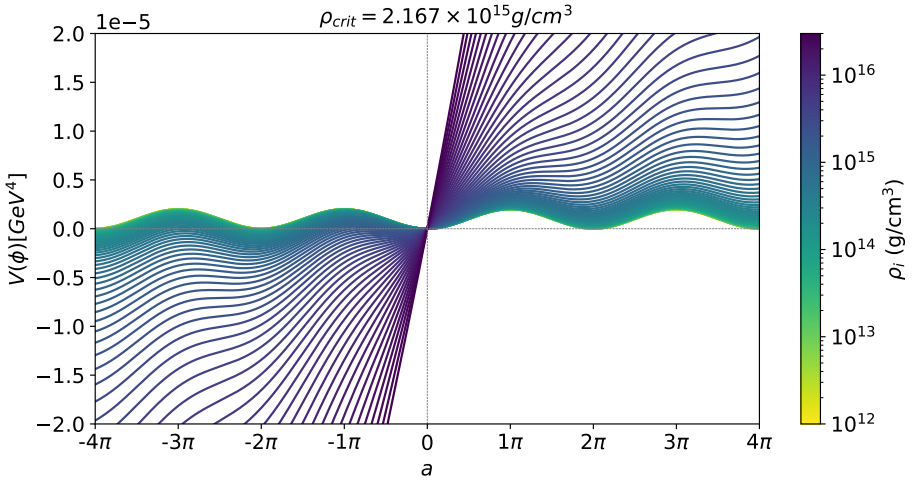

Figure 7.2: Effective potential for the ALP field under different density conditions. Model parameters are chosen such that $\rho_c = 2.167 \times 10^{15}$ g/cm^3. For $\rho \ll \rho_c$, the linear term is negligible, while for $\rho \gg \rho_c$, it dominates, rendering the potential effectively linear.

In the stable region ($\rho < \rho_c$), where the potential has discrete minima, the ALP has an effective mass determined by the curvature of the potential at the minimum, $a_{\min}$. This mass is given by

$$m_{\text{eff}}^2 = V''_{\text{eff}}(a_{\min}) = m_a^2 \sqrt{1 - \left(\frac{\rho}{\rho_c}\right)^2}. \tag{7.11}$$

This expression highlights the impact of the CP-violating coupling: as the density increases, the effective mass of the ALP decreases, extending the range

of the corresponding fifth force mediated by the field. In non-relativistic settings, this range is given by $\lambda_{\rm C} = 1/m_{\rm eff}$ instead of $\lambda_{\rm C} = 1/m_a$. For relativistic systems, the effective mass is modified due to the inclusion of pressure contributions, with the density ρ replaced by $-T = \rho - 3P$ in the potential, where P is the pressure.

While rare, scenarios in which $\rho - 3P < 0$ can arise in highly relativistic environments, such as the cores of dense neutron stars, where the pressure becomes comparable to or exceeds the energy density. In such cases, the trace $T = -\rho + 3P$ becomes positive, and it is the quantity $-T$ that appears in the effective potential. As a result, the ALP potential tilts in the opposite direction. This behavior has been observed in several realistic nuclear EoS used to model high-density matter [255–259]. While the sign of the tilt reverses, the qualitative dynamics—field destabilization above a critical density and the loss of discrete minima—remain unchanged. This inversion does not occur in cosmological settings, where matter is effectively pressureless and $T \approx -\rho$, ensuring that $-T > 0$ and the tilt direction remains fixed.

Although a detailed discussion of UV-complete couplings lies beyond the scope of this work, the analysis presented here extends naturally to the quark-level description. In such scenarios, the trace of the nucleonic energy-momentum tensor is replaced by its quark-level counterpart, modifying interaction terms like $a \sum_{i=n,p} T_i/\mu_i$ to $a \sum_q T_q/\mu_q$, where μ_q denotes the scalar coupling scale for each quark flavor. While these modifications can affect the precise value of the critical density and the detailed form of the effective potential, the overall phenomenological behavior remains qualitatively unchanged.

This chapter has established the theoretical foundation for understanding the behavior of CP-violating ALPs in matter-rich environments. Derived from a minimal low-energy effective field theory and reinterpreted in the language of scalar-tensor theories, the resulting dynamics reveal novel features—particularly the density-dependent tilting and destabilization of the scalar potential. These results form the conceptual basis for the cosmological and astrophysical applications explored in the chapters that follow.

8 Cosmology of CP-Violating ALPs

"They wander in darkness seeking light, failing to realize that the light is in the heart of the darkness"

– Manly P. Hall

Having established the theoretical framework for CP-violating ALPs in the previous chapter, we now turn to their cosmological implications. In particular, we explore how the density-dependent effective potential modifies the dynamics of the ALP field in an expanding universe. This chapter focuses on the consequences of this mechanism for the cosmic expansion history. We now turn to the cosmological effects of ALP-nucleon Yukawa couplings. In a flat FLRW Universe, the cosmological principle requires that the field depends only on time, $a \equiv a(t)$. The resulting equation of motion, derived from Eqn. (7.9), becomes

$$\ddot{a} + 3H\dot{a} + m_a^2 f_a \sin\left(\frac{a}{f_a}\right) + \frac{\rho_b(t)}{\mu} = 0\,, \tag{8.1}$$

where $\rho_b(t)$ is the baryon density, given by $\rho_b(t) = 3H^2 M_{Pl}^2 \Omega_{b,0}(1+z)^3$, and H is the Hubble parameter. As we move further back in time, $\rho_b(t)$ increases, altering the ALP potential. Depending on the model parameters, the potential minima form at late times when $\rho_b < \rho_c$, while the potential becomes destabilized at earlier times when $\rho_b > \rho_c$. The transition between these regimes occurs at a *critical redshift*, z_c, when $\rho_b = \rho_c$. Using the equation for $\rho_b(t)$ and substituting $\rho_c = \mu f_a m_a^2$, I found the critical redshift to be

$$z_c = \left(\frac{\mu f_a m_a^2}{3H_0^2 M_{Pl}^2 \Omega_{b,0}}\right)^{\frac{1}{3}} - 1. \tag{8.2}$$

Notably, the effective action in Eqn. (7.1) remains valid when quarks are confined, when $z \leq z_{\rm QCD} \sim 10^{12}$. Thus, the expression for z_c holds as long as $z_c \leq z_{\rm QCD}$. At redshifts beyond $z_{\rm QCD}$, a UV-complete theory describing the ALP-quark CP-violating couplings would be required. However, as noted earlier, the qualitative behavior remains unchanged: the ALP potential would have been destabilized at sufficiently high densities. In this work, the dynamical influence of ALP-quark couplings is incorporated by treating their effects as initial conditions for the field value and velocity at the onset of the EFT's validity; this allows for an estimation of the expected effects of ALP-quark interactions within the low-energy regime.

Since our EFT assumes confined quarks, it is only valid at redshifts $z < z_{\rm QCD}$. To ensure consistency with this regime, I modified the open-source code from reference [3] to generate Fig. 8.1. The figure illustrates the regions of parameter space where the critical redshift z_c, remains below $z_{\rm QCD}$ for different values of f_a. The shaded regions represent experimental bounds from previous works, while the dashed lines are our original work and indicate where the ALP potential transitions from being destabilized to having well-defined minima, occurring entirely within the quark-confined regime of the EFT. With this setup, we can now explore the effects of the ALP field on the evolution of the Universe, starting from the early Universe and tracing its impact through to the present day.

8.1 Early Universe: Destabilized Cosmology

As discussed, the ALP potential becomes destabilized when $\rho_b > \rho_c$. This occurs at sufficiently early times, sometime after inflation, when baryon densities exceed the critical density ρ_c, kickstarting the ALP field. This could be problematic because the coupling in Eqn. (7.1) predicts that the nucleon masses depend on the ALP field as

$$m_N = \bar{m}_N \left(1 + \frac{a}{\mu}\right), \tag{8.3}$$

implying that as the ALP field evolves away from zero, the masses of protons and neutrons vary accordingly where $\bar{m}_N$ is the nucleon mass when the field is at $a = 0$. Such variations can lead to significant cosmological implications.

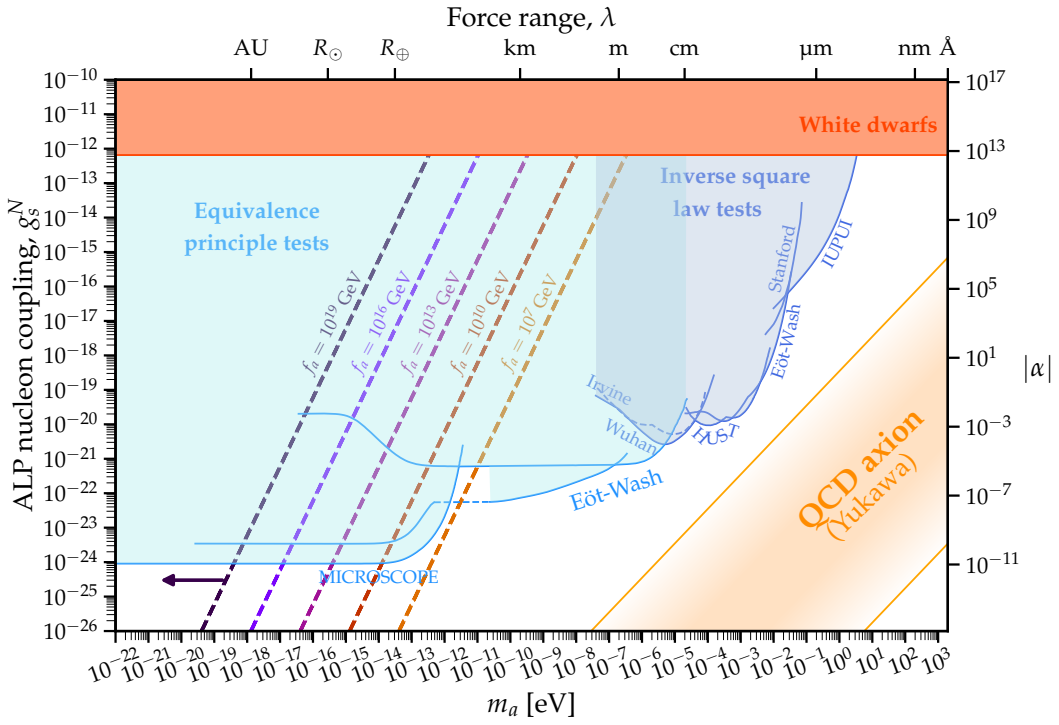

Figure 8.1: CP-violating ALP parameter space g_s^N vs m_a; we remind the reader that $g_s^N = m_N/\mu$. The ALP-nucleon Yukawa couplings mediate fifth-forces on length scales given in the top legend with strength relative to gravity $\alpha = F_{ALP}/F_{grav}$ given in the right legend. The dashed lines show regions (indicated by the arrow) where the ALP is destabilized before the QCD phase transition i.e., $z_c < z_{QCD}$ in Eqn. (8.2) for different values of f_a indicated in the figure. The blue region shows constraints from inverse-square law tests of gravity [234, 237, 238, 242, 243], the light blue region shows bounds from tests of WEP [230, 232], and the dark orange region shows the astrophysical limits from white dwarf cooling [260]. The QCD axion region highlights the expected parameter space for the QCD axion. The figure was created by modifying the open-source code from reference [3].

In particular, a change in the proton mass between BBN and the time of the CMB formation modifies the baryon number density inferred from the CMB. This affects the Thomson scattering rate, leading to changes in the damping of small-scale ($\ell \gtrsim 1000$) CMB anisotropies [261–263]. Observations currently constrain such variations to be below 5% [263]. Additionally, when the ALP field is destabilized, its EoS deviates from that of CDM with $w = 0$. If the ALP is assumed to constitute dark matter today, such deviations imply that the dark matter contribution would have been absent in the early Universe, thereby modifying the standard ΛCDM evolution. Another potential issue arises from the ALP's kinetic energy. As the field evolves, its kinetic energy could diverge since the potential is unbounded from below, dominating the energy budget of the Universe and leading to an early ALP-dominated kination phase.

To quantitatively examine the early dynamics of the ALP field, we consider the radiation-dominated era, where the ALP evolves with general initial conditions a_0 and $\dot{a}_0$ set sometime after inflation. For clarity, the initial conditions remain unspecified as they could, in principle, result from the dynamics of ALP-quark coupling prior to the QCD phase transition at $z > z_{\rm QCD} \sim 10^{12}$. In this regime, we can neglect the bare potential since the density-dependent linear term dominates and the ALP's equation of motion in Eqn. (8.1), reduces to

$$\ddot{a} + 3H\dot{a} = -\frac{\rho_{QCD}}{\mu}\left(\frac{t_{QCD}}{t}\right)^{\frac{3}{2}}, \tag{8.4}$$

where $\rho_{\rm QCD} \approx 1.8 \times 10^{-12}\,{\rm GeV}^4$ is the baryon density at the QCD phase transition, and $t_{\rm QCD} \approx 2 \times 10^{-5}\,{\rm s}$[1]. It is important to note that this baryonic density is significantly smaller than the total density of the Universe at the QCD transition, $\rho \sim 5 \times 10^{-3}\,{\rm GeV}^4$. In Eqn. (8.4), we neglected the bare potential term, a valid approximation at early times. However, this approximation breaks down as the driving term redshifts as $t^{-3/2}$. The timescale at which the bare

[1]All parameters are derived from Planck 2018 results [10].

potential becomes significant can be estimated as when the restoring term becomes comparable to the driving term, finding

$$t_{break} = \frac{1}{\sqrt{2} m_a}, \tag{8.5}$$

where we have assumed $a/f_a \ll 1$. Eqn. (8.4) with initial conditions $a(t_{QCD}) = a_0$ and $\dot{a}(t_{QCD}) = \dot{a}_0$ admits an analytical solution and is given by

$$\begin{aligned} a(t) = a_0 + 2\dot{a}_0 t_{QCD} \left(1 - \sqrt{\frac{t_{QCD}}{t}}\right) \\ + \frac{2\rho_{QCD} t_{QCD}^{3/2}}{\mu} \left(2\sqrt{\frac{t_{QCD}}{t}} - \frac{t_{QCD}}{t} - 1\right)\sqrt{t}\,. \end{aligned} \tag{8.6}$$

At sufficiently late times, the contributions from a_0 and $\dot{a}_0$ become negligible, and the field evolves asymptotically as $a(t) \propto -\sqrt{t}$. This solution remains valid until the bare potential becomes significant, at which point the field settles into its nearest minimum. Explicitly, the solution asymptotes to

$$a(t) = -\frac{2\rho_{QCD} t_{QCD}^{3/2}}{\mu}\sqrt{t} \tag{8.7}$$

To constrain the ALP parameter space, we use the observational limit that the nucleon mass can vary by no more than 5%. From Eqn. (8.3), the fractional change in the nucleon mass is given by

$$\frac{\Delta m_N}{\bar{m}_N} \equiv \frac{m_N - \bar{m}_N}{\bar{m}_N} = \frac{\Delta a}{\mu} \tag{8.8}$$

We define t_N as the time when this fractional change reaches 5%, and substituting this condition into Eqns. (8.8) and (8.7), to find

$$t_N = \frac{\mu^4}{1600 \rho_{QCD}^2 t_{QCD}^3}. \tag{8.9}$$

This result provides a constraint on μ, but several considerations must be addressed before drawing such a conclusion. First, the analysis relies on a series of approximations that may break down under certain conditions. Second, the

constraint applies only if the baryon density at the time of the CMB formation, $\rho_{\rm CMB} \approx 2.3 \times 10^{-36}\,{\rm GeV}^4$, exceeds the critical density ρ_c. If this condition is not met, the potential minima reappear earlier, reducing the field excursion and weakening the constraint. Nevertheless, a constraint can still be derived if this effect is properly accounted for.

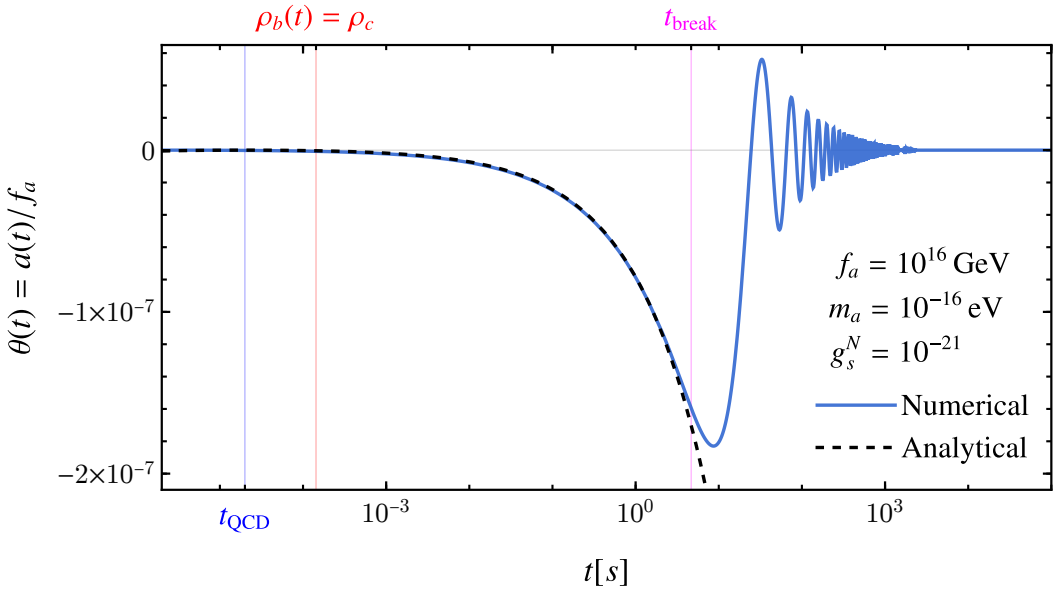

Figure 8.2: Cosmological evolution of the ALP field. The solid blue line represents the numerical solution obtained by solving the Klein-Gordon equation in Eqn. (8.1) while the dashed black line shows the approximate analytical solution from Eqn. (8.6). The parameters used were $g_s^N = 10^{-21}$ ($\mu = 9.38 \times 10^{20}$ GeV), $f_a = 10^{16}$ GeV, and $m_a = 10^{-16}$ eV. The solid red vertical line marks the time at which the effective potential stabilizes, i.e., $\rho(t) = \rho_c$, the solid blue vertical line indicates the time of the QCD phase transition, and the solid magenta vertical line shows the estimated time $t_{\rm break}$ (Eqn. (8.5)) when the analytic solution in Eqn. (8.6) is estimated to break down.

I have further examined the scenario discussed above by numerically solving Eqn. (8.1) in a radiation-dominated Universe to test the validity of our approximations. An example of the solution is shown in Fig. 8.2, where the numerical result quickly converges to the $a \propto -\sqrt{t}$ scaling derived analytically. Similar behavior was observed for other parameter choices, reinforcing the robustness of the analytic constraint $\mu < 7 \times 10^{18}$ GeV for parameter values of m_a and

f_a where $\rho_b < \rho_c$. This constraint is further supported by tests of the WEP presented in Fig. 8.1.

Regarding the possibility of the destabilized ALP leading to an over-closure of the Universe at late times, the asymptotic solution in Eqn. (8.7) rules out this scenario. The solution $a \sim -\sqrt{t}$ demonstrates that the kinetic energy, $\dot{a}^2/2$, decreases over time, while the potential energy remains bounded due to its cosine form. This behavior occurs because the density term in the ALP's equation of motion redshifts as the Universe expands. Notably, this suggests the potential for a kination phase in the early Universe; however, a detailed investigation of this scenario would require understanding the ALP-quark coupling, which lies beyond the scope of this work.

8.2 Late Universe: Stabilized Cosmology

Once the ALP field stabilizes with well-defined minima, its dynamics become dominated by oscillations around these minima. The minima of the effective potential appear at $z = z_c$, after which the field transitions to this stabilized phase. As shown in Fig. 8.2, the field rolls toward the nearest time-dependent minimum, driven by the density-dependent term in Eqn. (8.1), and begins oscillating. The time-dependent position of the minima is given by

$$a_{\min}(t) = -f_a \arcsin\left(\frac{\rho_b(t)}{\rho_c}\right) + 2\pi n f_a \,. \tag{8.10}$$

For late times, when $\rho_b(t) \ll \rho_c$, the KG equation can be rewritten by splitting the field into a slowly varying minimum position $a_{\min}(t)$ and a perturbation $\delta a(t)$, as $a(t) = a_{\min}(t) + \delta a(t)$. Substituting this form into the equation of motion and neglecting the time derivatives of $a_{\min}(t)$, one obtains

$$\ddot{\delta a} + 3H\dot{\delta a} + m_{\text{eff}}^2(t)\delta a = 0. \tag{8.11}$$

The approximations $\dot{a}_{\min} \approx 0$ and $\ddot{a}_{\min} \approx 0$ are justified by the slow evolution of the minimum due to the gradual decrease in the baryon density, $\rho(t)$. Specifically, $\rho_b(t)$ evolves on a Hubble timescale, scaling as $\rho_b(t) \propto a^{-3}$. The resulting time derivatives of $a_{\min}(t)$ are suppressed by the Hubble rate, which is much

smaller than the ALP oscillation frequency m_a. This hierarchy of timescales ensures that $a_{\rm min}(t)$ evolves adiabatically and can be treated as effectively static over the timescales of $\delta a(t)$ oscillations. Under these conditions, the perturbation $\delta a(t)$ executes damped harmonic oscillations about the minimum, with a period determined by $m_{\rm eff}^{-1}(t)$. At late times, when $\rho_b(t) \ll \rho_c$, the effective mass approximates to $m_{\rm eff} \sim m_a$ as seen from Eqn. (7.11). The component $\delta a(t)$ thus behaves like CDM with an EoS parameter $w = 0$, consistent with standard ALP dark matter scenarios [43, 44]. On the other hand, the component $a_{\rm min}(t)$, induced by the CP-violating couplings, behaves as dynamical dark energy in the form of a time-dependent cosmological constant. To find the EoS, we start from its definition

$$w_{\rm DE} = \frac{P_a}{\rho_a} = \frac{\dot{a}_{\rm min}^2 - 2V_{eff}(a_{\rm min})}{\dot{a}_{\rm min}^2 + 2V_{eff}(a_{\rm min})}, \tag{8.12}$$

where ρ_a and P_a are the energy density and pressure of the ALP field. At late times, when $\rho_b(t) \ll \rho_c$, the ALP stabilizes around its minima

$$a_{\rm min}(t) = -f_a \frac{\rho(t)}{\rho_c}\,, \tag{8.13}$$

where we expanded the full expression for $a_{\rm min}(t)$ in Eqn. (8.10) to leading order and neglected the $2\pi n f_a$ term, focusing on a single minimum. Taking the time derivative, we find

$$\dot{a}_{\rm min}(t) = -f_a \frac{\dot{\rho}(t)}{\rho_c}. \tag{8.14}$$

For the potential term, we expand the effective potential $V_{\rm eff}(a)$ in Eqn. (7.8) to leading order in a/f_a and find

$$V_{\rm eff}(a) \approx \frac{1}{2} m_a^2 a_{\rm min}^2\,. \tag{8.15}$$

Substituting $a_{\rm min}(t)$ into this expression gives

$$V(a_{\rm min}) = \frac{1}{2} m_a^2 f_a^2 \frac{\rho_b(t)^2}{\rho_c^2}\,. \tag{8.16}$$

Substituting Ens. (8.13), (8.14), and (8.16) into the EoS definition, Eqn. (8.12), yields

$$w_{\rm DE} = \frac{f_a^2 \frac{\dot{\rho_b}^2}{\rho_c^2} - m_a^2 f_a^2 \frac{\rho_b}{\rho_c}}{f_a^2 \frac{\dot{\rho_b}^2}{\rho_c^2} + m_a^2 f_a^2 \frac{\rho_b}{\rho_c}}\,. \tag{8.17}$$

To find $\dot{\rho}_b$, we use the continuity equation

$$\dot{\rho}_b + 3H_0(\rho_b + P_b) = 0 \tag{8.18}$$

where here, we set $H(t) = H_0$ to find the EoS at the present time. Solving for $\dot{\rho}_b$, we find

$$\dot{\rho}_b = -3H_0\rho_b \tag{8.19}$$

where $P_b = 0$ for baryons. Substituting this into Eqn. (8.17), we obtain:

$$w_{\rm DE} = \frac{9H_0^2 - m_a^2}{9H_0^2 + m_a^2}. \tag{8.20}$$

For typical ALP masses, $H_0/m_a \ll 1$, where $H_0 = 10^{-33}$ eV, we expand the EoS to a leading-order and find

$$w_{\rm DE} = -1 + 18\frac{H_0^2}{m_a^2}. \tag{8.21}$$

This result shows that for ALP masses in the range $m_a \sim 10^{-31}$-$10^{-32}\,$eV, detectable deviations of the dark energy EoS from the ΛCDM value $w = -1$ can occur. These deviations are a direct consequence of the CP-violating coupling, which shifts the field's VEV to a time-dependent minimum $a_{\rm min}(t)$. The field dynamically tracks this evolving minimum. For larger ALP masses, $w_{\rm DE}$ approaches -1, recovering the behavior of a cosmological constant.

It is important to emphasize the origin of the DE component in this framework. In standard quintessence models of DE, a scalar field slowly rolls down a shallow potential, and its potential energy dominates over kinetic energy, driving an EoS near $w \gtrapprox -1$. In contrast, in the CP-violating ALP scenario considered here, DE arises not from slow rolling per se, but from the scalar field tracking a time-dependent minimum induced by its coupling to baryonic matter. Specifically, the CP-violating interaction introduces an additional term $\rho_b(t)a/\mu$ in the

effective potential, which evolves with the background baryon density $\rho_b(t)$. As the Universe expands and baryons dilute, the position of the minimum shifts in time, following Eqn. (8.10). The ALP field dynamically follows this moving minimum with a slow response set by the Hubble friction. Because the field remains close to the minimum and its kinetic energy stays subdominant, its EoS remains close to $w \approx -1$ as found in Eqn (8.21), effectively acting as DE. This behavior mimics a slowly rolling quintessence field, but the source of acceleration is distinct: it originates from the ALP's coupling to a time-evolving background rather than from motion in a fixed scalar potential.

For ALPs with masses comparable to the Hubble scale, $m_a \sim H_0 \sim 10^{-33}\,\mathrm{eV}$, the oscillation period becomes comparable to the age of the Universe. In this regime, the field slowly rolls toward the nearest minimum, exhibiting behavior distinct from the CDM-like oscillations observed at larger masses. A detailed discussion of this scenario is presented in our original publication [54].

8.3 Summary

In this chapter, I analyzed the cosmological consequences of CP-violating ALPs, focusing on their effects on nucleon masses and the evolution of dark matter and dark energy. The tilting mechanism induced by their CP-violating coupling led to distinct stabilized and destabilized regimes, with a critical redshift z_c marking their transition. Observational constraints required $\mu > 7 \times 10^{18}, \mathrm{GeV}$ to ensure deviations in nucleon masses remain below 5%, ensuring consistency with ΛCDM. In the stabilized regime, the oscillatory behavior of the ALP field mimicked cold dark matter, while its tracking of a time-dependent minimum contributed to dark energy dynamics.

These results highlight the potential of CP-violating ALPs to unify dark matter and dark energy within a single theoretical framework. Observationally, this unified proposal would motivate specific signatures arising from the shared scalar field dynamics. In particular, the coupling of ALPs to baryonic matter leads to time-dependent variations in nucleon masses, potentially affecting baryon clustering and the evolution of cosmic structure [261–263]. This could yield distinctive, correlated observational features between LSS—sensitive to baryonic clustering—and precision measurements of the dark energy equation

of state from supernovae or BAO. The identification of such correlations would constitute a robust test of the unified scenario, offering a means to distinguish it from models where dark matter and dark energy are treated independently.

On the theoretical side, while ALPs have well-established UV completions in string theory and other frameworks [198, 222], the origin of CP-violating ALP couplings remains under development. Recent works have proposed mechanisms where such couplings can arise from complex phases in heavy fermion sectors or higher-dimensional operators [209]. Additionally, CP-violating ALPs have been considered in connection with baryogenesis and leptogenesis, offering avenues for linking dark sector dynamics with the observed matter–antimatter asymmetry [225, 264]. These theoretical extensions motivate further exploration into how CP-violating ALPs may be embedded within UV-complete theories and contribute to broader questions in early universe cosmology.

9 Astrophysical Consequences of CP-Violating ALPs

"Out beyond ideas of wrongdoing and rightdoing, there is a field. I will meet you there."

– Rumi

To explore the astrophysical consequences of the ALP coupling discussed in the previous chapter, we focus on stars as the astrophysical objects of interest. As noted in the previous chapter, our EFT is equivalent to a scalar-tensor modified theory of gravity. In this framework, the ALP couples to matter fields through a Yukawa interaction, resulting in a density-dependent shift in the field's VEV. This shift implies that the ALP field value inside stars may deviate from its asymptotic value in the surrounding low-density galactic environment. The asymptotic VEV is determined by minimizing the effective potential in the ambient background, while the field value at the star's center depends on the local density and whether it is energetically favorable for the field to minimize the effective potential under these conditions [265, 266].

The density dependence of the effective potential introduces a spatial variation in the ALP field, with distinct behavior in the high-density interior of the star and the low-density exterior. The field's profile must transition smoothly between the value dictated by the star's central density and the asymptotic value set by the ambient environment. This behavior is illustrated in Fig. 9.1, taken from our article [54].

Previous studies have investigated potential signatures of ALP fields, often treating stars as static, non-dynamical sources [267–273]. These works primarily focus on the induced ALP field profile and its external effects, such as fifth-force interactions, while largely neglecting the back-reaction of the ALP field on

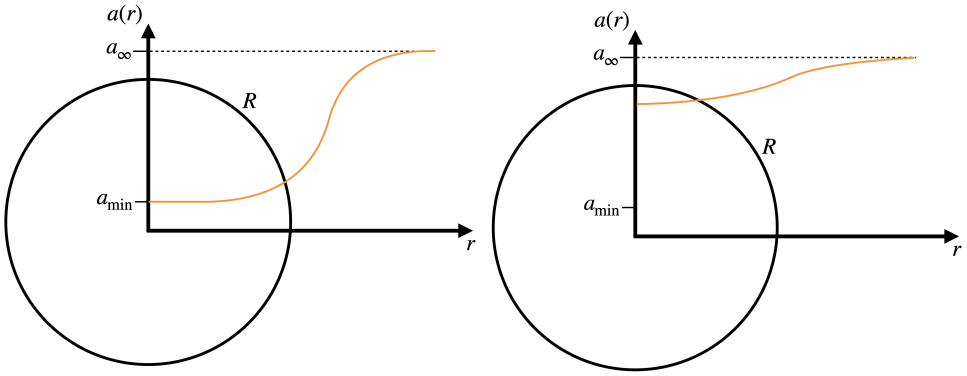

Figure 9.1: Behavior of the ALP inside astrophysical objects of radius R when the effective potential is stabilized. This figure was created by my advisor and is reproduced here from [54]. The asymptotic field value is a_∞, but the density-dependent effective potential causes the field to deviate from this inside astrophysical bodies. *Left:* Case where the field minimizes V_{eff}. There is a large gradient energy cost to doing this. *Right:* If it is not energetically favorable for the field to minimize V_{eff} due to the gradient energy cost, then the field does not make large excursions from a_∞. The field mediates a fifth force proportional to ∇a, so the scenario in the left figure is expected to alter stellar structure. If the density becomes sufficiently high such that the ALP effective potential is destabilized, the field could potentially run away to large values.

the star itself. This back-reaction, driven by the density-dependent effective potential and inhomogeneous boundary conditions, can significantly influence the local matter distribution, altering the object's internal equilibrium and observable properties, particularly the mass-radius relationship.

Building on these foundational studies, this chapter examines both the ALP-induced field profile and its back-reaction on stellar equilibrium to provide a more complete understanding of the astrophysical role of CP-violating ALPs.

9.1 Energetic considerations

The ALP field responds to the local density of matter through its effective potential, $V_{\rm eff}$. While the asymptotic field value, a_∞, is set by the ambient density in the surrounding environment, the higher density inside a star perturbs the field configuration. In extreme cases where the local star density exceeds the critical density, $\rho > \rho_c$, the effective potential in Eqn. (7.8) becomes destabilized,

rendering the potential energy unbounded from below. In principle, the field could move to arbitrarily large negative values to minimize the potential energy. However, the total energy—not just the potential energy—governs the field's configuration. Moving the field to $-\infty$ would incur a significant gradient energy cost, as the field must transition smoothly to the asymptotic value, a_∞, set by the ambient background density at large distances. This gradient energy prevents the field from running to arbitrarily negative values. Instead, the field settles at a finite displacement, Δa, balancing the gradient energy and the effective potential. The displacement Δa can be estimated by minimizing the total energy of the system, given by

$$E = \int \mathrm{d}^3\vec{x}\left(\frac{1}{2}\dot{a}^2 + \frac{1}{2}|\nabla a|^2 + V_{eff}(a)\right) \tag{9.1}$$

where V_{eff} is that of Eqn. (7.8). For a static, spherically symmetric star, the ALP field can be expressed as $a(r) = a_\infty + \Delta a(r)$, where a_∞ is the asymptotic value in the ambient environment, and $\Delta a(r)$ is the deviation due to the star's density. In the destabilized regime, where the density contribution dominates, $\rho a(r)/\mu \gg V(a)$, the total energy of the system can be approximated assuming uniform mass M and radius R for the star. We can further approximate $\mathrm{d}^3x \sim R^3$, $\rho \sim 3M/4\pi R^3$, and $|\nabla a| \sim \Delta a/R$, and the total energy becomes

$$E \approx \frac{1}{2}R(\Delta a)^2 + \frac{3M}{4\pi\mu}(a_\infty + \Delta a). \tag{9.2}$$

Minimizing this energy yields the field displacement

$$\Delta a = -\frac{3M}{4\mu R}. \tag{9.3}$$

This result shows that the largest field excursions occur in the most compact objects, where the ratio M/R is highest. Such conditions are characteristic of neutron stars, making them ideal targets for studying the astrophysical effects of CP-violating ALP couplings. Since Eqn. (9.3) predicts a non-zero

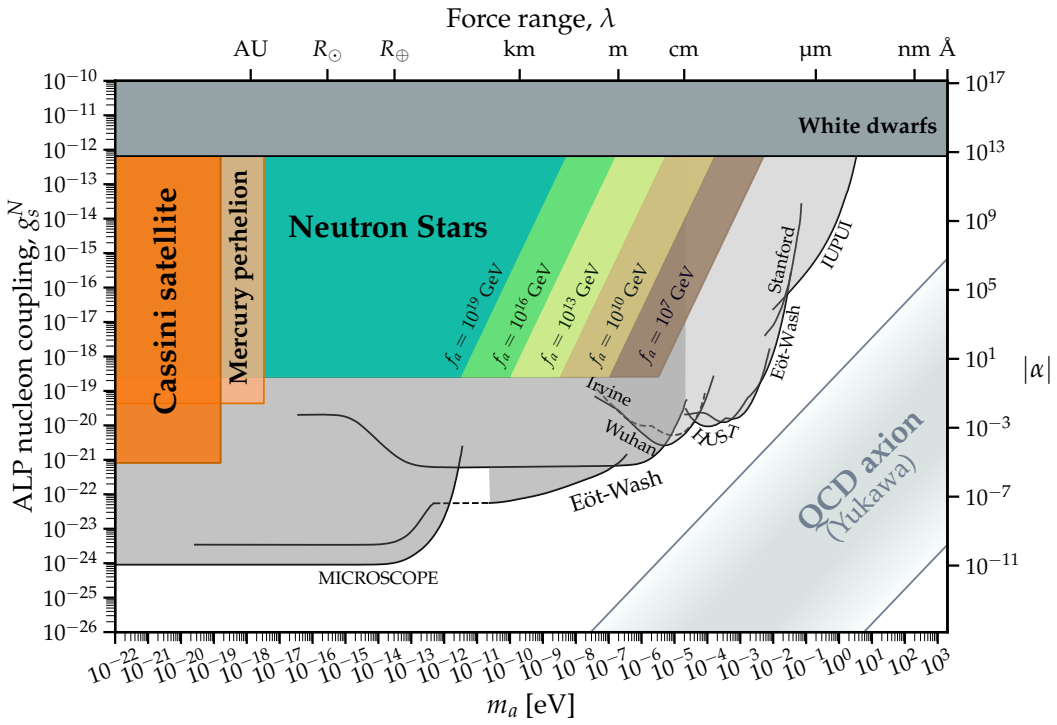

Figure 9.2: Region plot showing where the ALP potential becomes destabilized inside neutron stars, indicated by $\rho_{NS} > \rho_c$, with a typical neutron star density of $\rho_{NS} = 10^{14}$ g/cm^3. We show five regions, labeled by their respective axion decay constants, for which the change in the neutron mass detailed in Eqn. (9.5) is $|\Delta m_n/\bar{m}_n| \geq 1$. Moreover, in yellow, we show the bounds from the perihelion of Mercury [90], and in red, the bounds from the Cassini satellite [274]; both are derived in Section 9.6. In gray, we show existing constraints from tests of the inverse-square law [234, 237, 238, 242, 243], white dwarf cooling [260], and WEP violation searches [230, 232]. Lastly, the QCD axion region indicates where the QCD axion is expected to live [3]. The plot was generated by adapting the open-source code from O'Hare et al. [3].

field displacement, the mass of nucleons at the center of neutron stars deviates from the neutron mass measured in the laboratory by an amount

$$\frac{\Delta m_n}{\bar{m}_n} = \frac{\Delta a}{\mu} = -\frac{3M}{4R\mu^2}\,, \tag{9.4}$$

where we have substituted Δa from Eqn. (9.3) into Eqn. 8.8. For a typical neutron star with $M = 1\,\mathrm{M}_\odot$ and $R = 12$ km, this shift becomes

$$\left|\frac{\Delta m_n}{\bar{m}_n}\right| = \left(\frac{3.7 \times 10^{18}\ \mathrm{GeV}}{\mu}\right)^2. \tag{9.5}$$

This result places stringent constraints on CP-violating couplings. For ALP parameters f_a, m_a such that $\rho_{\mathrm{NS}} > \rho_c$, the condition $\mu < 3.7 \times 10^{18}$ GeV leads to $|\Delta m_n/\bar{m}_n| > 1$, implying a significant change in the neutron mass that exceeds its laboratory-measured value. Such a deviation is unphysical, as it would either result in a vanishing neutron mass or destabilize the neutron star entirely. To avoid this, the coupling scale μ must satisfy $\mu > 3.7 \times 10^{18}$ GeV, ensuring that $|\Delta m_n/\bar{m}_n| < 1$ and the neutron star remains stable.

Fig. 9.2 illustrates the excluded parameter space, calculated for a typical neutron star density of $\rho_{\mathrm{NS}} = 10^{14}$ g/cm^3. In the excluded region, where $\mu < 3.7 \times 10^{18}$ GeV, the gravitational fine-structure constant, $\alpha_G = G m_n^2$, approaches zero, indicating that the neutron star becomes unbound. The constraint $\mu < 3.7 \times 10^{18}$ GeV represents a novel result unique to this work, providing stringent bounds on CP-violating ALP interactions.

9.2 Modified TOV Equations

As shown in Eqn. (9.3), the effects of the coupled ALP on the structure of stellar objects are proportional to their compactness. This motivates the focus on neutron stars, which are among the most compact astrophysical objects. To quantify these effects, it is necessary to derive the mass-radius relationship by solving the modified Tolman-Oppenheimer-Volkoff (TOV) equations, incorporating the back-reaction of the ALP field.

In this section, I present a derivation of the modified TOV equations for a static, spherically symmetric, non-relativistic object, explicitly accounting for the contributions of the coupled ALP. While scalar-tensor theories and their associated TOV equations have been studied in the literature, the specific form of the modified TOV equations derived here has not appeared before. They are obtained by applying the scalar-tensor formalism to the EFT with CP-violating ALP developed in this work. For additional details on the theoretical framework of scalar-tensor , readers are referred to Appendix C. Those unfamiliar with the standard TOV equations or neutron star properties may consult Appendix B, which provides a brief overview of their physics in the context of GR and the numerical determination of the mass-radius relationship. The derivation begins by considering a static, spherically symmetric metric of the form

$$ds^2 = -e^{\nu(r)}dt^2 + e^{\lambda(r)}dr^2 + r^2 d\Omega^2\,, \tag{9.6}$$

where $\nu(r)$ and $\lambda(r)$ are functions of the radial coordinate r only, reflecting the assumptions of staticity and spherical symmetry. The quantity $\mathrm{d}\Omega^2$ denotes the metric on the unit 2-sphere, explicitly given by $\mathrm{d}\Omega^2 = \mathrm{d}\Theta^2 + \sin^2\Theta \mathrm{d}\phi^2$, where Θ is the polar angle and ϕ is the azimuthal angle. The metric and its inverse are given by

$$g_{\mu\nu} = \mathrm{diag}\big(-e^{\nu(r)}, e^{\lambda(r)}, r^2, r^2\sin\Theta\big) \tag{9.7}$$

$$g^{\mu\nu} = \mathrm{diag}\left(-e^{-\nu(r)}, e^{-\lambda(r)}, \frac{1}{r^2}, \frac{1}{r^2\sin\Theta}\right) \tag{9.8}$$

Here, I use the capital theta, Θ, for the angular coordinate, reserving the lowercase theta, θ, for the dimensionless ALP field, following conventions in the literature. The starting point for the derivation is the Einstein frame action

$$S_E = \int \mathrm{d}^4x\sqrt{-g}\left[\frac{M_{\rm Pl}^2 R}{2} - \frac{1}{2}\nabla_\mu a \nabla^\mu a - V(a)\right] + S_m[\tilde{g}_{\mu\nu}; \Psi]\,, \tag{9.9}$$

where $V(a)$ is the bare ALP potential, given by Eqn. (7.2).

As discussed in Appendix C, matter follows the geodesics of the Jordan frame metric $\tilde{g}_{\mu\nu} = A(a)g_{\mu\nu}$. In this model, the coupling function is given by $A(a) = 1 + a/\mu$, where μ is the cut-off scale. In the regime $a/\mu \ll 1$, the

coupling function simplifies to $A(a) \approx 1$, effectively making the Einstein and Jordan frames equivalent for practical purposes. However, the derivative of the coupling function, $A'(a) = 1/\mu$, remains significant, introducing factors of μ. This approximation allows us to work in the Einstein frame for mathematical clarity, while ensuring the results remain physically interpretable in the Jordan frame.

Under the assumptions of staticity and spherical symmetry, the scalar field a depends only on the radial coordinate, $a \equiv a(r)$. To derive the equations governing the system, we solve the Einstein field equations in the presence of both matter and the scalar field

$$G_{\mu\nu} = R_{\mu\nu} - \frac{1}{2} R g_{\mu\nu} = 8\pi G\big(T_{\mu\nu} + T^{a}_{\mu\nu}\big)\,, \tag{9.10}$$

where $R_{\mu\nu}$ is the Ricci tensor, R is the Ricci scalar, $T_{\mu\nu}$ is the energy-momentum tensor (EM tensor) for matter, and $T^{a}_{\mu\nu}$ is the EM tensor for the ALP field.

First, we focus on the EM tensor for matter, which is given by

$$T_{\mu\nu} = (\rho + p) U_\mu U_\nu + p g_{\mu\nu}\,, \tag{9.11}$$

where $\rho(r)$ and $p(r)$ are the energy density and pressure, respectively. For static solutions, the four-velocity U_μ is normalized as $U_\mu U^\mu = -1$, yielding

$$U_\mu = \begin{pmatrix} e^{\nu(r)/2} & 0 & 0 & 0 \end{pmatrix}, \qquad U^\mu = \begin{pmatrix} e^{-\nu(r)/2} \\ 0 \\ 0 \\ 0 \end{pmatrix}. \tag{9.12}$$

Substituting these expressions, the energy-momentum tensor simplifies to

$$T^{\mu}_{\ \nu} = \begin{pmatrix} -\rho(r) & 0 & 0 & 0 \\ 0 & p(r) & 0 & 0 \\ 0 & 0 & p(r) & 0 \\ 0 & 0 & 0 & p(r) \end{pmatrix}, \tag{9.13}$$

with a trace

$$T = g_{\mu}^{\ \nu} T^{\mu}_{\ \nu} = -\rho(r) + 3p(r)\,. \tag{9.14}$$

Next, for the ALP $a(r)$, the EM tensor is given by

$$T^{a}_{\ \mu\nu} = \nabla_\mu a \nabla_\nu a - g_{\mu\nu}\left(V(a) + \frac{1}{2} g^{\alpha\beta}\nabla_\alpha a \nabla_\beta a\right), \tag{9.15}$$

with components

$$\begin{aligned} T^{a\ \mu}_{\ \ \nu} = \mathrm{diag}[&- V(a) - \frac{1}{2} e^{-\lambda(r)} a'(r)^2, -V(a) + \frac{1}{2} e^{-\lambda(r)} a'(r)^2, \\ &- V(a) - \frac{1}{2} e^{-\lambda(r)} a'(r)^2, -V(a) - \frac{1}{2} e^{-\lambda(r)} a'(r)^2] \end{aligned}.$$

The Einstein equations follow from the computation of the Ricci tensor and Ricci scalar. Using the metric $g_{\mu\nu}$ in Eqn. (9.6), the non-zero components of the Einstein tensor are found to be

$$G^{t}_{\ t} = -\frac{e^{-\lambda(r)}\left(r\lambda'(r) + e^{\lambda(r)} - 1\right)}{r^2}, \tag{9.16}$$

$$G^{r}_{\ r} = \frac{e^{-\lambda(r)}\left(r\nu'(r) - e^{\lambda(r)} + 1\right)}{r^2}, \tag{9.17}$$

$$G^{\theta}_{\ \theta} = G^{\phi}_{\ \phi} = \frac{e^{-\lambda(r)}(-\lambda'(r)(r\nu'(r)+2) + 2r\nu''(r) + r\nu'(r)^2 + 2\nu'(r))}{4r}. \tag{9.18}$$

To solve for the metric functions $\lambda(r)$ and $\nu(r)$, we focus on the tt and rr components of the Einstein equations in Eqn. (9.10). From the tt equation, we obtain

$$\frac{e^{-\lambda(r)}\big(r\lambda'(r)+e^{\lambda(r)}-1\big)}{r^2} = 4\pi G\big[2\rho(r)+e^{-\lambda(r)}a'(r)^2+2V(a(r))\big]\,, \tag{9.19}$$

while the rr equation yields

$$\frac{e^{-\lambda(r)}\big(r\nu'(r)-e^{\lambda(r)}+1\big)}{r^2} = 4\pi G\big[2p(r)+e^{-\lambda(r)}a'(r)^2-2V(a(r))\big]. \tag{9.20}$$

From these, the differential equations for $\nu(r)$ and $\lambda(r)$ are derived as

$$\frac{d\nu}{dr} = \frac{e^{\lambda}-1}{r} + \left[8\pi r G e^{\lambda}\big(p-m_a^2 f_a^2[1-\cos(\theta)]\big)+4\pi r G f_a^2\left(\frac{d\theta}{dr}\right)^2\right], \tag{9.21}$$

$$\frac{d\lambda}{dr} = \frac{1-e^{\lambda}}{r} + \left[8\pi r G e^{\lambda}\big(\rho+m_a^2 f_a^2[1-\cos(\theta)]\big)+4\pi r G f_a^2\left(\frac{d\theta}{dr}\right)^2\right], \tag{9.22}$$

where $V(a)$ has been substituted using Eqn. (7.2). Following conventions, we rescale the ALP field as $a(r)\to\theta(r)f_a$, where $\theta(r)$ is dimensionless.

The final two equations to derive are the KG equation, governing the evolution of the ALP field, and the hydrostatic equilibrium equation. The KG equation is derived in detail in Section C.3 and takes the form

$$\Box a = \frac{\mathrm{d}V_{eff}(a)}{\mathrm{d}a}, \tag{9.23}$$

where the effective potential is given by

$$V_{\text{eff}}(a) = V(a) - T\ln A(a)\,, \tag{9.24}$$

with T being the trace of the matter energy-momentum tensor, as defined in Eqn. (9.14). In contrast to cosmological settings where pressure is negligible, the pressure term $3P$ contributes significantly to the trace in neutron stars and must be retained. Many realistic equations of state [255–259], yield values where both ρ and P play an important role in determining T. As such, we use the full expression $T=-\rho+3P$ in the effective potential and the corresponding

KG equation. Substituting this and rescaling the ALP field as $a(r) \to \theta(r) f_a$, the effective potential becomes

$$V_{\text{eff}}(a) = m_a^2 f_a^2 \left[1 - \cos\frac{a}{f_a}\right] + (\rho - 3p)\frac{a}{\mu}\,. \tag{9.25}$$

After rescaling the ALP field as $a(r) \to \theta(r) f_a$, the effective potential simplifies to

$$V(\theta) = m_a^2 f_a^2 [1 - \cos\theta] + (\rho - 3p)\frac{\theta f_a}{\mu}\,, \tag{9.26}$$

where the leading-order Taylor expansion $\ln A(a) \approx a/\mu$ has been applied. The final form of the KG equation, expressed in terms of θ, is

$$\frac{d^2\theta}{dr^2} + \frac{d\theta}{dr}\left(\frac{2}{r} - \frac{1}{2}\frac{d\lambda}{dr} + \frac{1}{2}\frac{d\nu}{dr}\right) - m_a^2 e^{\lambda}\sin(\theta) = \frac{(\rho - 3p)e^{\lambda}}{f_a \mu}\,. \tag{9.27}$$

The hydrostatic equilibrium equation is derived through the conservation of the matter energy-momentum tensor. In general relativity, this conservation law is expressed as $\nabla_\mu T^{\mu\nu} = 0$. In our theory, where matter species follow geodesics of the Jordan frame metric, the conserved energy-momentum tensor satisfies

$$\tilde{\nabla}_\mu \tilde{T}^{\mu\nu} = 0\,, \tag{9.28}$$

in the Jordan frame. Transforming this conservation equation to the Einstein frame yields

$$\nabla_\mu T^{\mu\nu} = \frac{A'(a)}{A(a)} T \nabla^\nu a\,, \tag{9.29}$$

where a detailed derivation is provided in [275]. Since this equation is central to the analysis, I will provide a detailed, step-by-step derivation to illustrate how the modifications from the theory arise and alter the standard GR result. To derive the hydrostatic equilibrium equation, we focus on the radial component of the conservation equation, $\nu = r$. We begin by addressing the left-hand side of Eqn. (9.29), where the covariant derivative of $T^{\mu r}$, by definition, is

$$\nabla_\mu T^{\mu r} = \partial_\mu T^{\mu r} + \Gamma^\mu_{\mu\lambda} T^{\lambda r} + \Gamma^r_{\mu\lambda} T^{\mu\lambda}\,, \tag{9.30}$$

with the Christoffel symbols, $\Gamma^{\alpha}_{\beta\gamma}$, given by

$$\Gamma^{\alpha}_{\beta\gamma} = \frac{1}{2} g^{\alpha\sigma} (\partial_\beta g_{\gamma\sigma} + \partial_\gamma g_{\sigma\beta} - \partial_\sigma g_{\beta\gamma}) \,. \tag{9.31}$$

To guide the reader, the flow of the derivation is outlined as follows:

1. Each term on the right-hand side of Eqn. (9.30) is treated separately. These terms are then substituted back into Eqn. (9.30) to fully evaluate the left-hand side of Eqn. (9.29).

2. The right-hand side of Eqn. (9.29), which introduces coupling to the scalar field via the trace of the matter EM tensor in Eqn. (9.14) is treated explicitly.

3. Combining the left- and right-hand sides yields the final form of the modified hydrostatic equilibrium equation.

Before diving into the derivation, it is helpful to summarize the non-zero components of the energy-momentum tensor with upper indices, $T^{\mu\nu}$. These are given by

$$T^{\mu\nu} = \mathrm{diag}\left(\rho(r) e^{-\nu(r)} \,, p(r) e^{-\lambda(r)} \,, \frac{p(r)}{r^2} \,, \frac{p}{r^2 \sin\theta} \right) \tag{9.32}$$

The first term in Eqn. (9.30) is straightforward

$$\partial_\mu T^{\mu r} = \partial_t T^{tr} + \partial_r T^{rr} + \partial_\theta T^{\theta r} + \partial_\phi T^{\phi r} \tag{9.33}$$

Since the matter EM tensor is diagonal, all terms except for $\partial_r T^{rr}$ vanish, leading to

$$\begin{aligned} \partial_\mu T^{\mu r} = \partial_r T^{rr} &= \partial_r \big(p(r) e^{-\lambda(r)} \big) \\ &= e^{-\lambda(r)} \frac{\mathrm{d}p(r)}{\mathrm{d}r} - p(r) e^{-\lambda(r)} \lambda'(r) \,, \end{aligned} \tag{9.34}$$

The second term in Eqn. (9.30), $\Gamma^{\mu}_{\mu\lambda}T^{\lambda r}$, is more intricate. The contraction of index λ implies that contributions arise only from diagonal components of the EM tensor, when $\lambda = r$. Thus, the second term simplifies to

$$\begin{aligned}\Gamma^{\mu}_{\mu\lambda}T^{\lambda r} &= \Gamma^{\mu}_{\mu r}T^{rr} \\ &= \Gamma^{\mu}_{\mu r}p(r)e^{-\lambda(r)}\end{aligned} \tag{9.35}$$

Next, we expand the sum over the Christoffel symbols in $\Gamma^{\mu}_{\mu r}$, which is

$$\Gamma^{\mu}_{\mu r} = \Gamma^{t}_{tr} + \Gamma^{r}_{rr} + \Gamma^{\theta}_{\theta r} + \Gamma^{\phi}_{\phi r}. \tag{9.36}$$

Using the definition of the Christoffel symbols from Eqn. (9.31), we write a general expression

$$\Gamma^{\mu}_{\mu r} = \frac{1}{2}g^{\mu\sigma}(\partial_{\mu}g_{r\sigma} + \partial_{r}g_{\sigma\mu} - \partial_{\sigma}g_{\mu r})\,. \tag{9.37}$$

When $\mu = r$, the only non-zero contribution in the summation occurs when $\sigma = r$ since the metric is diagonal. Thus,

$$\Gamma^{r}_{rr} = \frac{1}{2}g^{rr}\partial_{r}g_{rr} = \frac{\lambda'(r)}{2}\,. \tag{9.38}$$

For the other components, when $\mu = t, \theta, \phi$, let us denote $\mu = i$, where $i = t, \theta, \phi$. For these cases, the general expression becomes

$$\Gamma^{i}_{ir} = \frac{1}{2}g^{i\sigma}(\partial_{i}g_{r\sigma} + \partial_{r}g_{\sigma i} - \partial_{\sigma}g_{ir})\,. \tag{9.39}$$

Here, the only surviving terms are $\partial_r g_{\sigma i}$, and these are non-zero only when $\sigma = i$. Evaluating for each index leads to

$$\Gamma^{t}_{tr} = \frac{1}{2}g^{tt}\partial_{r}g_{tt} = \frac{\nu'(r)}{2} \tag{9.40}$$

$$\Gamma^{\theta}_{\theta r} = \frac{1}{2}g^{\theta\theta}\partial_{r}g_{\theta\theta} = \frac{1}{r} \tag{9.41}$$

$$\Gamma^{\phi}_{\phi r} = \frac{1}{2}g^{\phi\phi}\partial_{r}g_{\phi\phi} = \frac{1}{r} \tag{9.42}$$

Substituting Eqns. (9.38), (9.40), (9.41), and (9.42) into Eqn. (9.36), we find

$$\Gamma^{\mu}_{\mu r} = \frac{\nu'(r) + \lambda'(r)}{2} + \frac{2}{r} \tag{9.43}$$

Substituting this result back into Eqn. (9.35), we obtain

$$\Gamma^{\mu}_{\mu\lambda} T^{\lambda r} = \left(\frac{\nu'(r) + \lambda'(r)}{2} + \frac{2}{r} \right) p(r) e^{-\lambda(r)} \tag{9.44}$$

The last term in Eqn. (9.30), $\Gamma^{r}_{\mu\lambda} T^{\mu\lambda}$, involves a simultaneous summation over the indices μ and λ. Since $T^{\mu\nu}$ is diagonal, only terms where $\mu = \lambda$ contribute, simplifying the expression to

$$\Gamma^{r}_{\mu\lambda} T^{\mu\lambda} = \Gamma^{r}_{tt} T^{tt} + \Gamma^{r}_{rr} T^{rr} + \Gamma^{r}_{\theta\theta} T^{\theta\theta} + \Gamma^{r}_{\phi\phi} T^{\phi\phi} \,. \tag{9.45}$$

We already have Γ^{r}_{rr} from Eqn .(9.38). To find the remaining Christoffel symbols, we use the general formula from Eqn. (9.31). For Γ^{r}_{ii}, where $i = t, \theta, \phi$, the expression becomes

$$\Gamma^{r}_{ii} = \frac{1}{2} g^{r\alpha} (\partial_i g_{i\alpha} + \partial_i g_{\alpha i} - \partial_\alpha g_{ii})$$

Since the metric is diagonal, the only surviving component of $g^{r\alpha}$ is when $\alpha = r$. Thus, the above equation reduces to

$$\Gamma^{r}_{ii} = \frac{1}{2} g^{rr} (\partial_i g_{ir} + \partial_i g_{ri} - \partial_r g_{ii}) \,, \tag{9.46}$$

Here, only the last term, $\partial_r g_{ii}$, is non-zero because the first two terms vanish for a diagonal metric. Evaluating each component yields

$$\Gamma^{r}_{tt} = -\frac{1}{2} g^{rr} \partial_r g_{tt} = \frac{1}{2} e^{-\lambda(r)+\nu(r)} \nu'(r) \,, \tag{9.47}$$

$$\Gamma^{r}_{\theta\theta} = -\frac{1}{2} g^{rr} \partial_r g_{\theta\theta} = -r e^{\lambda(r)} \,, \tag{9.48}$$

$$\Gamma^{r}_{\phi\phi} = -\frac{1}{2} g^{rr} \partial_r g_{\phi\phi} = -r e^{\lambda(r) \sin\theta} \,. \tag{9.49}$$

Substituting Eqns. (9.38), (9.47), (9.48), (9.49), and the components of $T^{\mu\nu}$ from Eqn. (9.32) into Eqn. (9.45), we obtain

$$\Gamma^r_{\mu\lambda} T^{\mu\lambda} = e^{-\lambda(r)} \left[\frac{1}{2} \nu'(r) \rho(r) + \frac{p(r)\lambda'(r)}{2} - \frac{2p(r)}{r} \right] \tag{9.50}$$

This completes the evaluation of the final term in Eqn. (9.30). Finally, we combine Eqns. (9.34), (9.44), and (9.50) to write the left-hand side of the conservation equation as

$$\nabla_\mu T^{\mu r} = e^{-\lambda(r)} \left[\frac{\mathrm{d}p(r)}{\mathrm{d}r} + \frac{1}{2}(p(r) + \rho(r))\nu'(r) \right] \tag{9.51}$$

Thus, the conservation of the EM tensor becomes

$$e^{-\lambda(r)} \left[\frac{\mathrm{d}p(r)}{\mathrm{d}r} + \frac{1}{2}(p(r) + \rho(r))\nu'(r) \right] = \frac{A'(a)}{A(a)} T \nabla^r a \,. \tag{9.52}$$

The right-hand is easier to treat. First, we note that the covariant derivative of the scalar field is equivalent to a partial derivative

$$\nabla^r a = g^{r\alpha} \nabla_\alpha a = e^{-\lambda(r)} \partial_r a \,, \tag{9.53}$$

where we used the metric component $g^{rr} = e^{-\lambda(r)}$. Additionally, from earlier discussions, we know that $A'(a) = 1/\mu$, and we set $A(a) = 1$ which is always valid in the regime of our EFT. Substituting these into Eqn. (9.52), we obtain

$$e^{-\lambda(r)} \left[\frac{\mathrm{d}p(r)}{\mathrm{d}r} + \frac{1}{2}(p(r) + \rho(r))\nu'(r) \right] = e^{-\lambda(r)} \frac{T}{\mu} \partial_r a(r) \,, \tag{9.54}$$

where, after rescaling the field $a(r) \to \theta(r) f_a$ as before, and rearranging the above equation, we find

$$\frac{\mathrm{d}p}{\mathrm{d}r} = -\frac{1}{2}(\rho + p)\frac{\mathrm{d}\nu}{\mathrm{d}r} + \frac{f_a}{\mu}(3p - \rho)\frac{\mathrm{d}\theta}{\mathrm{d}r} \tag{9.55}$$

This equation is the modified hydrostatic equilibrium equation in the presence of an ALP coupled to matter. The full system of the modified TOV equations includes Eqn. (9.21), which evolves $\nu(r)$; Eqn. (9.22), which evolves $\lambda(r)$;

Eqn. (9.27), the Klein-Gordon equation that evolves the scalar field $\theta(r)$; and Eqn. (9.55), which governs hydrostatic equilibrium. Together, these form a system of four coupled differential equations for $\nu(r)$, $\lambda(r)$, $\theta(r)$, and $p(r)$. However, this system is underdetermined, as it involves four equations but five variables. The additional variable is the matter energy density, $\rho(r)$. To close the system, we must assume an EoS that relates the energy density to the pressure

$$\rho \equiv \rho(p)\,. \tag{9.56}$$

The choice of EoS is critical, as it affects neutron star structure and properties. Numerous realistic EoSs have been developed based on nuclear physics models, with one widely used example being APR [255], which we adopt in this work. These EoSs are extensively studied in neutron star modeling [276–284], but a detailed discussion is beyond the scope of this dissertation.

Lastly, it is important to verify that the modified hydrostatic equilibrium equation in Eqn. (9.55) reduces to the standard GR hydrostatic equilibrium equation in the absence of a scalar field. When the scalar field is removed, the $\mathrm{d}\theta/\mathrm{d}r$ term vanish, leaving

$$\frac{\mathrm{d}p}{\mathrm{d}r} = -\frac{1}{2}(\rho + p)\frac{\mathrm{d}\nu}{\mathrm{d}r}\,. \tag{9.57}$$

In GR, $\nu'(r)$ is determined from Eqn. (9.21) in the limit where the ALP parameters are set to zero. Additionally, $e^{-\lambda(r)}$ has the analytical solution

$$e^{-\lambda(r)} = 1 - \frac{2Gm(r)}{r} \tag{9.58}$$

which satisfies Eqn. (9.22) when the ALP contributions vanish. Here, $m(r)$ is the enclosed mass within radius r, defined as

$$m(r) = \int_0^r 4\pi r^2 \rho \mathrm{d}r \tag{9.59}$$

This verifies that the modified TOV equations recover the standard GR solutions in the absence of a scalar field, ensuring consistency with GR as a limiting case.

9.3 Numerical Solutions

Deriving the system of equations is only the first step; solving them presents its own challenges. To set the stage for the solution process, we begin by reviewing the system of equations and clarifying our goal. Within the star, I derived the stellar structure equations and found

$$\frac{\mathrm{d}p}{\mathrm{d}r} = -\frac{1}{2}(\rho + p)\frac{\mathrm{d}\nu}{\mathrm{d}r} + \frac{f_a}{\mu}\rho\frac{\mathrm{d}\theta}{\mathrm{d}r} \tag{9.60}$$

$$\frac{d^2\theta}{dr^2} + \frac{d\theta}{dr}\left(\frac{2}{r} - \frac{1}{2}\frac{d\lambda}{dr} + \frac{1}{2}\frac{d\nu}{dr}\right) - m_a^2 e^{\lambda}\sin(\theta) = \frac{\rho e^{\lambda}}{f_a \mu}\,. \tag{9.61}$$

$$\frac{d\nu}{dr} = \frac{e^{\lambda} - 1}{r} + \left[8\pi r G e^{\lambda}\big(p - m_a^2 f_a^2[1 - \cos(\theta)]\big) + 4\pi r G f_a^2\left(\frac{d\theta}{dr}\right)^2\right], \tag{9.62}$$

$$\frac{d\lambda}{dr} = \frac{1 - e^{\lambda}}{r} + \left[8\pi r G e^{\lambda}\big(\rho + m_a^2 f_a^2[1 - \cos(\theta)]\big) + 4\pi r G f_a^2\left(\frac{d\theta}{dr}\right)^2\right], \tag{9.63}$$

where we use the APR EoS [255] to close our system of equations, enabling us to express $p \equiv p(\rho)$.

The stellar system of equations is a mixed initial-boundary value problem. The equations governing the metric potentials, $\nu(r)$ and $\lambda(r)$, and the pressure $p(r)$ are initial value problems (IVPs). Their evolution depends on initial conditions at the center of the star ($r = 0$), where the central density, ρ_{central}, is a free parameter that determines the star's mass and radius. Additionally, the central metric potential, ν_{central}, reflects a choice of time-coordinate, which can be shifted under the gauge transformation $t \to e^{\nu_0/2}t$. This gauge freedom allows us to extract the star's mass later in the analysis. The star's surface is defined as the point R where the pressure, and hence the density, drops to zero, $\rho(R) = 0$. At this boundary, the metric potentials and their derivatives must remain continuous to ensure physical consistency.

In contrast, the KG equation for the ALP is a boundary value problem (BVP) because it requires conditions at both the center and spatial infinity. At the center, spherical symmetry imposes the condition $\frac{d\theta}{dr}|_{r=0} = 0$, while at infinity, the field must asymptote to its ambient value, $\lim_{r\to\infty}\theta(r) = \theta_\infty$ with its derivative approaching zero $\lim_{r\to\infty}\theta'(r) = 0$. The asymptotic value $\theta_\infty = a_\infty/f_a$ minimizes the effective potential in the galactic ambient density,

which we take as $\rho_\infty = 0$ for simplicity. Although the actual galactic density, $\rho_{\text{gal}} \sim 10^{-24}\,\text{g/cm}^3$, slightly shifts the minimum, this effect is negligible. These boundary conditions uniquely determine the central field value, θ_{central}, ensuring that the field solution matches smoothly across the star's interior and exterior. Solving for θ_{central} is a key part of this analysis, as it establishes the full profile of the ALP field, both inside and outside the star.

9.3.1 Interior Stellar System

Before discussing the solutions of the interior and exterior systems together, it is important to address a subtlety in the interior system. Due to the singularity at $r = 0$, numerical integration cannot begin precisely at the center of the star. To avoid this issue, we define initial conditions at a small distance from the center, r_i, where $r_i \ll R$ and R is the radius of the neutron star, typically on the order of 10^6 cm. For this work, we set $r_i = 10^{-15}$ cm.

To ensure consistency, the metric potentials, scalar field, and density are expanded as power series, to second order, in r about $r = 0$:

$$\rho(r) = \rho_{\text{central}} + \rho_1 r + \rho_2 r^2 + \mathcal{O}(r^3)\,, \tag{9.64}$$

$$\nu(r) = \nu_{\text{central}} + \nu_1 r + \nu_2 r^2 + \mathcal{O}(r^3)\,, \tag{9.65}$$

$$\lambda(r) = \lambda_{\text{central}} + \lambda_1 r + \lambda_2 r^2 + \mathcal{O}(r^3)\,, \tag{9.66}$$

$$\theta(r) = \theta_{\text{central}} + \theta_1 r + \theta_2 r^2 + \mathcal{O}(r^3)\,. \tag{9.67}$$

The first-order coefficients $(\rho_1, \nu_1, \lambda_1, \theta_1)$ vanish due to physical considerations. Spherical symmetry about the center of the star imposes that the scalar field and the metric functions be even functions of r, leading to vanishing first derivatives at the origin. Specifically, $\theta'(r = 0) = 0$ eliminates θ_1, and $\nu'(r = 0) = 0$ sets $\nu_1 = 0$. Additionally, $\lambda_{\text{central}} = 0$ reflects the absence of enclosed mass at $r = 0$. The density and pressure are maximum at the center and decrease symmetrically outward, requiring $\rho_1 = 0$. Substituting these expansions into the interior system of equations, I derive relationships between the second-order

coefficients $(\rho_2, \nu_2, \lambda_2, \theta_2)$, the central values $(\rho_{\text{central}}, \nu_{\text{central}}, \theta_{\text{central}})$, and the ALP parameters. These coefficients yield the initial conditions at r_i

$$\rho(r_i) = \rho_{\text{central}} - \alpha r_i^2 \,, \tag{9.68}$$

$$\nu(r_i) = \nu_{\text{central}} + \beta r_i^2 \,, \tag{9.69}$$

$$\lambda(r_i) = \gamma r_i^2 \,, \tag{9.70}$$

$$\theta(r_i) = \theta_{\text{central}} + \eta r_i^2 \,, \tag{9.71}$$

where $\alpha, \beta, \gamma, \eta$ are complicated functions of the ALP parameters and the central values. These initial conditions provide a consistent starting point for the numerical integration of the interior equations. The integration proceeds outward until the density drops to zero, defining the radius of the star, R. Beyond this radius, the exterior system of equations governs the scalar field and metric potentials.

9.3.2 Exterior Stellar System

Finding the exterior system of equations is straightforward, by setting the density and pressure to zero, we find

$$\frac{d\nu}{dr} = \frac{e^{\lambda}-1}{r} + \frac{1}{c^4}\left[-8\pi r m_a^2 f_a^2 G(1-\cos(\theta))e^{\lambda} + 4\pi r G f_a^2 \left(\frac{d\theta}{dr}\right)^2\right], \tag{9.72}$$

$$\frac{d\lambda}{dr} = \frac{1-e^{\lambda}}{r} + \frac{1}{c^4}\left[8\pi r m_a^2 f_a^2 G(1-\cos(\theta))e^{\lambda} \quad + 4\pi r G f_a^2 \left(\frac{d\theta}{dr}\right)^2\right], \tag{9.73}$$

$$\frac{d^2\theta}{dr^2} - \frac{d\theta}{dr}\left(-\frac{2}{r} + \frac{1}{2}\frac{d\lambda}{dr} - \frac{1}{2}\frac{d\nu}{dr}\right) - m_a^2 e^{\lambda}\sin(\theta) = 0 \,, \tag{9.74}$$

and the KG must satisfy

$$\theta'(r=0) = 0 \,, \tag{9.75}$$

$$\theta(r=r_f) = 0 \,, \tag{9.76}$$

$$\theta'(r=r_f) = 0 \,, \tag{9.77}$$

where r_f is the upper limit of our integration, chosen to be far from the star's radius. Condition (9.75) ensures spherical symmetry, while conditions (9.76)-(9.77) demand that the ALP settles in its VEV in the absence of matter. Additionally, the solutions must match smoothly across the star's radius, further complicating the scenario. This requires that

$$\theta(r = R^-) = \theta(r = R^+), \tag{9.78}$$

$$\theta'(r = R^-) = \theta'(r = R^+), \tag{9.79}$$

where $\theta(r = R^-)$ is the value of the field at the star's radius determined from the interior solution of the IVP, and $\theta(r = R^+)$ is the value of the field at the radius determined from the exterior solution of the BVP. The radius R is determined from the interior solution by halting the integration when the step size falls below 10^{-8}. The goal is to find the central field value θ_{central} that satisfies the boundary conditions and ensures continuity in Eqns. (9.78)-(9.79). One might consider using shooting methods; however, the system is overdetermined, as the KG equation only requires two boundary conditions, but we have three, in addition to the complexity of ensuring continuity across the radius. Therefore, I devised an algorithm that dynamically finds θ_{central} to satisfy the continuity in Eqns. (9.75)-(9.79) and the boundary conditions in Eqns. (9.75)-(9.77).

9.3.3 Numerical Algorithm

I devised an algorithm to solve the mixed initial-boundary value problem derived in Sections 9.3.1 and 9.3.2 using the `Python` package `SciPy` [285]. The algorithm combines several numerical methods, as follows

1. The `LSODA` method [286, 287] is utilized to solve the interior system as a IVP with a sensible initial guess for $\theta(0) = \theta_{central}$ and setting $\theta'(0) = 0$, satisfying (9.75). LSODA automatically detects stiffness and switches between non-stiff (Adams) [288] and stiff (BDF) [289] solvers accordingly.

2. The `solve_bvp` function from `SciPy` is utilized to solve the exterior BVP system. This method employs a fourth-order collocation algorithm with residual control [290] and solves the collocation system using a damped

Newton method with an affine-invariant criterion function [291]. The boundary conditions are set as $\theta(r_f) = 0$ and $\theta'(R^+) = \theta'(R^-)$, where $\theta'(R^-)$ is the value at the radius determined from the IVP solution in step 1. These ensure continuity and satisfy Eqns. (9.76) and (9.79). The collocation method approximates the solution by fitting piece-wise polynomials over a mesh and iteratively adjusts them to reduce the residuals. This approach is particularly effective for smooth solutions and allows flexible mesh refinement to ensure numerical accuracy.

3. The `Nelder-Mead` minimization algorithm [292, 293] is employed to minimize a custom-defined `cost` function without the need for gradients, making it suitable for complicated problems where the gradients are computationally expensive or inaccessible. I use a mean squared error (MSE) cost function that the algorithm minimizes, $cost = |\theta'(r_f) - 0|^2 + |\theta(r = R^-) - \theta(r = R^+)|^2$. The first term corresponds to satisfying (9.77) while the second one addresses (9.78). To restrict ourselves to physical solutions, we penalize solutions where $\theta(r) > 0$ and null solutions $\theta(r < R) = 0$. Due to the difference in the scales of each term, I normalize the terms with equal weights to ensure that minimizing the cost is fair to both terms. Nelder-Mead is a simplex-based optimization method [292] that explores the parameter space using geometric transformations such as reflection, expansion, and contraction. It does not require derivative information and is robust in low-dimensional, noisy, or non-smooth optimization landscapes.

The algorithm guarantees that if a solution exists, it will converge, provided a sensible initial guess for θ_{central}. The pseudocode is detailed in Algorithm 1. To find an initial guess for the central field value, θ_{central}, we assume a constant density star with central density ρ_{cent}. Using Eqn. (9.3), the field value that minimizes the Hamiltonian is given by

$$\theta_{central} = -\frac{R^2 \rho_{cent}}{\mu f_a}\,, \tag{9.80}$$

where I set $R = 12$ km, the radius for a typical neutron star. Once the algorithm converges, we obtain the star's radius R and the central field value θ_{central}. To

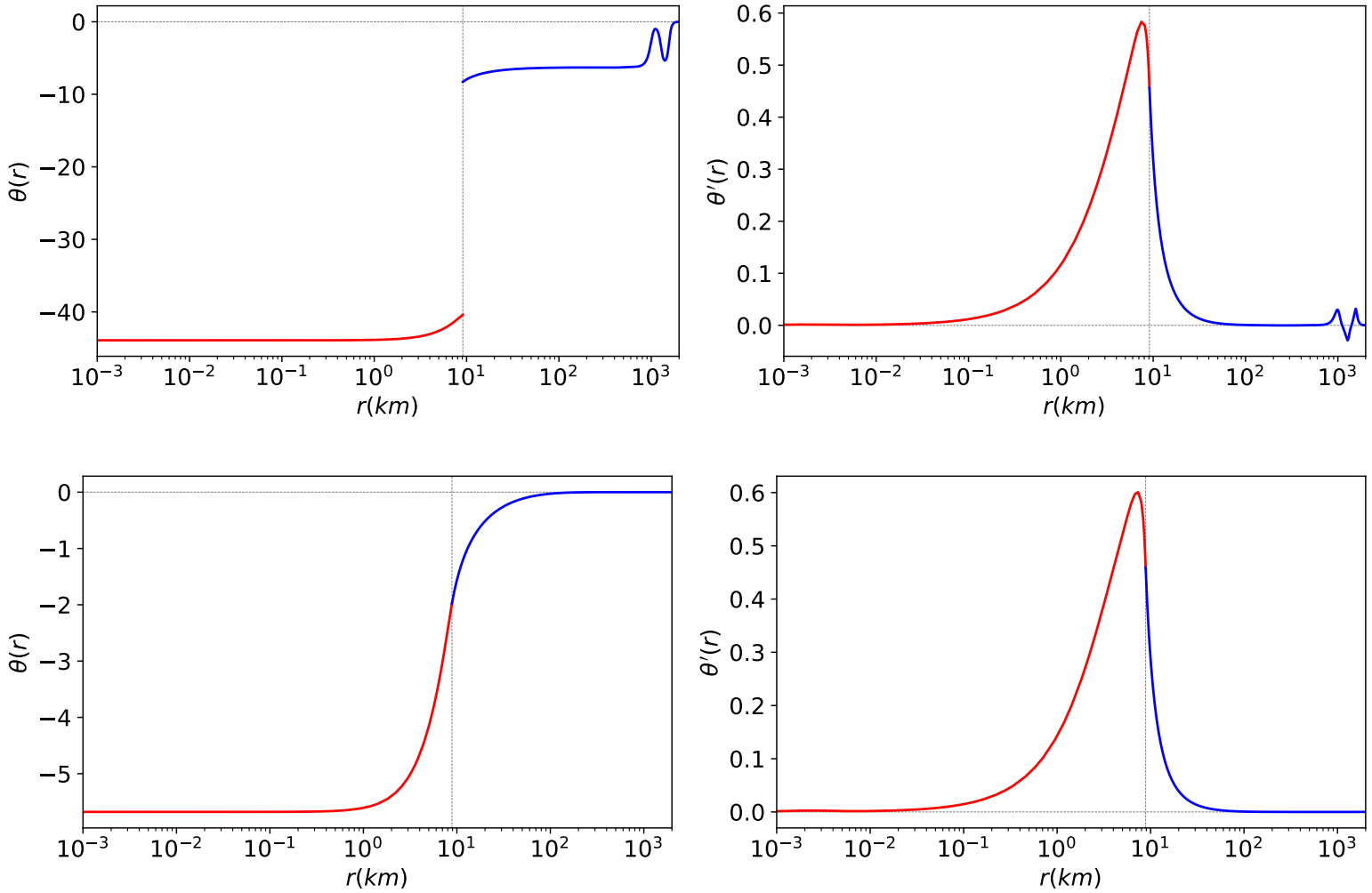

Figure 9.3: The profile of an ALP inside a neutron star with a destabilized potential at the center ($\rho_c > \rho_{central}$). *Top*: The field profile with our initial guess, as given by Eqn. (9.80). This initial guess is far from the true solution, as indicated by the mismatch across the boundary; however, the derivative is smooth due to it being one of our boundary conditions. *Bottom*: The field profile after running our algorithm, where the minimizer has converged towards the correct solution.

Algorithm 1 Pseudocode for solving the BVP using a combination of methods

Initialize θ_c with a sensible initial guess
repeat
  Interior IVP:
  Set initial conditions (I.C.): $\rho_i, \nu_i, \lambda_i, \theta_i$ such that $\theta(0) = \theta_{central}$, and $\theta'(0) = 0$
  Solve the interior IVP using `LSODA` to obtain $\rho(r), \nu(r), \lambda(r), \theta(r), \theta'(r)$ for $r \leq R$
  Boundary Conditions for Exterior BVP:
  Set boundary conditions (B.C.): $\nu(R) = \nu(R^-), \lambda(R) = \lambda(R^-), \theta(r_f) = 0$, $\theta'(R) = \theta'(R^-)$
  Exterior BVP:
  Solve the exterior BVP using `solve_bvp` to obtain $\theta(r)$ and $\theta'(r)$ for $R \leq r \leq r_f$
  Calculate Cost:
  Compute the cost function: cost $= |\theta'(r_f) - 0|^2 + |\theta(r = R^-) - \theta(r = R^+)|^2$
  if $\theta(r_i \leq r \leq r_f) \geq 0$ **then**
    Penalize the cost
  end if
  Update:
  Update $\theta_{central}$ using the `Nelder-Mead` algorithm to minimize the cost.
until $|\theta^{(i)}_{central} - \theta^{(i-1)}_{central}| < \times 10^{-9}$

determine the star's mass, we employ the asymptotic expansion of the metric potential

$$\lim_{r\to\infty} \nu(r) = A\left(1 - \frac{2GM}{r}\right), \tag{9.81}$$

where A is a constant reflecting the freedom in the choice of the time coordinate, as discussed earlier. The values of A and M are obtained by matching the numerical solutions for $\nu(r)$ and $\nu'(r)$ to this asymptotic form. From this, the mass M of the neutron star can be calculated. For a benchmark model with $g_s^N = 6 \times 10^{-22}, m_a = 2.8 \times 10^{-12}\text{eV}, f_a = 10^{15}\text{GeV}$, and $\rho_{cent} = 6.18 \times 10^{15}$ g/cm^3, I present the field profile before and after running the optimization algorithm in Fig. 9.3. The field begins with the initial guess given by Eqn. (9.80), which is refined by the algorithm to achieve the final optimized solution. The

full implementation of the algorithm, including the benchmark model and additional examples, is publicly available in a GitHub repository.

9.4 Results

Due to the complexity of the stellar system, equations, and the algorithm used to solve them, solving for a single neutron star takes approximately 20 to 30 minutes. To mitigate this computational cost, I parallelized the code using Python's `ThreadPoolExecutor`, enabling simultaneous computation of multiple neutron star configurations. This approach leveraged the multicore architecture of the UH HPC MANA cluster, allowing up to 40 stars to be solved in parallel and reducing the total runtime per star to a fraction of the original.

Using this setup, I conducted a detailed analysis of the mass-radius relationship for neutron stars across a broad parameter space, spanning the ranges of $m_a \in [10^{-12}, 10^{-15}]$ eV, $f_a \in [10^{15}, 6\times10^{19}]$ GeV, and $g_s^N \in [9\times10^{-25}, 1\times10^{-19}]$, or equivalently $\mu \in [9 \times 10^{19}, 10^{25}]$ GeV.

Our results reveal negligible deviations from GR, with modifications to the mass-radius relationship on the order of $\Delta M/M \sim 10^{-3}$ at maximum. This strongly suggests that, for these parameter ranges, CP-violating ALP have no significant effect on the structure of neutron stars. The central densities of the stars analyzed span the range $\rho_{\text{central}} \in [4 \times 10^{14}, 1.8 \times 10^{16}]\,\text{g/cm}^3$.

Fig. 9.4 shows our results, the mass-radius relationships for neutron stars under GR and our EFT. Even for a model with $\mu = 9 \times 10^{19}\,\text{GeV}$, which approaches the cut-off of the theory, deviations remain minimal. This confirms that CP-violating ALPs in this parameter range are unlikely to produce significant modifications to neutron star structure.

Fig. 9.5 illustrates the relationship between the ALP central value θ_{central} and the central density ρ_{central} of the neutron star. This plot highlights the phenomenology described in Section 9.1. Specifically, when $\rho_{\text{central}} < \rho_c$, the ALP VEV shifts away from the CP-conserving value of $\theta = 0$, as the potential remains stable. In contrast, when $\rho_{\text{central}} > \rho_c$, the ALP potential becomes destabilized and lacks a minimum. However, the ALP field does not roll to infinity, as the gradient energy cost inhibits such behavior as predicted. The figure compares two distinct models: one where the potential is destabilized

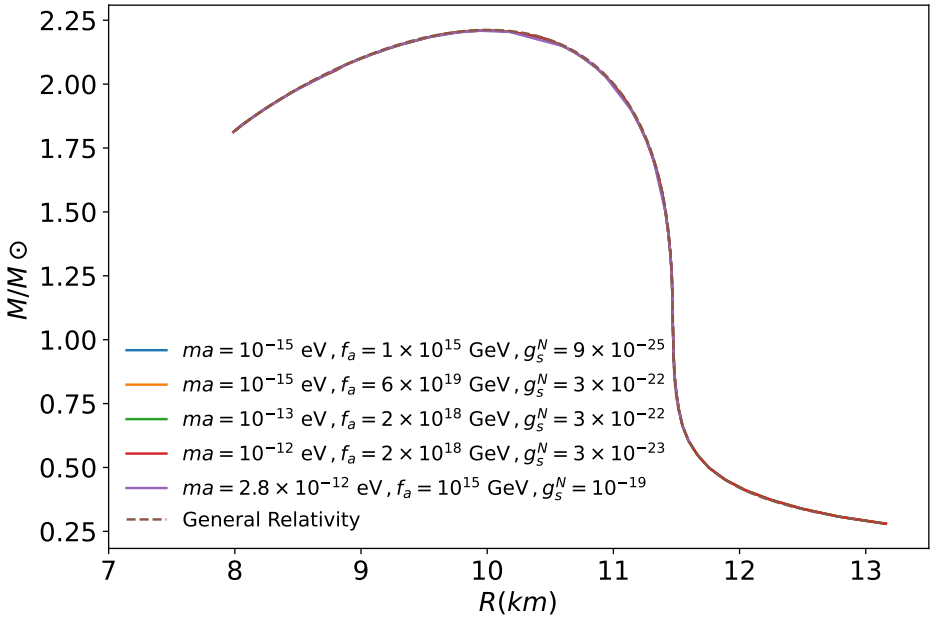

Figure 9.4: Comparison of the mass-radius relationship for neutron stars predicted by GR and the modified theory incorporating the CP-violating ALP. Deviations from GR predictions are present but are negligible, with differences on the $\delta M/M = 10^{-3}$ level.

($\rho_c > \rho_{\text{central}}$) and one where it remains stable ($\rho_c < \rho_{\text{central}}$). While both models exhibit similar trends, the values of θ_{central} differ by four orders of magnitude, reflecting the further rolling of the ALP field in the destabilized potential scenario. This difference underscores the interplay between the ALP potential and gradient energy in determining the field's profile.

9.5 Interpretation of results

To understand the negligible deviations observed in our results, it is important to examine the theoretical aspects and energetic considerations governing CP-violating ALPs in neutron stars, which we now discuss in greater detail.

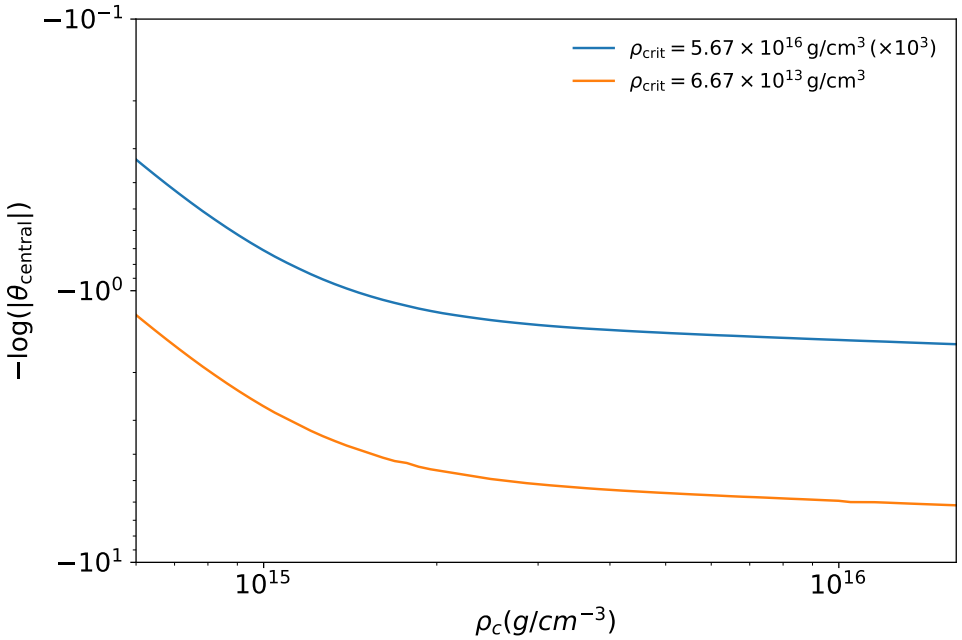

Figure 9.5: The relationship between the ALP central value θ_{central} and the central density ρ_{central} of neutron stars. Two scenarios are compared: one where the potential is destabilized ($\rho_c > \rho_{\text{central}}$) and one where it is stable ($\rho_c < \rho_{\text{central}}$), shown in orange and blue, respectively. While both models exhibit similar trends, θ_{central} is larger for the destabilized case by approximately 10^4. Note that the stable case is multiplied by 10^3 for visual clarity.

The suppression of deviations in neutron star structure can be explained by considering a static, spherically-symmetric non-relativistic object. The ALP KG equation in such a system simplifies to

$$\frac{1}{r^2}\frac{\mathrm{d}}{\mathrm{d}r}\left(r^2\frac{\mathrm{d}a(r)}{\mathrm{d}r}\right) - \frac{\mathrm{d}V_{eff}(a)}{\mathrm{d}a} = 0. \tag{9.82}$$

At large distances, the field tends to the asymptotic value a_∞, which minimizes V_{eff} in the ambient galactic density. At the star's center, the field is displaced from this value. When $\rho > \rho_c$, the potential destabilizes, leading to a field displacement of order $\Delta a \sim 3M/4\mu R$. Conversely, when $\rho < \rho_c$, the field either minimizes the effective potential at the star's central density or balances potential and gradient energy, whichever is energetically more favorable.

However, deviations from GR in neutron star structure are suppressed due to the constant ALP-nucleon coupling and the effective ALP mass remaining close to the bare mass m_a. The latter prevents phenomena such as *screening mechanisms* [23, 265, 294] or *spontaneous scalarization*[295], which are observed in other scalar-tensor theories. Instead, the field scales as

$$a(r) \sim \frac{M}{4\pi\mu r}e^{-m_a r}. \tag{9.83}$$

Deviations from GR are expected only when the Compton wavelength $\lambda_{\mathrm{C}} \sim m_a^{-1}$ exceeds the characteristic size of the star, $R \sim 10$ km, allowing the ALP field to coherently influence the entire star. In this work, the masses we used were chosen to satisfy this condition where we used $m_a \lesssim 10^{-12}$ with a corresponding Compton wavelength of $\lambda_{\mathrm{C}} \gtrsim 198$ km. However, this condition alone is insufficient to generate observable deviations. The strength of the ALP-mediated fifth force must also satisfy

$$\frac{F_5}{F_N} = \frac{1}{4\pi G\mu^2} \gtrsim 1\,, \tag{9.84}$$

where F_5 and F_N are the ALP-mediated fifth-force and gravitational force per unit mass, respectively. For $\mu \gtrsim 9 \times 10^{19}$ GeV, which is the parameter space explored here, the fifth force is heavily suppressed, with $F_5/F_N \ll 1$. To reach the threshold $F_5/F_N \gtrsim 1$, μ would need be as low as $\mu \lesssim \sqrt{2}M_{\mathrm{Pl}} \sim 3.4 \times 10^{18}$

This lower limit on μ is problematic for two reasons. First, it violates the bound derived from Eqn. (9.5), which ensures the validity of the EFT. This bound enforces $a/\mu \ll 1$ to prevent issues such as vanishing neutron masses due to high coupling constants. Second, such low values of μ are already excluded by experimental constraints from WEP tests as shown in Fig. 9.2.

In summary, while the condition $\lambda_C > R$ is satisfied for low ALP masses, $m_a \lesssim 10^{-12}$ eV, the suppression of the fifth force due to large values of $\mu \gtrsim 9 \times 10^{19}$ GeV ensures that deviations from GR remain negligible. The dual constraints from the EFT validity and WEP tests further restrict $\mu \lesssim 3.7 \times 10^{18}$ GeV, leaving no viable parameters for observable modification to neutron star structure.

9.6 Complementary Constraints from Solar System Tests

In addition to the constraints derived from Eqn. (9.5), further bounds on CP-violating ALPs arise from solar system tests of GR, particularly through the Parameterized Post-Newtonian (PPN) framework. This framework measures deviations from GR in weak-field regimes [90] and is particularly sensitive to scalar-tensor theories, where the coupling of a scalar field to matter modifies the gravitational field. For these constraints to apply, the Compton wavelength of the ALP ($\lambda_C \sim m_a^{-1}$) must exceed the characteristic length scale of the experiment, as detailed below. Two key PPN parameters provide relevant bounds

1. γ: This parameter governs the Shapiro time-delay effect and the bending of light by massive bodies. Observations from the Cassini satellite during a conjunction with Earth at 8.43 AU in 2002 constrained $|\gamma - 1| < 2 \times 10^{-5}$ [274]. This bound applies to ALP masses $m_a \lesssim (8.43\,\text{AU})^{-1} \sim 1.6 \times 10^{-19}\,\text{eV}$, ensuring the ALP Compton wavelength exceeds the experimental scale.

2. β: This parameter affects the perihelion advance of orbiting bodies. Observations of Mercury's perihelion constrained $|\beta - 1| < 8 \times 10^{-5}$ [90].

This bound applies to ALP masses $m_a \lesssim (0.4\,\mathrm{AU})^{-1} \sim 3.3 \times 10^{-18}\,\mathrm{eV}$, similarly requiring the Compton wavelength to exceed the orbital radius of Mercury.

For ALPs with masses satisfying these conditions, the Compton wavelength is sufficiently large to treat the ALP as effectively massless on the relevant experimental scales. The expressions for $\gamma-1$ and $\beta-1$ in scalar-tensor theories are generally derived in terms of the scalar field coupling strength [89, 296–298]. However, the specific form used here

$$\gamma - 1 = -4\frac{M_{\mathrm{Pl}}^2}{2M_{\mathrm{Pl}}^2 + \mu^2}, \quad \beta - 1 = -2\frac{M_{\mathrm{Pl}}^4}{(2M_{\mathrm{Pl}}^2 + \mu^2)^2}, \tag{9.85}$$

are adapted from this framework and expressed in terms of the ALP-nucleon coupling parameters relevant to this analysis. My contribution involves using these equations to calculate specific bounds on μ and g_s^N based on observational constraints from the Cassini satellite and Mercury's perihelion. Applying these constraints, I found that the γ bound requires $\mu > 1.16 \times 10^{21}\,\mathrm{GeV}$ ($g_s^N < 8.07 \times 10^{-22}$) while the β bound requires $\mu > 2.16 \times 10^{19}\,\mathrm{GeV}$ ($g_s^N < 4.36 \times 10^{-20}$).

These constraints are shown in Fig. 9.2. Together with neutron star analyses, they provide complementary bounds on CP-violating ALPs, further restricting their parameter space in weak-field regimes.

9.7 Summary

In this chapter, we investigated the effects of CP-violating ALPs on neutron star stability and structure, deriving a lower bound of $\mu > 3.7 \times 10^{18}$, GeV to prevent unphysical modifications to neutron masses. To incorporate ALP-mediated effects, I derived the modified Tolman–Oppenheimer–Volkoff equations, accounting for the field's back-reaction on stellar structure. Numerical solutions revealed negligible deviations from general relativity, with $\Delta M/M \sim 10^{-3}$ being the largest observed change, emphasizing the robustness of GR predictions. These findings underscore the limited impact of CP-violating ALPs on neutron stars within the explored parameter space, while providing a robust computa-

tional framework for further study of scalar fields in high-density astrophysical environments.

Part V

Closing Thoughts and Prespectives

10 Final Insights and Outlook

"Oh traveler, the road is longer than you know,
yet every step is a new universe to show.
In your heart lies the compass, true and wise,
look inward for the light that never dies."

– Salah Jahin

This chapter brings together the key findings and contributions of my PhD research, highlighting the main challenges addressed, solutions proposed, and suggested future directions. My work, spanning four peer-reviewed publications, advances cosmology by introducing a dynamical-systems framework that unifies early and late dark energy via phase-space attractors; refining observational constraints on dynamical dark energy models with DESI data; and exploring novel CP-violating ALP phenomenology through Yukawa-like couplings to baryonic matter-including neutron star destabilization via density-dependent potentials and early-universe field excursions-while deriving new bounds on ALP parameter space and proposing a potential unified dark-sector scheme.

The research presented in this dissertation has been published in Physical Review D [50–52], with the last paper accepted in the Journal of Cosmology and Astroparticle Physics (JCAP) [54] and in the production phase. Below, I summarize the findings, challenges, and potential avenues for future exploration based on this body of work.

10.1 The Hubble Tension and Early Dark Energy

In Chapter 4, we presented the attractive early dark energy (@EDE) framework, a unification scheme that combines early and late dark energy within a dynamical systems approach. This framework was designed to address the Hubble tension while evading the early dark energy coincidence problem by relying on the phase space structure of the dynamical system. The onset of EDE coincides naturally with matter-radiation equality due to a dynamical saddle point, while the late-time acceleration of the Universe emerges as a global attractor. These features make the @EDE framework theoretically appealing as it reduces the need for fine-tuning in the model parameters.

Despite its theoretical strengths, the fiducial @EDE model, motivated by a double exponential potential from string theory, encountered challenges in reconciling with observational data. The framework, while innovative, revealed tensions that ultimately prevent it from resolving the Hubble tension under the tested configurations.

10.1.1 Challenges and Observational Constraints

The @EDE model introduces a non-zero energy injection during the early Universe, contributing approximately $f_{\rm ede} \simeq 3.39\%$ to the total energy budget at $z \sim 10^7$. This energy density, initially peaking, dilutes as the scalar field transitions to the matter attractor, maintaining a persistent fractional contribution of $\sim 1.33\% - 1.37\%$ until the late dark energy attractor dominates. While this dynamical behavior theoretically allows @EDE to unify early and late dark energy, its impact on the background and perturbation dynamics leads to significant deviations from observational data.

The presence of @EDE in the early Universe reduces the sound horizon size, r_s, while enhancing the early ISW effect due to the decay of gravitational potentials, $\Phi + \Psi$, in the Newtonian gauge [166]. This enhancement arises from an increase in the early expansion rate, $H(z)$, which accelerates the decay of gravitational potentials and boosts power in the first CMB peak and lower multipoles. Additionally, the higher $H(z)$ causes perturbation modes to enter

the horizon earlier, shifting the oscillation modes of the Sachs-Wolfe effect and altering the positions of the CMB peaks. In the late Universe, the persistent energy density contribution of @EDE primarily reduces the angular diameter distance, D_A, while also amplifying the late ISW effect due to the time evolution of gravitational potentials in the presence of the lingering non-clustering energy density of @EDE. These changes collectively exacerbate the tension between the observed angular size of the sound horizon, θ_*, and the shifts induced by r_s and D_A. Consequently, @EDE increases the power in the CMB temperature spectrum at lower multipoles, contributing to inconsistencies in the fit to the data.

When ΛCDM parameters are allowed to vary in the presence of @EDE, significant shifts are observed to compensate for its effects. An increase in ω_c is required to suppress the enhanced early ISW effect and match the height of the first CMB peak [108, 167, 168]. Simultaneously, ω_c must decrease to maintain consistency with θ_*, as changes in D_A dominate. This trade-off introduces competing demands on ω_c, which cannot be resolved simultaneously. Additionally, increases in ω_b and slight decreases in H_0 attempt to mitigate shifts in θ_*, but these adjustments further worsen the overall fit to the data.

The @EDE framework cannot simultaneously meet the observational requirements for matching the height and position of the CMB peaks. To counteract the enhanced early ISW effect, ω_c must increase, but maintaining consistency with θ_* requires a decrease in ω_c. This irreconcilable tension prevents @EDE from resolving the Hubble tension, with posteriors aligning more closely with a ΛCDM-like Universe.

While @EDE provides a novel theoretical framework, its incompatibility with the current observational constraints highlights the need for further model refinement.

10.1.2 Future Directions for @EDE

While the fiducial @EDE model does not provide a satisfactory fit to current observational data, it opens the door to future refinements and extensions of the framework. Within the four-dimensional phase space analyzed in this work, we identified a second scalar potential with the qualitative features required for the

scalar to function as @EDE. However, the near-identical background evolution and fixed points of this alternative potential suggest that it would not offer significant improvements in fitting the data. This motivates the exploration of broader frameworks and novel approaches to model building.

One promising direction involves expanding to higher-dimensional phase spaces for the dynamical system. Introducing additional degrees of freedom and free parameters could decouple the properties of the EDE and dark matter saddles, potentially mitigating the scalar dark matter contribution during the matter-dominated era. Such extensions would enlarge the set of possible models, enabling configurations where the scalar field's contribution during the matter epoch becomes negligible.

Another avenue is the investigation of non-minimal scalar field theories known to form dynamical systems. For instance, coupled quintessence models, where the scalar field is conformally coupled to dark matter [82], provide fixed points similar to the uncoupled case. However, in these models, the scalar's equation of state at each fixed point depends on the strength of the coupling to dark matter. This dependence could enable scenarios where the EoS at the dark matter saddle satisfies $w_\phi > 0$, causing the scalar to redshift during the matter era and diminish its late-time contributions. Such behavior could address the issue that caused our fiducial model to poorly fit the data.

K-essence theories, where the scalar field has a non-canonical kinetic term, as comprehensively reviewed in [147], or disformal quintessence models, where the scalar is derivatively coupled to dark matter [299, 300], could also provide valuable insights. The derivative interactions in these theories induce a non-zero sound speed for the scalar field, allowing it to cluster on small scales. This clustering could suppress the late ISW enhancement, improving consistency with observations.

10.1.3 Concluding Remarks

The lack of a concordance model capable of resolving the Hubble tension while remaining consistent with all current observations limits our ability to interpret data from cosmological missions and astrophysical surveys. As next-generation

missions begin to deliver data, discovering the origin of the Hubble tension becomes increasingly urgent.

Several upcoming cosmological surveys are expected to significantly enhance our ability to test early- and late-time modifications to ΛCDM, making it increasingly urgent to uncover the origin of the Hubble tension. These include the *Euclid Mission* [301], launched in July 2023, which will provide deep imaging and spectroscopy to constrain dark energy and the expansion history; the *Nancy Grace Roman Space Telescope* [302] (formerly WFIRST), scheduled for launch in 2027, which will conduct wide-field infrared surveys of large-scale structure; the *Vera C. Rubin Observatory* [303], expected to begin operations in 2025 with its Legacy Survey of Space and Time (LSST), offering deep optical imaging across the southern sky; and the *CMB-S4* experiment [304–306], planned to begin observations in the early 2030s, which will map the CMB with unprecedented sensitivity. These missions, along with ongoing efforts such as the *Dark Energy Spectroscopic Instrument (DESI)* [307], which released its first data in 2024 [35], are expected to refine measurements of H_0 and provide critical insight into the physics underlying the tension.

Any new physics underlying this tension must be grounded in quantum field theory principles, ensuring naturalness and freedom from fine-tuning and coincidence problems. Moreover, the physics should ideally connect with other observed phenomena, such as late dark energy.

This work represents progress in addressing the fine-tuning and coincidence issues associated with early dark energy. By proposing a unified framework for early and late dark energy as manifestations of a single scalar degree of freedom, this study has provided valuable insights into the challenges of resolving the Hubble tension. While the fiducial @EDE model does not improve on ΛCDM, the theoretical lessons learned lay a foundation for future research. These insights inspire further exploration of dynamical systems and scalar field theories in cosmology, advancing our knowledge to better understand the Universe's evolution.

10.2 The Microphysics of Dark Energy

In Part III, we explored the microphysics of dark energy through two theoretically motivated models: the single-exponential quintessence model and the pixelated dark energy model. Analyzed in light of DESI, DESY5, and Union3 datasets, these models were chosen for their potential to address tensions between ΛCDM and observational evidence suggesting thawing dark energy.

The single-exponential quintessence model evolves its EoS gradually from $w_0 = -1$ to $w_0 = -0.936^{+0.038}_{-0.064}$, struggling to account for low-redshift anomalies observed in supernovae and BAO data. The pixelated dark energy model, while introducing a UV-complete mechanism via discrete units or "pixels," is only marginally preferred over ΛCDM, with a best-fit improvement of $\Delta\chi^2_{\text{best fit}} = -3.76$. Importantly, for the time-dependent case, we identified the parameters needed to provide a fit as good as the CPL parameterization, demonstrating the potential of this framework to compete with leading dark energy models.

10.2.1 Challenges and Observational Constraints

The observational constraints reveal theoretical limitations in both models. For the single-exponential quintessence model, the gradual evolution in $w(z)$ fails to accommodate the steep variations required at $z \sim 0.5$, underscoring its inability to resolve tensions in low-redshift data. While its simplicity is theoretically appealing, this rigidity prevents it from aligning with the data's preference for thawing dark energy.

The pixelated dark energy model, despite being marginally preferred over ΛCDM, struggles with the fixed relationship between w_0 and w_a, defined by $w_a = -\frac{3}{2}\Omega_m(1+w_0)$. This limitation, arising from the assumption of a constant pixel growth rate Γ, restricts the variability in $w(z)$. However, our analysis of the time-dependent case revealed that by introducing higher-order corrections, such as $\ddot{N}/N^2$, the model can relax the fixed relationship between w_0 and w_a, allowing w_a to reach more negative values, and potentially achieving a fit as good as the CPL parameterization. These findings highlight the importance of extending the framework to include time-dependent dynamics in the pixel growth mechanism.

10.2.2 Future Directions

To address the limitations of these models, future investigations should focus on refining their theoretical frameworks and enhancing flexibility in their EoS evolution.

For the single-exponential quintessence model, sharper potentials, such as hill-top or plateau models, may better capture the rapid variations in $w(z)$ around $z \sim 0.5$. Additionally, scalar field frameworks involving phase transitions, such as symmetron dark energy [308, 309], or mass-varying neutrino scenarios [129, 133, 310, 311], could provide the steep transitions required by observational data.

For the pixelated dark energy model, introducing a time-dependent pixel growth rate, $\Gamma(t)$, could not only relax the fixed relationship between w_0 and w_a but also match the observational fit achieved by the CPL parameterization. As demonstrated in Subsection 5.2.3, incorporating terms like $\ddot{N}/N^2$ allows for greater flexibility in $w(z)$ evolution. Future analyses should include a full MCMC exploration of the extended parameter space to precisely constrain Γ_0 and Γ_1, the key parameters governing the pixel growth rate and its acceleration. Furthermore, scenarios where $\Gamma(t)$ is influenced by thermal or quantum events [197] may yield more realistic dynamics.

Beyond these specific models, other scalar field frameworks, such as coupled quintessence [82, 299, 300], k-essence [77, 312, 313], and multi-field models [314], should be investigated for their ability to capture steep variations in $w(z)$ and match observations. Modified gravity theories [23, 48, 315, 316] and UV-complete models [196, 197, 317] also offer promising avenues for addressing the dynamical nature of dark energy.

Finally, addressing potential systematics in observational data, such as BAO modeling assumptions and redshift biases, will be critical for refining constraints on w_0, w_a, and other key parameters. These efforts will bridge the gap between the landscape of theoretical models and observational precision, paving the way for a deeper understanding of the microphysics of dark energy.

10.2.3 Concluding Remarks

This work has advanced our understanding of the theoretical and observational challenges associated with dynamical dark energy. By examining two distinct models—the single-exponential quintessence model and the pixelated dark energy model—we identified key limitations that underscore the broader need for steep transitions in $w(z)$ at $z \sim 0.5$ to match observational data.

The single-exponential quintessence model, while rooted in theoretical simplicity, struggled to account for low-redshift anomalies due to its gradual EoS evolution. Meanwhile, the pixelated dark energy model, despite its marginal preference over ΛCDM, demonstrated significant potential when extended to include time-dependent dynamics, achieving a fit comparable to the CPL parameterization. Furthermore, the pixelated dark energy model's current performance suggests that new, high-precision datasets could elevate its preference to statistically significant levels, offering a compelling alternative to traditional parameterizations that are not rooted in theoretical physics.

These findings emphasize the importance of bridging the gap between the landscape of theoretical models and precise observational data. Future models must not only align with observational constraints but also be rooted in and motivated by physical principles. Ultimately, the microphysics of dark energy remains one of the most compelling frontiers in cosmology, demanding both innovative theoretical frameworks and rigorous observational scrutiny.

10.3 The Implications of CP-Violating ALPs

In this final chapter, we summarize the findings of Part IV, which explored the cosmological and astrophysical implications of CP-violating axion-like particles coupled to baryonic matter via Yukawa interactions.

10.3.1 Challenges and Findings

In the cosmological context, we examined the impact of CP-violating ALPs across stabilized and destabilized regimes. The analysis highlighted how CP-violating couplings tilt the ALP potential, causing the disappearance of discrete minima beyond a critical density ρ_c. This effect introduced a critical redshift,

z_c, marking the transition between destabilized and stabilized regimes. In the destabilized regime, the ALP field induced deviations in nucleon masses that could alter the standard ΛCDM evolution. Observational constraints imposed a lower limit of $\mu > 7 \times 10^{18}, \text{GeV}$ to ensure these deviations remained within 5%, a novel result unique to this work.

In the stabilized regime, the ALP field exhibited damped oscillations around a time-dependent minimum, simultaneously acting as dark matter (through oscillatory dynamics) and dark energy (via slow tracking of the minimum). This dual role provided a coherent framework that distinguishes CP-violating ALPs from traditional scalar field models of dark energy. These findings emphasized the potential of CP-violating ALPs to extend the standard cosmological model and unify the behaviors of dark matter and dark energy.

In the astrophysical context, we explored the effects of CP-violating ALPs on neutron stars, deriving a lower bound of $\mu > 3.7 \times 10^{18}, \text{GeV}$ to prevent unphysical alterations to neutron masses that could lead to instability of neutron stars, potentially unbounding them. To incorporate ALP effects into neutron star structure, I derived the modified Tolman–Oppenheimer–Volkoff equations, accounting for the ALP-mediated back-reaction. These equations presented unique computational challenges due to their mixed initial-boundary value nature, rendering traditional shooting and relaxation methods ineffective.

To address these challenges, I developed a custom numerical algorithm tailored to this problem. The algorithm utilized the `LSODA` method to solve the interior equations as an initial value problem, capturing the pressure and ALP profiles starting from the neutron star core. For the exterior equations, which were better suited to a boundary value approach, I employed the `solve_bvp` method. To ensure continuity between the interior and exterior solutions at the neutron star radius, the algorithm dynamically adjusted the central field value, θ_{central}, using a `Nelder-Mead` optimization routine. This combination of techniques allowed for an accurate and stable solution to the modified TOV equations.

Despite the complexity of the modified TOV equations and the inclusion of ALP effects, the numerical solutions revealed negligible deviations from the predictions of general relativity in the mass-radius relationship, with the maximum observed deviation being $\Delta M/M \sim 10^{-3}$. This lack of significant

deviation can be attributed to several factors, including the suppression of ALP-mediated fifth forces at large values of μ, where $F_5/F_N \ll 1$, with F_5 and F_N denoting the ALP-mediated fifth force and gravitational force per unit mass, respectively. Achieving an observable deviation would require $\mu < 2\sqrt{M_{\mathrm{Pl}}} \approx 3.7 \times 10^{18}$ GeV, which conflicts with the previously established lower bound for maintaining neutron star stability.

Complementary bounds derived from solar system tests of general relativity, such as those from Cassini and Mercury's perihelion advance, provided additional restrictions, reinforcing the results. Together, these findings underscored the limited impact of CP-violating ALPs on neutron stars within the explored parameter space while highlighting the novel computational framework developed to achieve these results.

10.3.2 Future Directions

Future work could extend the theoretical framework presented in this thesis to investigate several promising avenues. One compelling direction is the development of models incorporating ALPs as sources of dark energy, particularly exploring their role in early dark energy scenarios aimed at resolving the Hubble tension.

Canonical early dark energy models often rely on ALP-like periodic potentials [108, 125], but these face theoretical challenges such as fine-tuning of the potential to avoid predicting excessive dark matter at late times [50, 137]. Combining the destabilization mechanism and time-dependent ALP mass explored in this work could provide a more natural alternative, addressing some of these challenges.

Another intriguing application involves the relaxion mechanism, which seeks to resolve fine-tuning problems associated with the Higgs or the cosmological constant [318, 319].

Relaxion models, which address fine-tuning problems such as the electroweak hierarchy [319], typically involve scalar potentials with linear terms that induce slow rolling until stabilization is achieved via back-reaction, often through coupling to gauge fields [320, 321]. The CP-violating ALP potentials studied in this work differ in that destabilization arises from the ambient matter

density. Incorporating CP-violating Yukawa couplings to matter into relaxion frameworks could offer an alternative stabilization mechanism, where the relaxion is halted not by gauge dynamics but by interactions with dense matter environments. This introduces the possibility of environment-dependent stabilization and novel phenomenological signatures, such as field trapping in astrophysical structures or induced EDMs [322, 323], enriching the scope of relaxion model building.

Additionally, the novel features identified in this thesis could be generalized to dark sector models, where ALPs interact with dark gauge fields or other exotic particles. Such extensions might yield new signatures that are less constrained by current observational data, expanding the scope for theoretical and experimental exploration. Observationally, upcoming cosmological surveys and gravitational wave detectors offer an exciting opportunity to test these extended models and their predictions. These efforts could further refine the parameter space and enhance our understanding of how CP-violating ALPs influence the evolution of the Universe and its astrophysical structures.

10.3.3 Concluding Remarks

This project has explored the role of CP-violating axion-like particles (ALPs) in both cosmological and astrophysical settings. The cosmological analysis revealed that these ALPs can exhibit a dual behavior: the bare potential drives dark matter-like oscillations, while the CP-violating coupling introduces a time-dependent minimum that tracks like dark energy. This dual behavior offers a novel pathway for scalar-field-based unification of dark matter and dark energy.

In the astrophysical regime, the derivation of modified stellar structure equations and their numerical implementation has offered a robust foundation for examining the interplay between scalar fields and compact objects, such as neutron stars. These equations were used to constrain the viable parameter space of CP-violating ALPs. Although no significant deviations from general relativity were found, the results provide robust bounds on the ALP couplings and ensure compatibility with compact object stability.

These findings suggest directions for future exploration of CP-violating ALPs across broader contexts. In dark sector extensions, ALPs could couple to hidden gauge groups or exotic particles, introducing new dynamics with fewer constraints from visible-sector data [222, 324]. In the early universe, CP-violating ALPs could participate in baryogenesis mechanisms through their Yukawa couplings to matter [325, 326]. As for gravitational wave probes, while this work found no observable impact of CP-violating ALPs on neutron star structures, further studies could explore whether such fields affect neutron star mergers at a detectable level in strong-field regimes. Regarding gravitational wave phenomena, while the deviations in neutron star structure identified in this work remain below observable thresholds, extensions involving stronger couplings or dark sector interactions could result in measurable effects [267, 327, 328]. These might include altered tidal deformability or waveform modifications in neutron star mergers, which can be tested by current and future observatories such as LIGO, Virgo, and the Einstein Telescope.

A Pixelated Dark Energy Equation of State

This appendix provides the derivation of the EoS for the pixelated dark energy model, as first presented in [197]. While not new to this work, the derivation is included for completeness, detailing how the time-dependent EoS is derived and connected to the CPL parameterization for comparison with observational data and and implementation in `CLASS`.

To derive the EoS for the pixelated DE model around the today, we start with the Friedmann equation for a Universe containing matter and a time-dependent cosmological constant[1] given by Eqn. (5.4). The Friedmann equation becomes

$$H^2 = \frac{1}{3M_{\rm Pl}^2}(\rho_m + \rho_\Lambda), \tag{A.1}$$

where ρ_m and ρ_Λ are the densities of matter and dark energy, respectively. The energy density associated with $\Lambda(t)$ is found through the relation $\rho_\Lambda = \Lambda(t)M_{\rm Pl}^2$ and becomes

$$\rho_\Lambda(t) = \frac{8\pi^2 M_{\rm Pl}^2}{l_s^2 N(t)}\,. \tag{A.2}$$

For the dark energy fluid to be compatible with a Friedmann Universe, it must satisfy the continuity equation

$$\dot{\rho}_\Lambda + 3H(t)(\rho_\Lambda + P_\Lambda) = 0\,, \tag{A.3}$$

which leads to

$$P_\Lambda = \rho_\Lambda\left(-1 + \frac{\dot{N}(t)}{3H(t)N(t)}\right), \tag{A.4}$$

[1] The assumption is justified since the energy density of radiation in the Universe, today, is negligible compared to the energy density of matter and dark energy [9]

where we can identify the EoS to be

$$w(t) = -1 + \frac{\dot{N}(t)}{3HN(t)}\,. \tag{A.5}$$

To connect the above equation to the CPL parameterization, we start with the Hubble parameter expressed in terms of the density parameters

$$H(a) = \frac{\Omega_m H_0^2}{a^3} + \frac{\Lambda}{3}\,. \tag{A.6}$$

Expanding $H(a)$ to first order in a Taylor series around $a = 1$, which corresponds to the present-day epoch, we find

$$H(a) = H_0\left[1 + \frac{3}{2}\Omega_m(1-a) + \mathcal{O}((1-a)^2)\right]. \tag{A.7}$$

Substituting this expression into Eqn. (A.5), the EoS becomes

$$w(a) = -1 + \frac{\dot{N}}{3H_0N} - \frac{1}{2}\Omega_m\frac{\dot{N}}{H_0N}(1-a), \tag{A.8}$$

where we have assumed the simplest and best-motivated pixelated DE model with a constant Γ, which allows higher-order terms to be neglected [197].

Here, we can see that the equation of state takes a form similar to the CPL parameterization if we define w_0 and w_a as

$$w_0 = -1 + \frac{\Gamma}{3H_0}, \tag{A.9}$$

$$w_a = -\frac{1}{2}\Omega_m\frac{\Gamma}{H_0}, \tag{A.10}$$

$$w(a) = w_0 + w_a(1-a), \tag{A.11}$$

where

$$\Gamma \equiv \frac{\dot{N}}{N} \tag{A.12}$$

represents the growth or decay rate of the pixels, with the sign determining whether $N(t)$ increases or decreases over time.

B Neutron Stars

Since we will study the effects of the ALPs on neutron stars, it is worthwhile to review the basics of these objects. A typical main sequence star reaches the end of its life by exhausting its nuclear fuel. When so happens, the thermal pressure from the radiation produced by nuclear reactions cannot fight the gravitational pressure and instability emerges. The inner, denser, regions of the star collapse first, forming a shock wave that is transferred to the outer layers, blowing them away. Shortly after, a "core" is left behind which, depending on the initial mass of the star, could become a white dwarf, neutron star, or a black hole.

When a massive star, typically in the mass range of $8 - 25 M_\odot$, exhausts its nuclear fuel, the core that remains after this explosion can collapse further to form a neutron star; only supernovae Type-II, Ib, and Ic are known to birth a neutron star. These remnants are the most known compact objects in the universe with masses typically ranging from about $1 - 2.2 M_\odot$, but packed into a sphere with a radius of about 10 to 12 km with core densities $\rho_{core} = 10^{14} - 10^{15}$ g/cm^3, denser than the core of atomic nuclei.

They were first hypothesized by Walter Baade and Fritz Zwicky in 1934 [329, 330], shortly after the discovery of the neutron by James Chadwick in 1932 [331].

Baade and Zwicky proposed that a supernova could result in the formation of a neutron star, describing it as a compact, dense remnant composed primarily of neutrons, a theory that arose from the realization that the collapse of a star's core could be halted by neutron degeneracy pressure. This marked the first suggestion that such dense objects could exist, laying the groundwork for the discovery and study of neutron stars in astrophysics.

In 1939, Tolman [332] and, independently, Oppenheimer and Volkoff [333] derived the relativistic equations that describe the structure of a static star with spherical symmetry by solving the Einstein's field equations. These equations

are now known as the TOV equations. They predicted that the maximum mass for a stable static neutron star is $M_{max} \sim 0.7M_{\odot}$. The reason behind their estimation is that they assumed that the neutrons in the interior did not interact, which highlighted the importance of nuclear forces to the structure of these objects. Fast-forward to the late 1950s, the nucleon-nucleon interactions was an active area of research and Cameron [334] managed to get a more realistic estimate of $M_{max} \sim 2M_{\odot}$ using the effective nuclear potential published by Skyrme [335]. This was the first step towards reaching a more realistic equation of state for neutron stars; a topic that is still a topic of research until this day.

Since then, various equations of state has been published by including that account for different nucleon-nucleon and three-nucleon interactions [276–281]. Notably, the APR equation of state is most commonly used to model the nuclear matter in neutron stars, predicting a maximum mass of $2.2M_{\odot}$ and constraining the maximum mass predicted by realistic models of nuclear forces to $2.5M_{\odot}$ [255]. For in-depth review of the various equation of state, their physics, and interactions they include, please refer to the following references [282–284].

B.1 Tolman–Oppenheimer–Volkoff in General Relativity

To determine the mass-radius relationship of stars, we solve equations that describe the balance between pressure gradients and gravitational forces within the stellar structure. For non-relativistic stars, such as main sequence stars, this balance is well-captured by the Newtonian hydrostatic equilibrium equation

$$\frac{dp}{dr} = -\frac{Gm(r)\rho(r)}{r^2}\,, \tag{B.1}$$

where $p(r)$ is the pressure, $\rho(r)$ is the mass density, and $m(r)$ is the mass enclosed within a shell of radius r. This equation represents the condition that the outward pressure gradient must counteract the inward gravitational pull for a star to remain stable. While the Newtonian equation works well for non-relativistic stars, it fails to describe compact objects like neutron stars, where strong gravitational fields and relativistic effects dominate. To address

these limitations, the relativistic TOV equations. They consist of two coupled differential equations. The first is the relativistic hydrostatic equilibrium equation

$$\frac{dp}{dr} = -\frac{(\rho + p)(Gm(r) + 4\pi G r^3 p)}{r(r - 2Gm(r))}\,, \tag{B.2}$$

and the second is the mass equation

$$\frac{dm}{dr} = 4\pi r^2 \rho\,, \tag{B.3}$$

and an equation of state (EoS) relating pressure and density, such that $\rho \equiv \rho(p)$.

Here, ρ represents the energy density of the star rather than its mass density, and $p(r)$ represents the pressure. These equations are derived from the Einstein field equations under the assumptions of a static, spherically symmetric metric and a perfect fluid interior.

The TOV equations alone do not fully determine the mass-radius relationship; they must be supplemented by an equation of state that relates pressure and energy density, $\rho \equiv \rho(p)$. The equation of state encapsulates the microphysical properties of the stellar material and is crucial for obtaining numerical solutions.

As previously discussed, numerous equations of state exist in the literature; however, we focus exclusively on the APR EoS [255] for the remainder of this thesis. To solve the TOV equations, we impose the initial conditions: central pressure $p(r = 0) = p_c$, and enclosed mass at the center $m(r = 0) = 0$. The star radius R is defined such that $p(r = R) = 0$. The total mass is then obtained by integrating Eqn. (B.3) from $r = 0$ to $r = R$.

A subtle issue arises when solving the system numerically: the TOV equation encounters a singularity at the center of the star ($r = 0$). To avoid this, we define the initial conditions at a small distance from the center, r_i, where $r_i \ll R$, with R being the neutron star radius, typically on the order of 10^6 cm. Additionally, we transform the dependent variable from p to ρ via the equation of state. By expressing $m(r)$ and $\rho(r)$ as power series and Taylor expanding around the singularity, we obtain the leading-order initial conditions

$$\rho_i = \rho_c - \beta_i^2, \tag{B.4}$$

$$m_i = \gamma r_i^3. \tag{B.5}$$

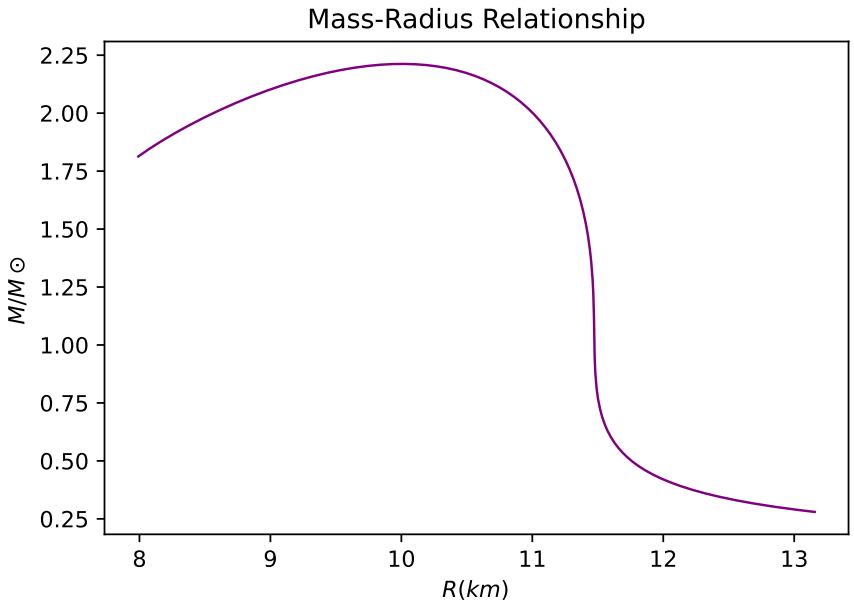

Figure B.1: The mass-radius relationship for neutron stars using the APR EoS and looping over central densities $4 \times 10^{14} - 2 \times 10^{16}$ g/cm^3.

We can then numerically solve the equations to obtain the mass-radius relationship, as shown in Fig. B.1.

C Conformal Scalar-Tensor Theories

This appendix provides a brief overview of scalar-tensor theories and conformal transformations, focusing specifically on the tools required to derive the modified Klein-Gordon equation and stellar structure equations in these theories. For a more in-depth treatment of scalar-tensor theories and their broader implications, readers are referred to [48, 88–90].

C.1 Conformal transformations

Scalar-tensor theories introduce one or more scalar fields that modifies gravitational interactions, often appearing in two mathematically equivalent but conceptually distinct frames: the *Einstein frame* and the *Jordan frame*. These frames are related by a conformal transformation of the metric

$$\tilde{g}_{\mu\nu} = A^2(\phi) g_{\mu\nu} \,, \tag{C.1}$$

where $\tilde{g}_{\mu\nu}$ is the transformed metric (Jordan frame metric), and $g_{\mu\nu}$ is the original metric (Einstein frame metric). This implies that the determinant of the transformed metric is

$$\sqrt{-\tilde{g}} = A^4(\phi)\sqrt{-g} \,. \tag{C.2}$$

This transformation not only links the two frames but also modifies how physical quantities, such as distances, masses, and energy densities, are interpreted in each frame. Specifically, conformal transformations preserve the causal structure of spacetime, ensuring that light cones remain invariant, but they

rescale quantities in a way that depends on the scalar field ϕ. To maintain clarity throughout this appendix, quantities defined in the Jordan frame will be denoted with a tilde to distinguish them from their Einstein frame counterparts. This transformation is equivalent to

$$\mathrm{d}\tilde{s}^2 = A^2(\phi)\mathrm{d}s^2\,, \tag{C.3}$$

indicating that lengths and time intervals are rescaled locally by $A(\phi)$. While this introduces a field-dependent modification, it preserves the angle between vectors, thereby maintaining the local causal structure of spacetime.

To understand the equivalence between frames, we start with the *Einstein frame* action, where the scalar field is minimally coupled to gravity but non-minimally coupled to matter through the coupling function $A(\phi)$. The action in the Einstein frame is given by

$$S_E = \int \mathrm{d}^4x\sqrt{-g}\left[\frac{M_{\mathrm{Pl}}^2 R}{2} - \frac{1}{2}\nabla_\mu\phi\nabla^\mu\phi - V(\phi)\right] + S_m[\tilde{g}_{\mu\nu};\Psi]. \tag{C.4}$$

where R is the Ricci scalar, ϕ is the scalar field, $V(\phi)$ is the scalar potential, and S_m describes the matter sector. In the Einstein frame, the scalar field is minimally coupled to gravity but non-minimally coupled to the matter field Ψ via the metric $\tilde{g}_{\mu\nu} = A^2(\phi)g_{\mu\nu}$. This coupling modifies the dynamics of test particles in the presence of a gravitational field. By applying a conformal transformation, we migrate to the *Jordan frame*, where the action takes the form

$$S_J = \int \mathrm{d}^4x\sqrt{-\tilde{g}}\left[\frac{M_{\mathrm{Pl}}^2\tilde{R}}{2A^2(\phi)} - \frac{1}{2}\tilde{\nabla}_\mu\phi\tilde{\nabla}^\mu\phi - A^{-4}(\phi)V(\phi)\right] + S_m[\tilde{g}_{\mu\nu};\Psi], \tag{C.5}$$

where $\tilde{\nabla}_\mu$ is the covariant derivative in the Jordan frame. In the Jordan frame, the scalar field is non-minimally coupled to the Ricci scalar $\tilde{R}$, while matter fields remain minimally coupled to the metric $\tilde{g}_{\mu\nu}$. A key distinction between the frames is that the motion of matter, governed by S_m, depends explicitly on the Jordan frame metric $\tilde{g}_{\mu\nu}$.

This dependence ensures that the energy-momentum tensor of matter is covariantly conserved in the Jordan frame:

$$\tilde{\nabla}_\mu \tilde{T}^{\mu\nu} = 0\,. \tag{C.6}$$

The conservation law implies that matter follows geodesics of the Jordan frame metric [336–339]. However, geodesic motion alone does not ensure the full WEP, which also requires that all test bodies fall identically regardless of their internal composition. Scalar-tensor theories can violate WEP if the scalar field couples differently to different matter species or generates composition-dependent forces [340].

It is important to clarify how the scalar field enters the dynamics in each frame. In the Jordan frame, the matter action S_m depends only on the metric $\tilde{g}_{\mu\nu}$ and does not contain ϕ explicitly. However, because $\tilde{g}_{\mu\nu} = A^2(\phi) g_{\mu\nu}$, the scalar field still influences matter indirectly through the metric. This contrasts with the Einstein frame, where the scalar field couples directly to matter via the conformal factor. Thus, even though ϕ is not an explicit argument in S_m in the Jordan frame, it still affects matter dynamics through its role in shaping the spacetime geometry.

Despite their differences, the Einstein and Jordan frames represent the same underlying physics. A conformal transformation reinterprets how the scalar field influences gravity and matter. In the Einstein frame, the scalar field modifies the effective gravitational constant and interacts with matter directly through $A(\phi)$. Conversely, in the Jordan frame, the scalar field alters the spacetime geometry and interacts with matter indirectly.

C.2 Transformation of The Energy-Momentum Tensor

In GR, the energy-momentum tensor for matter is defined as

$$T^{\mu\nu} = \frac{2}{\sqrt{-g}} \frac{\delta S_m}{\delta g_{\mu\nu}}\,. \tag{C.7}$$

This corresponds to the Einstein frame energy-momentum tensor in scalar-tensor theories. However, since S_m is coupled to $\tilde{g}_{\mu\nu}$ in the Jordan frame, the energy-momentum tensor becomes frame-dependent. Because the matter action S_m is defined using the Jordan frame metric $\tilde{g}_{\mu\nu}$, the energy-momentum tensor derived from it differs from the one defined in the Einstein frame using $g_{\mu\nu}$. These are two distinct energy-momentum tensors, $\tilde{T}^{\mu\nu}$ and $T^{\mu\nu}$, each corresponding to their respective frames. Although they encode the same physical content, their components differ due to the conformal rescaling of the metric. To relate them, we begin with the energy-momentum tensor in the Jordan frame

$$\tilde{T}^{\mu\nu} = \frac{2}{\sqrt{-\tilde{g}}} \frac{\delta S_m}{\delta \tilde{g}_{\mu\nu}} \,. \tag{C.8}$$

Using the conformal transformation in Eqn. (C.1), we expand

$$\tilde{T}^{\mu\nu} = \frac{2}{A^4(\phi)\sqrt{-g}} \frac{\delta S_m}{\delta g_{\mu\nu}} \frac{\delta g_{\mu\nu}}{\delta \tilde{g}_{\mu\nu}} \,, \tag{C.9}$$

and, since $\delta g_{\mu\nu}/\delta \tilde{g}_{\mu\nu} = 1/A^2(\phi)$, this simplifies to

$$\tilde{T}^{\mu\nu} = A^{-6}(\phi) T^{\mu\nu} \,. \tag{C.10}$$

Furthermore, the conservation of the energy-momentum tensor in the Einstein frame can be derived to be [275]

$$\nabla^\mu T^{\mu\nu} = \frac{A'(\phi)}{A(\phi)} T \nabla^\nu \phi \,, \tag{C.11}$$

where $T = g_{\mu\nu} T^{\mu\nu}$ is the trace of the energy-momentum tensor in the Einstein frame.

C.3 Modified Klein-Gordon Equation

To derive the modified KG equation in the Einstein frame, we vary the action in Eqn. (C.4) with respect to the scalar field ϕ. The variation of the action is

$$\delta S_E = \int \mathrm{d}^4x \sqrt{-g} \left[-\frac{1}{2} \delta(\nabla_\mu \phi \nabla^\mu \phi) - \delta(V(\phi)) \right] + \delta S_m \,. \tag{C.12}$$

We first address the variation of the kinetic term while writing $\nabla_\mu\phi\nabla^\mu\phi = g^{\mu\nu}\nabla_\mu\phi\nabla_\nu\phi$. This gives

$$\begin{aligned}\delta(g^{\mu\nu}\nabla_\mu\phi\nabla_\nu\phi) &= g^{\mu\nu}[\delta(\nabla_\mu\phi)\nabla_\nu\phi + \nabla_\mu\phi\delta(\nabla_\nu\phi)] \\ &= g^{\mu\nu}[\nabla_\mu\delta(\phi)\nabla_\nu\phi + \nabla_\mu\phi\nabla_\nu(\delta\phi)] \\ &= 2\nabla_\mu(\delta\phi)\nabla^\mu\phi \end{aligned} \tag{C.13}$$

Next, we apply integration by parts

$$\begin{aligned}\nabla_\mu(\delta\phi)\nabla^\mu\phi &= \nabla_\mu(\delta\phi\nabla^\mu\phi) - \delta\phi\nabla_\mu\nabla^\mu\phi \\ &= -\delta\phi\nabla_\mu\nabla^\mu\phi \end{aligned} \tag{C.14}$$

where the surface term $\nabla_\mu(\delta\phi\nabla^\mu\phi)$ vanishes under the requirement that the field approaches zero at spatial infinity. Thus, the variation of the kinetic term becomes

$$\delta(\nabla_\mu\phi\nabla^\mu\phi) = -2\delta\phi\nabla_\mu\nabla^\mu\phi\,. \tag{C.15}$$

The variation of the potential term is straightforward

$$\delta(V(\phi)) = \frac{\mathrm{d}V(\phi)}{\mathrm{d}\phi}\delta\phi\,. \tag{C.16}$$

Substituting Eqns. (C.15) and (C.16) into (C.12) yields

$$\delta S_E = \int \mathrm{d}^4x\sqrt{-g}\left[\nabla_\mu\nabla^\mu\phi - \frac{\mathrm{d}V(\phi)}{\mathrm{d}\phi}\right]\delta\phi + \delta S_m\,. \tag{C.17}$$

The uncoupled KG equation is evident in the variation above. Applying the principle of least action,

$$\frac{\delta S_E}{\delta\phi} = 0\,, \tag{C.18}$$

leads to the modified KG equation

$$\Box\phi - \frac{\mathrm{d}V(\phi)}{\mathrm{d}\phi} + \frac{1}{\sqrt{-g}}\frac{\delta S_m}{\delta\phi} \tag{C.19}$$

where $\Box = \nabla_\mu \nabla^\mu$ is the d'Alembertian operator. The term $\frac{\delta S_m}{\delta \phi}$ accounts for the coupling between the scalar field ϕ and matter. To evaluate this term, we vary the matter action as follows

$$\frac{\delta S_m}{\delta \phi} = \frac{\delta S_m}{\delta \tilde{g}_{\mu\nu}} \frac{\tilde{g}_{\mu\nu}}{\delta \phi} \,. \tag{C.20}$$

Using the definition of the energy-momentum tensor in the Jordan frame, Eqn. (C.8), and the conformal transformation in Eqn. (C.1), this becomes

$$\frac{\delta S_m}{\delta \phi} = \tilde{T}^{\mu\nu} \frac{\delta \tilde{g}_{\mu\nu}}{\delta \phi} \frac{\sqrt{-\tilde{g}}}{2} \,. \tag{C.21}$$

Transforming quantities from the Jordan frame to the Einstein frame and simplifying, we find

$$\begin{aligned} \frac{\delta S}{\delta \phi} = \tilde{T}^{\mu\nu} \frac{\delta \tilde{g}_{\mu\nu}}{\delta \phi} \frac{\sqrt{-\tilde{g}}}{2} &= \tilde{T}^{\mu\nu} g_{\mu\nu} \frac{\delta A^2(\phi)}{\delta \phi} \frac{A^4(\phi)\sqrt{-g}}{2} \\ &= A^{-6}(\phi) T^{\mu\nu} g_{\mu\nu} \frac{\delta A^2(\phi)}{\delta \phi} \frac{A^4(\phi)\sqrt{-g}}{2} \\ &= A^{-2}(\phi) T^{\mu\nu} g_{\mu\nu} A^2(\phi) \frac{\delta \ln A(\phi)}{\delta \phi} \sqrt{-g} \\ &= T \frac{\delta \ln A(\phi)}{\delta \phi} \sqrt{-g} \end{aligned} \tag{C.22}$$

Substituting this into Eqn. (C.19), we obtain the modified KG equation

$$\Box \phi - \frac{\mathrm{d}V(\phi)}{\mathrm{d}\phi} + T \frac{\mathrm{d} \ln A(\phi)}{\mathrm{d}\phi} = 0 \,, \tag{C.23}$$

where we see that the dynamics of the scalar field are governed by an effective potential

$$V_{eff}(\phi) = V(\phi) - T \ln A(\phi) \,. \tag{C.24}$$

If the matter action includes multiple matter fields j with different coupling functions, $S_m[\tilde{g}^{(j)}_{\mu\nu}; \Psi_j]$, where $\tilde{g}^{(j)}_{\mu\nu} = A_j^2(\phi) g_{\mu\nu}$ are the Jordan frame metrics, the modified KG equation generalizes to

$$\Box \phi - \frac{\mathrm{d}V(\phi)}{\mathrm{d}\phi} + \sum_j T_j \frac{\mathrm{d} \ln A_j(\phi)}{\mathrm{d}\phi} = 0 \,. \tag{C.25}$$

and the effective potential becomes

$$V_{eff}(\phi) = V(\phi) - \sum_j T_j \ln A_j(\phi)\,. \tag{C.26}$$

C.4 Yukawa–Coupling equivalence in the EFT limit

Starting from Chapter 6 onwards, we parameterize the ALP interaction with nucleons by a Yukawa term $-\phi g_s^N \bar{\Psi}\Psi$[1]. The purpose of this subsection is to explicitly show that this form *follows directly* from the scalar–tensor framework reviewed above: specifically, that the Einstein-frame matter action with the conformal coupling function

$$A(\phi) = e^{\phi/\mu}, \tag{C.27}$$

the same form adopted in the main text, reduces precisely to the Yukawa interaction when the scalar field excursion satisfies $\phi \ll \mu$, which is the regime of validity for the EFT we study. This establishes the equivalence between the conformal scalar–tensor theory and the Yukawa coupling at the level of the matter action, ensuring that the thesis remains fully self-contained. Here, μ is related to the scalar–nucleon coupling g_s^N by

$$\mu = \frac{m_N}{g_s^N}, \tag{C.28}$$

where m_N is the nucleon mass and g_s^N is a dimensionless coupling constant (assumed equal for protons and neutrons). Although a Yukawa interaction is historically rooted in particle physics, in this context it arises naturally from

[1]Throughout this appendix, we denote the general scalar field by ϕ, while in the main text the axion-like particle is denoted by a. This difference is purely notational and does not affect the arguments, derivations, or conclusions.

the structure of the conformal scalar–tensor theory.[2] Since the EFT is valid only for field excursions much smaller than the cutoff, we expand

$$A(\phi) = 1 + \frac{\phi}{\mu} + \mathcal{O}\big((\phi/\mu)^2\big). \tag{C.29}$$

Keeping only the leading order, the matter part of the Einstein-frame action (C.4) becomes

$$\begin{aligned} S_m &= \int \mathrm{d}^4x\sqrt{-g}\, m_N A(\phi)\bar{\Psi}\Psi \\ &= \int \mathrm{d}^4x\sqrt{-g}\, \big[m_N\bar{\Psi}\Psi + g_s^N\phi\bar{\Psi}\Psi\big], \end{aligned} \tag{C.30}$$

which is exactly the Yukawa interaction

$$\mathcal{L}_{\text{int}} = -g_s^N\phi\bar{\Psi}\Psi \tag{C.31}$$

added to the usual Dirac mass term, $m_N\bar{\Psi}\Psi$. To connect this result with the form appearing in the modified KG equation (C.23), we note that for a free Dirac fermion, the on-shell trace of the energy–momentum tensor is

$$T = -m_N\bar{\Psi}\Psi, \tag{C.32}$$

hence

$$\bar{\Psi}\Psi = -\frac{T}{m_N}. \tag{C.33}$$

Substituting this relation into Eqn. (C.30), the interaction term can be rewritten as

$$\mathcal{L}_{\text{int}} = \frac{\phi}{\mu}T, \tag{C.34}$$

demonstrating that the $T\,\mathrm{d}\ln A/\mathrm{d}\phi$ coupling appearing in the modified KG equation is nothing more than the familiar Yukawa coupling in disguise. In particular, although the scalar–tensor theory induces a coupling $\sim \phi T/\mu$, and the Yukawa coupling is $\sim \phi g_s^N\bar{\Psi}\Psi$, these match perfectly because $g_s^N = m_N/\mu$. Thus, the "$1/\mu$" factor arising in the scalar–tensor formulation precisely

[2] Specifically, it follows from expanding the conformal factor $A(\phi)$ in the EFT regime.

reproduces the particle-physics Yukawa structure after accounting for the relation between $\bar{\Psi}\Psi$ and T.

The generalization to multiple fermion species where the couplings are not equal is immediate: for each species j, one introduces couplings $g_s^{(j)}$ and corresponding scales $\mu_j = m_j/g_s^{(j)}$, obtaining

$$\mathcal{L}_{\text{int}} = -\sum_j g_s^{(j)} \phi \bar{\Psi}_j \Psi_j, \tag{C.35}$$

or equivalently

$$\mathcal{L}_{\text{int}} = \phi \sum_j \frac{T_j}{\mu_j}, \tag{C.36}$$

matching the structure used throughout the thesis.

Bibliography

[1] J. Lesgourgues. "The Cosmic Linear Anisotropy Solving System (CLASS) I: Overview". In: (Apr. 2011). arXiv:1104.2932.

[2] D. Blas, J. Lesgourgues, and T. Tram. "The Cosmic Linear Anisotropy Solving System (CLASS) II: Approximation schemes". In: *JCAP* 07 (2011), p. 034. DOI: 10.1088/1475-7516/2011/07/034. arXiv: 1104.2933 [astro-ph.CO].

[3] C. A. J. O'Hare and E. Vitagliano. "Cornering the axion with CP-violating interactions". In: *Phys. Rev. D* 102.11 (2020), p. 115026. DOI: 10.1103/PhysRevD.102.115026. arXiv: 2010.03889 [hep-ph].

[4] A. Einstein. "The foundation of the general theory of relativity." In: *Annalen Phys.* 49.7 (1916). Ed. by J.-P. Hsu and D. Fine, pp. 769–822. DOI: 10.1002/andp.19163540702.

[5] F. W. Dyson, A. S. Eddington, and C. Davidson. "A Determination of the Deflection of Light by the Sun's Gravitational Field, from Observations Made at the Total Eclipse of May 29, 1919". In: *Phil. Trans. Roy. Soc. Lond. A* 220 (1920), pp. 291–333. DOI: 10.1098/rsta.1920.0009.

[6] A. Friedmann. "Über die Krümmung des Raumes". In: *Zeitschrift fur Physik* 10 (Jan. 1922), pp. 377–386. DOI: 10.1007/BF01332580.

[7] A. Friedmann. "Über die Möglichkeit einer Welt mit konstanter negativer Krümmung des Raumes". In: *Zeitschrift fur Physik* 21.1 (Dec. 1924), pp. 326–332. DOI: 10.1007/BF01328280.

[8] M. Asgari et al. "KiDS-1000 Cosmology: Cosmic shear constraints and comparison between two point statistics". In: *Astron. Astrophys.* 645 (2021), A104. DOI: 10.1051/0004-6361/202039070. arXiv: 2007.15633 [astro-ph.CO].

[9] N. Aghanim et al. "Planck 2018 results. VIII. Gravitational lensing". In: *Astron. Astrophys.* 641 (2020), A8. DOI: 10.1051/0004-6361/201833886. arXiv: 1807.06210 [astro-ph.CO].

[10] N. Aghanim et al. "Planck 2018 results. VI. Cosmological parameters". In: *Astron. Astrophys.* 641 (2020). [Erratum: Astron.Astrophys. 652, C4 (2021)], A6. DOI: 10.1051/0004-6361/201833910. arXiv: 1807.06209 [astro-ph.CO].

[11] S. Perlmutter et al. "Measurements of Ω and Λ from 42 High Redshift Supernovae". In: *Astrophys. J.* 517 (1999), pp. 565–586. DOI: 10.1086/307221. arXiv: astro-ph/9812133.

[12] A. G. Riess et al. "Observational evidence from supernovae for an accelerating universe and a cosmological constant". In: *Astron. J.* 116 (1998), pp. 1009–1038. DOI: 10.1086/300499. arXiv: astro-ph/9805201.

[13] S. Alam et al. "Completed SDSS-IV extended Baryon Oscillation Spectroscopic Survey: Cosmological implications from two decades of spectroscopic surveys at the Apache Point Observatory". In: *Phys. Rev. D* 103.8 (2021), p. 083533. DOI: 10.1103/PhysRevD.103.083533. arXiv: 2007.08991 [astro-ph.CO].

[14] H. du Mas des Bourboux et al. "The Completed SDSS-IV Extended Baryon Oscillation Spectroscopic Survey: Baryon Acoustic Oscillations with Lyα Forests". In: *Astrophys. J.* 901.2 (2020), p. 153. DOI: 10.3847/1538-4357/abb085. arXiv: 2007.08995 [astro-ph.CO].

[15] V. C. Rubin, N. Thonnard, and W. K. Ford Jr. "Rotational properties of 21 SC galaxies with a large range of luminosities and radii, from NGC 4605 /R = 4kpc/ to UGC 2885 /R = 122 kpc/". In: *Astrophys. J.* 238 (1980), p. 471. DOI: 10.1086/158003.

[16] D. Clowe et al. "A direct empirical proof of the existence of dark matter". In: *Astrophys. J. Lett.* 648 (2006), pp. L109–L113. DOI: 10.1086/508162. arXiv: astro-ph/0608407.

[17] M. Davis et al. "The Evolution of Large Scale Structure in a Universe Dominated by Cold Dark Matter". In: *Astrophys. J.* 292 (1985). Ed. by M. A. Srednicki, pp. 371–394. DOI: 10.1086/163168.

[18] S. D. M. White. "Formation and evolution of galaxies: Lectures given at Les Houches, August 1993". In: *Les Houches Summer School on Cosmology and Large Scale Structure (Session 60)*. Aug. 1994, pp. 349–430. arXiv: astro-ph/9410043.

[19] J. R. Bond, G. Efstathiou, and J. Silk. "Massive Neutrinos and the Large Scale Structure of the Universe". In: *Phys. Rev. Lett.* 45 (1980). Ed. by M. A. Srednicki, pp. 1980–1984. DOI: 10.1103/PhysRevLett.45.1980.

[20] R. E. Angulo and O. Hahn. "Large-scale dark matter simulations". In: (Dec. 2021). DOI: 10.1007/s41115-021-00013-z. arXiv: 2112.05165 [astro-ph.CO].

[21] V. Springel et al. "Simulating the joint evolution of quasars, galaxies and their large-scale distribution". In: *Nature* 435 (2005), pp. 629–636. DOI: 10.1038/nature03597. arXiv: astro-ph/0504097.

[22] G. R. Blumenthal et al. "Formation of Galaxies and Large Scale Structure with Cold Dark Matter". In: *Nature* 311 (1984). Ed. by M. A. Srednicki, pp. 517–525. DOI: 10.1038/311517a0.

[23] A. Joyce et al. "Beyond the Cosmological Standard Model". In: *Phys. Rept.* 568 (2015), pp. 1–98. DOI: 10.1016/j.physrep.2014.12.002. arXiv: 1407.0059 [astro-ph.CO].

[24] P. Bull et al. "Beyond ΛCDM: Problems, solutions, and the road ahead". In: *Phys. Dark Univ.* 12 (2016), pp. 56–99. DOI: 10.1016/j.dark.2016.02.001. arXiv: 1512.05356 [astro-ph.CO].

[25] B. P. Abbott et al. "GW170817: Observation of Gravitational Waves from a Binary Neutron Star Inspiral". In: *Phys. Rev. Lett.* 119.16 (2017), p. 161101. DOI: 10.1103/PhysRevLett.119.161101. arXiv: 1710.05832 [gr-qc].

[26] F. Beutler et al. "The 6dF Galaxy Survey: Baryon Acoustic Oscillations and the Local Hubble Constant". In: *Mon. Not. Roy. Astron. Soc.* 416 (2011), pp. 3017–3032. DOI: 10.1111/j.1365-2966.2011.19250.x. arXiv: 1106.3366 [astro-ph.CO].

[27] A. J. Ross et al. "The clustering of the SDSS DR7 main Galaxy sample – I. A 4 per cent distance measure at $z = 0.15$". In: *Mon. Not. Roy. Astron. Soc.* 449.1 (2015), pp. 835–847. DOI: 10.1093/mnras/stv154. arXiv: 1409.3242 [astro-ph.CO].

[28] S. Alam et al. "The clustering of galaxies in the completed SDSS-III Baryon Oscillation Spectroscopic Survey: cosmological analysis of the DR12 galaxy sample". In: *Mon. Not. Roy. Astron. Soc.* 470.3 (2017), pp. 2617–2652. DOI: 10.1093/mnras/stx721. arXiv: 1607.03155 [astro-ph.CO].

[29] A. G. Riess et al. "Cosmic Distances Calibrated to 1% Precision with Gaia EDR3 Parallaxes and Hubble Space Telescope Photometry of 75 Milky Way Cepheids Confirm Tension with ΛCDM". In: *Astrophys. J. Lett.* 908.1 (2021), p. L6. DOI: 10.3847/2041-8213/abdbaf. arXiv: 2012.08534 [astro-ph.CO].

[30] A. G. Riess et al. "A Comprehensive Measurement of the Local Value of the Hubble Constant with 1 km/s/Mpc Uncertainty from the Hubble Space Telescope and the SH0ES Team". In: *Astrophys. J. Lett.* 934.1 (2022), p. L7. DOI: 10.3847/2041-8213/ac5c5b. arXiv: 2112.04510 [astro-ph.CO].

[31] K. C. Wong et al. "H0LiCOW – XIII. A 2.4 per cent measurement of H0 from lensed quasars: 5.3σ tension between early- and late-Universe probes". In: *Mon. Not. Roy. Astron. Soc.* 498.1 (2020), pp. 1420–1439. DOI: 10.1093/mnras/stz3094. arXiv: 1907.04869 [astro-ph.CO].

[32] T. M. C. Abbott et al. "Dark Energy Survey Year 3 results: Cosmological constraints from galaxy clustering and weak lensing". In: *Phys. Rev. D* 105.2 (2022), p. 023520. DOI: 10.1103/PhysRevD.105.023520. arXiv: 2105.13549 [astro-ph.CO].

[33] D. Rubin et al. "Union Through UNITY: Cosmology with 2,000 SNe Using a Unified Bayesian Framework". In: (Nov. 2023). arXiv: 2311.12098 [astro-ph.CO].

[34] T. M. C. Abbott et al. "The Dark Energy Survey: Cosmology Results With ˜1500 New High-redshift Type Ia Supernovae Using The Full 5-year Dataset". In: (Jan. 2024). arXiv: 2401.02929 [astro-ph.CO].

[35] A. G. Adame et al. "DESI 2024 VI: Cosmological Constraints from the Measurements of Baryon Acoustic Oscillations". In: (Apr. 2024). arXiv: 2404.03002 [astro-ph.CO].

[36] E. J. Copeland, A. R. Liddle, and D. Wands. "Exponential potentials and cosmological scaling solutions". In: *Phys. Rev. D* 57 (1998), pp. 4686–4690. DOI: 10.1103/PhysRevD.57.4686. arXiv: gr-qc/9711068.

[37] E. J. Copeland, M. Sami, and S. Tsujikawa. "Dynamics of dark energy". In: *Int. J. Mod. Phys. D* 15 (2006), pp. 1753–1936. DOI: 10.1142/S021827180600942X. arXiv: hep-th/0603057.

[38] R. R. Caldwell and M. Kamionkowski. "The Physics of Cosmic Acceleration". In: *Ann. Rev. Nucl. Part. Sci.* 59 (2009), pp. 397–429. DOI: 10.1146/annurev-nucl-010709-151330. arXiv: 0903.0866 [astro-ph.CO].

[39] K. Bamba et al. "Dark energy cosmology: the equivalent description via different theoretical models and cosmography tests". In: *Astrophys. Space Sci.* 342 (2012), pp. 155–228. DOI: 10.1007/s10509-012-1181-8. arXiv: 1205.3421 [gr-qc].

[40] S. Tsujikawa. "Quintessence: A Review". In: *Class. Quant. Grav.* 30 (2013), p. 214003. DOI: 10.1088/0264-9381/30/21/214003. arXiv: 1304.1961 [gr-qc].

[41] W. Hu, R. Barkana, and A. Gruzinov. "Cold and fuzzy dark matter". In: *Phys. Rev. Lett.* 85 (2000), pp. 1158–1161. DOI: 10.1103/PhysRevLett.85.1158. arXiv: astro-ph/0003365.

[42] R. Liu, W. Hu, and H. Xiao. "Warm and Fuzzy Dark Matter: Free Streaming of Wave Dark Matter". In: (June 2024). arXiv: 2406.12970 [hep-ph].

[43] D. J. E. Marsh. "Axion Cosmology". In: *Phys. Rept.* 643 (2016), pp. 1–79. DOI: 10.1016/j.physrep.2016.06.005. arXiv: 1510.07633 [astro-ph.CO].

[44] F. Chadha-Day, J. Ellis, and D. J. E. Marsh. "Axion dark matter: What is it and why now?" In: *Sci. Adv.* 8.8 (2022), abj3618. DOI: 10.1126/sciadv.abj3618. arXiv: 2105.01406 [hep-ph].

[45] G. Jungman, M. Kamionkowski, and K. Griest. "Supersymmetric dark matter". In: *Phys. Rept.* 267 (1996), pp. 195–373. DOI: 10.1016/0370-1573(95)00058-5. arXiv: hep-ph/9506380.

[46] S. Nojiri and S. D. Odintsov. "Modified gravity with negative and positive powers of the curvature: Unification of the inflation and of the cosmic acceleration". In: *Phys. Rev. D* 68 (2003), p. 123512. DOI: 10.1103/PhysRevD.68.123512. arXiv: hep-th/0307288.

[47] S. Nojiri and S. D. Odintsov. "Introduction to modified gravity and gravitational alternative for dark energy". In: *eConf* C0602061 (2006). Ed. by A. Borowiec, p. 06. DOI: 10.1142/S0219887807001928. arXiv: hep-th/0601213.

[48] T. Clifton et al. "Modified Gravity and Cosmology". In: *Phys. Rept.* 513 (2012), pp. 1–189. DOI: 10.1016/j.physrep.2012.01.001. arXiv: 1106.2476 [astro-ph.CO].

[49] S. Nojiri, S. D. Odintsov, and V. K. Oikonomou. "Modified Gravity Theories on a Nutshell: Inflation, Bounce and Late-time Evolution". In: *Phys. Rept.* 692 (2017), pp. 1–104. DOI: 10.1016/j.physrep.2017.06.001. arXiv: 1705.11098 [gr-qc].

[50] O. F. Ramadan, T. Karwal, and J. Sakstein. "Attractive proposal for resolving the Hubble tension: Dynamical attractors that unify early and late dark energy". In: *Phys. Rev. D* 109.6 (2024), p. 063525. DOI: 10.1103/PhysRevD.109.063525. arXiv: 2309.08082 [astro-ph.CO].

[51] O. F. Ramadan, J. Sakstein, and D. Rubin. "DESI constraints on exponential quintessence". In: *Phys. Rev. D* 110.4 (2024), p. L041303. DOI: 10.1103/PhysRevD.110.L041303. arXiv: 2405.18747 [astro-ph.CO].

[52] J. J. Heckman, O. F. Ramadan, and J. Sakstein. "First constraints on a pixelated universe in light of DESI observations". In: *Phys. Rev. D* 111.2 (2025), p. 023510. DOI: 10.1103/PhysRevD.111.023510. arXiv: 2406.04408 [astro-ph.CO].

[53] S. Panda, Y. Sumitomo, and S. P. Trivedi. "Axions as Quintessence in String Theory". In: *Phys. Rev. D* 83 (2011), p. 083506. DOI: 10.1103/PhysRevD.83.083506. arXiv: 1011.5877 [hep-th].

[54] O. F. Ramadan, J. Sakstein, and D. Croon. "Cosmology and Astrophysics of CP-Violating Axions". In: (Aug. 2024). arXiv: 2408.02294 [hep-ph].

[55] D. Brout et al. "The Pantheon+ Analysis: Cosmological Constraints". In: *Astrophys. J.* 938.2 (2022), p. 110. DOI: 10.3847/1538-4357/ac8e04. arXiv: 2202.04077 [astro-ph.CO].

[56] F. Zwicky. "Die Rotverschiebung von extragalaktischen Nebeln". In: *Helv. Phys. Acta* 6 (1933), pp. 110–127. DOI: 10.1007/s10714-008-0707-4.

[57] F. Zwicky. "On the Masses of Nebulae and of Clusters of Nebulae". In: *Astrophys. J.* 86 (1937), pp. 217–246. DOI: 10.1086/143864.

[58] V. C. Rubin, W. K. Ford Jr., and N. Thonnard. "Extended rotation curves of high-luminosity spiral galaxies. IV. Systematic dynamical properties, Sa through Sc". In: *Astrophys. J. Lett.* 225 (1978), pp. L107–L111. DOI: 10.1086/182804.

[59] D. M. Scolnic et al. "The Complete Light-curve Sample of Spectroscopically Confirmed SNe Ia from Pan-STARRS1 and Cosmological Constraints from the Combined Pantheon Sample". In: *Astrophys. J.* 859.2 (2018), p. 101. DOI: 10.3847/1538-4357/aab9bb. arXiv: 1710.00845 [astro-ph.CO].

[60] E. Aprile et al. "Dark Matter Search Results from a One Ton-Year Exposure of XENON1T". In: *Phys. Rev. Lett.* 121.11 (2018), p. 111302. DOI: 10.1103/PhysRevLett.121.111302. arXiv: 1805.12562 [astro-ph.CO].

[61] D. S. Akerib et al. "Projected WIMP sensitivity of the LUX-ZEPLIN dark matter experiment". In: *Phys. Rev. D* 101.5 (2020), p. 052002. DOI: 10.1103/PhysRevD.101.052002. arXiv: 1802.06039 [astro-ph.IM].

[62] R. D. Peccei and H. R. Quinn. "CP Conservation in the Presence of Instantons". In: *Phys. Rev. Lett.* 38 (1977), pp. 1440–1443. DOI: 10.1103/PhysRevLett.38.1440.

[63] R. D. Peccei and H. R. Quinn. "Constraints Imposed by CP Conservation in the Presence of Instantons". In: *Phys. Rev. D* 16 (1977), pp. 1791–1797. DOI: 10.1103/PhysRevD.16.1791.

[64] N. Du et al. "A Search for Invisible Axion Dark Matter with the Axion Dark Matter Experiment". In: *Phys. Rev. Lett.* 120.15 (2018), p. 151301. DOI: 10.1103/PhysRevLett.120.151301. arXiv: 1804.05750 [hep-ex].

[65] V. Anastassopoulos et al. "New CAST Limit on the Axion-Photon Interaction". In: *Nature Phys.* 13 (2017), pp. 584–590. DOI: 10.1038/nphys4109. arXiv: 1705.02290 [hep-ex].

[66] A. Boyarsky et al. "Sterile neutrino Dark Matter". In: *Prog. Part. Nucl. Phys.* 104 (2019), pp. 1–45. DOI: 10.1016/j.ppnp.2018.07.004. arXiv: 1807.07938 [hep-ph].

[67] M. Milgrom. "A Modification of the Newtonian dynamics as a possible alternative to the hidden mass hypothesis". In: *Astrophys. J.* 270 (1983), pp. 365–370. DOI: 10.1086/161130.

[68] B. Famaey and S. McGaugh. "Modified Newtonian Dynamics (MOND): Observational Phenomenology and Relativistic Extensions". In: *Living Rev. Rel.* 15 (2012), p. 10. DOI: 10.12942/lrr-2012-10. arXiv: 1112.3960 [astro-ph.CO].

[69] C. Skordis and T. Zlosnik. "New Relativistic Theory for Modified Newtonian Dynamics". In: *Phys. Rev. Lett.* 127.16 (2021), p. 161302. DOI: 10.1103/PhysRevLett.127.161302. arXiv: 2007.00082 [astro-ph.CO].

[70] J. D. Bekenstein. "Relativistic gravitation theory for the MOND paradigm". In: *Phys. Rev. D* 70 (2004). [Erratum: Phys.Rev.D 71, 069901 (2005)], p. 083509. DOI: 10.1103/PhysRevD.70.083509. arXiv: astro-ph/0403694.

[71] S. Weinberg. "The Cosmological Constant Problem". In: *Rev. Mod. Phys.* 61 (1989). Ed. by J.-P. Hsu and D. Fine, pp. 1–23. DOI: 10.1103/RevModPhys.61.1.

[72] P. J. E. Peebles and B. Ratra. "The Cosmological Constant and Dark Energy". In: *Rev. Mod. Phys.* 75 (2003). Ed. by J.-P. Hsu and D. Fine, pp. 559–606. DOI: 10.1103/RevModPhys.75.559. arXiv: astro-ph/0207347.

[73] T. Padmanabhan. "Cosmological constant: The Weight of the vacuum". In: *Phys. Rept.* 380 (2003), pp. 235–320. DOI: 10.1016/S0370-1573(03)00120-0. arXiv: hep-th/0212290.

[74] H. E. S. Velten, R. F. vom Marttens, and W. Zimdahl. "Aspects of the cosmological "coincidence problem"". In: *Eur. Phys. J. C* 74.11 (2014), p. 3160. DOI: 10.1140/epjc/s10052-014-3160-4. arXiv: 1410.2509 [astro-ph.CO].

[75] N. Dalal et al. "Testing the cosmic coincidence problem and the nature of dark energy". In: *Phys. Rev. Lett.* 87 (2001), p. 141302. DOI: 10.1103/PhysRevLett.87.141302. arXiv: astro-ph/0105317.

[76] N. Sivanandam. "Is the Cosmological Coincidence a Problem?" In: *Phys. Rev. D* 87.8 (2013), p. 083514. DOI: 10.1103/PhysRevD.87.083514. arXiv: 1203.4197 [astro-ph.CO].

[77] C. Armendariz-Picon, V. F. Mukhanov, and P. J. Steinhardt. "A Dynamical solution to the problem of a small cosmological constant and late time cosmic acceleration". In: *Phys. Rev. Lett.* 85 (2000), pp. 4438–4441. DOI: 10.1103/PhysRevLett.85.4438. arXiv: astro-ph/0004134.

[78] T. Chiba. "Tracking K-essence". In: *Phys. Rev. D* 66 (2002), p. 063514. DOI: 10.1103/PhysRevD.66.063514. arXiv: astro-ph/0206298.

[79] R. J. Scherrer. "Purely kinetic k-essence as unified dark matter". In: *Phys. Rev. Lett.* 93 (2004), p. 011301. DOI: 10.1103/PhysRevLett.93.011301. arXiv: astro-ph/0402316.

[80] J. Khoury and A. Weltman. "Chameleon cosmology". In: *Phys. Rev. D* 69 (2004), p. 044026. DOI: 10.1103/PhysRevD.69.044026. arXiv: astro-ph/0309411.

[81] J. Khoury and A. Weltman. "Chameleon fields: Awaiting surprises for tests of gravity in space". In: *Phys. Rev. Lett.* 93 (2004), p. 171104. DOI: 10.1103/PhysRevLett.93.171104. arXiv: astro-ph/0309300.

[82] L. Amendola. "Coupled quintessence". In: *Phys. Rev. D* 62 (2000), p. 043511. DOI: 10.1103/PhysRevD.62.043511. arXiv: astro-ph/9908023.

[83] J. Valiviita, E. Majerotto, and R. Maartens. "Instability in interacting dark energy and dark matter fluids". In: *JCAP* 07 (2008), p. 020. DOI: 10.1088/1475-7516/2008/07/020. arXiv: 0804.0232 [astro-ph].

[84] A. Mukherjee. "Spherical collapse in DGP braneworld cosmology". In: (Aug. 2020). arXiv: 2008.08979 [astro-ph.CO].

[85] M. Li. "A Model of holographic dark energy". In: *Phys. Lett. B* 603 (2004), p. 1. DOI: 10.1016/j.physletb.2004.10.014. arXiv: hep-th/0403127.

[86] A. H. Guth. "The Inflationary Universe: A Possible Solution to the Horizon and Flatness Problems". In: *Phys. Rev. D* 23 (1981). Ed. by L.-Z. Fang and R. Ruffini, pp. 347–356. DOI: 10.1103/PhysRevD.23.347.

[87] A. D. Linde. "A New Inflationary Universe Scenario: A Possible Solution of the Horizon, Flatness, Homogeneity, Isotropy and Primordial Monopole Problems". In: *Phys. Lett. B* 108 (1982). Ed. by L.-Z. Fang and R. Ruffini, pp. 389–393. DOI: 10.1016/0370-2693(82)91219-9.

[88] C. Brans and R. H. Dicke. "Mach's principle and a relativistic theory of gravitation". In: *Phys. Rev.* 124 (1961). Ed. by J.-P. Hsu and D. Fine, pp. 925–935. DOI: 10.1103/PhysRev.124.925.

[89] T. Damour and G. Esposito-Farese. "Tensor-scalar gravity and binary pulsar experiments". In: *Phys. Rev. D* 54 (1996), pp. 1474–1491. DOI: 10.1103/PhysRevD.54.1474.

[90] C. M. Will. "The Confrontation between General Relativity and Experiment". In: *Living Rev. Rel.* 17 (2014), p. 4. DOI: 10.12942/lrr-2014-4. arXiv: 1403.7377 [gr-qc].

[91] M. S. Turner. "Coherent Scalar Field Oscillations in an Expanding Universe". In: *Phys. Rev. D* 28 (1983), p. 1243. DOI: 10.1103/PhysRevD.28.1243.

[92] L. Hui et al. "Ultralight scalars as cosmological dark matter". In: *Phys. Rev. D* 95.4 (2017), p. 043541. DOI: 10.1103/PhysRevD.95.043541. arXiv: 1610.08297 [astro-ph.CO].

[93] A. R. Khalife et al. "Review of Hubble tension solutions with new SH0ES and SPT-3G data". In: *JCAP* 04 (2024), p. 059. DOI: 10.1088/1475-7516/2024/04/059. arXiv: 2312.09814 [astro-ph.CO].

[94] E. Di Valentino et al. "In the realm of the Hubble tension—a review of solutions". In: *Class. Quant. Grav.* 38.15 (2021), p. 153001. DOI: 10.1088/1361-6382/ac086d. arXiv: 2103.01183 [astro-ph.CO].

[95] E. Abdalla et al. "Cosmology intertwined: A review of the particle physics, astrophysics, and cosmology associated with the cosmological tensions and anomalies". In: *JHEAp* 34 (2022), pp. 49–211. DOI: 10.1016/j.jheap.2022.04.002. arXiv: 2203.06142 [astro-ph.CO].

[96] O. H. E. Philcox et al. "Combining Full-Shape and BAO Analyses of Galaxy Power Spectra: A 1.6\% CMB-independent constraint on H_0". In: *JCAP* 05 (2020), p. 032. DOI: 10.1088/1475-7516/2020/05/032. arXiv: 2002.04035 [astro-ph.CO].

[97] N. Schöneberg, J. Lesgourgues, and D. C. Hooper. "The BAO+BBN take on the Hubble tension". In: *JCAP* 10 (2019), p. 029. DOI: 10.1088/1475-7516/2019/10/029. arXiv: 1907.11594 [astro-ph.CO].

[98] G. D'Amico et al. "The Cosmological Analysis of the SDSS/BOSS data from the Effective Field Theory of Large-Scale Structure". In: *JCAP* 05 (2020), p. 005. DOI: 10.1088/1475-7516/2020/05/005. arXiv: 1909.05271 [astro-ph.CO].

[99] W. Yuan et al. "Consistent Calibration of the Tip of the Red Giant Branch in the Large Magellanic Cloud on the Hubble Space Telescope Photometric System and a Re-determination of the Hubble Constant". In: *Astrophys. J.* 886 (2019), p. 61. DOI: 10.3847/1538-4357/ab4bc9. arXiv: 1908.00993 [astro-ph.GA].

[100] J. Soltis, S. Casertano, and A. G. Riess. "The Parallax of ω Centauri Measured from Gaia EDR3 and a Direct, Geometric Calibration of the Tip of the Red Giant Branch and the Hubble Constant". In: *Astrophys. J. Lett.* 908.1 (2021), p. L5. DOI: 10.3847/2041-8213/abdbad. arXiv: 2012.09196 [astro-ph.GA].

[101] G. S. Anand et al. "Comparing Tip of the Red Giant Branch Distance Scales: An Independent Reduction of the Carnegie-Chicago Hubble Program and the Value of the Hubble Constant". In: *Astrophys. J.* 932.1 (2022), p. 15. DOI: 10.3847/1538-4357/ac68df. arXiv: 2108.00007 [astro-ph.CO].

[102] R. I. Anderson, N. W. Koblischke, and L. Eyer. "Small-amplitude Red Giants Elucidate the Nature of the Tip of the Red Giant Branch as a Standard Candle". In: *Astrophys. J. Lett.* 963.2 (2024), p. L43. DOI: 10.3847/2041-8213/ad284d. arXiv: 2303.04790 [astro-ph.CO].

[103] A. J. Shajib et al. "TDCOSMO. XII. Improved Hubble constant measurement from lensing time delays using spatially resolved stellar kinematics of the lens galaxy". In: *Astron. Astrophys.* 673 (2023), A9. DOI: 10.1051/0004-6361/202345878. arXiv: 2301.02656 [astro-ph.CO].

[104] W. D. Kenworthy et al. "Measurements of the Hubble Constant with a Two-rung Distance Ladder: Two Out of Three Ain't Bad". In: *Astrophys. J.* 935.2 (2022), p. 83. DOI: 10.3847/1538-4357/ac80bd. arXiv: 2204.10866 [astro-ph.CO].

[105] M. Rigault et al. "Confirmation of a Star Formation Bias in Type Ia Supernova Distances and its Effect on Measurement of the Hubble Constant". In: *Astrophys. J.* 802.1 (2015), p. 20. DOI: 10.1088/0004-637X/802/1/20. arXiv: 1412.6501 [astro-ph.CO].

[106] M. Rigault et al. "Strong Dependence of Type Ia Supernova Standardization on the Local Specific Star Formation Rate". In: *Astron. Astrophys.* 644 (2020), A176. DOI: 10.1051/0004-6361/201730404. arXiv: 1806.03849 [astro-ph.CO].

[107] R. Wojtak and J. Hjorth. "Consistent extinction model for type Ia supernovae in Cepheid-based calibration galaxies and its impact on H0". In: *Mon. Not. Roy. Astron. Soc.* 533.2 (2024), pp. 2319–2334. DOI: 10.1093/mnras/stae1977. arXiv: 2403.10388 [astro-ph.CO].

[108] V. Poulin, T. L. Smith, and T. Karwal. "The Ups and Downs of Early Dark Energy solutions to the Hubble tension: A review of models, hints and constraints circa 2023". In: *Phys. Dark Univ.* 42 (2023), p. 101348. DOI: 10.1016/j.dark.2023.101348. arXiv: 2302.09032 [astro-ph.CO].

[109] T. Karwal and M. Kamionkowski. "Dark energy at early times, the Hubble parameter, and the string axiverse". In: *Phys. Rev. D* 94.10 (2016), p. 103523. DOI: 10.1103/PhysRevD.94.103523. arXiv: 1608.01309 [astro-ph.CO].

[110] V. Poulin et al. "Cosmological implications of ultralight axionlike fields". In: *Phys. Rev. D* 98.8 (2018), p. 083525. DOI: 10.1103/PhysRevD.98.083525. arXiv: 1806.10608 [astro-ph.CO].

[111] J. C. Hill et al. "Early dark energy does not restore cosmological concordance". In: *Phys. Rev. D* 102.4 (2020), p. 043507. DOI: 10.1103/PhysRevD.102.043507. arXiv: 2003.07355 [astro-ph.CO].

[112] M. M. Ivanov et al. "Constraining Early Dark Energy with Large-Scale Structure". In: *Phys. Rev. D* 102.10 (2020), p. 103502. DOI: 10.1103/PhysRevD.102.103502. arXiv: 2006.11235 [astro-ph.CO].

[113] T. L. Smith and V. Poulin. "Current small-scale CMB constraints to axionlike early dark energy". In: *Phys. Rev. D* 109.10 (2024), p. 103506. DOI: 10.1103/PhysRevD.109.103506. arXiv: 2309.03265 [astro-ph.CO].

[114] E. McDonough et al. "Observational constraints on early dark energy". In: *Int. J. Mod. Phys. D* 33.11 (2024), p. 2430003. DOI: 10.1142/S0218271824300039. arXiv: 2310.19899 [astro-ph.CO].

[115] P. Agrawal et al. "Rock 'n' roll solutions to the Hubble tension". In: *Phys. Dark Univ.* 42 (2023), p. 101347. DOI: 10.1016/j.dark.2023.101347. arXiv: 1904.01016 [astro-ph.CO].

[116] D. J. Eisenstein and M. J. White. "Theoretical uncertainty in baryon oscillations". In: *Phys. Rev. D* 70 (2004), p. 103523. DOI: 10.1103/PhysRevD.70.103523. arXiv: astro-ph/0407539.

[117] G. Steigman. "Neutrinos And Big Bang Nucleosynthesis". In: *Adv. High Energy Phys.* 2012 (2012), p. 268321. DOI: 10.1155/2012/268321. arXiv: 1208.0032 [hep-ph].

[118] C. D. Kreisch, F.-Y. Cyr-Racine, and O. Doré. "Neutrino puzzle: Anomalies, interactions, and cosmological tensions". In: *Phys. Rev. D* 101.12 (2020), p. 123505. DOI: 10.1103/PhysRevD.101.123505. arXiv: 1902.00534 [astro-ph.CO].

[119] M. C. Gonzalez-Garcia et al. "Global fit to three neutrino mixing: critical look at present precision". In: *JHEP* 12 (2012), p. 123. DOI: 10.1007/JHEP12(2012)123. arXiv: 1209.3023 [hep-ph].

[120] E. Di Valentino et al. "Nonminimal dark sector physics and cosmological tensions". In: *Phys. Rev. D* 101.6 (2020), p. 063502. DOI: 10.1103/PhysRevD.101.063502. arXiv: 1910.09853 [astro-ph.CO].

[121] K. Vattis, S. M. Koushiappas, and A. Loeb. "Dark matter decaying in the late Universe can relieve the H0 tension". In: *Phys. Rev. D* 99.12 (2019), p. 121302. DOI: 10.1103/PhysRevD.99.121302. arXiv: 1903.06220 [astro-ph.CO].

[122] R. R. Caldwell, M. Kamionkowski, and N. N. Weinberg. "Phantom energy and cosmic doomsday". In: *Phys. Rev. Lett.* 91 (2003), p. 071301. DOI: 10.1103/PhysRevLett.91.071301. arXiv: astro-ph/0302506.

[123] X. Li and A. Shafieloo. "A Simple Phenomenological Emergent Dark Energy Model can Resolve the Hubble Tension". In: *Astrophys. J. Lett.* 883.1 (2019), p. L3. DOI: 10.3847/2041-8213/ab3e09. arXiv: 1906.08275 [astro-ph.CO].

[124] A. Hernández-Almada et al. "Generalized Emergent Dark Energy: observational Hubble data constraints and stability analysis". In: *Mon. Not. Roy. Astron. Soc.* 497.2 (2020), pp. 1590–1602. DOI: 10.1093/mnras/staa2052. arXiv: 2002.12881 [astro-ph.CO].

[125] V. Poulin et al. "Early Dark Energy Can Resolve The Hubble Tension". In: *Phys. Rev. Lett.* 122.22 (2019), p. 221301. DOI: 10.1103/PhysRevLett.122.221301. arXiv: 1811.04083 [astro-ph.CO].

[126] R. Murgia, G. F. Abellán, and V. Poulin. "Early dark energy resolution to the Hubble tension in light of weak lensing surveys and lensing anomalies". In: *Phys. Rev. D* 103.6 (2021), p. 063502. DOI: 10.1103/PhysRevD.103.063502. arXiv: 2009.10733 [astro-ph.CO].

[127] Y. Akrami et al. "*Planck* intermediate results. LVII. Joint Planck LFI and HFI data processing". In: *Astron. Astrophys.* 643 (2020), A42. DOI: 10.1051/0004-6361/202038073. arXiv: 2007.04997 [astro-ph.CO].

[128] N. Aghanim et al. "Planck 2018 results. V. CMB power spectra and likelihoods". In: *Astron. Astrophys.* 641 (2020), A5. DOI: 10.1051/0004-6361/201936386. arXiv: 1907.12875 [astro-ph.CO].

[129] J. Sakstein and M. Trodden. "Early Dark Energy from Massive Neutrinos as a Natural Resolution of the Hubble Tension". In: *Phys. Rev. Lett.* 124.16 (2020), p. 161301. DOI: 10.1103/PhysRevLett.124.161301. arXiv: 1911.11760 [astro-ph.CO].

[130] M.-X. Lin et al. "Dark matter trigger for early dark energy coincidence". In: *Phys. Rev. D* 107.10 (2023), p. 103523. DOI: 10.1103/PhysRevD.107.103523. arXiv: 2212.08098 [astro-ph.CO].

[131] C. Jing, S. Tian, and Z.-H. Zhu. "Early dark energy triggered by spacetime dynamics that encodes cosmic radiation-matter transition". In: *Phys. Rev. D* 109.4 (2024), p. 044016. DOI: 10.1103/PhysRevD.109.044016. arXiv: 2402.03684 [gr-qc].

[132] H. Wang and Y.-S. Piao. "Trapped early dark energy". In: *Phys. Lett. B* 856 (2024), p. 138914. DOI: 10.1016/j.physletb.2024.138914. arXiv: 2401.08812 [gr-qc].

[133] M. Carrillo González et al. "Neutrino-Assisted Early Dark Energy: Theory and Cosmology". In: *JCAP* 04 (2021), p. 063. DOI: 10.1088/1475-7516/2021/04/063. arXiv: 2011.09895 [astro-ph.CO].

[134] M. Carrillo González et al. "Neutrino-Assisted Early Dark Energy is a Natural Resolution of the Hubble Tension". In: (Feb. 2023). arXiv: 2302.09091 [astro-ph.CO].

[135] T. Karwal et al. "Chameleon early dark energy and the Hubble tension". In: *Phys. Rev. D* 105.6 (2022), p. 063535. DOI: 10.1103/PhysRevD.105.063535. arXiv: 2106.13290 [astro-ph.CO].

[136] T. L. Smith et al. "Early dark energy is not excluded by current large-scale structure data". In: *Phys. Rev. D* 103.12 (2021), p. 123542. DOI: 10.1103/PhysRevD.103.123542. arXiv: 2009.10740 [astro-ph.CO].

[137] T. Rudelius. "Constraints on early dark energy from the axion weak gravity conjecture". In: *JCAP* 01 (2023), p. 014. DOI: 10.1088/1475-7516/2023/01/014. arXiv: 2203.05575 [hep-th].

[138] N. Arkani-Hamed et al. "The String landscape, black holes and gravity as the weakest force". In: *JHEP* 06 (2007), p. 060. DOI: 10.1088/1126-6708/2007/06/060. arXiv: hep-th/0601001.

[139] B. Heidenreich, M. Reece, and T. Rudelius. "Repulsive Forces and the Weak Gravity Conjecture". In: *JHEP* 10 (2019), p. 055. DOI: 10.1007/JHEP10(2019)055. arXiv: 1906.02206 [hep-th].

[140] E. McDonough and M. Scalisi. "Towards Early Dark Energy in string theory". In: *JHEP* 10 (2023), p. 118. DOI: 10.1007/JHEP10(2023)118. arXiv: 2209.00011 [hep-th].

[141] M. Cicoli et al. "Early Dark Energy in Type IIB String Theory". In: *JHEP* 06 (2023), p. 052. DOI: 10.1007/JHEP06(2023)052. arXiv: 2303.03414 [hep-th].

[142] V. I. Sabla and R. R. Caldwell. "No H_0 assistance from assisted quintessence". In: *Phys. Rev. D* 103.10 (2021), p. 103506. DOI: 10.1103/PhysRevD.103.103506. arXiv: 2103.04999 [astro-ph.CO].

[143] V. I. Sabla and R. R. Caldwell. "Microphysics of early dark energy". In: *Phys. Rev. D* 106.6 (2022), p. 063526. DOI: 10.1103/PhysRevD.106.063526. arXiv: 2202.08291 [astro-ph.CO].

[144] A. Adil, A. Albrecht, and L. Knox. "Quintessential cosmological tensions". In: *Phys. Rev. D* 107.6 (2023), p. 063521. DOI: 10.1103/PhysRevD.107.063521. arXiv: 2207.10235 [astro-ph.CO].

[145] L. Brissenden, K. Dimopoulos, and S. Sánchez López. "Non-oscillating early dark energy and quintessence from α-attractors". In: *Astropart. Phys.* 157 (2024), p. 102925. DOI: 10.1016/j.astropartphys.2024.102925. arXiv: 2301.03572 [astro-ph.CO].

[146] S. Wiggins. *Introduction To Applied Nonlinear Dynamical Systems And Chaos*. 1990. ISBN: 978-1-4757-4067-7. DOI: 10.1007/978-1-4757-4067-7.

[147] S. Bahamonde et al. "Dynamical systems applied to cosmology: dark energy and modified gravity". In: *Phys. Rept.* 775-777 (2018), pp. 1–122. DOI: 10.1016/j.physrep.2018.09.001. arXiv: 1712.03107 [gr-qc].

[148] S. H. Strogatz. *Nonlinear Dynamics and Chaos*. Westview Press, 1994.

[149] J. Guckenheimer and P. Holmes. *Nonlinear Oscillations, Dynamical Systems, and Bifurcations of Vector Fields*. Springer, 1983.

[150] T. Barreiro, E. J. Copeland, and N. J. Nunes. "Quintessence arising from exponential potentials". In: *Phys. Rev. D* 61 (2000). astro-ph/9910214, p. 127301. DOI: 10.1103/PhysRevD.61.127301.

[151] S.-Y. Zhou. "A New Approach to Quintessence and Solution of Multiple Attractors". In: *Phys. Lett. B* 660 (2008), pp. 7–12. DOI: 10.1016/j.physletb.2007.12.020. arXiv: 0705.1577 [astro-ph].

[152] W. Fang et al. "Exact Analysis of Scaling and Dominant Attractors Beyond the Exponential Potential". In: *Class. Quant. Grav.* 26 (2009), p. 155005. DOI: 10.1088/0264-9381/26/15/155005. arXiv: 0810.4193 [hep-th].

[153] W. K. Hastings. "Monte Carlo sampling methods using Markov chains and their applications". In: *Biometrika* 57.1 (1970), pp. 97–109.

[154] N. Metropolis et al. "Equation of state calculations by fast computing machines". In: *The journal of chemical physics* 21.6 (1953), pp. 1087–1092.

[155] J. Torrado and A. Lewis. "Cobaya: Code for Bayesian Analysis of hierarchical physical models". In: *JCAP* 05 (2021). arXiv:2005.05290, p. 057. DOI: 10.1088/1475-7516/2021/05/057.

[156] W. J. Handley, M. P. Hobson, and A. N. Lasenby. "PolyChord: nested sampling for cosmology". In: *Mon. Not. Roy. Astron. Soc.* 450.1 (2015). arXiv:1502.01856, pp. L61–L65. DOI: 10.1093/mnrasl/slv047.

[157] A. Lewis. "GetDist: a Python package for analysing Monte Carlo samples". In: (Oct. 2019). arXiv: 1910.13970 [astro-ph.IM].

[158] A. G. Riess et al. "Large Magellanic Cloud Cepheid Standards Provide a 1% Foundation for the Determination of the Hubble Constant and Stronger Evidence for Physics beyond ΛCDM". In: *Astrophys. J.* 876.1 (2019). arXiv:1903.07603, p. 85. DOI: 10.3847/1538-4357/ab1422.

[159] L. Herold, E. G. M. Ferreira, and E. Komatsu. "New Constraint on Early Dark Energy from Planck and BOSS Data Using the Profile Likelihood". In: *Astrophys. J. Lett.* 929.1 (2022), p. L16. DOI: 10.3847/2041-8213/ac63a3. arXiv: 2112.12140 [astro-ph.CO].

[160] Y. S. Murakami et al. "Leveraging SN Ia spectroscopic similarity to improve the measurement of H_0". In: (May 2023). arXiv: 2306.00070 [astro-ph.CO].

[161] K. V. Berghaus and T. Karwal. "Thermal friction as a solution to the Hubble and large-scale structure tensions". In: *Phys. Rev. D* 107.10 (2023), p. 103515. DOI: 10.1103/PhysRevD.107.103515. arXiv: 2204.09133 [astro-ph.CO].

[162] E. V. Linder and T. L. Smith. "Dark Before Light: Testing the Cosmic Expansion History through the Cosmic Microwave Background". In: *JCAP* 04 (2011), p. 001. DOI: 10.1088/1475-7516/2011/04/001. arXiv: 1009.3500 [astro-ph.CO].

[163] E. Calabrese et al. "Limits on Dark Radiation, Early Dark Energy, and Relativistic Degrees of Freedom". In: *Phys. Rev. D* 83 (2011), p. 123504. DOI: 10.1103/PhysRevD.83.123504. arXiv: 1103.4132 [astro-ph.CO].

[164] V. Pettorino, L. Amendola, and C. Wetterich. "How early is early dark energy?" In: *Phys. Rev. D* 87 (2013), p. 083009. DOI: 10.1103/PhysRevD.87.083009. arXiv: 1301.5279 [astro-ph.CO].

[165] M. Doran and G. Robbers. "Early dark energy cosmologies". In: *JCAP* 06 (2006), p. 026. DOI: 10.1088/1475-7516/2006/06/026. arXiv: astro-ph/0601544.

[166] C.-P. Ma and E. Bertschinger. "Cosmological perturbation theory in the synchronous and conformal Newtonian gauges". In: *Astrophys. J.* 455 (1995), pp. 7–25. DOI: 10.1086/176550. arXiv: astro-ph/9506072.

[167] L. Knox and M. Millea. "Hubble constant hunter's guide". In: *Phys. Rev. D* 101.4 (2020), p. 043533. DOI: 10.1103/PhysRevD.101.043533. arXiv: 1908.03663 [astro-ph.CO].

[168] S. Vagnozzi. "Consistency tests of ΛCDM from the early integrated Sachs-Wolfe effect: Implications for early-time new physics and the Hubble tension". In: *Phys. Rev. D* 104.6 (2021), p. 063524. DOI: 10.1103/PhysRevD.104.063524. arXiv: 2105.10425 [astro-ph.CO].

[169] M. Chevallier and D. Polarski. "Accelerating universes with scaling dark matter". In: *Int. J. Mod. Phys. D* 10 (2001), pp. 213–224. DOI: 10.1142/S0218271801000822. arXiv: gr-qc/0009008.

[170] E. V. Linder. "Exploring the expansion history of the universe". In: *Phys. Rev. Lett.* 90 (2003), p. 091301. DOI: 10.1103/PhysRevLett.90.091301. arXiv: astro-ph/0208512.

[171] V. Barger, E. Guarnaccia, and D. Marfatia. "Classification of dark energy models in the (w(0), w(a)) plane". In: *Phys. Lett. B* 635 (2006), pp. 61–65. DOI: 10.1016/j.physletb.2006.02.018. arXiv: hep-ph/0512320.

[172] R. J. Scherrer. "Mapping the Chevallier-Polarski-Linder parametrization onto Physical Dark Energy Models". In: *Phys. Rev. D* 92.4 (2015), p. 043001. DOI: 10.1103/PhysRevD.92.043001. arXiv: 1505.05781 [astro-ph.CO].

[173] W. J. Wolf and P. G. Ferreira. "Underdetermination of dark energy". In: *Phys. Rev. D* 108.10 (2023), p. 103519. DOI: 10.1103/PhysRevD.108.103519. arXiv: 2310.07482 [astro-ph.CO].

[174] D. Shlivko and P. Steinhardt. "Assessing observational constraints on dark energy". In: (May 2024). arXiv: 2405.03933 [astro-ph.CO].

[175] E. Ó. Colgáin et al. "Does DESI 2024 Confirm ΛCDM?" In: (Apr. 2024). arXiv: 2404.08633 [astro-ph.CO].

[176] M. Cortês and A. R. Liddle. "Interpreting DESI's evidence for evolving dark energy". In: (Apr. 2024). arXiv: 2404.08056 [astro-ph.CO].

[177] Y. Carloni, O. Luongo, and M. Muccino. "Does dark energy really revive using DESI 2024 data?" In: (Apr. 2024). arXiv: 2404.12068 [astro-ph.CO].

[178] D. Wang. "The Self-Consistency of DESI Analysis and Comment on "Does DESI 2024 Confirm ΛCDM?"" In: (Apr. 2024). arXiv: 2404.13833 [astro-ph.CO].

[179] H. Wang and Y.-S. Piao. "Dark energy in light of recent DESI BAO and Hubble tension". In: (Apr. 2024). arXiv: 2404.18579 [astro-ph.CO].

[180] D. Wang. "Constraining Cosmological Physics with DESI BAO Observations". In: (Apr. 2024). arXiv: 2404.06796 [astro-ph.CO].

[181] W. Yin. "Cosmic clues: DESI, dark energy, and the cosmological constant problem". In: *JHEP* 05 (2024), p. 327. DOI: 10.1007/JHEP05(2024)327. arXiv: 2404.06444 [hep-ph].

[182] Y. Tada and T. Terada. "Quintessential interpretation of the evolving dark energy in light of DESI". In: (Apr. 2024). arXiv: 2404.05722 [astro-ph.CO].

[183] K. V. Berghaus, J. A. Kable, and V. Miranda. "Quantifying Scalar Field Dynamics with DESI 2024 Y1 BAO measurements". In: (Apr. 2024). arXiv: 2404.14341 [astro-ph.CO].

[184] W. J. Wolf et al. "Scant evidence for thawing quintessence". In: (Aug. 2024). arXiv: 2408.17318 [astro-ph.CO].

[185] S. Bhattacharya et al. "Cosmological constraints on curved quintessence". In: (May 2024). arXiv: 2405.17396 [astro-ph.CO].

[186] A. Pérez-Fernández et al. "Fiducial-Cosmology-dependent systematics for the DESI 2024 BAO Analysis". In: (June 2024). arXiv: 2406.06085 [astro-ph.CO].

[187] A. Bault et al. "Impact of Systematic Redshift Errors on the Cross-correlation of the Lyman-α Forest with Quasars at Small Scales Using DESI Early Data". In: (Feb. 2024). arXiv: 2402.18009 [astro-ph.CO].

[188] C. Wetterich. "The Cosmon model for an asymptotically vanishing time dependent cosmological 'constant'". In: *Astron. Astrophys.* 301 (1995), pp. 321–328. arXiv: hep-th/9408025.

[189] P. Binetruy. "Models of dynamical supersymmetry breaking and quintessence". In: *Phys. Rev. D* 60 (1999), p. 063502. DOI: 10.1103/PhysRevD.60.063502. arXiv: hep-ph/9810553.

[190] B. Ratra and P. J. E. Peebles. "Cosmological Consequences of a Rolling Homogeneous Scalar Field". In: *Phys. Rev. D* 37 (1988), p. 3406. DOI: 10.1103/PhysRevD.37.3406.

[191] R. R. Caldwell, R. Dave, and P. J. Steinhardt. "Cosmological imprint of an energy component with general equation of state". In: *Phys. Rev. Lett.* 80 (1998), pp. 1582–1585. DOI: 10.1103/PhysRevLett.80.1582. arXiv: astro-ph/9708069.

[192] J. Carron, M. Mirmelstein, and A. Lewis. "CMB lensing from Planck PR4 maps". In: *JCAP* 09 (2022), p. 039. DOI: 10.1088/1475-7516/2022/09/039. arXiv: 2206.07773 [astro-ph.CO].

[193] F. J. Qu et al. "The Atacama Cosmology Telescope: A Measurement of the DR6 CMB Lensing Power Spectrum and Its Implications for Structure Growth". In: *Astrophys. J.* 962.2 (2024), p. 112. DOI: 10.3847/1538-4357/acfe06. arXiv: 2304.05202 [astro-ph.CO].

[194] M. S. Madhavacheril et al. "The Atacama Cosmology Telescope: DR6 Gravitational Lensing Map and Cosmological Parameters". In: *Astrophys. J.* 962.2 (2024), p. 113. DOI: 10.3847/1538-4357/acff5f. arXiv: 2304.05203 [astro-ph.CO].

[195] A. Gelman and D. B. Rubin. "Inference from Iterative Simulation Using Multiple Sequences". In: *Statist. Sci.* 7 (1992), pp. 457–472. DOI: 10.1214/ss/1177011136.

[196] J. J. Heckman et al. "F-theory and Dark Energy". In: *Fortsch. Phys.* 67.10 (2019), p. 1900057. DOI: 10.1002/prop.201900057. arXiv: 1811.01959 [hep-th].

[197] J. J. Heckman et al. "Pixelated Dark Energy". In: *Fortsch. Phys.* 67.11 (2019), p. 1900071. DOI: 10.1002/prop.201900071. arXiv: 1901.10489 [hep-th].

[198] P. Svrcek and E. Witten. "Axions In String Theory". In: *JHEP* 06 (2006), p. 051. DOI: 10.1088/1126-6708/2006/06/051. arXiv: hep-th/0605206.

[199] S. Alexander et al. "π-axion and π-axiverse of dark QCD". In: *Phys. Rev. D* 108.12 (2023), p. 123014. DOI: 10.1103/PhysRevD.108.123014. arXiv: 2304.11176 [hep-ph].

[200] F. Apers et al. "String Theory and the First Half of the Universe". In: (Jan. 2024). arXiv: 2401.04064 [hep-th].

[201] R. D. Peccei. "The Strong CP problem and axions". In: *Lect. Notes Phys.* 741 (2008). Ed. by M. Kuster, G. Raffelt, and B. Beltran, pp. 3–17. DOI: 10.1007/978-3-540-73518-2_1. arXiv: hep-ph/0607268.

[202] J. E. Kim and G. Carosi. "Axions and the Strong CP Problem". In: *Rev. Mod. Phys.* 82 (2010). [Erratum: Rev.Mod.Phys. 91, 049902 (2019)], pp. 557–602. DOI: 10.1103/RevModPhys.82.557. arXiv: 0807.3125 [hep-ph].

[203] C. A. J. O'Hare. "Cosmology of axion dark matter". In: *PoS* COSMICWISPers (2024), p. 040. DOI: 10.22323/1.454.0040. arXiv: 2403.17697 [hep-ph].

[204] J. E. Moody and F. Wilczek. "NEW MACROSCOPIC FORCES?" In: *Phys. Rev. D* 30 (1984), p. 130. DOI: 10.1103/PhysRevD.30.130.

[205] H. Georgi and L. Randall. "Flavor Conserving CP Violation in Invisible Axion Models". In: *Nucl. Phys. B* 276 (1986), pp. 241–252. DOI: 10.1016/0550-3213(86)90022-2.

[206] S. Bertolini, L. Di Luzio, and F. Nesti. "Axion-mediated forces, CP violation and left-right interactions". In: *Phys. Rev. Lett.* 126.8 (2021), p. 081801. DOI: 10.1103/PhysRevLett.126.081801. arXiv: 2006.12508 [hep-ph].

[207] L. Di Luzio. "CP-violating axions". In: *PoS* EPS-HEP2021 (2022), p. 513. DOI: 10.22323/1.398.0513. arXiv: 2108.09071 [hep-ph].

[208] I. G. Irastorza and J. Redondo. "New experimental approaches in the search for axion-like particles". In: *Prog. Part. Nucl. Phys.* 102 (2018), pp. 89–159. DOI: 10.1016/j.ppnp.2018.05.003. arXiv: 1801.08127 [hep-ph].

[209] L. Di Luzio, R. Gröber, and P. Paradisi. "Hunting for CP-violating axionlike particle interactions". In: *Phys. Rev. D* 104.9 (2021), p. 095027. DOI: 10.1103/PhysRevD.104.095027. arXiv: 2010.13760 [hep-ph].

[210] S. Coleman. *Aspects of Symmetry: Selected Erice Lectures*. Cambridge, U.K.: Cambridge University Press, 1985. ISBN: 978-0-521-31827-3. DOI: 10.1017/CBO9780511565045.

[211] C. A. Baker et al. "An Improved experimental limit on the electric dipole moment of the neutron". In: *Phys. Rev. Lett.* 97 (2006), p. 131801. DOI: 10.1103/PhysRevLett.97.131801. arXiv: hep-ex/0602020.

[212] K. A. Olive et al. "Review of Particle Physics". In: *Chin. Phys. C* 38 (2014), p. 090001. DOI: 10.1088/1674-1137/38/9/090001.

[213] F. Wilczek. "Problem of Strong P and T Invariance in the Presence of Instantons". In: *Phys. Rev. Lett.* 40 (1978), pp. 279–282. DOI: 10.1103/PhysRevLett.40.279.

[214] S. Weinberg. "A New Light Boson?" In: *Phys. Rev. Lett.* 40 (1978), pp. 223–226. DOI: 10.1103/PhysRevLett.40.223.

[215] P. Sikivie. "Of Axions, Domain Walls and the Early Universe". In: *Phys. Rev. Lett.* 48 (1982), pp. 1156–1159. DOI: 10.1103/PhysRevLett.48.1156.

[216] M. Kawasaki, K. Saikawa, and T. Sekiguchi. "Axion dark matter from topological defects". In: *Phys. Rev. D* 91.6 (2015), p. 065014. DOI: 10.1103/PhysRevD.91.065014. arXiv: 1412.0789 [hep-ph].

[217] G. Grilli di Cortona et al. "The QCD axion, precisely". In: *JHEP* 01 (2016), p. 034. DOI: 10.1007/JHEP01(2016)034. arXiv: 1511.02867 [hep-ph].

[218] J. E. Kim. "Weak Interaction Singlet and Strong CP Invariance". In: *Phys. Rev. Lett.* 43 (1979), p. 103. DOI: 10.1103/PhysRevLett.43.103.

[219] M. A. Shifman, A. I. Vainshtein, and V. I. Zakharov. "Can Confinement Ensure Natural CP Invariance of Strong Interactions?" In: *Nucl. Phys. B* 166 (1980), pp. 493–506. DOI: 10.1016/0550-3213(80)90209-6.

[220] M. Dine, W. Fischler, and M. Srednicki. "A Simple Solution to the Strong CP Problem with a Harmless Axion". In: *Phys. Lett. B* 104 (1981), pp. 199–202. DOI: 10.1016/0370-2693(81)90590-6.

[221] A. R. Zhitnitsky. "On Possible Suppression of the Axion Hadron Interactions. (In Russian)". In: *Sov. J. Nucl. Phys.* 31 (1980), p. 260.

[222] A. Arvanitaki et al. "String Axiverse". In: *Phys. Rev. D* 81 (2010), p. 123530. DOI: 10.1103/PhysRevD.81.123530. arXiv: 0905.4720 [hep-th].

[223] M. Cicoli, M. Goodsell, and A. Ringwald. "The type IIB string axiverse and its low-energy phenomenology". In: *JHEP* 10 (2012), p. 146. DOI: 10.1007/JHEP10(2012)146. arXiv: 1206.0819 [hep-th].

[224] G. Raffelt and L. Stodolsky. "Mixing of the Photon with Low Mass Particles". In: *Phys. Rev. D* 37 (1988), p. 1237. DOI: 10.1103/PhysRevD.37.1237.

[225] R. T. Co, L. J. Hall, and K. Harigaya. "Predictions for Axion Couplings from ALP Cogenesis". In: *JHEP* 01 (2021), p. 172. DOI: 10.1007/JHEP01(2021)172. arXiv: 2006.04809 [hep-ph].

[226] J. Jaeckel and A. Ringwald. "The Low-Energy Frontier of Particle Physics". In: *Ann. Rev. Nucl. Part. Sci.* 60 (2010), pp. 405–437. DOI: 10.1146/annurev.nucl.010909.083219. arXiv: 1002.0329 [hep-ph].

[227] M. Srednicki. "Axion Couplings to Matter. 1. CP Conserving Parts". In: *Nucl. Phys. B* 260 (1985), pp. 689–700. DOI: 10.1016/0550-3213(85)90054-9.

[228] L. Di Luzio et al. "The landscape of QCD axion models". In: *Phys. Rept.* 870 (2020), pp. 1–117. DOI: 10.1016/j.physrep.2020.06.002. arXiv: 2003.01100 [hep-ph].

[229] Y. Su et al. "New tests of the universality of free fall". In: *Phys. Rev. D* 50 (1994), pp. 3614–3636. DOI: 10.1103/PhysRevD.50.3614.

[230] G. L. Smith et al. "Short range tests of the equivalence principle". In: *Phys. Rev. D* 61 (2000), p. 022001. DOI: 10.1103/PhysRevD.61.022001.

[231] S. Schlamminger et al. "Test of the equivalence principle using a rotating torsion balance". In: *Phys. Rev. Lett.* 100 (2008), p. 041101. DOI: 10.1103/PhysRevLett.100.041101. arXiv: 0712.0607 [gr-qc].

[232] J. Bergé et al. "MICROSCOPE Mission: First Constraints on the Violation of the Weak Equivalence Principle by a Light Scalar Dilaton". In: *Phys. Rev. Lett.* 120.14 (2018), p. 141101. DOI: 10.1103/PhysRevLett.120.141101. arXiv: 1712.00483 [gr-qc].

[233] P. Touboul et al. "Result of the MICROSCOPE weak equivalence principle test". In: *Class. Quant. Grav.* 39.20 (2022), p. 204009. DOI: 10.1088/1361-6382/ac84be. arXiv: 2209.15488 [gr-qc].

[234] Y.-J. Chen et al. "Stronger Limits on Hypothetical Yukawa Interactions in the 30–8000 nm Range". In: *Phys. Rev. Lett.* 116.22 (2016), p. 221102. DOI: 10.1103/PhysRevLett.116.221102. arXiv: 1410.7267 [hep-ex].

[235] R. S. Decca et al. "Novel constraints on light elementary particles and extra-dimensional physics from the Casimir effect". In: *Eur. Phys. J. C* 51 (2007), pp. 963–975. DOI: 10.1140/epjc/s10052-007-0346-z. arXiv: 0706.3283 [hep-ph].

[236] A. A. Geraci et al. "Improved constraints on non-Newtonian forces at 10 microns". In: *Phys. Rev. D* 78 (2008), p. 022002. DOI: 10.1103/PhysRevD.78.022002. arXiv: 0802.2350 [hep-ex].

[237] D. J. Kapner et al. "Tests of the gravitational inverse-square law below the dark-energy length scale". In: *Phys. Rev. Lett.* 98 (2007), p. 021101. DOI: 10.1103/PhysRevLett.98.021101. arXiv: hep-ph/0611184 [hep-ph].

[238] J. G. Lee et al. "Test of the gravitational inverse-square law at the millimeter range, and new constraints on light bosons". In: *Phys. Rev. Lett.* 124 (2020), p. 101101. DOI: 10.1103/PhysRevLett.124.101101.

[239] L.-C. Tu et al. "Null Test of Newtonian Inverse-Square Law at Submillimeter Range with a Dual-Modulation Torsion Pendulum". In: *Phys. Rev. Lett.* 98 (2007), p. 201101. DOI: 10.1103/PhysRevLett.98.201101.

[240] S.-Q. Yang et al. "Test of the Gravitational Inverse Square Law at Millimeter Ranges". In: *Phys. Rev. Lett.* 108 (2012), p. 081101. DOI: 10.1103/PhysRevLett.108.081101.

[241] W.-H. Tan et al. "New Test of the Gravitational Inverse-Square Law at the Submillimeter Range with Dual Modulation and Compensation". In: *Phys. Rev. Lett.* 116.13 (2016), p. 131101. DOI: 10.1103/PhysRevLett.116.131101.

[242] W.-H. Tan et al. "Improvement for Testing the Gravitational Inverse-Square Law at the Submillimeter Range". In: *Phys. Rev. Lett.* 124.5 (2020), p. 051301. DOI: 10.1103/PhysRevLett.124.051301.

[243] J. K. Hoskins et al. "Experimental tests of the gravitational inverse square law for mass separations from 2-cm to 105-cm". In: *Phys. Rev. D* 32 (1985), pp. 3084–3095. DOI: 10.1103/PhysRevD.32.3084.

[244] C. A. J. O'Hare. "The International Axion Observatory: AxionLimits Compilation". In: (2020). https://cajohare.github.io/AxionLimits/.

[245] E. Hardy and R. Lasenby. "Stellar cooling bounds on new light particles: plasma mixing effects". In: *JHEP* 02 (2017), p. 033. DOI: 10.1007/JHEP02(2017)033. arXiv: 1611.05852 [hep-ph].

[246] J. A. Grifols and E. Masso. "Constraints on Finite Range Baryonic and Leptonic Forces From Stellar Evolution". In: *Phys. Lett. B* 173 (1986), pp. 237–240. DOI: 10.1016/0370-2693(86)90509-5.

[247] G. Raffelt. "Horizontal Branch Stars and the Neutrino Signal From SN1987A". In: *Phys. Rev. D* 38 (1988), pp. 3811–3812. DOI: 10.1103/PhysRevD.38.3811.

[248] G. G. Raffelt. "Particle physics from stars". In: *Ann. Rev. Nucl. Part. Sci.* 49 (1999), pp. 163–216. DOI: 10.1146/annurev.nucl.49.1.163. arXiv: hep-ph/9903472.

[249] M. Pospelov. "CP odd interaction of axion with matter". In: *Phys. Rev. D* 58 (1998), p. 097703. DOI: 10.1103/PhysRevD.58.097703. arXiv: hep-ph/9707431.

[250] R. Barbieri, A. Romanino, and A. Strumia. "On axion mediated macroscopic forces again". In: *Phys. Lett. B* 387 (1996), pp. 310–314. DOI: 10.1016/0370-2693(96)00957-4. arXiv: hep-ph/9605368.

[251] E. G. Adelberger et al. "Torsion balance experiments: A low-energy frontier of particle physics". In: *Prog. Part. Nucl. Phys.* 62 (2009), pp. 102–134. DOI: 10.1016/j.ppnp.2008.08.002.

[252] C. Wetterich. "Modified gravity and coupled quintessence". In: *Lect. Notes Phys.* 892 (2015), p. 57. DOI: 10.1007/978-3-319-10070-8_3. arXiv: 1402.5031 [astro-ph.CO].

[253] C. Burrage et al. "Fifth forces, Higgs portals and broken scale invariance". In: *JCAP* 11 (2018), p. 036. DOI: 10.1088/1475-7516/2018/11/036. arXiv: 1804.07180 [hep-th].

[254] R. Balkin et al. "Heavy neutron stars from light scalars". In: (July 2023). arXiv: 2307.14418 [hep-ph].

[255] A. Akmal, V. R. Pandharipande, and D. G. Ravenhall. "The Equation of state of nucleon matter and neutron star structure". In: *Phys. Rev. C* 58 (1998), pp. 1804–1828. DOI: 10.1103/PhysRevC.58.1804. arXiv: nucl-th/9804027.

[256] J. M. Lattimer and M. Prakash. "Neutron Star Observations: Prognosis for Equation of State Constraints". In: *Phys. Rept.* 442 (2007), pp. 109–165. DOI: 10.1016/j.physrep.2007.02.003. arXiv: astro-ph/0612440.

[257] F. Özel and P. Freire. "Masses, Radii, and the Equation of State of Neutron Stars". In: *Ann. Rev. Astron. Astrophys.* 54 (2016), pp. 401–440. DOI: 10.1146/annurev-astro-081915-023322. arXiv: 1603.02698 [astro-ph.HE].

[258] B. F. de Aguiar and R. F. P. Mendes. "Highly compact neutron stars and screening mechanisms: Equilibrium and stability". In: *Phys. Rev. D* 102.2 (2020), p. 024064. DOI: 10.1103/PhysRevD.102.024064. arXiv: 2006.10080 [gr-qc].

[259] T. Malik, H. Pais, and C. Providência. "Unified neutron star equations of state calibrated to nuclear properties". In: *Astron. Astrophys.* 689 (2024), A242. DOI: 10.1051/0004-6361/202449292. arXiv: 2401.10842 [nucl-th].

[260] S. Bottaro et al. "Stellar limits on scalars from electron-nucleus bremsstrahlung". In: *JCAP* 07 (2023), p. 071. DOI: 10.1088/1475-7516/2023/07/071. arXiv: 2303.00778 [hep-ph].

[261] J.-P. Uzan. "Varying Constants, Gravitation and Cosmology". In: *Living Rev. Rel.* 14 (2011), p. 2. DOI: 10.12942/lrr-2011-2. arXiv: 1009.5514 [astro-ph.CO].

[262] K. L. Greene and F.-Y. Cyr-Racine. "Thomson scattering: one rate to rule them all". In: *JCAP* 10 (2023), p. 065. DOI: 10.1088/1475-7516/2023/10/065. arXiv: 2306.06165 [astro-ph.CO].

[263] N. Schöneberg and L. Vacher. "The mass effect – Variations of masses and their impact on cosmology". In: (July 2024). arXiv: 2407.16845 [astro-ph.CO].

[264] K. S. Jeong, T. H. Jung, and C. S. Shin. "Adiabatic electroweak baryogenesis driven by an axionlike particle". In: *Phys. Rev. D* 101.3 (2020), p. 035009. DOI: 10.1103/PhysRevD.101.035009. arXiv: 1811.03294 [hep-ph].

[265] C. Burrage and J. Sakstein. "A Compendium of Chameleon Constraints". In: *JCAP* 11 (2016), p. 045. DOI: 10.1088/1475-7516/2016/11/045. arXiv: 1609.01192 [astro-ph.CO].

[266] C. Burrage and J. Sakstein. "Tests of Chameleon Gravity". In: *Living Rev. Rel.* 21.1 (2018), p. 1. DOI: 10.1007/s41114-018-0011-x. arXiv: 1709.09071 [astro-ph.CO].

[267] A. Hook and J. Huang. "Probing axions with neutron star inspirals and other stellar processes". In: *JHEP* 06 (2018), p. 036. DOI: 10.1007/JHEP06(2018)036. arXiv: 1708.08464 [hep-ph].

[268] R. Balkin et al. "The QCD axion at finite density". In: *JHEP* 07 (2020), p. 221. DOI: 10.1007/JHEP07(2020)221. arXiv: 2003.04903 [hep-ph].

[269] J. Zhang et al. "First Constraints on Nuclear Coupling of Axionlike Particles from the Binary Neutron Star Gravitational Wave Event GW170817". In: *Phys. Rev. Lett.* 127.16 (2021), p. 161101. DOI: 10.1103/PhysRevLett.127.161101. arXiv: 2105.13963 [hep-ph].

[270] R. Balkin et al. "Density induced vacuum instability". In: *SciPost Phys.* 14.4 (2023), p. 071. DOI: 10.21468/SciPostPhys.14.4.071. arXiv: 2105.13354 [hep-ph].

[271] R. Balkin et al. "Runaway relaxion from finite density". In: *JHEP* 06 (2022), p. 023. DOI: 10.1007/JHEP06(2022)023. arXiv: 2106.11320 [hep-ph].

[272] R. Balkin et al. "White dwarfs as a probe of exceptionally light QCD axions". In: *Phys. Rev. D* 109.9 (2024), p. 095032. DOI: 10.1103/PhysRevD.109.095032. arXiv: 2211.02661 [hep-ph].

[273] F. Anzuini et al. "Axion sourcing in dense stellar matter via CP-violating couplings". In: *Phys. Rev. D* 109.8 (2024), p. 083030. DOI: 10.1103/PhysRevD.109.083030. arXiv: 2311.13776 [hep-ph].

[274] B. Bertotti, L. Iess, and P. Tortora. "A test of general relativity using radio links with the Cassini spacecraft". In: *Nature* 425 (2003), pp. 374–376. DOI: 10.1038/nature01997.

[275] J. Sakstein. "Astrophysical Tests of Modified Gravity". PhD thesis. Cambridge U., DAMTP, 2014. DOI: 10.17863/CAM.16133. arXiv: 1502.04503 [astro-ph.CO].

[276] R. B. Wiringa, V. Fiks, and A. Fabrocini. "Equation of state for dense nucleon matter". In: *Phys. Rev. C* 38 (1988), pp. 1010–1037. DOI: 10.1103/PhysRevC.38.1010.

[277] N. K. Glendenning and S. A. Moszkowski. "Reconciliation of neutron star masses and binding of the lambda in hypernuclei". In: *Phys. Rev. Lett.* 67 (1991), pp. 2414–2417. DOI: 10.1103/PhysRevLett.67.2414.

[278] J. M. Lattimer and F. D. Swesty. "A Generalized equation of state for hot, dense matter". In: *Nucl. Phys. A* 535 (1991), pp. 331–376. DOI: 10.1016/0375-9474(91)90452-C.

[279] F. Douchin and P. Haensel. "A unified equation of state of dense matter and neutron star structure". In: *Astron. Astrophys.* 380 (2001), p. 151. DOI: 10.1051/0004-6361:20011402. arXiv: astro-ph/0111092.

[280] S. Typel et al. "Composition and thermodynamics of nuclear matter with light clusters". In: *Phys. Rev. C* 81 (2010), p. 015803. DOI: 10.1103/PhysRevC.81.015803. arXiv: 0908.2344 [nucl-th].

[281] S. Goriely, N. Chamel, and J. M. Pearson. "Further explorations of Skyrme-Hartree-Fock-Bogoliubov mass formulas. XII: Stiffness and stability of neutron-star matter". In: *Phys. Rev. C* 82 (2010), p. 035804. DOI: 10.1103/PhysRevC.82.035804. arXiv: 1009.3840 [nucl-th].

[282] C. Drischler, J. W. Holt, and C. Wellenhofer. "Chiral Effective Field Theory and the High-Density Nuclear Equation of State". In: *Ann. Rev. Nucl. Part. Sci.* 71 (2021), pp. 403–432. DOI: 10.1146/annurev-nucl-102419-041903. arXiv: 2101.01709 [nucl-th].

[283] J. M. Lattimer. "Neutron Stars and the Nuclear Matter Equation of State". In: *Annu. Rev. Nucl. Part. Sci.* 71 (2023), pp. 433–465. DOI: 10.1146/annurev-nucl-102419-124827.

[284] C. Y. Tsang et al. "Determination of the equation of state from nuclear experiments and neutron star observations". In: *Nature Astron.* 8.3 (2024), pp. 328–336. DOI: 10.1038/s41550-023-02161-z. arXiv: 2310.11588 [nucl-th].

[285] P. Virtanen et al. "SciPy 1.0–Fundamental Algorithms for Scientific Computing in Python". In: *Nature Meth.* 17 (2020), p. 261. DOI: 10.1038/s41592-019-0686-2. arXiv: 1907.10121 [cs.MS].

[286] A. C. Hindmarsh. "ODEPACK, A Systematized Collection of ODE Solvers". In: *IMACS Transactions on Scientific Computation* 1 (1983), pp. 55–64. URL: https://computing.llnl.gov/sites/default/files/ODEPACK_pub1_u88007.pdf.

[287] A. C. Hindmarsh. *ODEPACK: Ordinary differential equation solver library*. Astrophysics Source Code Library, record ascl:1905.021. May 2019.

[288] J. D. Lambert. "Computer Solution of Ordinary Differential Equations". In: *The Computer Journal* 19.2 (May 1976), pp. 155–155. ISSN: 0010-4620. DOI: 10.1093/comjnl/19.2.155. eprint: https://academic.oup.com/comjnl/article-pdf/19/2/155/1138926/19-2-155.pdf. URL: https://doi.org/10.1093/comjnl/19.2.155.

[289] R. A. Willoughby. "Numerical Initial Value Problems in Ordinary Differential Equations (C. William Gear)". In: *SIAM Review* 15.3 (1973), pp. 676–678. DOI: 10.1137/1015088. eprint: https://doi.org/10.1137/1015088. URL: https://doi.org/10.1137/1015088.

[290] J. Kierzenka and L. F. Shampine. "A BVP solver based on residual control and the Maltab PSE". In: *ACM Trans. Math. Softw.* 27.3 (Sept. 2001), pp. 299–316. ISSN: 0098-3500. DOI: 10.1145/502800.502801. URL: https://doi.org/10.1145/502800.502801.

[291] U. M. Ascher, R. Matheij, and R. D. Russell. *Numerical Solution of Boundary Value Problems for Ordinary Differential Equations*. Philadelphia: Society for Industrial and Applied Mathematics, 1995. DOI: 10.1137/1.9781611971231. URL: https://doi.org/10.1137/1.9781611971231.

[292] J. A. Nelder and R. Mead. "A Simplex Method for Function Minimization". In: *The Computer Journal* 7.4 (1965), pp. 308–313. DOI: 10.1093/comjnl/7.4.308.

[293] F. Gao and L. Han. "Implementing the Nelder-Mead simplex algorithm with adaptive parameters". In: *Comput. Optim. Appl.* 51.1 (2012), pp. 259–277. DOI: 10.1007/s10589-010-9329-3.

[294] J. Sakstein et al. "Beyond the Standard Model Explanations of GW190521". In: *Phys. Rev. Lett.* 125.26 (2020), p. 261105. DOI: 10.1103/PhysRevLett.125.261105. arXiv: 2009.01213 [gr-qc].

[295] H. O. Silva et al. "Spontaneous scalarization of black holes and compact stars from a Gauss-Bonnet coupling". In: *Phys. Rev. Lett.* 120.13 (2018), p. 131104. DOI: 10.1103/PhysRevLett.120.131104. arXiv: 1711.02080 [gr-qc].

[296] T. Damour and G. Esposito-Farese. "Tensor multiscalar theories of gravitation". In: *Class. Quant. Grav.* 9 (1992), pp. 2093–2176. DOI: 10.1088/0264-9381/9/9/015.

[297] G. Esposito-Farese. "Tests of scalar-tensor gravity". In: *AIP Conf. Proc.* 736.1 (2004). Ed. by C. J. A. P. Martins et al., pp. 35–52. DOI: 10.1063/1.1835173. arXiv: gr-qc/0409081.

[298] J. Sakstein. "Tests of Gravity with Future Space-Based Experiments". In: *Phys. Rev. D* 97.6 (2018), p. 064028. DOI: 10.1103/PhysRevD.97.064028. arXiv: 1710.03156 [astro-ph.CO].

[299] J. Sakstein. "Towards Viable Cosmological Models of Disformal Theories of Gravity". In: *Phys. Rev. D* 91.2 (2015), p. 024036. DOI: 10.1103/PhysRevD.91.024036. arXiv: 1409.7296 [astro-ph.CO].

[300] J. Sakstein and S. Verner. "Disformal Gravity Theories: A Jordan Frame Analysis". In: *Phys. Rev. D* 92.12 (2015), p. 123005. DOI: 10.1103/PhysRevD.92.123005. arXiv: 1509.05679 [gr-qc].

[301] L. Amendola et al. "Cosmology and fundamental physics with the Euclid satellite". In: *Living Rev. Rel.* 21.1 (2018), p. 2. DOI: 10.1007/s41114-017-0010-3. arXiv: 1606.00180 [astro-ph.CO].

[302] R. Akeson et al. "The Wide Field Infrared Survey Telescope: 100 Hubbles for the 2020s". In: (2019). arXiv: 1902.05569 [astro-ph.IM]. URL: https://arxiv.org/abs/1902.05569.

[303] Ž. Ivezić et al. "LSST: from Science Drivers to Reference Design and Anticipated Data Products". In: *Astrophys. J.* 873.2 (2019), p. 111. DOI: 10.3847/1538-4357/ab042c. arXiv: 0805.2366 [astro-ph].

[304] K. N. Abazajian et al. "CMB-S4 Science Book, First Edition". In: (Oct. 2016). arXiv: 1610.02743 [astro-ph.CO].

[305] K. Abazajian et al. "CMB-S4 Science Case, Reference Design, and Project Plan". In: (July 2019). arXiv: 1907.04473 [astro-ph.IM].

[306] M. H. Abitbol et al. "CMB-S4 Technology Book, First Edition". In: (June 2017). arXiv: 1706.02464 [astro-ph.IM].

[307] A. Aghamousa et al. "The DESI Experiment Part I: Science,Targeting, and Survey Design". In: (Oct. 2016). arXiv: 1611.00036 [astro-ph.IM].

[308] K. Hinterbichler and J. Khoury. "Symmetron Fields: Screening Long-Range Forces Through Local Symmetry Restoration". In: *Phys. Rev. Lett.* 104 (2010), p. 231301. DOI: 10.1103/PhysRevLett.104.231301. arXiv: 1001.4525 [hep-th].

[309] K. Hinterbichler et al. "Symmetron Cosmology". In: *Phys. Rev. D* 84 (2011), p. 103521. DOI: 10.1103/PhysRevD.84.103521. arXiv: 1107.2112 [astro-ph.CO].

[310] R. Fardon, A. E. Nelson, and N. Weiner. "Dark energy from mass varying neutrinos". In: *JCAP* 10 (2004), p. 005. DOI: 10.1088/1475-7516/2004/10/005. arXiv: astro-ph/0309800.

[311] A. W. Brookfield et al. "Cosmology of mass-varying neutrinos driven by quintessence: theory and observations". In: *Phys. Rev. D* 73 (2006). [Erratum: Phys.Rev.D 76, 049901 (2007)], p. 083515. DOI: 10.1103/PhysRevD.73.083515. arXiv: astro-ph/0512367.

[312] T. Chiba, T. Okabe, and M. Yamaguchi. "Kinetically driven quintessence". In: *Phys. Rev. D* 62 (2000), p. 023511. DOI: 10.1103/PhysRevD.62.023511. arXiv: astro-ph/9912463.

[313] C. Armendariz-Picon, V. F. Mukhanov, and P. J. Steinhardt. "Essentials of k essence". In: *Phys. Rev. D* 63 (2001), p. 103510. DOI: 10.1103/PhysRevD.63.103510. arXiv: astro-ph/0006373.

[314] M. Cicoli, G. Dibitetto, and F. G. Pedro. "Out of the Swampland with Multifield Quintessence?" In: *JHEP* 10 (2020), p. 035. DOI: 10.1007/JHEP10(2020)035. arXiv: 2007.11011 [hep-th].

[315] K. Koyama. "Cosmological Tests of Modified Gravity". In: *Rept. Prog. Phys.* 79.4 (2016), p. 046902. DOI: 10.1088/0034-4885/79/4/046902. arXiv: 1504.04623 [astro-ph.CO].

[316] P. G. Ferreira. "Cosmological Tests of Gravity". In: *Ann. Rev. Astron. Astrophys.* 57 (2019), pp. 335–374. DOI: 10.1146/annurev-astro-091918-104423. arXiv: 1902.10503 [astro-ph.CO].

[317] J. J. Heckman et al. "Exploring $2+2$ Answers to $3+1$ Questions". In: *Int. J. Mod. Phys. A* 37.34 (2022), p. 2250201. DOI: 10.1142/S0217751X22502013. arXiv: 2208.02267 [hep-th].

[318] L. F. Abbott. "A Mechanism for Reducing the Value of the Cosmological Constant". In: *Phys. Lett. B* 150 (1985), pp. 427–430. DOI: 10.1016/0370-2693(85)90459-9.

[319] P. W. Graham, D. E. Kaplan, and S. Rajendran. "Cosmological Relaxation of the Electroweak Scale". In: *Phys. Rev. Lett.* 115.22 (2015), p. 221801. DOI: 10.1103/PhysRevLett.115.221801. arXiv: 1504.07551 [hep-ph].

[320] A. Hook and G. Marques-Tavares. "Relaxation from particle production". In: *JHEP* 12 (2016), p. 101. DOI: 10.1007/JHEP12(2016)101. arXiv: 1607.01786 [hep-ph].

[321] T. Flacke et al. "Phenomenology of relaxion-Higgs mixing". In: *JHEP* 06 (2017), p. 050. DOI: 10.1007/JHEP06(2017)050. arXiv: 1610.02025 [hep-ph].

[322] K. Choi and S. H. Im. "Constraints on Relaxion Windows". In: *JHEP* 12 (2016), p. 093. DOI: 10.1007/JHEP12(2016)093. arXiv: 1610.00680 [hep-ph].

[323] I. Brivio and M. Trott. "Radiatively Generating the Higgs Potential and Electroweak Scale via the Seesaw Mechanism". In: *Phys. Rev. Lett.* 119.14 (2017), p. 141801. DOI: 10.1103/PhysRevLett.119.141801. arXiv: 1703.10924 [hep-ph].

[324] J. A. Dror, R. Laha, and T. Opferkuch. "Probing muonic forces with neutron star binaries". In: *Phys. Rev. D* 102.2 (2020), p. 023005. DOI: 10.1103/PhysRevD.102.023005. arXiv: 1909.12845 [hep-ph].

[325] J. R. Espinosa et al. "First Glimpses at Higgs' face". In: *JHEP* 12 (2012), p. 045. DOI: 10.1007/JHEP12(2012)045. arXiv: 1207.1717 [hep-ph].

[326] J. M. Cline and K. Kainulainen. "Electroweak baryogenesis at high bubble wall velocities". In: *Phys. Rev. D* 101.6 (2020), p. 063525. DOI: 10.1103/PhysRevD.101.063525. arXiv: 2001.00568 [hep-ph].

[327] V. Cardoso et al. "Testing strong-field gravity with tidal Love numbers". In: *Phys. Rev. D* 95.8 (2017). [Addendum: Phys.Rev.D 95, 089901 (2017)], p. 084014. DOI: 10.1103/PhysRevD.95.084014. arXiv: 1701.01116 [gr-qc].

[328] E. Berti, K. Yagi, and N. Yunes. "Extreme Gravity Tests with Gravitational Waves from Compact Binary Coalescences: (I) Inspiral-Merger". In: *Gen. Rel. Grav.* 50.4 (2018), p. 46. DOI: 10.1007/s10714-018-2362-8. arXiv: 1801.03208 [gr-qc].

[329] W. Baade and F. Zwicky. "Cosmic Rays from Super-Novae". In: *Proc. Nat. Acad. Sci.* 20.5 (1934), p. 259. DOI: 10.1073/pnas.20.5.259.

[330] W. Baade and F. Zwicky. "On Super-Novae". In: *Proc. Nat. Acad. Sci.* 20.5 (1934), pp. 254–259. DOI: 10.1073/pnas.20.5.254.

[331] J. Chadwick. "Possible Existence of a Neutron". In: *Nature* 129 (1932), p. 312. DOI: 10.1038/129312a0.

[332] R. C. Tolman. "Static Solutions of Einstein's Field Equations for Spheres of Fluid". In: *Phys. Rev.* 55 (1939), pp. 364–373. DOI: 10.1103/PhysRev.55.364.

[333] J. R. Oppenheimer and G. M. Volkoff. "On Massive Neutron Cores". In: *Phys. Rev.* 55 (1939), pp. 374–381. DOI: 10.1103/PhysRev.55.374.

[334] A. G. Cameron. "Neutron Star Models". In: *Astrophys. J.* 130 (1959), pp. 884–894. DOI: 10.1086/146780.

[335] T. Skyrme. "The effective nuclear potential". In: *Nucl. Phys.* 9 (1959), pp. 615–634. DOI: 10.1016/0029-5582(58)90345-6.

[336] T. Chiba and M. Yamaguchi. "Conformal-Frame (In)dependence of Cosmological Observations in Scalar-Tensor Theory". In: *JCAP* 10 (2013), p. 040. DOI: 10.1088/1475-7516/2013/10/040. arXiv: 1308.1142 [gr-qc].

[337] A. Stabile, A. Stabile, and S. Capozziello. "Conformal Transformations and Weak Field Limit of Scalar-Tensor Gravity". In: *Phys. Rev. D* 88.12 (2013), p. 124011. DOI: 10.1103/PhysRevD.88.124011. arXiv: 1310.7097 [gr-qc].

[338] E. J. Copeland, P. Millington, and S. S. Muñoz. "Fifth forces and broken scale symmetries in the Jordan frame". In: *JCAP* 02.02 (2022), p. 016. DOI: 10.1088/1475-7516/2022/02/016. arXiv: 2111.06357 [hep-th].

[339] A. Kuntz and E. Barausse. "Angular momentum sensitivities in scalar-tensor theories". In: *Phys. Rev. D* 109.12 (2024), p. 124001. DOI: 10.1103/PhysRevD.109.124001. arXiv: 2403.07980 [gr-qc].

[340] L. Hui, A. Nicolis, and C. Stubbs. "Equivalence Principle Implications of Modified Gravity Models". In: *Phys. Rev. D* 80 (2009), p. 104002. DOI: 10.1103/PhysRevD.80.104002. arXiv: 0905.2966 [astro-ph.CO].